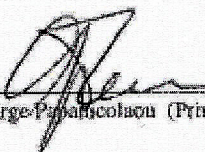# TIME-REVERSAL FOR TEMPORAL COMPRESSION AND SPATIAL FOCUSING OF ACOUSTIC WAVES IN ENCLOSURES

A DISSERTATION

SUBMITTED TO THE DEPARTMENT OF PHYSICS

AND THE COMMITTEE ON GRADUATE STUDIES

OF STANFORD UNIVERSITY

IN PARTIAL FULFILLMENT OF THE REQUIREMENTS

FOR THE DEGREE OF

DOCTOR OF PHILOSOPHY

Déborah Berebichez Selechnick

August 2004

I certify that I have read this dissertation and that, in my opinion, it is fully adequate in scope and quality as a dissertation for the degree of Doctor of Philosophy.

George Papanicolaou (Principal Adviser)

I certify that I have read this dissertation and that, in my opinion, it is fully adequate in scope and quality as a dissertation for the degree of Doctor of Philosophy.
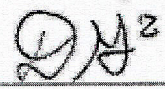
Renata Kallosh

I certify that I have read this dissertation and that, in my opinion, it is fully adequate in scope and quality as a dissertation for the degree of Doctor of Philosophy.

Kam Moler

I certify that I have read this dissertation and that, in my opinion, it is fully adequate in scope and quality as a dissertation for the degree of Doctor of Philosophy.

David Goldhaber-Gordon

Approved for the University Committee on Graduate Studies.

Abstract

Time-reversal is the process whereby a signal is emitted by a source and propagates in a medium with scatterers in it. The waves are recorded at a receiver over a time much larger than the original pulse width so as to capture the multiple scattering. The receiver then reverses the signal in time and re-emits it into the same channel. The waves back-propagate through the medium retracing the multiple scattering paths taken on the way to the receiver and ultimately refocus at the original source location in space and time. In richly scattering environments such as rooms with scatterers in them, time-reversal makes use of the detailed structure recorded as delay-spread to concentrate sound energy to a specific location at a certain time. Time-reversal in an enclosure with a single detector achieves a spatial resolution of one half of a wavelength of the initial sound signal.

A two-dimensional finite-difference time-domain code was set up to study the phenomena of time compression and spatial resolution of time-reversed acoustic signals in closed environments with strong reverberations. By varying several factors such as boundary conditions and the addition of randomly-placed detectors and scatterers to the enclosure, quality of spatial focusing is determined. Simulations are carried out for reflective and partially reflective boundaries, as well as for absorbing boundary conditions. In each case, the addition of scatterers and detectors is explored and its effect on quality of refocusing. In all cases, temporal and spatial resolution are determined by measuring the amplitude of the refocused peak and surrounding waveform. Also, RMS-delay of signals is ascertained.

The addition of scatterers reduces the size of side lobes surrounding the refocused peak. Multiple detectors provide better refocusing quality by increasing the signal to noise ratio at the source location. A lot of absorption destroys time-reversal focusing. To explain time-reversal effects in absorbing enclosures, results of the simulation code in enclosure with absorbing boundaries are compared with an analytic calculation in free-space. The similarities corroborate how absorption limits focusing in similar manner to free space.

Time-reversal decreases the probability of unwanted wave interference at places different

than the desired source location. It also minimizes the undesired effects of time dispersion. Thus, it is confirmed that time-reversal is advantageous for communications even when there is only partial knowledge of the channel. Moreover, due to high temporal resolution of signals, time-reversal permits bit streams of data to be transferred with low inter-symbol interference. Finally and foremost, by combining the spatial and temporal resolution of signals when using time-reversal, a communications link is established to simultaneously send distinct messages to different receiver locations in a room. The results of this research are threefold: time reversal is instrumental for carrying out communications in inhomogeneous environments; the space-time focusing is robust, and it is beneficial for high data-rate acoustic communications.

Acknowledgement

Contents

List of Tables

List of Figures

Chapter 1

Introduction

1

1.1 What is Time-Reversal?

In a typical time-reversal experiment a signal is emitted by a source and propagates in a medium with many scatterers in it. The waves are recorded at a receiver over a time much larger than the original pulse width so as to capture the multiple scattering. The receiver then reverses the signal in time and re-emits it into the same channel. The waves back-propagate through the medium retracing the multiple scattering paths taken on the way to the receiver and ultimately refocus at the original source location in space and time.

"In a time-reversal cavity the array completely surrounds the source and thus the time-reversed signals propagate backward through the medium and go through all the multiple scattering, reflections and refraction that they underwent in the forward direction. If the time-reversal operation is only performed on a limited angular area (a time-reversal mirror, TRM), a small part of the field radiated by the source is captured and time reversed, thus limiting reversal and focusing quality." [1]

The multiple reflections with the boundaries or obstacles in an enclosure, allow the redirection of one part of the initial wave toward the TRM, that would normally miss the transducer array. Thus boundaries or inhomogeneities produce multipathing and the TRM appears to have a much larger aperture than its physical size. [1]

1.2   Previous work

Derode *et al* [2] performed the first experiments showing the reversibility of an acoustic wave propagating through a random collection of scatterers with strong multiple-scattering contributions. In the experiment, a pint source generates a pulse which scatters through 2000 steel rods immersed in a water tank. The time-reversed waves are found to converge to their source and recover their original waveform, despite the high order of multiple scattering by the rods and the normal sensitivity to initial conditions of time-reversal processes. The observed spatial resolution of the initial pulse, after time-reversal, was one-sixth of the theoretical limit for the mirror's aperture. The improvement in spatial resolution comes from the fact that the array of random scatterers acts as a "pseudo-lens" with an angular aperture much wider than the size of the TRM alone. Or, as Fink puts it : "because of the scattering sample, the array is able to detect higher spatial frequencies than in a purely homogeneous medium. High frequencies that would have been lost otherwise are redirected toward the array, due to the presence of the scatterers in a large area." [1]

Snieder and Scales [3] carried out numerical simulations that show the fundamental difference between waves and particles in the presence of multiple scattering by random scatterers. Particle propagation turns out to be strongly unstable and a complete focusing on the source only take place if the velocities and positions of all particles are known exactly. In contrast, they observe wave propagation is significantly more stable. They are not so sensitive to initial conditions as particles are. The paper presents analytical and numerical evidence for the different stability properties of wave and particle propagation. The degree δ to which errors in the positions and velocities of particles destroy the quality of focusing in a time-reversal experiment, serves as a diagnostic of the stability of of the wave or particle propagation. In the case of particles, the critical length scale δ that causes a significant divergence to a future trajectory at a time $t + dt$ from the previous one at time t decreases exponentially with time. In the case of waves, however, the same parameter decreases as the square root of time. Physically, in the case of particles, each one follows a very specific trajectory, whereas waves propagate along all possible trajectories, visiting all scatterers in all possible combinations. [1]

Fink explains the time-reversal process' temporal compression of signals viewing it as a "time correlator." He also describes the spatial resolution as the quality of time-reversal as a "spatial correlator." He says that the time-reversed waves can be interpreted as an estimate of the space and time auto-correlation functions of the waves scattered by a random

medium. [1] He refers to the fact that the medium itself computes a point to point correlation function (a matched field) between the source and receiver. This space-time correlation ensures that spatial focusing and temporal compression of the signal occur.

There are two main aspects investigated during the time-reversal experiment: the temporal compression of the signal at the source location, and the spatial resolution of the time-reversed wave around the source location.

In a time-reversal cavity (TRC), the transducer array samples a closed surface surrounding the acoustic source. Just like the multiple scattering process widens the effective TRM aperture, the reflections from the boundaries of waves propagating in waveguides or cavities have the same widening of the aperture effect. Essentially, it is like replacing some of the TRC transducers by reflecting boundaries that help redirect one part of the incident wave toward the TRM aperture. " Thus, spatial information is converted into the time domain and the reversal quality depends crucially on the duration of the time-reversal window, i.e. the length of the recording to be reversed." [1]

In [4], experiments conducted by Roux in ultrasonic waveguides are reported. It shows how a TRM is able to compensate for the distortions induced by multi-paths in an acoustic transmission. In a water waveguide of length L ∼ 800mm with a vertical depth of H ∼ 40mm a source pulse is generated at one end and received at the other end by a TRM. The results show a temporal compression of the signal nearly identical to the one obtained in time-reversal experiments trough a random media in free space. As for spatial resolution, the time-reversed field focuses on a spot of size much smaller than that obtained with a comparable TRM in free space. This can be explained by the "barber shop effect," where just like in a medium bounded by two mirrors, the effective TRM is not only the physical TRM, but also a set of "virtual TRMs" that expand the effective aperture of the TRM. If one takes into account the first ten arrivals, the theoretical effective aperture of the mirror array is ten times larger than the physical aperture.

It was, perhaps, the work of A. Parvulescu in 1967 that first suggested the idea of using time-reversal in communications. [5] Investigating ocean and underwater acoustics, Parvulescu and Clay performed single-channel time-reversal in shallow water at sea with one transducer working in a time-reversed mode. Their results displayed temporal compression of the signal. However, the spatial resolution later attained with different TRMs, did not come out of the experiments.

It was not until Jackson [6] that the theory of time-reversal in underwater acoustics was developed. Dowling [7] utilized the first arrival of a sequence of pulses as a filter for

subsequent arrivals. This was carried out when the pulses were traveling in a highly refracting medium. He concludes that this form of processing, called "passive phase-conjugate (PPC) processing" achieves temporal compression in multi-path random media.

Later, the work of William Kuperman *et al* consolidated a broad kind of experiments that constitutes a solid demonstration of time-reversal communications in underwater acoustics. Kuperman *et al* have performed various underwater acoustics experiments since 1996. [8] [9], [10]. The experiments involved the use of a 120 m deep ocean waveguide and a 24-element TRM. At the frequencies of 500 Hz and 3.5 kHz they were able to obtain time-reversal focusing from distances of 7 km to 30 km. They argue that temporal variations in the ocean due to surface and internal waves degrade the focus of the signal in time-reversal. However, this degradation is tolerable if the average Green function is not severely perturbed by these time changes. [8] Moreover, they achieved a shift of the focal range of approximately 10 % by changing the central frequency of the TRM prior to retransmission. [9]

Recently, Yon *et al* applied the technique of time-reversal to audible range acoustics. [11] The experiments are carried out in a room with many obstacles such as tables and people for acoustic wave propagation. Roux *et al* had already demonstrated that time-reversal takes advantage of multiple reflections in a waveguide to produce better spatial refocusing than in free space. [12] Similarly, Yon reports: "In the case of propagation in a reverberating medium, such as our room, time reversal gives results that appear to be even better than those obtained in free space."[1]

It is interesting to note that among some of the effects produced by boundaries in reverberant enclosures is the fact that the waves arriving at the focal point after time-reversal propagate as if they were actually emitted from "multiple sets of virtual sources. These sources are the images of the actual emitting antenna with respect to the different interfaces in the rooms (walls or furniture)." [2] This gives the illusion of an infinite array of detectors, and that is why the spatial focusing results are so good. In his paper [11], Yon argues that the width of the focusing spot does is independent of antenna size (something we also find in our experiments). He claims the size of the spot is "always $\lambda_0/2$," [3] where λ_0 is the central wavelength of the original pulse.

Larraza *et al* study non-coherent communications, where energy is the only measurement carried out by the receiver, and phase-information is not required. They carry out experiments with a slowly time-varying environment and obtains good spatial and temporal results

---

[1] [11], p. 1536
[2] [11], p. 1536
[3] [11], p. 1536

with time-reversal. [13] and [14] Thus, proving the usefulness of time-reversal in this kind of communications.

Derode *et al* reports success when experimenting with transmitting and spatially focusing ultrasound codes to specific receivers. [15]

Fink has also carried out time-reversal experiments with elastic waves propagating in a silicon (silicon has low absorption) wafer. [1] The wafer has the shape of a chaotic billiard table which displays ergodic properties. "The chaotic stadium geometry ensures that each acoustic ray radiated by the source will pass, after several reflections, sufficiently close to any point of the cavity." [1] The reverberant acoustic field created as no information is lost to the outside. The ergodic properties of the wafer make it possible to collect the information not at a full TRM, but at a single point in space. Draeger and Fink [16] [10] [17] [18] showed both theoretically and experimentally that it is possible to obtain time-reversal focusing using a single TR channel operating in a closed cavity. The field is measured at one point over a very long period of time compared to the initial pulse duration. The time-reversed wave is re-emitted from this same point and focusing is obtained at the original source location. The results show temporal compression of the pulse and spatial resolution around the source location of size half the wavelength of the flexural wave. We see that in the case of a single channel time-reversal, a chaotic geometry is actually helpful in ensuring that most positions in the cavity will be visited by the traveling waves. "The procedure approaches the performance of a closed TRC, which has an aperture of 360degrees. Hence, a one-point time-reversal in a chaotic cavity produces better results than a TRM in an open system. Using reflections at the edge, focusing quality is not aperture limited and, in addition, the time-reversed collapsing wavefront approaches the focal spot from all directions" [1]

In a chaotic cavity, the spatial resolution is independent of the TRM aperture [1]. "A similar result has been observed in the time-reversal experiment conducted in multiply scattering medium. A clear refocusing has been obtained with only a single array element. The focusing process works with broadband pulses (the transducer center frequency is 3.5 MHz with a 50% bandwidth at -6 dB). For each individual frequency there is no focusing and the estimate of the spatial correlation is very noisy. However, for a large bandwidth, if we have statistical decorrelation of the wave fields for different frequencies, the time-reversed field is self-averaging." [1]

Early experiments in time-reversal acoustics are described in [2], whereas some more recent papers on the subject are [19], [20], [1] and [15]. Carrying out time-reversal in a waveguide for which the medium inside is randomly inhomogeneous dramatically improves

the spatial resolution of the back-propagated signal compared to the one obtained in a homogeneous waveguide. The reason for this super-resolution is that multiple scattering due to the medium's inhomogeneities provides information about the medium from many more directions than if randomness were absent, and steers it to the receiver. The propagating wave bounces from different angles that would have remained unexplored in a homogeneous medium. It is this angle diversity that provides detailed information about the channel and yields a waveform with delay-spread in time. This information is then used by the time-reversal process to achieve sharp spatial focusing. Moreover, the frequency diversity characteristic of the broadband signals used in time-reversal make it a statistically stable process that does not depend on the realization of the medium. [21], [22], [4], [23], [24]. Other experiments that show the ability of time-reversal to improve the focusing of a signal in inhomogeneous media are developed in [25].

An important application of time-reversal is in communications. This is because by focusing signals in space and time, it enables efficient and secure communication links. Experiments in communications using time-reversal were carried out in a shallow water environment [26], as well as with ultrasound waves in a laboratory [15]. Time-reversal experiments in the ocean are reported in [27]. Recently there has been experimental and theoretical work on underwater acoustic communication by passive-phase conjugation [28], as well as numerical simulations on time-reversal in multiple input/single output systems [29]. Finally, experiments in an enclosure using single-channel communications are carried out in [30].

Recently, James V. Candy *et al.* demonstrates how time-reversal is helpful for communications in a reverberant channel. He argues "T/R receivers are capable of extracting the transmitted coded sequence from noisy microphone sensor measurements with zero-symbol error."[4]

1.3   Motivation

The use of time-reversal in the field of wireless communications is relatively a new field.

Generally, the capacity of wireless systems is greatly increased by using multi-elemnt arrays at both the transmitter and receiver antennas. [[32]] By constraining the channel bandwidth and the total transmitted power, spatial diversity in localization of antennas yields very large capacity. In most multiple-input multiple-output (MIMO) array systems, the channel characteristic is not known at the transmitter. This is because an unpractical

---

[4] [31], p. 1621

and very fast feedback link between transmitter and receiver would be needed to transmit the channel information. Sophisticated signal processing can explout the spatial extension of the array to define and separate the original transmitter that sent the signal. Furthermore, having a feedback loop takes a finite time of information transmission, which would make the assumption that the channel is unchanging an invalid one. So, most MIMO systems operate without knowledge of the channel at the transmitter. "Multiple-input multiple-output (MIMO) communication techniques make use of multi-element antenna arrays at both the TX (transmitter) and RX (receiver) side of a radio link and have been shown theoretically to drastically improve the capacity over more traditional single-input multiple-output (SIMO) systems." [5]

Multi-pathing is then, benefcial for MIMO communication systems. The spatial diversity gained from the collection of the signal at several receiver antennas located in different places proves to be advantageous in increaisng capacity f the channel. However, work is being done to determine the addition of a time-reversal step in the beginning of the communications link in order for the transmitter to learn the channel. With the addition of this knowledge, it is expected that communications will be more efficient. Some results on this area Arnold's paper have shown that the capacity does not increase, but that spatial focusing of the transmitted signals is greatly improved. Thus, tere is an advantage to use time-reversal in combination with MIMO wireless systems.

1.4 Outline

---

[5] [33], p. 1083

Chapter 2

Physics of Room Acoustics: Sound Waves

Some of the concepts in this chapter are based on similar introductions to acoustics by Heinrich Kuttruff in his book *Room Acoustics* [34], Leo L. Beranek's book *Acoustics* [35] as well as David T. Blackstock's *Fundamentals of physical acoustics* [36]

The section "Defining Acoustical Quantities" follows the definitions employed in Beranek's book. The derivation of the wave equation is carried out from Newton's equations of motion and the sections on sound energy and intensity are written in a manner affine to Beranek's approach. Finally, the section on general impedance boundaries displays the standard derivation using harmonic plane waves.

2.1   Introduction

A sound occurs when a disturbance causes a sudden alteration in pressure that propagates through air or other elastic materials and can be detected by an instrument or a person. Pressure is a scalar quantity, defined as force per unit area, specifically the area perpendicular to where the force is applied. When a force is applied to a volume of gas, it makes the individual particles compress into a tighter volume. This force is proportional to the added pressure times the area where the force is applied. If the compression occurs slowly, the temperature in the gas remains constant. The process is said to be *isothermal* and it is possible to write

$$\Delta P = - K \, \Delta V \qquad \text{slow process} \tag{2.1}$$

where ΔP and ΔV are infinitesimal changes in pressure and volume respectively and K is a constant. The reason for the minus sign is that a positive increment in pressure causes the volume to decrease. The heat in the gas flows from some areas to others in order to maintain the overall temperature the same. In contrast, if the volume changes rapidly, heat has no time to travel and share energy with other particles in the gas. Temperature increases for compressions and decreases for expansions, and the process is called *adiabatic*. The incremental pressure (above the equilibrium pressure) produced is

$$\Delta P = -1.4\, K\, \Delta V \qquad \text{fast process, diatomic gas} \qquad (2.2)$$

Sound waves are essentially adiabatic oscillations in a gas. The temperature changes that occur during an adiabatic process cause the molecules in the gas to move quicker and to collide more frequently with the walls of a container. Thus, there is a greater momentum transfer per collision than in an isothermal process.

The changes in incremental pressure, also called "acoustic pressure," cause an alternation between compressions and rarefactions of certain areas in the gas. The particles move from areas of higher pressure to adjacent areas of lower pressure displacing other particles who were in their equilibrium positions by imparting momentum unto them. This creates sound waves that propagate throughout the entire volume.

The particles in the gas change position sinusoidally with a frequency ν and a cycle period τ that repeats the waveform every period. The particle displacement undulate with the same frequency as the force causing the motion. Phase differences represent the way two waveforms are aligned with respect to each other. The particle velocity is in phase with the pressure oscillations that in turn are 90° out of phase with the particle displacement. Usually, with time, there is dissipation of the sound waves which decay as they interact with the rest of the gas or other elements. As this occurs, most of the energy stored in the waves gets converted into heat.

Large variations in pressure produce loud sounds determined by a large amplitude of the waves. There is a very large range of perceptible sound amplitudes, thus, it is common to use logarithmic units called Decibels and abbreviated db. On the decibel scale, 0.0 db corresponds to about the normal threshold of hearing and 130 db to the point at which sound becomes painful. It is reasonable to expect that the pressure change δp and density change $\delta \rho$ are very small compared to their equilibrium values in a gas p_0 and ρ_0 respectively.

Any acoustical signal can be unambiguously described by its time function $s(t)$ where

s denotes a sound pressure, a component of particle velocity, or the instantaneous density of air, for instance. [1] If $s(t)$ is a sine or cosine function -or an exponential with imaginary exponent- we speak of a harmonic signal. Fourier Theorem says that virtually all signals can be considered as superposition of harmonics.

2.2   Defining Acoustical Quantities

Before we derive the acoustical wave equation, it is important to define a series of physical quantities that describe sound propagation in gases. The following is a list of practical definitions that will be used throughout the chapter when discussing different aspects of acoustics. Throughout the thesis we shall use the standard mks system of measurement.

The *mean free path length* is defined as the distance the molecules travel before colliding with other molecules. For sound to be created, the regions over which pressure and density change must be much larger than the mean free path. As a result of this, physical quantities will not be described in terms of each of its constituent particles, but as their average value over a region of gas.

The pressure in the atmosphere is commonly taken to be $p_0 = 1.013 x 10^5 N/m^2$, and referred to as *standard atmospheric pressure* or static pressure. This corresponds to a barometric reading of 0.760 m Hg at $0°C$. In contrast, instantaneous sound pressure $p(t)$ at a point is the additional change in pressure from the static pressure at a given instant resulting from the presence of a sound wave. The microbar (μb) is a usual unit of measurement for pressure and is equivalent to $0.1 N/m^2$. Furthermore, the *effective sound pressure p* at a point is the root-mean-square (rms) value of the instantaneous sound pressure over a time interval at that point. [2]

The equilibrium density of air ρ_0 is given by

$$\rho_0 = 1.29 \frac{273}{T} \frac{p_0}{0.76} \ \text{kg} / \text{m}^3 \tag{2.3}$$

where T is the absolute temperature in degrees Kelvin and p_0 is the barometric pressure in meters of mercury. At normal room temperature of $T = 295°K$ $(22°C)$, and for a static pressure of $p_0 = 0.751$ m Hg, the ambient density is $\rho_0 = 1.18 \ kg / m^3$.

---

[1] [34], p. 15
[2] definition taken from [35]

The speed of sound in air, c, is given by the formula

$$c = 331.4 \sqrt{1 + \frac{\theta}{273}} \text{ m/s} \tag{2.4}$$

Sound in air travels with a speed that is very closely independent of frequency. In reality, as temperature changes, the velocity of sound is affected and the medium is no longer at rest. However, the effects of temperature change in rooms is so small it can be neglected in room acoustics. At a normal room temperature of $\theta = 22°$, $c = 344.8$ m/s.

The instantaneous particle velocity at a point $\mathbf{v}(t)$ is the velocity, due to the sound wave only, of a given infinitesimal part of the medium at a given instant. It is measured over and above any motion of the medium as a whole. The *effective particle velocity* at a point is the root mean square of the instantaneous particle velocity.

The *acoustic impedance Z_A* at a given surface is defined as the complex ratio of effective sound pressure averaged over the surface to effective volume velocity through it.

$$Z_A = \frac{p}{U} \qquad\qquad \text{N-s/m}^5 \qquad\qquad \text{(mks acoustic ohms)} \tag{2.5}$$

where U is the volume velocity given by multiplying the instantaneous particle velocity times the perpendicular area through which the gas flows.

The *specific acoustic impedance Z_s* is the complex ratio of the effective sound pressure at a point of an acoustic medium or mechanical device to the effective particle velocity at that point.

$$Z_s = \frac{p}{v} \qquad\qquad \text{N-s/m}^3 \qquad\qquad \text{(mks rayls)} \tag{2.6}$$

The *characteristic impedance $\rho_0 c$* is the ratio of the effective sound pressure at a given point to the effective particle velocity at that point in a free, plane progressive sound wave. It is equal to the product of the density of the medium times the speed of sound in the medium and its unit is the mks rayl. For air $\rho_0 c = 407$ mks rayls which is valid for a temperature of $22°$ C and a barometric pressure of 0.751 m Hg.

Sound intensity I is the average rate at which sound energy is transmitted through a unit area perpendicular to the specified direction at the point considered. It is measured in a specific direction at a point. In a plane or spherical free-progressive sound wave the intensity in the direction of propagation is

$$I = \frac{p^2}{\rho_0 c} \qquad\qquad \text{watts /m}^2 \tag{2.7}$$

Sound energy density D is the sound energy in a given infinitesimal part of the gas divided by the volume of that part of the gas. In a plane wave, the sound energy density at a point is

$$D = \frac{p^2}{\rho_0 c^2} \qquad \text{watt-s}/\text{m}^3 \tag{2.8}$$

The *acoustic intensity level* is a quantity that expresses the ratio of two sound intensities in logarithmic form, and its unit is the decibel.

$$\text{Acoustic intensity level} = 10 \log_{10}\left(\frac{I_1}{I_2}\right) \qquad \text{db} \tag{2.9}$$

where I_1 and I_2 are two sound intensities. Alternatively, it can also be expressed as

$$\text{Acoustic intensity level} = 20 \log_{10}\left(\frac{p_1}{p_2}\right) \qquad \text{db} \tag{2.10}$$

where p_1 and p_2 are the effective sound pressures at different points.

The *sound pressure level* (SPL) of a sound, in decibels, is

$$\text{SPL} = 20 \log_{10}\left(\frac{p}{p_\text{ref}}\right) \qquad \text{db} \tag{2.11}$$

where p is the measured effective pressure of the sound to a reference effective sound pressure p_ref. A common value used for p_ref is $0.0002\,\mu$bar $(2\,x\,10^{-5}\,\text{N}/\text{m}^2)$ and it should always be stated explicitly.

Finally, the *acoustic power level* (PWL) is defined as

$$\text{PWL} = 10 \log_{10}\left(\frac{W}{W_\text{ref}}\right) \qquad \text{db} \tag{2.12}$$

where W is the acoustic power radiated by the source and the reference acoustic power is $W_\text{ref} = 10^{-13}$ watt.

2.3 Derivation of the Acoustic Wave Equation

Sound propagation is a result of mechanical forces and the properties of gases, so the derivation of the equations of sound propagation is a consequence of Newton's laws. In Figure 2.1 we present a volume element of gas with density ρ. We suppose a differential of pressure $p(x_0 + \Delta x) - p(x_0)$ is acting on the surface area elements $d\mathbf{S}$ on the right $(x_0 + \Delta x)$ and left

(x_0) faces of the cube. The volume of the cube is $V = \Delta x |d\mathbf{S}|$. For any volume element in the gas such as this, there is as much gas leaving the volume as there is gas entering the volume by crossing its surface dS. We concentrate on $d\mathbf{S}$, an element of the surface area pointing in the normal direction $\hat{n}$ at the position $(x_0 + \Delta x)$. Since $\mathbf{v}$ is the gas velocity at this surface, it is the component of $\mathbf{v}$ in the direction of $d\mathbf{S}$ which is responsible for transporting the mass out of V. Therefore, the mass flowing out of V is $\rho\, \mathbf{v} \cdot d\mathbf{S}\, dt$.   In terms of the mass flux
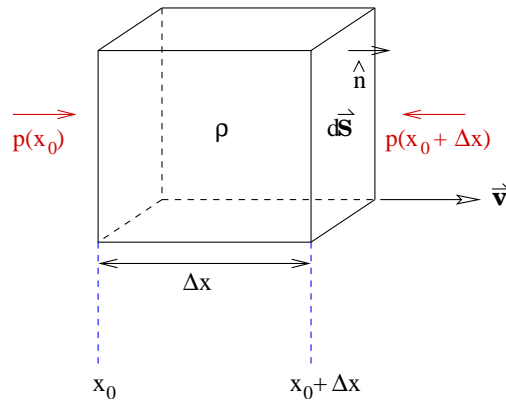
Figure 2.1: Diagram of volume element in a gas with density ρ. A differential of pressure $p(x_0 + \Delta x) - p(x_0)$ is acting on the surface area elements $|d\mathbf{S}|$ on the right $(x_0 + \Delta x)$ and left (x_0) faces of the cube. The velocity of the surface area at $(x_0 + \Delta x)$ is $\mathbf{v}$. The normal $\hat{n}$ is consider pointing to the right of this surface to the outside of the volume

(mass per unit time) $\rho\, \mathbf{v} \cdot d\mathbf{S}$, we obtain the total rate of change of mass in the volume by integrating this over the entire surface S

$$\text{flux out of V} = -\oint_{\partial V} \rho\mathbf{v} \cdot d\mathbf{S} \tag{2.13}$$

The minus sign is added to designate mass as decreasing. We use the divergence theorem to write this integral as

$$-\oint_{\partial V} \rho\mathbf{v} \cdot d\mathbf{S} = -\int_V \nabla \cdot (\rho\mathbf{v})\, dV \tag{2.14}$$

On the other hand, the total mass in the volume is $M = \int_V \rho dV$, so its rate of change is given by

$$\frac{dM}{dt} = \frac{d}{dt} \int_V \rho dV = \int_V \frac{\partial \rho}{\partial t} dV \tag{2.15}$$

Because the rate of change of mass in the volume element should be equal to the mass flux leaving the volume, equations (2.14) and (2.15) must be equal

$$\int_V \frac{\partial \rho}{\partial t} dV = -\int_V \nabla \cdot (\rho \mathbf{v}) \, dV \tag{2.16}$$

$$\int_V \left[\frac{\partial \rho}{\partial t} + \nabla \cdot (\rho \mathbf{v}) \right] dV = 0 \tag{2.17}$$

This last equation is valid for any volume V, which means the integrand should vanish, leaving us with the equation of continuity

$$\boxed{\frac{\partial \rho}{\partial t} + \nabla \cdot (\rho \mathbf{v}) = 0} \tag{2.18}$$

Using Newton's Second Law, the net force on the volume element of gas equals its mass times its acceleration, we write the force per unit volume on an element of gas

$$\mathbf{f} = \rho \frac{d\mathbf{v}}{dt} \tag{2.19}$$

Independently, we consider the force per unit volume exerted by the pressure directed into the volume element of gas. Pressure is defined as force per unit area, where the area is perpendicular to the direction in which the force is being applied. As seen from Figure 2.1, this is

$$\mathbf{f} = \frac{p(x_0) - p(x_0 + \Delta x)}{\Delta x} = -\frac{\partial p}{\partial x} \tag{2.20}$$

In terms of the definition of gradient in the $\hat{x}$ direction, the total force on the element is

$$\mathbf{f} = -\nabla p \tag{2.21}$$

which is the force due to the pressure gradient acting on a volume element of gas. Since both equations (2.19) and (2.21) express the force on the unit volume of gas they must be equal

$$\mathbf{f} = \rho \frac{d\mathbf{v}}{dt} = -\nabla p \tag{2.22}$$

To complete the former equation of motion though, we want to generalize the velocity of a few molecules in the gas, $\mathbf{v}$, to one of the whole volume element as measured from a stationary laboratory observing the gas in motion. For this we use the Eulerian coordinate

system (please see Appendix 1 for full derivation) and obtain

$$\frac{D\mathbf{v}}{Dt} = \frac{\partial \mathbf{v}}{\partial t} + (\mathbf{v} \cdot \nabla)\mathbf{v} \tag{2.23}$$

where we use D to mean the derivative of the velocity of the entire volume element. Finally, the equation of motion (2.22) becomes Euler's equation:

$$\boxed{\rho[\frac{\partial \mathbf{v}}{\partial t} + (\mathbf{v} \cdot \nabla)\mathbf{v}] = -\nabla p} \tag{2.24}$$

Since, in acoustics, the pressure change δp and density change $\delta \rho$ are very small compared to their equilibrium values. Therefore, we shall linearize the equation of continuity (2.18) and Euler's equation (2.24) keeping terms of up to first order in these small changes. We write the pressure, density and velocity in the gas as

$$p = p_0 + \delta p \qquad \rho = \rho_0 + \delta \rho \qquad \mathbf{v} = \delta \mathbf{v} \tag{2.25}$$

where we have picked an quiescent state for the gas in equilibrium with $\mathbf{v}_0 = 0$. We use a simple Taylor expansion to expand the pressure as

$$p_0 + \delta p = f(\rho_0 + \delta \rho) = f(\rho_0) + \delta \rho f'(\rho_0) \tag{2.26}$$

where $f'(\rho_0)$ is the derivative of $f(\rho)$ evaluated at $\rho = \rho_0$, which is given by

$$f'(\rho_0) = (dp/d\rho)_{\rho_0} \tag{2.27}$$

The continuity equation (2.18) becomes

$$\frac{\partial (\rho_0 + \delta \rho)}{\partial t} + \nabla \cdot (\rho_0 + \delta \rho)(\delta \mathbf{v}) = 0 \tag{2.28}$$

$$\frac{\partial (\delta \rho)}{\partial t} + (\nabla \cdot \rho_0)\delta \mathbf{v} + (\nabla \cdot \delta \rho)\delta \mathbf{v} = 0 \tag{2.29}$$

Neglecting quantities of second order in small fluctuations, we obtain

$$\frac{\partial (\delta \rho)}{\partial t} + \rho_0 \nabla \cdot \delta \mathbf{v} = 0 \tag{2.30}$$

For Euler's equation (2.24) we have

$$(\rho_0 + \delta\rho)\left[\frac{\partial(\delta\mathbf{v})}{\partial t} + (\delta\mathbf{v} \cdot \nabla)\,\delta\mathbf{v}\right] = -\nabla\,(p_0 + \delta p) \tag{2.31}$$

which, neglecting terms of second order in small fluctuations, yields

$$\rho_0\frac{\partial\mathbf{v}}{\partial t} = -\nabla p \tag{2.32}$$

where for simplicity, from now on, we rename the velocity $\delta\mathbf{v} = \mathbf{v}$ and the acoustic pressure $\delta p = p$.

Because acoustics occurs when the change in density and pressure are small and gradual, sound waves propagating in a gas constitute an isentropic process where the conditions in the gas are the same before and after the disturbance passes through. This means that the flow of waves is reversible. From equations (2.26) and (2.27) we know $\delta p = \delta\rho\,(dp/d\rho)_{\rho_0}$, which is valid for isentropic flow. By the chain rule

$$\frac{\partial p}{\partial t} = \left(\frac{\partial p}{\partial\rho}\right)\frac{\partial\rho}{\partial t} \tag{2.33}$$

which helps us write equation(2.30) in terms of only p and $\mathbf{v}$

$$\frac{\partial p}{\partial t} + \rho_0\left(\frac{dp}{d\rho}\right)_{\rho_0}\nabla\cdot\mathbf{v} = 0 \tag{2.34}$$

We want to use equations (2.34) and (2.32) to obtain an equation solely in terms of the acoustic pressure p. We take the time derivative of the former and the divergence of the latter, which results in

$$\frac{\partial^2 p}{\partial t^2} + \rho_0\left(\frac{dp}{d\rho}\right)_{\rho_0}\frac{\partial\,(\nabla\cdot\mathbf{v})}{\partial t} = 0 \tag{2.35}$$

and

$$\frac{\partial\,(\nabla\cdot\mathbf{v})}{\partial t} + \left(\frac{1}{\rho_0}\right)\nabla^2 p = 0 \tag{2.36}$$

Finally, solving for the right terms, we obtain the homogeneous wave equation

$$\boxed{\frac{\partial^2 p}{\partial t^2} - c^2\nabla^2 p = 0} \tag{2.37}$$

with the speed of sound, c, given by

$$c = \sqrt{\left(\frac{\partial p}{\partial \rho_0}\right)_0} \tag{2.38}$$

In a sound wave, the variation of pressure with density is adiabatic: it allows no heat flow. This determines the following relation between pressure and volume

$$pV^\gamma = const \tag{2.39}$$

Since $\rho = M/V$,

$$p = const\, \rho^\gamma \tag{2.40}$$

from which we get $dp/d\rho = \gamma p/\rho$. Using equation (2.38), we write the speed of sound as $c = \sqrt{\gamma p/\rho}$. Now, we make use of the thermodynamic relation $pV = Nk_BT$. Expressing the mass of the gas as $M = mN$ where m is the mass of a molecule and N is the number of molecules, we get

$$c = \sqrt{\frac{\gamma kT}{m}} \tag{2.41}$$

which leads us to the conclusion that the speed of sound depends solely on the temperature of the gas, and not on pressure or density. Also, from thermodynamics,

$$kT = \frac{1}{3}m < v^2 > \tag{2.42}$$

where $< v^2 >$ is the mean square of the speed of the molecules, which yield

$$c = \left(\frac{\gamma}{3}\right)^{1/2} v_{av} \tag{2.43}$$

Thus, the speed of sound is of the same order of magnitude as the speed of the molecules.

Besides equation (2.38), we can also define the speed of sound in terms of the compressibility of the gas in which sound waves travel. Isothermal compressibility determines how the gas responds to changes in pressure when the entropy is constant and is given by

$$\kappa_S = -\frac{1}{V}\left(\frac{\partial V}{\partial p}\right)_S \tag{2.44}$$

The speed of sound can be expressed in terms of this adiabatic compressibility with the

formula

$$c = \frac{1}{\sqrt{\rho \kappa_S}} \qquad (2.45)$$

2.3.1   Solutions to the Wave Equation

The wave equation (2.37) is an initial boundary value problem that requires specific boundary and initial conditions. As a simple example of a common technique used to solve this problem, we derive the solution for the one-dimensional, homogeneous wave equation with Dirichlet boundary conditions

$$p(0,t) = p(L,t) = 0 \qquad (2.46)$$

and initial conditions

$$p(x,0) = f(x) \qquad \qquad \frac{\partial p}{\partial t}(x,0) = 0 \qquad (2.47)$$

We use separation of variables to solve the wave equation (2.37), which means we declare

$$p(x,t) = X(x)\,T(t) \qquad (2.48)$$

plugging this solution into the wave equation yields the following

$$\frac{1}{X}\frac{d^2 X}{dx^2} = \frac{1}{c^2}\frac{1}{T}\frac{d^2 T}{dt^2} = -k^2 \qquad (2.49)$$

We now have two equations, each in terms of only one variable: space or time. The solution for X(x) is given by sines and cosines:

$$X(x) = A\cos(kx) + B\sin(kx) \qquad (2.50)$$

Similarly, if we set $k^2 c^2 = w^2$, the solution for T(t) becomes

$$T(t) = C\cos(wt) + D\sin(wt), \qquad (2.51)$$

where $c \equiv w/k$.

Now, we apply the boundary conditions $p(0,t) = p(L,t) = 0$ to the equation for X(x) (2.50) and obtain

$$A = 0 \qquad \qquad kL = m\pi, \qquad (2.52)$$

where m is an integer $m = 0, \pm 1, \pm 2, \pm 3, ...$ This makes the first term in equation (2.50)

disappear and imposes a condition on the values that the wavenumber k can take.

We go back to equation (2.48) for the pressure and obtain the following

$$p_m(x, t) = [C_m \cos(w_m t) + D_m \sin(w_m t)] \sin\left(\frac{m\pi x}{L}\right) \tag{2.53}$$

where we have absorbed the B_m into the coefficients C_m and D_m.

It is time to apply the initial condition $\dot{p}(x, 0) = 0$, which makes $D_m = 0$. Therefore, equation (2.53) becomes

$$p_m(x, t) = C_m \cos(w_m t) \sin\left(\frac{m\pi x}{L}\right) \tag{2.54}$$

The general solution is a sum over all possible values of m

$$p(x, t) = \sum_{m=1}^{\infty} C_m \cos(w_m t) \sin\left(\frac{m\pi x}{L}\right) \tag{2.55}$$

We use the property of orthonormality for sines, namely

$$\int_0^L \sin\left(\frac{l\pi x}{L}\right) \sin\left(\frac{m\pi x}{L}\right) dx = \frac{1}{2} L \delta_{lm}, \tag{2.56}$$

where δ_{lm} is the Kronecker δ given by

$$\delta_{lm} \equiv \begin{cases} 1 & m = n, \\ 0 & m \neq n \end{cases} \tag{2.57}$$

to integrate the two sides of equation (2.55):

$$\int_0^L p(x, 0) \sin\left(\frac{l\pi x}{L}\right) dx = \sum_{m=1}^{\infty} C_m \sin\left(\frac{l\pi x}{L}\right) \sin\left(\frac{m\pi x}{L}\right) dx \tag{2.58a}$$

$$= \sum_{m=1}^{\infty} C_m \frac{1}{2} L \delta_{lm} \tag{2.58b}$$

$$= \frac{1}{2} L C_l, \tag{2.58c}$$

Finally, we conclude that the coefficients C_l are determined by the following equation

$$C_l = \frac{2}{L} \int_0^L p(x, 0) \sin\left(\frac{l\pi x}{L}\right) dx. \tag{2.59}$$

This is used to compute a different coefficient C_l for each initial distortion $p(x,0)$. The final solution for the pressure is given by equation (2.55), with the coefficient C_l determined by equation (2.59).

Similarly, for higher dimensions the procedure of separation of variables can be used. As the boundary and initial conditions get more complex, finding an analytic solution to the problem becomes more and more intricate.

Also, the inhomogeneous wave equation results from including a driving force such as a signal in the problem, and it is written like

$$\frac{\partial^2 p}{\partial t^2} - c^2 \nabla^2 p = f(x,y,t) \tag{2.60}$$

2.4   Energy Density

Sound waves propagating in a gas constitute and isentropic process, which means it is adiabatic (no heat exchanges with other systems) and also reversible (at any point in time, the process may be halted and run in reverse to obtain the original state). When heat transfer to a system is zero $Q = 0$, the *First Law of Thermodynamics* states

$$\Delta E + W = 0 \tag{2.61}$$

where E is the internal energy of the system and W is the work done by the system.

The kinetic energy of a gas where sound waves propagate is given by the *motion* of the gas molecules, and can be expressed as

$$E_K = \frac{1}{2}\frac{M}{v^2} \tag{2.62}$$

or as an energy density D_{KE}

$$D_{KE} = \frac{1}{2}\rho_0 v^2 \tag{2.63}$$

Expressed by equation (2.61), the energy in an adiabatic process is done by work on the system. Considering a small volume V_0 as the one in figure 2.1, a sound wave disturbance, does work by applying pressure to the volume of gas

$$W = -\int_{V_1}^{V_2} p dV \tag{2.64}$$

where V_1 and V_2 are the initial and final volumes. The *Gas Law* was displayed earlier in equation (2.39). If we differentiate both sides of it we obtain :

$$\frac{dV}{V} = -\frac{1}{\gamma}\frac{dp}{p} \tag{2.65}$$

Sound waves We consider a small change in volume $V = V_0 + \tau$. Considering the instantaneous density is equal to the average density of the gas $\delta\rho \approx \rho_0$, and using the total pressure in terms of the equilibrium and acoustic pressures we

$$\frac{dV}{V_0 + \tau} = -\frac{1}{\gamma}\frac{dp}{p_0 + \delta p} \tag{2.66}$$

Using the fact that $\delta p << p_0$ and $\tau << V_0$, we get

$$\frac{d\tau}{V_0} = -\frac{1}{\gamma}\frac{dp}{p_0} \tag{2.67}$$

where we have also differentiated the last equation to get an expression for a small change in volume $d\tau$. Finally, we plug this expression in equation (2.64) and solve for the work

$$W \quad = \quad -\int_0^p \frac{V_0 p}{\gamma p_0}dp \quad = \quad \frac{V_0 p^2}{2\gamma p_0} \tag{2.68}$$

We express the total energy density then, as

$$D = D_{\text{KE}} + D_{\text{PE}} = \frac{1}{2}\left(\rho_0 v^2 + \frac{p^2}{2\gamma p_0}\right) \tag{2.69}$$

2.4.1 Energy Density for Plane Waves

For a plane wave traveling in the positive $\hat{x}$ direction

$$p(x,t) = \text{Re}\left[p_i\, e^{i(\omega t - kx)}\right] \tag{2.70}$$

$p_i = |p_i|\, e^{i\theta}$ and θ is the phase. From Euler's equation (2.32), the magnitude of the particle velocity is

$$v(x,t) = \frac{1}{\rho_0 c}\, p(x,t) \tag{2.71}$$

where $c = \omega/k$. From equation (2.69), the instantaneous energy density for a plane wave is given by

$$D = \frac{1}{2}\left(\rho_0 \frac{1}{\rho_0^2 c^2}|p(x,t)|^2 + \frac{|p(x,t)|^2}{2\gamma p_0}\right) = \tag{2.72a}$$

$$= \frac{p_i^2}{\rho_0 c^2}\cos^2(\omega t - kx + \theta) \tag{2.72b}$$

The last equation says both the kinetic and potential energy densities are the same at a given point in space and that they vary sinusoidally from zero to twice their average value. All energy is being transported away from the source. Averaged over one half of a cycle period $t = \pi/\omega$ the *average energy density* is

$$D_{avg} = \frac{\bar{p}_i^2}{\rho_0 c^2} \qquad \text{watt-s/m}^3 \tag{2.73}$$

where we have used the definition $\rho_0 c^2 \equiv \gamma p_0$ and $|p_i|$ is the magnitude of the rms value in time of the sound pressure at any point in the wave.

2.5   Sound Energy Flow: Intensity

Due to the law of conservation of energy, the total acoustic energy emerging from a source must be completely accounted for in the system. At any section of cross-area in the system, we shall be able to measure the amount of energy flowing through that area and it should be equal to the power emanating form the source minus any intervening losses.[3]

Considering again figure 2.1, intensity is the energy flow (energy per time or power) through a unit area where the normal to the area points in the direction we measure the intensity. The general definition of power is $\mathbf{f} \cdot \mathbf{v}$ so, for the volume of gas

$$p\mathbf{v} \cdot \Delta\mathbf{S} = \mathbf{i} \cdot \Delta\mathbf{S} \tag{2.74}$$

where $\mathbf{i}$ is the instantaneous energy flow per unit area. The intensity is time average of $\mathbf{i}$

$$\mathbf{I} = \frac{1}{t_{av}}\int_0^{t_{av}} p\mathbf{v}\,dt \tag{2.75}$$

where t_{av} depends on the kind of wave. For periodic waves t_{av} is the period whereas for

---

[3] [35], p. 43

transients it is the duration of the transient signal. Intensity is always measured in the direction of particle velocity, so we can assume that and write the former equation as a scalar product

$$I = \frac{1}{t_{av}} \int_0^{t_{av}} pv \, dt \tag{2.76}$$

For plane waves

$$I = \frac{1}{t_{av}} \int_0^{t_{av}} \frac{p^2}{\rho_0 c} \, dt \tag{2.77}$$

where we have used equation (2.71) for the velocity in terms of pressure. Introducing the root-mean-square of the sound pressure as

$$p_{rms} = \left(\frac{1}{t_{av}} \int_0^{t_{av}} p^2 dt \right)^2 = \left(\bar{p}^2 \right)^{1/2} \tag{2.78}$$

where the overbar indicates time-averaging, we rewrite equation (2.77) as

$$I = \frac{\bar{p}^2}{\rho_0 c} \tag{2.79}$$

which implies

$$I = cD_{avg} \tag{2.80}$$

Finally, for spherical waves, the total power at *any* radius r from the source is equal to

$$P = 4\pi r^2 \, I \tag{2.81}$$

By the law of conservation of energy the power is the same at any distance from the source so that the intensity varies inversely proportional to r^2.

In section 2.2 we defined the energy density as the sound energy in a part of the gas divided by the volume of that part of the gas (see equation (2.8)). Close to an acoustic source, the energy density is higher than further away from it. [35]

2.6   Reflection and Scattering

Since waves carry energy and momentum, when they encounter an obstacle in their path such as a wall or boundary, they will impart some or all of their energy and momentum in the collision. Depending on the conditions at the boundaries, waves get partially or totally reflected. This interaction of the wave with a boundary causes the incident wave to split into a

reflected and a transmitted new wave after the collision. The reflected wave originates at the boundary and travels in the opposite direction as the incident one, whereas the transmitted wave crosses the boundary and travels in the same direction as the incident wave. Or, if the material at the boundary is absorbing, the transmitted wave can be absorbed partially into it. No matter what happens during a collision, the *total* energy and momentum are conserved in the process.

Besides the exchange of energy and momentum with a boundary, when waves pass through a boundary between two media of different densities, their velocity will change from that on the first medium. This means that the direction of propagation will also get altered. This phenomenon is called "refraction." Still a different property of waves is "diffraction" which says that they are able to flow around the edges of obstacles.

The characteristics of boundaries such as the material and structure determine the amplitude and phase of the reflected and transmitted waves. The amount of energy reflected, transmitted or absorbed at a boundary depends on how the incident wave interacts with the specific boundary. When a wave is reflected, there can arise constructive interference between incident and reflected waves. This causes a standing wave pattern where the two waves superimpose and add their amplitudes at the corresponding peaks and cancel the amplitudes at the nodes. Standing waves are responsible for sound reverberation in enclosures. In the following list, we define the four different scenarios that can occur as a sound wave hits a boundary.

1. Reflection from a Hard Boundary

2. Reflection from a Soft Boundary

3. Reflection and Transmission from an Impedance Discontinuity

4. Absorption by the boundary

1. Reflection from an acoustically "hard" boundary occurs when the net force on the incident wave at the boundary is zero. It is also called a "pressure-release" boundary since the force is given by the derivative of the pressure with respect to the normal $\hat{n}$.

$$\frac{\partial p}{\partial n} = 0 \qquad \text{Neumann boundary} \qquad (2.82)$$
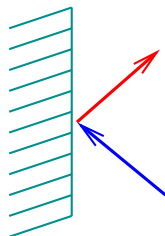
Figure 2.2: Reflection from a hard boundary: an incident wave (blue arrow) arrives at a boundary where the net force is zero. This produces a reflected wave (red arrow) whose amplitude and phase remain the same as the ones of the incident wave. The reflected wave propagates in the opposite direction as the incident one, with the same speed and amplitude and the same phase. Mathematically, this is referred to as a *Neumann* boundary.

2. Reflection from a soft boundary occurs when the pressure at the boundary is zero. After the incident wave collides with the boundary, all its energy is reflected back in a reflected wave originating at the boundary and traveling in the opposite direction. In contrast to a hard boundary though, this time the reflected wave has the same speed and amplitude as the incident one, but it undergoes a 180° phase change.

$$p = 0 \qquad \text{Dirichlet boundary} \qquad (2.83)$$
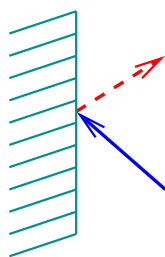
Figure 2.3: Reflection from a soft boundary: an incident wave (blue arrow) arrives at a boundary where the pressure is zero. This produces a reflected wave (red arrow) whose amplitude and speed remain the same as the ones of the incident wave. The reflected wave propagates in the opposite direction as the incident one, and it undergoes a 180° phase change. Mathematically, this is referred to as a *Dirichlet* boundary

3. In most real cases however, when a wave encounters a boundary, some of its energy gets reflected back, and part of it is transmitted forward. As an intermediate case between soft and hard boundaries, there is reflection and transmission from an impedance discontinuity.
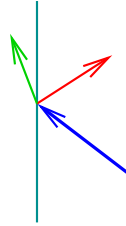
Figure 2.4: Reflection and transmission from an impedance discontinuity: an incident wave (blue arrow) arrives at a boundary that separates two different media, each with its own sound velocity, density and characteristic impedance. This produces a reflected wave (red arrow) and a transmitted wave (green arrow). Throughout the process energy and momentum are conserved. Mathematically, this case will be treated in the following section

4. Finally, there is case where the entire energy of the incident wave is absorbed by the boundary. Depending of the characteristic properties of the material at the boundary, all incident energy will be transformed into heat or other forms as it dissipates in the boundary.
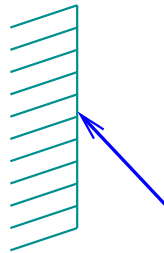
Figure 2.5: Absorption at a boundary: an incident wave (blue arrow) arrives at a boundary and gets absorbed by it. The energy gets converted into heat or other forms and dissipates in the material.

2.6.1   Reflection and Transmission at an Impedance Discontinuity

According to the equations of acoustics, specifically equation (2.32), when a wave crosses an impedance discontinuity from one medium into a different one, conservation of momentum in gases holds and it is written in Euler's equation

$$\nabla p = -\rho_0 \frac{\partial \mathbf{v}}{\partial t} \tag{2.84}$$

As this happens, depending on the amount of incident energy that is not absorbed by the material at the boundary, the rest of the energy will deliver two new waves: a reflected and a transmitted one. To explore this ideas, we consider an incident pressure plane wave in one dimension. A plane wave is characterized by all of its properties being constant along a series of planes perpendicular to the traveling direction. That is, its properties only change with distance as it propagates on its axis of motion. In Figure 2.6, a harmonic incident wave travels in medium 1, and gives way to a reflected wave in the same medium that travels in the backward direction. Furthermore, a transmitted wave emerges in medium 2 and propagates in the forward direction. The boundary between both media occurs at $x = 0$. From figure

Medium 2   Medium 1

$$Z_2 = \rho_2 c_2 \qquad\qquad\qquad Z_1 = \rho_1 c_1$$
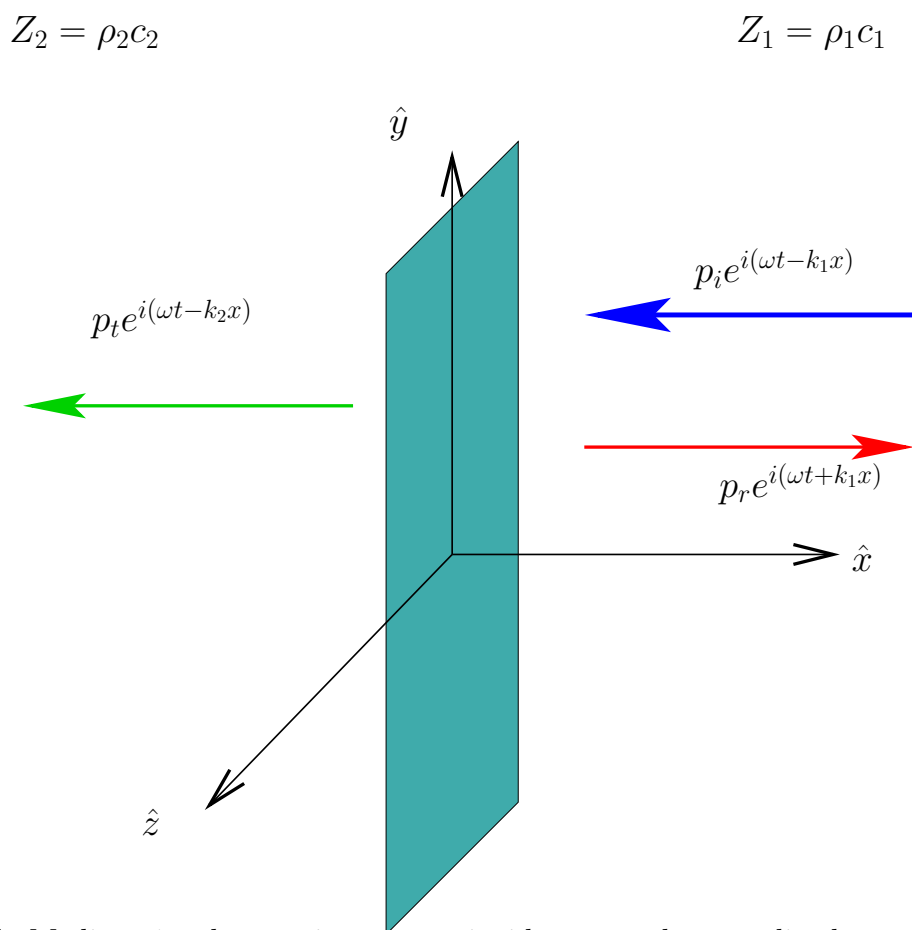
Figure 2.6: In Medium 1, a harmonic pressure incident wave has amplitude p_i and impinges on a boundary at $x = 0$, traveling in the positive x-direction with velocity $c = \frac{\omega}{k}$. It gives rise to two new harmonic pressure waves: a reflected pressure wave with amplitude p_r traveling in the negative x-direction, and a transmitted wave with amplitude p_t continuing in the positive x-direction toward Medium 2. $\omega = 2\pi f$ is the frequency of oscillation, and $k = 2\pi/\lambda$ is the wave number.

(2.6), in one dimension, the general solution to the wave equation in medium 1 is

$$p_i \exp^{i(\omega t - kx)} + p_r \exp^{i(\omega t + kx)} \tag{2.85}$$

where the second derivatives of both terms must exist. Since sound waves are longitudinal pressure waves, these expressions are constant in any plane perpendicular to the x-axis. Applying the conservation of momentum equation (2.84) to equation (2.85), we obtain the particle velocity in medium 1, which by continuity should be the same as the velocity of the transmitted wave propagating in medium 2

$$v = v_x = \frac{1}{\rho_0 c}[-p_i \exp^{i(\omega t - kx)} + p_r \exp^{i(\omega t + kx)}] \tag{2.86}$$

From equations (2.91), (2.86) and (2.85), for a plane wave propagating in the positive x-direction such as the incident wave, $p_r = 0$ and for plane propagating in the negative x-direction the ratio of sound pressure and particle velocity is given by

$$Z = \left(\frac{p}{v_n}\right)_{x=0} = \pm \rho_0 c \tag{2.87}$$

Notice that this ratio is frequency independent. This is called the "characteristic impedance" of the medium. For air at normal conditions its value is:

$$\rho_0 c = 414 kg m^{-2} s^{-1} \tag{2.88}$$

To formulate a mathematical analysis of this scenario, we appeal to the principles of conservation of energy and momentum. Based on physical grounds, for a stationary boundary, we require that pressure and particle velocity normal to the boundary be continuous at the boundary $(x = 0)$

$$p_i + p_r = p_t \tag{2.89a}$$

$$v_i + v_r = v_t \tag{2.89b}$$

Dividing equation (2.100a) by equation (2.100b) we obtain at the boundary

$$\frac{p_i + p_r}{v_i + v_r} = \frac{p_t}{v_t} \tag{2.90}$$

The wall impedance Z is defined as the ratio of pressure to particle velocity normal to the wall generated by the incident sound pressure wave at the boundary

$$Z = \left(\frac{p}{v_n}\right)_{x=0} \tag{2.91}$$

In general, Z is a complex quantity, and a function of the angle of wave incidence. Using the fact that the pressure waves are all orthogonal to the boundary and with the help of equation (2.91), we transform equation (2.90) to

$$\left(\frac{v_i - v_r}{v_i + v_r}\right) Z_1 = Z_2 \tag{2.92}$$

where Z_1 and Z_2 are the characteristic impedances of medium 1 and medium 2. Employing the expressions for the wave pressure at the boundary, we derive the reflection and transmission factors

$$R = \frac{p_r}{p_i} = \frac{Z_2 - Z_1}{Z_2 + Z_1}, \qquad T = \frac{p_t}{p_i} = \frac{2Z_2}{Z_2 + Z_1} \tag{2.93}$$

This results imply that when an incident wave $p_i \exp^{i(\omega t - kx)}$ encounters a boundary, the reflected wave coming off the boundary will be smaller in magnitude by the reflection factor R

$$p_r \exp^{i(\omega t + kx)} = R\, p_i \exp^{i(\omega t - kx)}. \tag{2.94}$$

Similarly, the transmitted wave that follows through the boundary will be smaller in magnitude by the transmission factor T

$$p_t \exp^{i(\omega t - kx)} = T\, p_i \exp^{i(\omega t - kx)} \tag{2.95}$$

Since the energy density of a plane wave is proportional to the square of the pressure amplitude (see equation 2.69), during reflection, the energy of the reflected wave is smaller than the incident one by a factor of $|R|^2$. Therefore, the energy lost in the process is of the order of $1 - |R|^2$. The *absorption coefficient* α is the fraction of energy lost to absorption at the wall and it is given by

$$\alpha = 1 - |R|^2 \tag{2.96}$$

The remainder of the energy either gets transmitted into medium 2, or else gets absorbed by the boundary. The reflection factor, R, prescribes the changes in both amplitude and phase that the reflected wave will go through after it leaves the boundary and it is a function of the

material and quality of the boundary. Since it is generally a complex quantity, a different way of writing the reflection factor is

$$R = |R| \exp^{i\chi} \tag{2.97}$$

where the phase angle χ and the magnitude $|R|$ are frequency dependent. Also, both $|R|$ and χ vary with the direction of the incident wave.

2.6.2 Wave Reflection and Scattering off Walls in an Enclosure

For the case of room acoustics we consider medium 1 to be the room were waves propagate, and medium 2 is the surface at the walls of the room. A solid surface such as a wall can be characterized by its *specific surface impedance* Z_s defined earlier in equation (2.6). Considering once again propagation only in the $\hat{x}$ direction for simplicity, We make $Z_1 = Z_{\text{air}}$ and $Z_2 = Z_{\text{wall}}$ to write the reflection coefficient as

$$\text{R} = \frac{Z_{\text{wall}} - \rho c}{Z_{\text{wall}} + \rho c} \tag{2.98}$$

where we have used the characteristic impedance of air for medium 1 $Z_{\text{air}} = \rho c$. ρ is the acoustic density of air in the room and c is the velocity of sound. In this case, the absorption coefficient is the fraction of energy lost to absorption at the wall and completely describes the acoustical properties of a surface for all angles of incidence and all frequencies. From its definition in equation (2.96), we write

$$\alpha = 1 - \left| \frac{Z_{\text{wall}} - \rho c}{Z_{\text{wall}} + \rho c} \right|^2 \tag{2.99}$$

For example, if the walls in a room are constructed out of brick, the absorption coefficient for frequencies from 125 Hz to 250 Hz is $\alpha = 0.01$, that is, only 1% of the energy gets absorbed by the walls. Similarly, for frequencies between 1/2 kHz and 4 kHz the value of the coefficient is $\alpha = 0.02$ which means only 2% of the energy gets absorbed by the walls. However, if the walls are covered with an absorbent material such as plaster on wood wool, the absorption coefficient is $\alpha = 0.40$ for frequencies around 125 Hz and decreases for a range up to 4 kHz too 10%.

Applying the boundary conditions (2.89) for an incident wave $p(x,t) = p_i e^{i(\omega t - kx)}$ we write

the pressure and normal velocity relations at the wall

$$p_i + p_r = p_t \tag{2.100a}$$

$$\frac{p_i - p_r}{\rho c} = \frac{p_t}{Z_{\text{wall}}} \tag{2.100b}$$

From these, we solve for the amplitude of the reflected wave in medium 1 as a function of the impedance of medium 2, the characteristic impedance of air and the amplitude of the incident wave:

$$p_r = \frac{\left(1 - \dfrac{\rho c}{Z_{\text{wall}}}\right)}{\left(1 + \dfrac{\rho c}{Z_{\text{wall}}}\right)} p_i \tag{2.101}$$

If the wall constitutes a hard acoustic boundary the impedance of the wall is much larger than the characteristic impedance of air in the room. Equation (2.102a) shows that the amplitude of the reflected wave is equal to the incident one, which of course means no energy gets transmitted to the wall.

$$
\begin{array}{llll}
\text{(Neumann)} & Z_{\text{wall}} \gg \rho c & p_r = p_i & \text{(2.102a)} \\
\text{(Dirichlet)} & Z_{\text{wall}} \ll \rho c & p_r = -p_i & \text{(2.102b)}
\end{array}
$$

In contrast, in the case for a soft acoustic boundary the impedance of the wall is much smaller than the characteristic impedance of air in the room. As it is shown in (2.102b), this causes the reflected wave to have equal magnitude to the incident one, but a $180°$ phase shift from it. From equation (2.99), we can express the wall impedance as a function of the energy absorption coefficient α

$$Z_{\text{wall}} = \rho c \frac{\left(1 - \sqrt{1 - \alpha}\right)}{\left(1 + \sqrt{1 - \alpha}\right)} \tag{2.103}$$

A wall that does not reflect any energy back ($R = 0$) is said to be totally absorbent, and has an absorption coefficient of maximum value 1. This wall is characterized as being "matched to the sound field." If $R = 1$ (in-phase reflection, $\chi = 0$), the wall is hard; in the case of $R = -1$ (phase reversal, $\chi = \pi$), it is a soft wall. In both cases $\alpha = 0$, so there is no absorption of sound energy. The case of soft walls occurs very rarely in room acoustics and only in limited frequency ranges.

2.7 Is the "Plane-Wave" Approximation Sufficiently Good for Room Acoustics?

If an acoustic source is placed very close to the walls of an enclosure, as in Figure 2.7, the emergent waves incident on the wall cannot be considered as plane waves. There is significant curvature of the spherical wavefront that the plane wave approximation ceases to be valid, and one needs to consider what happens when considering spherical waves. In this case, the wavefronts are concentric spheres with a point source at their common center. In the appropriate spherical polar coordinates r, θ and ϕ, the wave equation reads:

$$\frac{1}{r^2}\frac{\partial}{\partial r}\left(r^2\frac{\partial p\left(r,t\right)}{\partial r}\right) + \frac{1}{r^2\sin\theta}\frac{\partial}{\partial\theta}\left(\sin\theta\frac{\partial p\left(r,t\right)}{\partial\theta}\right) + \frac{1}{r^2\sin^2\theta}\frac{\partial^2 p\left(r,t\right)}{\partial\phi^2} = \frac{1}{c^2}\frac{\partial^2 p\left(r,t\right)}{\partial t^2} \quad (2.104)$$

For waves in an isotropic medium pressure is independent of θ and ϕ, equation(2.104)reduces
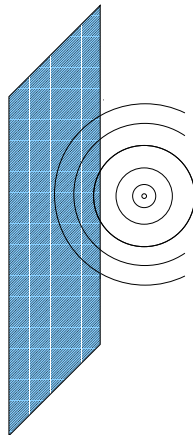
Figure 2.7: If a source is close to the boundaries of an enclosure, the plane wave approximation becomes invalid. One must instead use the expression for spherical waves.

to

$$\frac{\partial^2 p\left(r,t\right)}{\partial r^2} + \frac{2}{r}\frac{\partial p\left(r,t\right)}{\partial r} = \frac{1}{c^2}\frac{\partial^2 p\left(r,t\right)}{\partial t^2} \quad (2.105)$$

After introducing a new variable

$$\varphi(r,t) = rp(r,t) \quad (2.106)$$

the equation becomes

$$\frac{\partial^2\varphi}{\partial r^2} = \frac{1}{c^2}\frac{\partial^2\varphi}{\partial t^2} \quad (2.107)$$

The general solution to this equation for $r \neq 0$ is of the form:

$$\varphi(r, t) = A_1 f(ct - r) + A_2 f(ct + r) \tag{2.108}$$

After applying the radiation condition requiring that $f(ct + r) = 0$, we write a harmonic solution:

$$\varphi(r, t) = A e^{i(\omega t - kr)} \tag{2.109}$$

and the pressure wave

$$p(r, t) = \frac{A}{r} e^{i(\omega t - kr)} \tag{2.110}$$

Now, applying equation (2.84) to equation (2.110) we obtain the particle velocity, which has a single non-vanishing component in the radial direction:

$$v_r = \frac{p}{\rho_0 c} \left(1 + \frac{1}{ikr}\right) \tag{2.111}$$

Thus, for a spherical sound wave, the ratio of sound pressure to particle velocity depends on the distance r and the frequency $\omega = kc$. Moreover, it is complex, i.e. between both quantities there is a phase difference. For distances which are large compared with the wavelength ($kr \gg 1$), the ratio p/v_r tends asymptotically to $\rho_0 c$, which is the characteristic impedance of the medium.

We have proved that the impedance at a boundary can be expressed as

$$Z = \pm \rho_0 c \qquad \text{for plane waves in the ($\pm$direction)} \tag{2.112a}$$

$$Z = \rho_0 c \left(1 + \frac{1}{ikr}\right)^{-1} \qquad \text{for spherical waves} \tag{2.112b}$$

For large values of kr, that is, for large distances or for high frequencies, equation (2.112b) approaches the value calculated by equation (2.112a). So, as long as $r \gg \lambda$ we can use the plane wave approximation. As we can see from these equations, for plane waves the characteristic impedance Z is real and frequency-independent. However, the same is not true for spherical waves.

2.8 Designing Numerical Impedance Boundary Conditions

In a computational domain, boundaries need to be created. They are imposed by the finite-difference scheme. First, we shall explore some initial attempts to implement physical absorbing boundary conditions for our numerically-simulated enclosure. It turns out that impedance boundary conditions that are used to truncate infinite domains are the subject of vast literature and many years of investigation. For numerical simulations of outdoors environments, the goal is to create numerical "artificial boundaries" where the computation stops, but the physical environment does not. This numerical schemes are concerned with simulating absorption in free space, where the desire is to destroy all possible reflections from the artificial boundaries of the numerical code. A complete review of these methods and research concerned with them in the past decade can be found in [[37]]. However, the same cannot be said for the case of designing numerical impedance conditions at the boundaries for simulation of closed physical domains such as rooms.

To the best of our knowledge, the author of this thesis found little information in the literature on the process of implementing numerical *partially* absorbing boundary conditions in finite-difference time-domain (FDTD) acoustic codes. Our desired is to design a discrete numerical boundary condition at the walls of the simulated enclosure, where some of the energy will be absorbed and some of it will continue to multiply scatter in the enclosure.

Under the category of impedance boundary conditions (IBC) are methods such as "perfectly matched layer approach" (PML), absorbing boundary conditions (ABC), radiation condition, transparent boundary conditions, etc, all concerned with simulation of absorption of waves that occurs in free-space. For example, the PML method originally created by Jean-Pierre Berenger surrounds the computational domain with layers of finite depth that absorb more and more incident energy. These layers are all seamlessly connected to each other so as not to introduce unphysical effects from the artificial boundaries between them. The process continues until enough of this layers manage to destroy all undesired reflections into the domain. This method can achieve excellent accuracy in destroying most waves that would otherwise be reflected back into the domain.

Initially, we experimented with the thought of implementing perfectly-matched-layers using the PML method, that do not completely eliminate all reflections. The idea was to create an intermediate case of PML to simulate physical enclosures in the time domain. However, doing this in practice may be difficult. The reason is that it requires lots of testing

to adjust and control the amount of reflection that is to be allowed back into the domain of the enclosure. It is imperative to carefully balance the act of absorption with the one of partial reflection at each layer, and to do the truncation at justified places. This should be done in such a manner that each layer absorbs more energy than the previous one, until the last layer makes all reflections disappear. This idea seems feasible, yet rather complex to implement. If one does not destroy partial reflections at each layer, it easy to introduce "unphysical effects" due to the artificial reflections that may be generated at the layer's interface and travel back into the enclosure domain.

There are computer simulations for acoustics in rooms that use the geometrical approach. That is, they model each ray as it departs from the source and gets reflected (or absorbed) specularly from surfaces. This technique is called "ray tracing," but is only suitable for acoustic waves of high-frequencies. Additionally, "methods based on Dirichlet-to-Neumann maps in boundary integral formulations or mode expansions are also applicable to finite domains with physical boundaries." [[38]].

These are only some examples of different ways of modeling acoustic waves in enclosures where there is partial wave reflection. The real physical phenomena of wave reflection off of surfaces depends on incident angle, material of the wall, materials absorbing different amounts of energy according to the frequency of the incident wave. Very few models can incorporate all the complexity of this multiple variable parameters. Most models either approximate some parameters or simply ignore them in order to simplify the simulation.

Our design of numerical absorption boundary conditions is based simply on the conservation of momentum in gases as it is determined by Euler's equation 2.84. In section 2.6.2 above, we derived an equation for the pressure and velocity normal to a boundary when waves traveling in air encounter a physical wall with impedance Z_{wall}. We write equation for the normal velocities at the boundaries (2.100b) here in a slightly different form

$$p_i - p_r = \left(\frac{\rho c}{Z_{\text{wall}}} \right) p_t \tag{2.113}$$

We define a "specific acoustic impedance parameter" κ

$$\kappa = \frac{Z_{\text{wall}}}{\rho c}, \qquad \text{where} \quad 0 \leq \kappa \leq 1 \tag{2.114}$$

as the ratio between the characteristic impedance of air and the specific acoustic impedance of the walls of an enclosure. From equation (2.113) and using the fact that conservation of

momentum at the boundary determines $p_t = p_i + p_r$, we can express the amplitude of a wave just reflected by the wall in an enclosure in terms of κ as

$$p_r = \frac{(\kappa - 1)}{(\kappa + 1)} p_i \tag{2.115}$$

This means that the reflection factor R in this case is given by $R = (\kappa - 1)/(\kappa + 1)$. Consequentially, the energy absorption coefficient α is given by

$$\alpha = 1 - \left| \frac{(\kappa - 1)}{(\kappa + 1)} \right|^2 \tag{2.116}$$

which gives an expression for the specific acoustic impedance parameter κ in terms of the energy absorption coefficient α

$$\kappa = \frac{\left(1 + \sqrt{1 - \alpha}\right)}{\left(1 - \sqrt{1 - \alpha}\right)} \tag{2.117}$$

At all boundaries of the enclosure momentum conservation should hold

$$\rho \frac{\partial \mathbf{v}}{\partial t} = - \nabla p \tag{2.118}$$

Substituting in the expression for the normal velocity of the particles hitting the wall $v_n = p Z_{\text{wall}}$ and multiplying both sides of the equation by the speed of sound c yields the following **absorbing boundary conditions** in terms of κ

$$\boxed{\frac{\partial p}{\partial t} = - \kappa c \frac{\partial p}{\partial n}} \tag{2.119}$$

where n implies the normal derivative at the boundary (with the correct interpretation for the sign at each boundary).

For our model, we allow κ to vary from zero to unity to model specific acoustic materials for which we have an absorption coefficient (determined experimentally, in tables in [35]. This allows us to numerically simulate enclosures with walls that range from perfectly-reflecting to strongly absorbing, and explore the results of carrying out time-reversal acoustics in the presence of absorption.

A simple analysis shows that our model is consistent with the Dirichlet and Neumann boundary conditions as well as with the totally absorbing wall. From equation (2.115) we see that there are three important cases to consider. When $\kappa = 0$, then the reflection factor is equal to $R = -1$ which means the specific acoustic impedance of the wall tends to zero

$Z_{\text{wall}} \to 0$. This takes us back to the case of a soft boundary with Dirichlet conditions for the pressure. One that reflects all wave energy and where the reflected wave comes off the boundary with a phase difference of 180° from the incident one. Now, if $\kappa = 1$, it means the specific acoustic impedance of the wall is matched to the characteristic impedance of air Z_{wall}. This makes the reflection factor equal to $R = 0$ as expected, since all energy is absorbed at an impedance-matched boundary. Finally, if $\kappa \to \infty$ asymptotically, it represents a very large specific acoustic impedance of the wall $Z_{\text{wall}} \to \infty$. Consequentially, the reflection factor is equal to $R = 1$ which implies all energy gets reflected back into the boundary and reflected waves are in phase with incident ones.

Chapter 3

Computational Simulation of Time-Reversal in an Acoustic Enclosure

3.1   Outline of Chapter

Purpose is to develop ability to carry out a numerical simulation of TR in a similar manner as the expts. at NPS. Given the difference in dimensions,i had to compromise and increase bandwidth. Since the code is my klaboratory I perform numerous checks to see if code is consistent, has error convergence, etc...

3.2   Acoustic Reverberation Experiments at the Naval Postgraduate School

Experiments by M.G. Heinemann, A. Larraza and K.B. Smith in an enclosure using time-reversal acoustics (TRA) show that it is possible to focus an acoustic wave within half a wavelength of sound [30]. At the Advanced Acoustics Research Laboratory in the Naval Postgraduate School (NPS) in Monterey, California, a reverberation chamber is constructed by surrounding an empty room with concrete walls. The goal of the acoustic reverberation experiments at NPS is to show how using TRA helps improve communication links in enclosures. An important factor is that TRA reduces the apparent reverberation of a room by tightly focusing an acoustic signal in space. Also, TRA takes advantage of multipathing

to focus acoustic energy at a specified location. This makes it a desirable technique for acoustics communications in enclosures.

The general purpose of a communications link is based on the principle of sending information from a source to a receiver in two different locations in space. Typically, this information is coded in the form of a specific waveform. When an initial signal is sent from a source location, it degrades while traveling to a different receiver location. Due to reflections from the boundaries and the existence of multi-paths, multiple copies of the signal interfere with each other. Reflected and refracted copies of the signal interact with the boundaries and interfere with each other throughout time. Ultimately, this causes the intended receiver to receive an "echo" of multiple arrivals due to the different propagation times of each path from source to receiver. Acoustic communications in enclosures faces many challenges, one of which is to recover the original waveform at the receiver after it has been corrupted by its interaction with multiple reflections from the boundaries in the medium.

More specifically, in a communications link, the signal degradation caused by multi-pathing is responsible for the undesired interference between symbols. Due to repeated arrivals of each symbol at a receiver location, different symbols interfere with each other. This inter-symbol interference (ISI) makes decoding the message at the receiver difficult. In principle, noise arising from multipathing would need to be eliminated in order to decode the signal with certainty. Often times, however, it is not possible to characterize this noise as the specific physical characteristics of the medium are unknown. Therefore, decoding at the receiver to eliminate multi-path noise becomes a challenging and complex endeavor.

In a typical application of the TRA method, an acoustic signal is transmitted from a point-like source and captured at a nearby microphone for an extended time. After digitizing the analog signal received by the microphone (or hydrophone), it is reversed in time and retransmitted into the medium from a co-located source. After some time, the time-reversed signal focuses in time and space at the point-like source. [30]

The use of TRA eliminates the multi-path structure because the different propagation paths from source to receiver all add coherently at the source location. This "results on a reduced ISI of the communication link and an increase of the allowable data transfer rate. Furthermore, due to spatial and temporal focusing there is a strong enhancement of the field at the focus location, which allows us to either decrease the power requirements of the system or increase the range of effectiveness in a waveguide propagation." [1]

When using the TRA technique, if the array of receivers/transmitters has sufficient width

---

[1] [30], p. 694

to provide ample angular spread, the spatial focusing of the signal can achieve a size of half a wavelength of sound. However, in the case of an enclosure, as stated by Fink in [10], a single receiver/transmitter element is sufficient to achieve the dramatic spatial focusing results that require a wide array in an unbounded space.

The experimental setup used for the TRA experiment at the NPS is displayed in Figure 3.1. The dimensions of the room are 2.59 m long, 2.41 m wide, and 2.83 m high as shown in the schematic of Figure (3.1). This experimental setup is used to explore acoustic communications in an enclosure using time-reversal. An initial pulse with center frequency $\nu = 9.5$ kHz and bandwidth $B = 750$ Hz is transmitted from a source located at coordinates (0.94, 0, 0) m. The initial pulse width, which is on the order of 1 ms, is shown in Figure 3.2, (a). Microphone 1 acts as a receiver and is located 1.5 m away from the source. A second microphone 2 is located approximately 2.5 m away from the source and 1 m away from microphone 1. After the initial signal is emitted by the source, the generated waves propagate through the enclosure and are recorded at a microphone for a time $T = 50$ ms. Figure 3.2, (b).
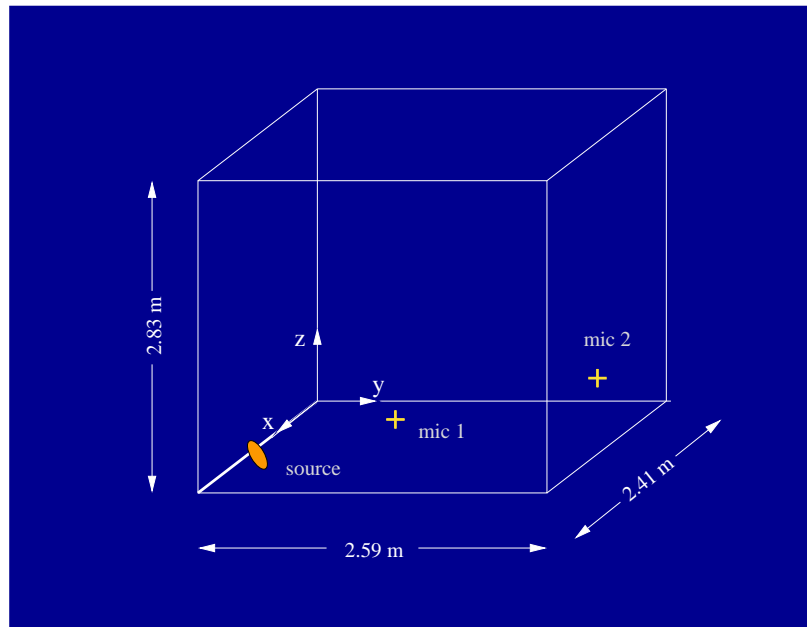
Figure 3.1: Larraza's experimental reverberation enclosure. Concrete walls of dimensions (2.59 m long, 2.41 m wide, 2.83 m high), one source, and two microphone receivers

In a typical time-reversal experiment a source located at point A emits an initial pulse that is recorded during a time T at a receiver location B. The receiver reverses the waveform

in time and re-emits it to the same medium. A second recording is made as the waves propagate backward in time and spatial and temporal focusing are observed at the source location A at time T.

Waves propagating between two different points A and B in space obey the principle of spatial-inversion symmetry. That is, waves propagating from point A to B undergo the same multi-path degradation as waves going point B to A. The location of source and receiver can be interchanged between both points obtaining the same waveform whether detected at point A or B. Translated to the experimental setup of Figure 3.1, this says that the waveform captured at microphone 1 after the source transmits a signal is the same as the one captured at the source had microphone 1 emitted the initial signal.

In the reverberant chamber experiment at the NPS, Larraza *et al* make use of this space-reversibility. After microphone 1 has recorded the wave field emitted from the source, the time-reversed wave field (see Figure 3.2, (c)) is fed back unto the source and is re-transmitted into the medium. With microphone 1 in its original location, the acoustic field in the enclosure is recorded a second time. Because of spatial reciprocity, the waveform will focus at the microphone 1 location at time T. The temporal compression of the signal is displayed in Figure 3.2, (d). At different points in the enclosure, the multi-paths do not add coherently and no focusing occurs.

Furthermore, it is possible to perform the same procedure by recording the generated waves at microphone 2 simultaneously for the same time $T = 50$ ms. After recording the two different wave fields obtained at each microphone, they are simultaneously fed into the source. Thus, the same initial signal will focus tightly in space around each microphone at time T.

The time-series generated for the same signal is different when it travels from source to microphone 1 than when it does to microphone 2. This is because the multiple reflections that a signal goes through depend on the specific path from source to receiver. This multi-path information is recorded in the form of a time series or "transfer function" as it is often called.

As depicted in Figure 3.1, the reverberant enclosure at NPS contains two microphone detectors and one source. During a "training period" before the communications protocol takes place, the source emits the initial signal into the reverberant enclosure. The emergent waveform propagates around the enclosure and is recorded for an extended time at microphones 1 and 2. The resulting reverberations in the enclosure are different for each travel path to the microphones. When this training session takes place, and each microphone has
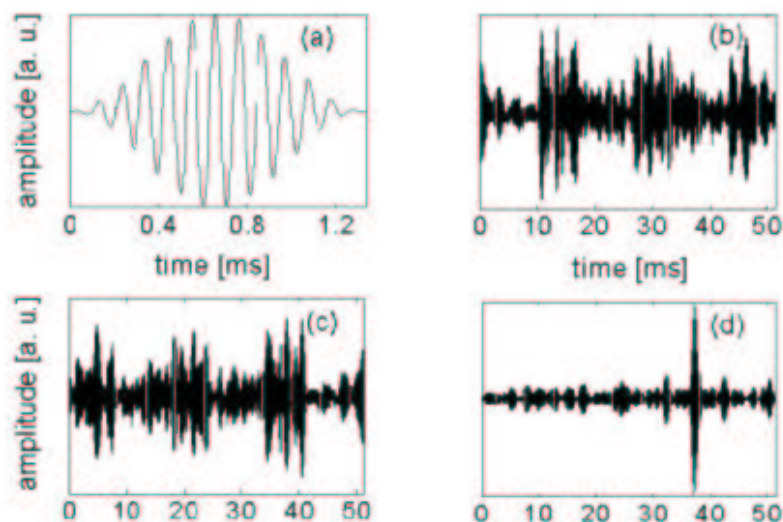
Figure 3.2: Figure taken from [30]. The four steps in the time-reversal process carried out in the reverberant room at the NPS are shown. Larraza's experimental results in a room using the time-reversal acoustic technique. A $9.5kHz$ pulse (bandwidth of $750Hz$) is generated at the source in the room (a). The resulting wave field is recorded by a microphone at a different location during a time $T = 50ms$ (b). The recorded signal is time-reversed and re-transmitted by the original source (c), yielding the time record at the microphone (d)

recorded the different transfer functions, the microphone has "learned the channel." For a specific channel, each transfer function implicitly carries (in the form of random scattering) the information about the multi-paths in the enclosure from source to microphone. The recorded waveform constitutes a characteristic stamp for the multipathing occurring for the particular link.

"Knowledge of the channel" should not be interpreted to mean that the microphones have knowledge of the specific location of the source nor of the other microphone. Also, it does not mean that the microphones know all the specific features such as corners, size, obstacles, etc about the enclosure. It simply means that by having a record of the transfer function, the source is equipped to send a signal and have it focus specifically at each microphone.

The communications algorithm used for the experiment consists of a set of four signals with different central frequencies. Four distinct signals have different central frequencies: 2, 4.5, 7, and 9.5 kHz and 750 Hz bandwidth. There are four distinct signals that define a 4-bit character. Different combinations of these four signals represent binary bits that are labeled as different symbols. Four center frequencies can be combined in 16 different ways (including the null symbol which has no acoustic energy). Each particular combination has one symbol assigned to it.

For a specific pulse of central frequency ν, the communication channel from source to microphone 1 is different than the one from source to microphone 2. During a training session, the four different initial signals are transmitted from the source. First the transfer function of all four signals is recorded for the channel formed by source and microphone 1. Then, the procedure is repeated using microphone 2. Each transfer function is made up of arrivals of the initial pulse as it is scattered through different paths on its way to the microphone. For a specific channel, each signal of frequency ν scatters in a unique way along its multi-path. This causes eight independent recordings of the occurring wave fields at the microphones. "The time record of each reception measured by the receiver provides the transfer function of the environment for those signals."[2]

After the training session, the eight different time-reversed transfer functions are fed into the source. Now, the source has the ability to send these time-reversed transfer functions and have them refocus at microphone 1 and 2 distinctly. The total number of signals the source can send is primarily limited by the system's bandwidth. The source transmits "each signal with sufficient time between transmissions for all multi-path structures to arrive at

---

[2] [30] p. 695

the receiver." [3]

Using the prescribed communications algorithm, the source is able to build 4 bit "symbols" from the time-reversed records of the four different signals. "A symbol is made up of one, two, three or all four center frequencies."[4] Also, the source can mix the four different frequency-pulses to compose different binary messages. Since the source has knowledge of both channels for all different frequencies, a duplex communication system can be established in the reverberant enclosure. Because each microphone has a unique transfer function of the environment, the source is able to send distinct simultaneous messages that will refocus as "message 1" in microphone 1 and "message 2" in microphone 2. The received messages at the two microphone locations are decoded using a matched-filter approach. It is then possible to have each microphone receive a unique message simultaneously with respect to the other.

To decrease the probability of overlap between different symbols, each new signal is separated from the next a minimum time equal to the temporal resolution of the signal at the focusing time. The criterion for the delay between subsequent symbol transmissions is the temporal resolution of the focus. Because the initial signals used "have a nominal temporal resolution of 1 ms, the source can transmit the 4-bit symbols at a nominal rate of 1000 symbols/s." [5]

The focused signals arriving back at the receiver have an improved signal to noise ratio (SNR) which can be improved by amplification and by using a larger window size. [10] For a communication system with one source and multiple receiver microphones it is possible to transmit multiple and distinct symbols to focus at different locations in the enclosure. This opens the possibility for multiple-channel acoustic communications systems in enclosures. The temporal and spatial focusing properties of the results obtained from the NPS experiment suggest that TRA is an especially good candidate for acoustic communications that use energy-detection methods, i.e. when no phase information is transmitted in the signal.

There are multiple uses for the TRA technique. It can improve sound quality in acoustic spaces, which is relevant to the field of architectural acoustics. In underwater acoustic communications it can create fast links that have the advantage of focusing in intended locations. Finally, an application to acoustic communications in buildings, such as sending data through an apparatus called "data blaster" so that it only transmits information that focuses in a desired location in a building.

---

[3] [30] p. 695
[4] [30] p. 695
[5] [30] p. 695

Wave equation is time-reversible.

3.3 Numerical Simulation of Time-Reversal Experiment

To explore the results of Larraza's experiments, we developed a finite-difference time-domain (FDTD) code that simulates an enclosure in two dimensions. The enclosure is shown in Figure 3.3. We are aware that the parameters used in our numerical simulation of an enclosure in two dimensions will not exactly match those used in the reverberant chamber at NPS.
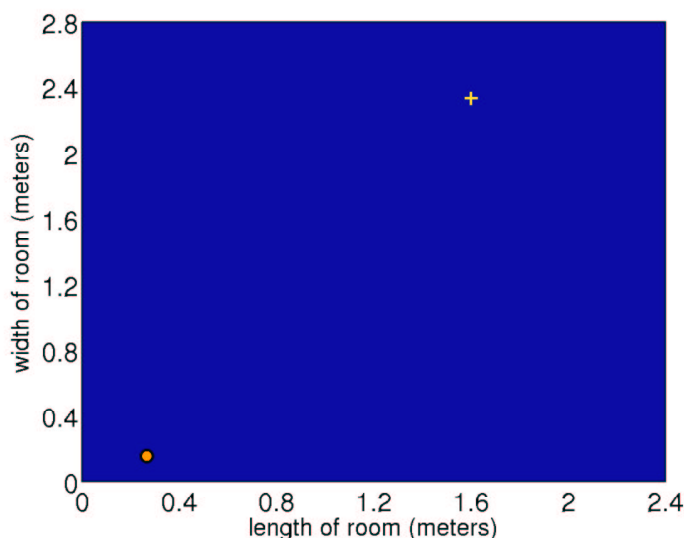
Figure 3.3: Setup of computational experiment. 2D enclosure of size (2.4, 2.8)m, a single detector (yellow cross) at (1.6, 2.3)m and a source (orange circle) at (0.31, 0.13)m

Our experiment in a computational environment, uses the (FDTD) code to solve the second order wave equation in two dimensions. It solves the equation in a square grid of size $(x_{len}, y_{len}) = (2.4, 2.8)m$. The spatial mesh grid consists of $8.1x10^5$ points, 900 per dimension. The separation between grid points in the mesh is equivalent to $\Delta x = 0.27$ cm in the $\hat{x}$ dimension and $\Delta y = 0.31$ cm in the $\hat{y}$ dimension. The acoustic pressure, p, is computed at each one of the spatial grid points using the center point and the two nearest neighbor points. This is done for approximately 10,000 time steps of size $\Delta t = 5\mu s$ each.

The capabilities of our computer equipment did not allow for the memory and speed required to formulate three-dimensional simulations. Nevertheless, results of numerical simulations in two dimensions replicate the physical phenomena to a great degree, and serve as

models that guide further research in higher dimensions.

Figure 3.3 shows the location of the source and detector in the enclosure. The numerical code simulates the transmission of a short signal in time from the source location and records the resulting wave field at the detector location. We call "detectors" what was previously referred to as "microphones" in the NPS laboratory experiment. The initial pulse, $f(t)$, emitted from the source, is written in equation 3.1 and shown in Figure 3.4.

$$f(t) = \cos\left(2\pi\nu\left(t - t_0\right)\right) \exp\left[-\frac{(t - t_0)^2}{t_w^2}\right] \tag{3.1}$$

The initial pulse is selected to resemble the one employed in the reverberant chamber experiment at NPS. All parameters in the numerical experiment were adjusted so that the model output estimates are consistent with the measured output values in the NPS laboratory experiment.

(a)

(b)
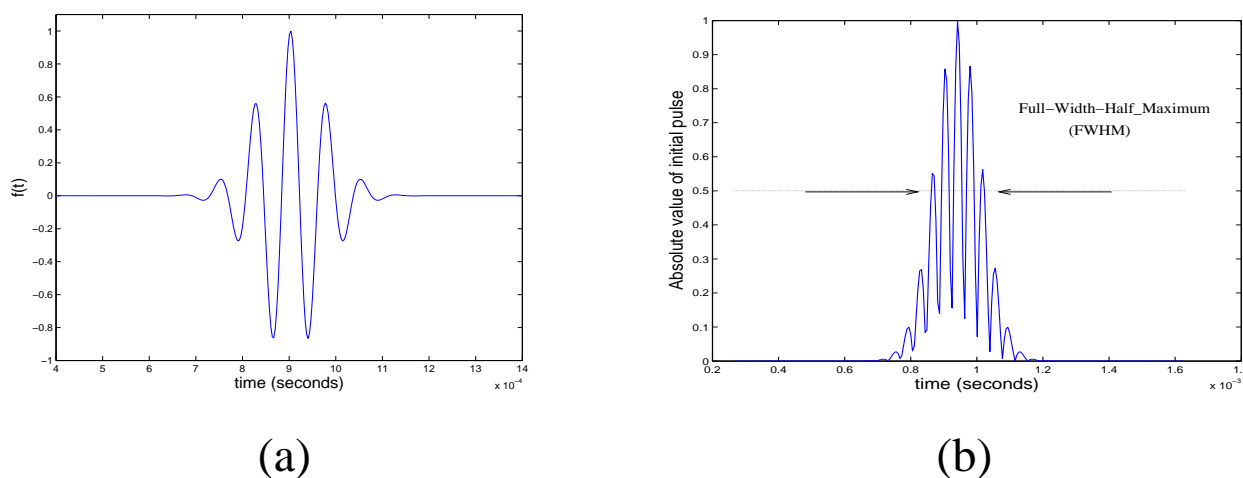
Figure 3.4: (a) Initial pulse $f(t)$. Central frequency $\nu = 13$ kHz, pulse width $\tau = 1/2$ ms, start time $t_0 = 0.9$ ms (b) Absolute value of initial pulse $f(t)$. Duration of the pulse in time is defined as the full-width-half-maximum (FWHM) width as shown in figure. It is the width of the pulse when at least 50% of the energy has left the source location. In our case, the pulse width is $\tau = 1/2ms$ which corresponds to a bandwidth of $B = 1/(2\tau) = 1kHz$

To recreate a point-like source, we consider the area of the source in space to be 1 pixel squared. The whole enclosure is formed of an area of $8.1x10^5$ squared pixels. Thus, the area occupied by the source is approximately one millionth of the entire enclosure. The pulse width of the initial pulse is $t_w = 1/2$ ms and we pick the recording time $T = 50$ ms in accordance with the experiment at NPS [30]. Then, our recording time, T, is equivalent to
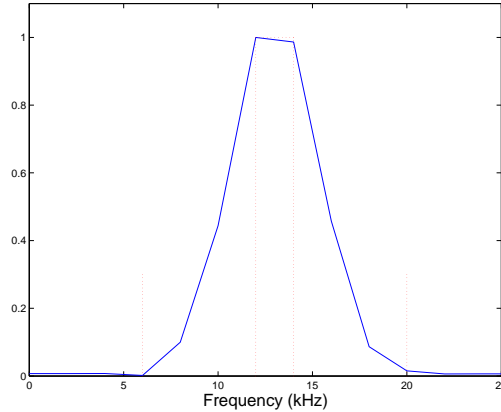
Figure 3.5: Initial pulse f(t). Central frequency $\nu = 13$ kHz, pulse width $\tau = 1/2$ ms, start time $t_0 = 0.9$ ms. Bandwidth $B = 1/2\tau = 1$ kHz

100 times the initial pulse-width.

In the "forward" phase of the time reversal process, an initial pulse is emitted by the source. After this takes place, the generated waves in the enclosure propagate through the medium and are recorded at a point-like detector in a different location. The detector records the wave field for a time $T = 50ms$. This wave field is exhibited in Figure 3.6 for a time reversal process carried out in an empty enclosure with reflecting boundaries. As seen in the figure, due to the kind of boundaries, the recorded signal does not decay in time. Thus, a truncation time T is picked on the order of 100 initial pulse width during which the signal is recorded.

The multi-path scattering with the boundaries in the enclosure causes many copies of the initial signal to arrive at the detector at different times.

We use an informal characterization for the direct arrivals which get to the detector before a time of 20 ms. In analogy with the formal terminology used in characterising the channel, we introduce the name for this initial section as the"ballistic" portion of the channel transfer function. As seen in Figure 3.6, there is a substantial gap around this time where no arrivals are received at the detector. We pick this gap as an arbitrary separation between the direct arrivals and the more diffuse coda that eventually arrives at the detector. We use the name "diffuse" to refer to the segment in the signal received from multiple scattering of the initial pulse.

The ballistic portion of the wavefield consists of the direct arrivals of the initial signal to the detector. The first arrival is called the "line-of-sight" (LOS) component. This pulse arrives at the detector undistorted because it has not interacted with any boundaries in
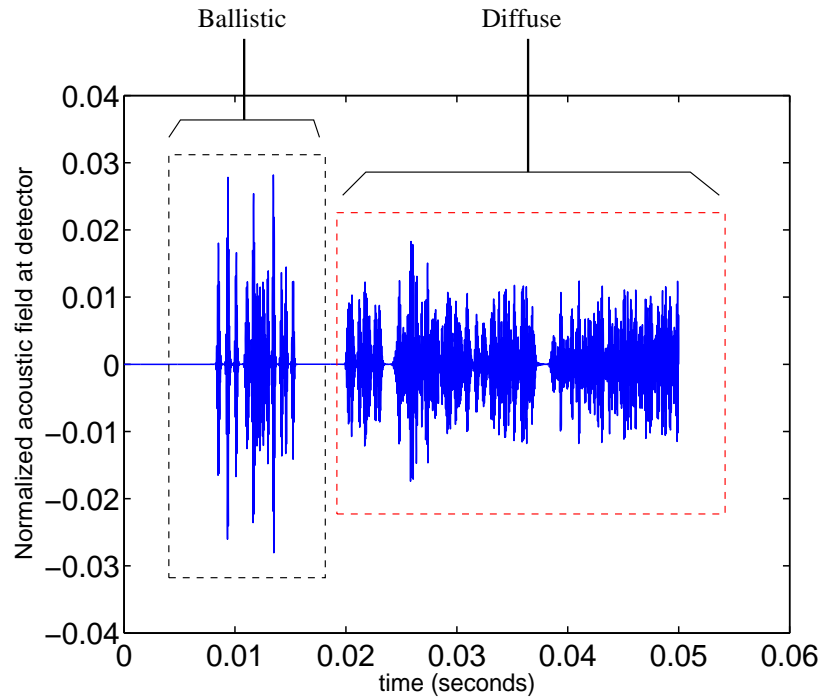
Figure 3.6: Wave field recorded at detector for a time-reversal numerical experiment in an enclosure with reflecting boundaries. We use an informal characterization for (a) the direct arrivals or "ballistic" portion of the channel transfer function and (b) the "diffuse" segment received after initial pulse has multiply scattered. Because of energy conservation in the enclosure, the wave field would remain ringing for an infinitely long time, i.e., the amplitude of its envelope does not decay with time. The recording of the acoustic field is truncated at a time = 50 ms

the enclosure. Subsequently, there are the arrivals of the pulse after it bounces off of one, two, three or four walls in the enclosure before it arrives at the detector. These are main arrivals coming from a few reflections with boundaries or other objects in the enclosure. In Section 3.6, we determine the first 16 paths that the initial pulse takes before arriving at the detector, and we compare the direct times of arrival with the ones calculated for each path. Eventually, sometime not necessarily right after the ballistic part, comes a long tail of diffuse arrivals. This coda arises from rich scattering in the environment.

In the "backward" portion of the time-reversal process, a similar numerical code reverses in time the wave field recorded at the detector. This is shown in Figure 3.7, (c). From a quiescent initial state, the time-reversed detector signal is emitted into the enclosure a second time. The waves multiply scatter and propagate for an additional recording time of $T = 50$ ms. When the medium does not change with time, it is understood that, the waves undergo the same reflections and scattering paths that the initial pulse went through during the forward phase of time-reversal. As a result, refocusing of the signal at the original source location occurs at a time equal to the recording window size of $T = 50$ ms. (shown in Figure 3.7, (d)).

Results obtained after this computational experiment display both tight localization of the refocusing spot around the source location and temporal compression of the re-transmitted signal to its original pulse-width. Just as in the experiment carried out in a reverberant chamber in the NPS laboratory, the results of this computational experiment show that a single element time reversal in a cavity "produces results that are as good as those produced by a wide aperture time-reversal array in an open system." [6] The quality of spatial focusing achieves tight localization of the pulse to within half a wavelength of sound; whereas temporal compression causes it to contract to its original pulse width. As Larraza suggests, "this result can be understood by noticing that due to reflections at the boundaries, the focusing quality is not aperture limited because the collapsing wave front approaches the focal region from all directions." [7].

3.3.1 Mathematical Formulation

Our numerical code solves the second-order wave equation in two dimensions as it is written in 4.5

---

[6] [30], p. 694
[7] [10]

(a) initial pulse

(b) detector

(c) time–reversed detector

(d) refocused pulse
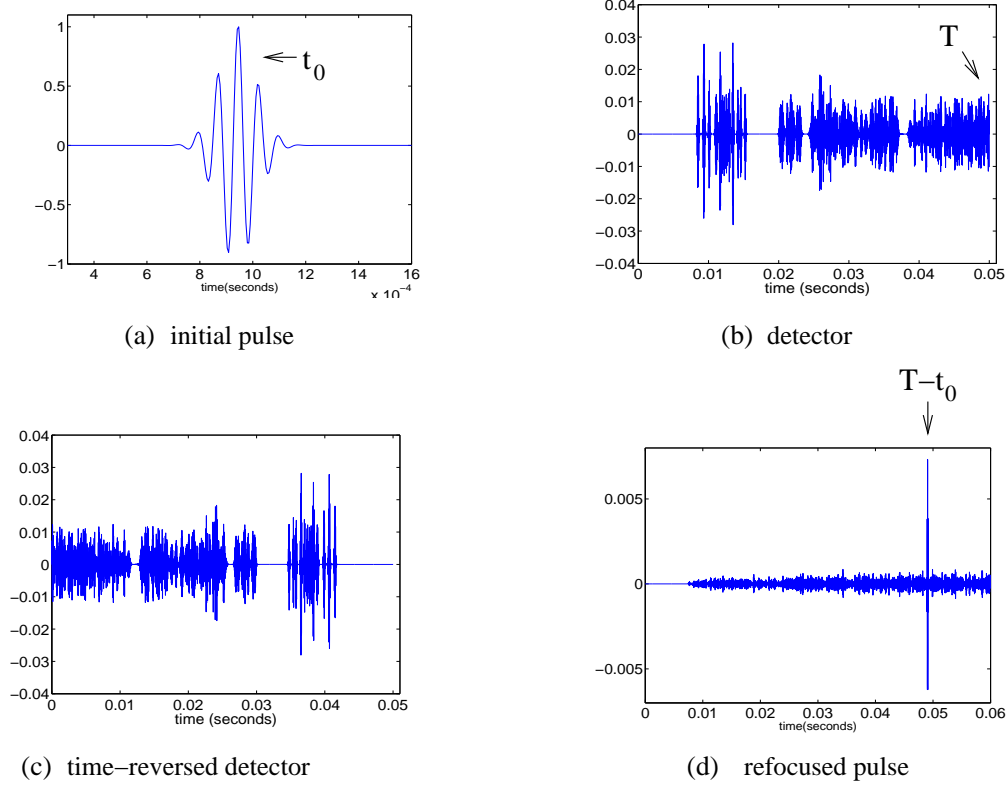
Figure 3.7: Computational simulation initial pulse of central frequency $13kHz$ and bandwidth of $B = 1/(2\tau)$ where $\tau = 1/2$ ms is the pulse width. $B = 1kHz$ generated in point in an enclosure of size (2.4, 2.8)m (a). The resulting wave field is recorded by a detector at a different location during a time T=50ms (b). The recorded signal is time reversed and re-transmitted by the original source (c), yielding the time record back at the source (d)

$$\frac{\partial^2 p}{\partial t^2} + c^2 \nabla^2 p = \delta(\mathbf{r} - \mathbf{r}_0)f(t) \qquad \text{Wave Equation} \qquad (3.2)$$

where $p = p(\mathbf{r}, t)$, and $\mathbf{r}_0$ is the source location. The position where we choose to make a measurement of the acoustic field is represented by $\mathbf{r}$.

Both the forward and the backward phases of the numerical time-reversal experiment initiate with the enclosure in a quiescent state, i.e., when the initial pressure as well as the first time-derivative of the pressure at the initial time is zero. Thus, the initial conditions for the acoustic pressure are indicated as follows

$$p(\mathbf{r}, t = 0) = 0 \tag{3.3}$$

$$\frac{\partial p}{\partial t}(\mathbf{r}, t = 0) = 0$$

The following physical parameters are used for the numerical experiment:

physical parameter	variable name	value
Frequency	ν	13 kHz
Pulse width	t_w	0.5 ms
Initial time	t_0	0.9 ms
Wavelength	λ	2.6 cm
Recording time	T	50 ms
Enclosure size	(x_{len}, y_{len})	$(2.4 , 2.8)$ m
Source location	$\mathbf{r_0}$	$(0.311 , 0.133)$ m

The speed of propagation of sound in air is $c = 343$ m/s, which corresponds to a wavelength $\lambda = c/\nu = 2.6$ cm. Since the dimensions of the enclosure in two dimensions are 2.4 m and 2.8 m in the $\hat{x}$ and $\hat{y}$ directions respectively, there are approximately 90 wavelengths per dimension in the room.

3.3.2   Boundary conditions

The key to studying enclosures is understanding boundary effects.

Class of Boundaries	Condition on Pressure	Parameter Values
Dirichlet	$p = 0$	
Neumann	$\frac{\partial p}{\partial n} = 0$	
Absorbing	$\frac{\partial p}{\partial t} = c\kappa \frac{\partial p}{\partial n}$	$0 \leqslant \kappa \leqslant 1$

3.4   Calibration of the Code

Our desire is to write a code that produces a numerical solution that is as close as possible to the true solution, if it could be calculated analytically. Thus, we must choose the numerical scheme as best as possible.

The code is calibrated to accurately reflect all physical parameters. Source and detector are placed in corresponding locations to the NPS laboratory enclosure as if a projection along the $\hat{z}$ (height) axis was taken, i.e. (looking at the floor of the reverberant chamber). The code solves the wave equation for the acoustic pressure, p, using the following second-order accurate scheme

$$p_{i,j}^{k+1} = 2\,p_{i,j}^k - p_{i,j}^{k-1} + c^2\,(\Delta t)^2 \left(\frac{p_{i+1,j}^k - 2\,p_{i,j}^k + p_{i-1,j}^k}{(\Delta x)^2} + \frac{p_{i,j+1}^k - 2\,p_{i,j}^k + p_{i,j-1}^k}{(\Delta y)^2} \right) \quad (3.4)$$

where we use centered differences for the three derivatives, i is the $\hat{x}$ dimension subscript, j is the $\hat{y}$ dimension subscript and k is the time superscript.

The Nyquist criterion requires that there be 10 grid points per wavelength to resolve the wave correctly. Thus, since $\lambda = 2.6$ cm, we determine the separation between grid points must be a maximum of 0.26 cm. Because of the dimensions of the enclosure, the number of points needed to resolve the mesh grid is 900 points per dimension.

It is an "explicit" scheme since the "future step" (k+1) only appears on the left side.

The "future step" $p_{i,j}^{k+1}$ needs two previous steps, "present" $p_{i,j}^{k}$ and "past" $p_{i,j}^{k-1}$. They should be given as initial conditions in the scheme.

The initial conditions we have are translated into finite differences as

$$p(t = 0) = 0 \qquad \rightarrow \qquad p_{i,j}^1 \qquad = 0 \tag{3.5}$$

$$p_t(t = 0) = 0 \qquad \rightarrow \qquad \frac{p_{i,j}^2 - p_{i,j}^0}{2\,\Delta t} = 0 \tag{3.6}$$

The latter second order approximation in 3.6 takes three grid points to calculate a first derivative. It is chosen so that the error it produces is of the order $O(\Delta x)^2$ or smaller. If we use a more simple approximation to the first derivative, like one that produces a $O(\Delta x)$ error, then this error would propagate in the code and we would not get convergence of second order to the real solution of the wave equation. [39]

The *truncation error* is introduced from writing all the finite difference approximations to the true derivatives. "We want the truncation error to tend to zero as the mesh size tends to zero." [8] Also, we want the *roundoff error* introduced by the finite number of digits used in calculating the answer at each step, to remain very small. The scheme calculates each new time step with a truncation error of order $O(\Delta t)^2 + O(\Delta x)^2 + O(\Delta y)^2$.

Using a *von Neumann* stability criterion [39], we will prove that this scheme is stable for [9]

$$\Delta t \leq \frac{\min(\Delta x, \Delta y)}{(\sqrt{2}\,c)} \tag{3.7}$$

Speaking for a moment about the wave equation in one dimension, the only relevant two grid sizes are Δx and Δt. The "Courant number" is defined as

$$\frac{\Delta t}{\Delta x} = \mu \tag{3.8}$$

where μ is a constant of order one. This is consistent with the fact that the scheme solves the wave equation.

In a sense, locking $\Delta t/\Delta x = \mu$ is picking the rate at which Δx and Δt approach zero. Thus, it makes sense to pick the specific rate as $\Delta t/\Delta x$ because it has the same form as the waves' propagation speed c.

---

[8]**??**, p. 191
[9] [40], p. 159

Now, back to our original discussion in two dimensions. To derive the stability criterion, from equation 3.4, we use separation of variables and try out the following solution for p_{ij}^k

$$p_{ij}^k = R_{ij}T^k \tag{3.9}$$

where R_{ij} governs the spatial part, and T^k the temporal one.

Just like when we solved the wave equation analytically, we look for solutions of equation (3.4), such that yield eigenmodes of the differential operator scheme. Thus, we assume $R_{ij}e^{(ii'k\Delta x + ji'k\Delta y)}$ where i' is the imaginary constant.

Plugging in equation 3.9 into 3.4, we obtain

$$\frac{T^{k+1} + T^{k-1}}{T^k} = 2\left(1 - s_1 - s_2\right) + s_1(e^{i'k\Delta x} + e^{-i'k\Delta x}) + s_2(e^{i'k\Delta y} + e^{-i'k\Delta y}) \tag{3.10}$$

Both sides have to equal a constant ξ, independent of i, j and k. Using this fact, we get

$$\xi + \xi^{-1} - 2 = 2s_1\left(\cos(k\Delta x) - 1\right) + 2s_2\left(\cos(k\Delta y) - 1\right) \tag{3.11}$$

which yields a second order equation for ξ

$$\xi^2 - 2\xi\left(1 + p_1 + p_2\right) + 1 = 0 \tag{3.12}$$

where we have denoted $p_1 = s_1\left(\cos(k\Delta x) - 1\right)$ and $p_2 = s_2\left(\cos(k\Delta y) - 1\right)$

The roots of equation 3.12 are

$$\xi = (1 + p_1 + p_2) \pm \sqrt{(1 + p_1 + p_2)^2 - 1} \tag{3.13}$$

We analyze the case when $p_1 = p_2 = p$.

$$\xi = (1 + 2p) \pm 2\sqrt{p^2 + p} \tag{3.14}$$

From its definition, we note that $p \leq 0$. Also, we see that p can range between two values: $p_{max} = 0$ and $p_{min} = -2s$, where $s = c^2\frac{\Delta t}{\Delta x}$.

As long as the growth factor's absolute value $|\xi|^2 \leq 1$, a necessary condition to have a stable scheme will be satisfied.

If $p = -1$, $\xi = -1$, if $p = 0$, $\xi = 1$. If $p < -1$, one of the roots of ξ will yield $|\xi| > 1$ so the scheme will be unstable. If, however, $p > -1$, we have the following solution for ξ

$$\xi = (1 + 2p) \pm 2i'\sqrt{-p^2 - p} \tag{3.15}$$

whose absolute value squared is

$$|\xi|^2 = (1 + 2p)^2 - 4(p^2 + p) = 1 \tag{3.16}$$

Thus, $\xi = \cos\theta + i'\sin\theta$ for some real number θ. It makes sense that the solutions oscillate in time, as they should for the wave equation.

From this, we conclude that, a necessary condition for stability is

$$0 \geq p \geq -1 \tag{3.17}$$

which, plugging back p in terms of s becomes

$$0 \geq s\,(\cos k\,\Delta x - 1\,) \geq -1 \tag{3.18}$$

which implies

$$0 \leq s \leq \frac{1}{2}$$

.

Finally, the stability criterion is

$$\Delta t \leq \frac{\Delta x}{\sqrt{2}\,c} \tag{3.19}$$

In this case we worked out a bound for the specific case when $\Delta x = \Delta y$. If, on the other hand, one is larger than the other, the minimum value between the two should be taken for the Courant number. In other words,

$$\Delta t \leq \frac{\min\,(\Delta x, \Delta y)}{\sqrt{2}\,c} \tag{3.20}$$

This is because if $\Delta x = \Delta y$, equation (3.19) gives an upper bound for Δt. Now, if instead $\Delta y \leq \Delta x$, the smaller bound is given by using Δy in the stability criterion.

This guarantees that Δt follows the rate of the smallest of the two grid measures. And since this is an upper bound, this ensures overall stability the scheme.

The code is accurate to within errors of second order with respect to the spatial grid-point separation Δx and Δy, and the temporal step size Δt.

3.4.1 Numerical Initial Conditions

Because our initial conditions for the pressure and the derivative of pressure with time are both zero, we need to use a higher order approximation to the pressure at the very fisrt time step. It is important to pick the right numerical initial condition for the pressure at the time dt, i.e. $p(x, y, dt)$ for the numerical code to preserve the desired order of magnitude of the truncation error produced by the code. Since our numerical code outputs a solution accurate to within $O(\Delta t)^2 + O(\Delta x)^2 + O(\Delta y)^2$, we expect the numerical initial step to maintain the accuracy of the code within the limits of this error.

For reference, the initial conditions evaluate the solution at the first time step $(t = dt)$, and use a forward difference approximation with second order error, consistent with the error in the rest of the code.

To figure out the initial conditions, we use a Taylor approximation. We start with the wave equation, only this time avoided writing the Laplacian for simplicity, supposing it is inside the source term $f(x, y, t)$.

$$p_{tt}(x, y, t) = f(x, y, t) \tag{3.21}$$

From equation 3.21, we integrate to obtain

$$p_t(x, y, t) = \int_0^t f(x, y, t)dt + p_t(x, y, 0) \tag{3.22}$$

Integrating a second time, we get an expression for the solution p

$$p(x, y, t) = \int_0^s \left(\int_0^t f(x, y, t)dt \right) ds + sp_t(x, y, 0) + p(x, y, 0) \tag{3.23}$$

where s is just a dummy integration variable for time. Finally, using a Taylor approximation for our source term

$$f(x, y, t) \approx f(x, y, 0) + s f'(x, y, 0) + O((\Delta t)^2)$$

where the prime $'$ denotes derivative with respect to time.

Plugging this expression for the source term in the integral of equation 3.23 and solving for it, we obtain

$$\int_0^s \left(\int_0^t f(x, y, t)dt \right) ds = f(x, y, 0)\frac{s^2}{2!} + f'(x, y, 0)\frac{s^3}{3!} + O(s^4) \tag{3.24}$$

Thus, our final expression for the pressure at the first time step $p(dt)$ p(x,y,dt) is

$$p(x, y, dt) = f(x, y, 0)\frac{(dt)^2}{2} + f'(x, y, 0)\frac{(dt)^3}{6} + dt p_t(x, y, 0) + p(x, y, 0) \qquad (3.25)$$

3.4.2 Numerical Boundary Conditions

For the Dirichlet boundary conditions $p = 0$, we simply set all the boundary's values equal to zero. We then solve the problem in a reduced-size domain inside the outlining zeros. For Mixed or Robin type boundary conditions $p + \alpha \partial p / \partial n = 0$ (of which Neumann boundaries are a specific case), we applied the "ghost point" method. At the boundaries of the computational domain, we compute the spatial derivatives using centered-finite differences. We consider one grid point inside the domain, and a second one just outside it (the ghost point). That is, let's say we need to calculate the first spatial derivative with the normal at the $(x = 0)$ boundary. If we used

$$p_x(x = 0, y, t) = \frac{p_{1,j}^k - p_{0,j}^k}{\Delta x}$$

for the derivative at the boundaries, it would introduce an error of $O((\Delta x)^2)$. Instead, we use a second order approximation to a first derivative in spatial coordinates:

$$p_x(x = 0, y, t) = \frac{p_{1,j}^k - p_{-1,j}^k}{2\Delta x} \qquad (3.26)$$

The point $p_{-1,j}^k$ is the ghost point and we use equation 3.26 to solve for it in terms of the known values of $p_x(x = 0, y, t)$ and $p_{1,j}^k$. This ensures that the error introduced by calculating these derivatives at the boundaries is of order $O((\Delta x)^2)$, as expected.

Write bc's for Absorption!!! cause they involve a deriv w/time.

3.4.3 Convergence Analysis

We verified the stability bound, obtained the appropriate Courant number and showed that above that number the code blows up. We also checked for consistency of the code. As part of a convergence test, it is important to check that as the distance between points in the grid decrases, i.e., as $\Delta_x \to 0$, the truncation error produced by the computer simulation rounding off numbers also approaches zero. Moreover, it is essential to find out the rate at which this happens and compare it to the error determined by the accuracy of our finite-difference scheme. Thus, in our case, since the error determined by our finite-difference

scheme is on the order of $O(\Delta t)^2 + O(\Delta x)^2 + O(\Delta y)^2$, we expect the convergence analysis to show that the maximum error between the analytic and computed solution approaches zero at this same rate.
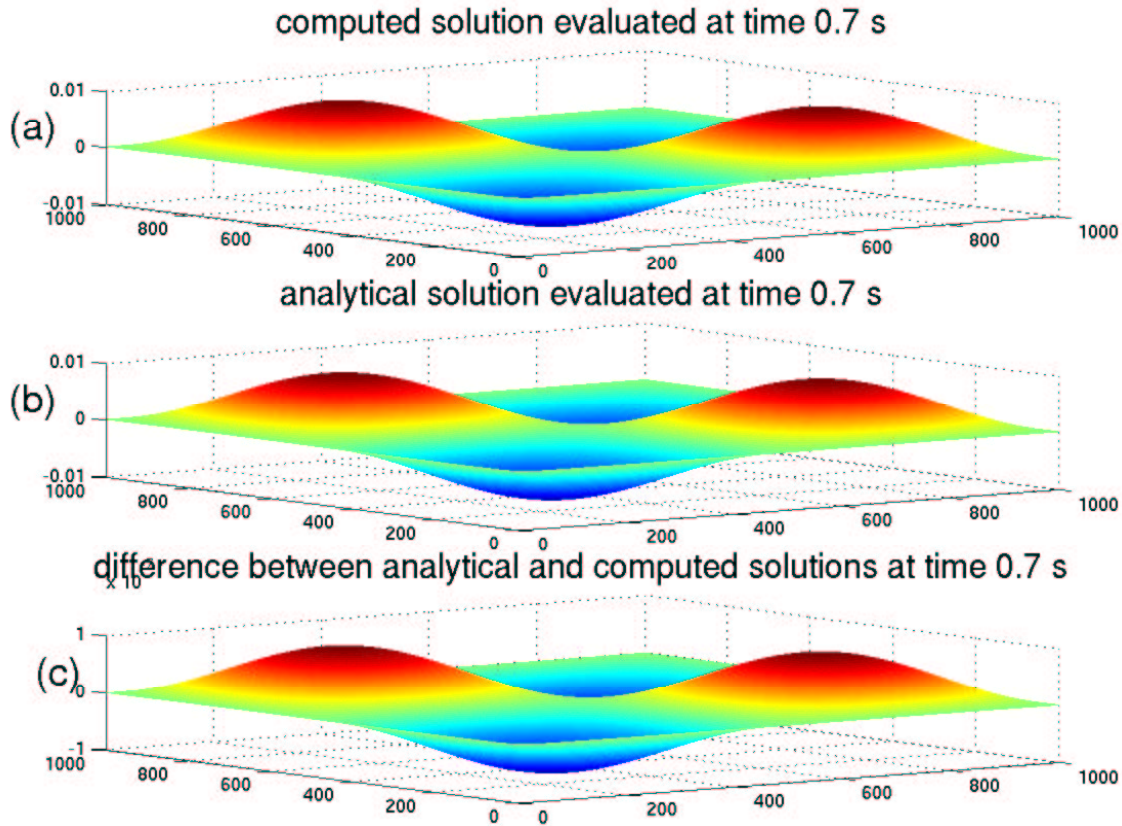
Figure 3.8: (a) computed solution using numerical code to solve the initial boundary value problem given in equations (3.27), evaluated at time 0.7 s. (b)plot of analytical solution evaluated at time 0.7 s (c) difference between analytical and computed solutions, i.e., $(p_{\text{analytical}} - p_{\text{computed}})$ on the order of 10^{-8}. The number of grid points in both spatial dimensions is 1000, and the separation between gridpoints is $\Delta_x = 1x10^{-3}$. Similarly, $\Delta_y = 1x10^{-3}$ and the time step is given by $\Delta_t = 7x10^{-4}$. Graph (c) shows the difference between both solutions at this time is on the order of $\epsilon = 1x10^{-7}$ which is approximately on the order of $O(\Delta t)^2 + O(\Delta x)^2 + O(\Delta y)^2$

To verify convergence, we perform grid-refinement analysis to verify that the approximate solution output by the computer model converges to the exact solution as the size of the grid-separation approaches zero. To do this, we take a simple known function and compute
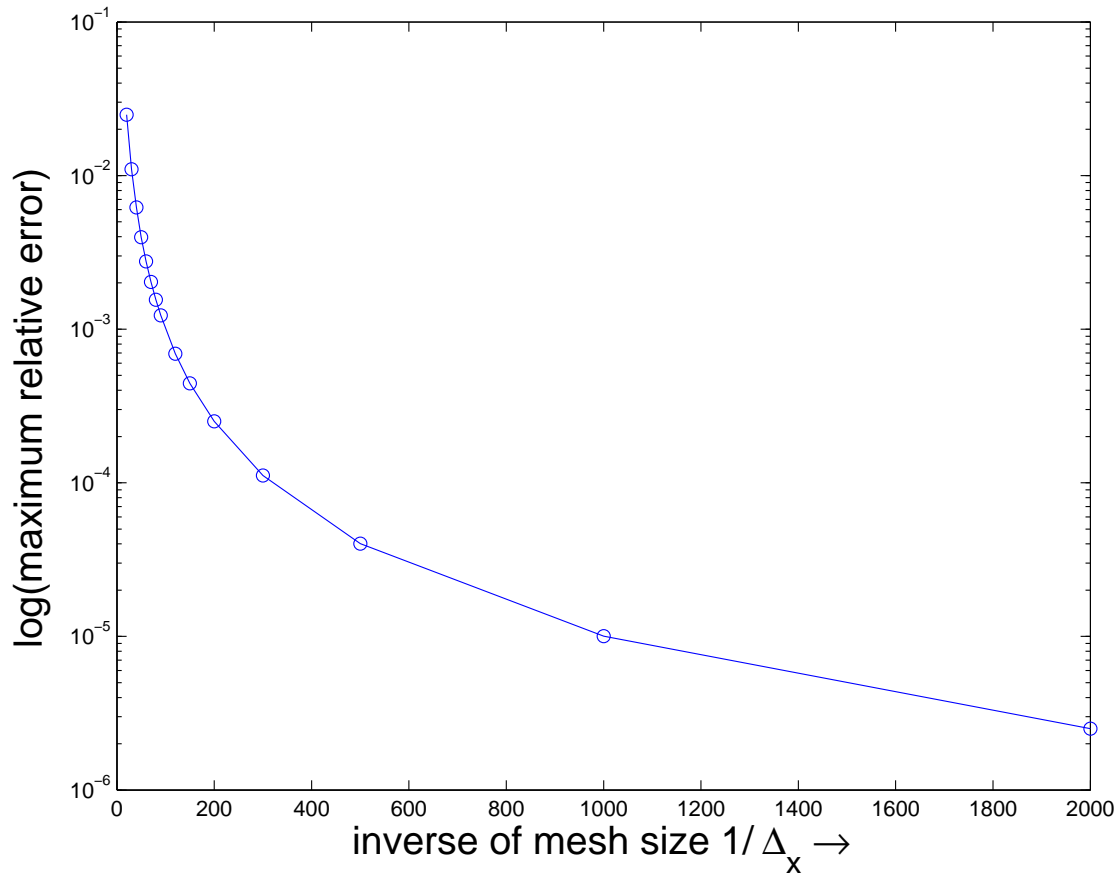
Figure 3.9: Plot of the logarithm of the error versus the inverse of the grid size. The error is calculated as the maximum of the relative error which is given by relative error $=$ $\frac{\left(p_{\text{computed}} - p_{\text{analytical}}\right)}{p_{\text{analytical}}}$ As the grid size decreases, $\Delta_x \rightarrow 0$, the error decreases at a rate of $O(\Delta t)^2 + O(\Delta x)^2 + O(\Delta y)^2$ which is consistent with the error determined by our finite-difeerence scheme
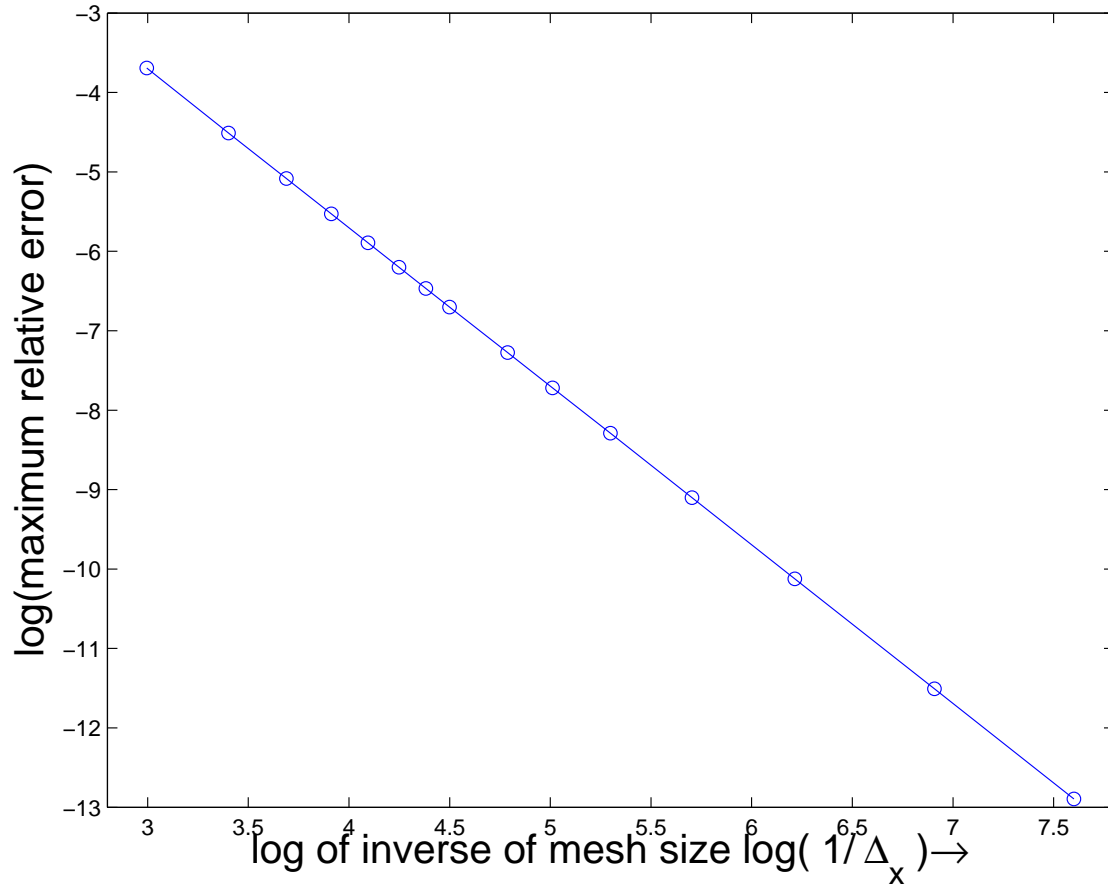
Figure 3.10: Plot of the logarithm of the error versus the logarithm of the inverse of the grid size. The error is calculated as the maximum of the relative error which is given by relative error $= \frac{\left(p_{\text{computed}} - p_{\text{analytical}}\right)}{p_{\text{analytical}}}$ The slope of 2 indicates the rate of convergence of the numerical code as in error $\approx \Delta x^c$ where c is the slope. As the grid size decreases, $\Delta_x \to 0$, the error decreases at a rate of $O(\Delta t)^2 + O(\Delta x)^2 + O(\Delta y)^2$ which is consistent with the error determined by our finite-difeerence scheme

the following initial boundary value problem with our code

$$p_{tt} = c^2(\,p_{xx}(x,y,t)\,+\,p_{yy}(x,y,t)\,),\qquad t>0$$
$$p(0,y,t)=0\,,\ p(x_{len},y,t)=0\,,\ p(x,0,t)=0\,,\ p(x,y_{len},t)=0$$
$$p(x,y,0)=\sin(2\pi x)\sin(2\pi y)\sin(4\pi t)),\qquad p_t(x,y,0)=0$$

We know the analytic solution to this problem is given by

$$p(x,y,t)=\sin(2\pi x)\sin(2\pi y)\left(\frac{1}{4\pi^2\sqrt{2}}\sin(2\sqrt{2}\pi t)-\frac{8}{\pi^2}sin(4\pi t)\right)\qquad (3.28)$$

We compute the solution to the problem stated in equations (3.27) using our code and compare the result obtained with the analytical solution given in (3.28). We repeat this process a number of times, each time decreasing the size of the mesh grid $\Delta_x \to 0$.

Subsequently, we do a least-square error analysis to evaluate the rate at which the relative error decreases as a function of reduction of mesh grid size. As the mesh size $\Delta_x \to 0$, the error decreases as a function of $\approx \Delta_x^2$ which is consistent with the error determined by our finite-difference scheme. For the calculation, we use the relative error between the computed and the analytic solutions to the problem, it is given by

$$\text{relative error} = \frac{(p(x,y,t)_{\text{computed}} - p(x,y,t)_{\text{analytical}})}{p(x,y,t)_{\text{analytical}}}\qquad (3.29)$$

In Figure 3.8, (a), we show a plot of the computed and analytical solutions as well as the difference between them. In part (b) we plot of the logarithm of the error versus the inverse of the grid size.

3.5 Analyzing Results of the Basic Time Reversal Experiment

Once convergence of the code is established, we can proceed to use a source term that more accurately models Larraza's original pulse in [30] For this pulse, we do not know the analytical answer to the wave equation, but we trust the results of our convergence analysis and run our simulation of time-reversal in a two-dimensional enclosure. The results obtained with the code are displayed in figure 4.2.
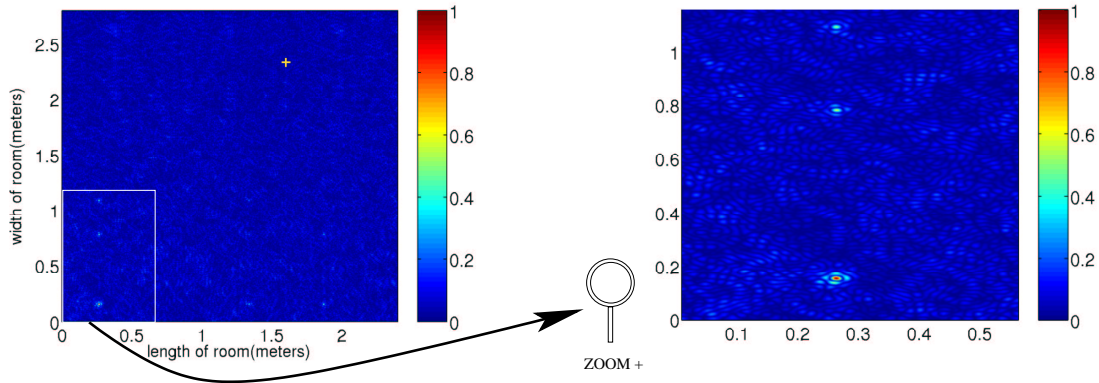
Figure 3.11: Contour map of normalized acoustic field at time of refocusing $t = T - t_0$. Snapshot of empty enclosure with highly reflective walls, source and a single detector. Refocused pulse is observed at original source location

3.5.1 Spatial Resolution

The results of the simulation in 4.2 display a refocused pulse at the original source location. Figure zooms in at the source location and shows a tight focusing of pulse within half a wavelength of sound.
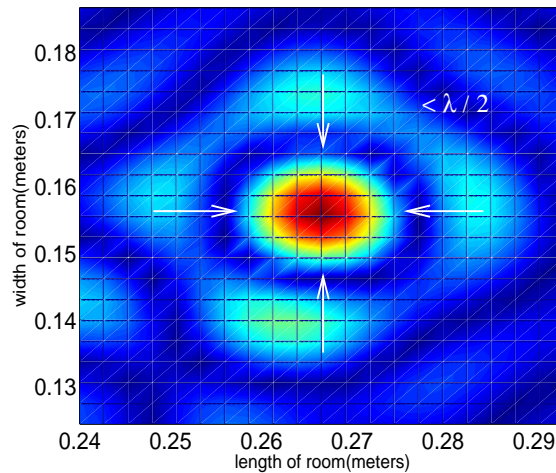
Figure 3.12: Spatial resolution of refocused pulse after time-reversal

To analyze the spatial resolution of the focused pulse, we measure its full width half at maximum (FWHM) size. The wavelength λ is 2.6 cm and the FWHM in both the x and y directions is 1.2 cm, which clearly proves the refocused signal has a spot size within $\lambda/2$. Figure 3.13 shows the one dimensional slices of the two-dimensional plot in Figure 3.12. It is

a plot of the acoustic field across the entire length of room while keeping the width location equal to the source's location along the width. This measurement is also carried for the opposite situation when taking the acoustic field across the width of the room while keeping the length constant at the source location. For both cases, we get a similar result where the spot size (in both range and width) is of size within $\lambda/2$.
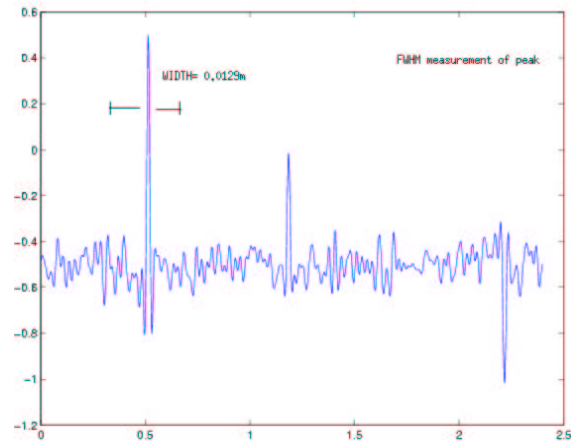
Figure 3.13: Acoustic field measured along the length of the room while the width coordinate is maintained constant at the source location Full-width-half-maximum measurement of the size of the focusing spot.

The results utilizing both constant and random Robin boundary conditions are the same. Spatially, we observe good refocusing at the source location. However, there are four side lobe peaks that measure up to 40% of the main refocused pulse in magnitude. These arise because in a reverberant enclosure where energy is conserved, there are image sources that act as if they were transmitting the time-reversed wave field into the medium. The same reflection paths cause similar side lobes in the case of highly reflecting boundary conditions such as Dirichlet or Neumann.

3.5.2   Delay Spread and Temporal Compression

When the boundary conditions in the enclosure are perfectly reflecting (Dirichlet), the delay spread is infinite. The acoustic field is trapped in the enclosure and has no method of decaying. In contrast, when absorption is present, some of the energy is being removed from the enclosure and thus affects the wave field recorded at the detector. In general, absorption causes the recorded wave field to have an approximately exponentially-decaying envelope that gives shape to the multiple scattering bounces registered in the wave field. The delay

spread Δ is longer in low-absorption environments than in highly absorbing ones. In his book, Mobile Communications Engineering, William C. Y. Lee states the common trend to consider the maximum delay time as measured 30 dB down from the highest level of the envelope [10]. When there are multiple scatterers present such as boundaries and furniture in an enclosure, the discrete pulses received at the detector become a continuous signal pulse with a pulse length Δ, commonly referred to as the "delay spread" [41]. The delay spread represents the time that it takes for most of the copies of an initial pulse to arrive at the detector.
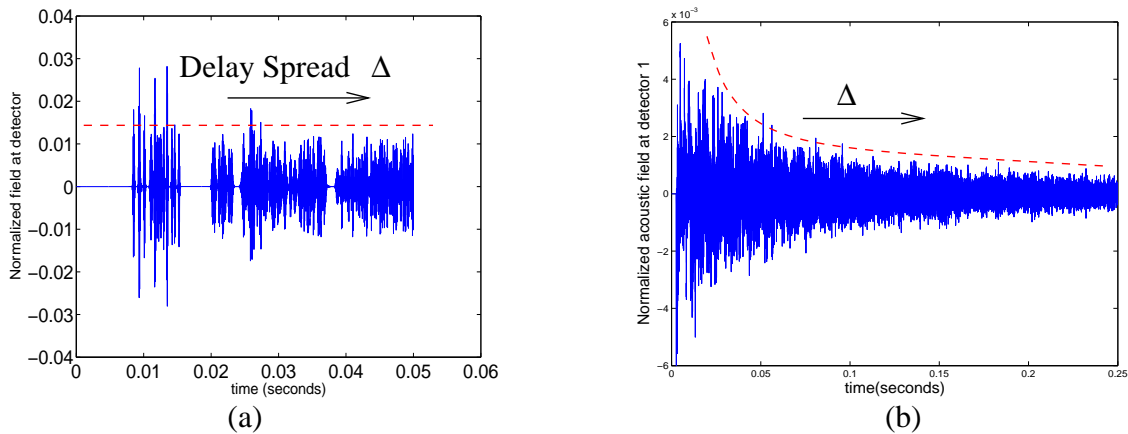
Figure 3.14: Typical channel transfer functions $h(t)$ obtained when an acoustic signal propagates in an enclosure. (a) When boundaries are perfectly-reflecting and energy is conserved, the envelope of $h(t)$ does not decay in time. (b) When absorption is present, in general, an exponentially-decaying envelope characterizes $h(t)$

When the boundary conditions in the enclosure are perfectly reflecting (Dirichlet), all energy is conserved. Therefore, the signal received at the detector rings for an infinitely long time, i.e., the amplitude of its envelope function does not decay with time (see Figure ??). In this case, a truncation time of $T = 50$ ms is chosen to stop the recording. The size of the recording window should generally be on the order of 50 to 100 times the initial pulse-width. This is the case in our numerical code for the recording time T is 100 times the pulse width. There exists a point in time when scattering paths and thus information about the enclosure will start repeating. When this occurs, increasing the window size does not improve the focusing of time-reversal. Typically, though, the larger this window size the more scattering information is collected in the wave field and the better temporal and spatial focusing results from time-reversal.

---

[10] [41], p.49-50

There is the possibility that two different signals of closely-spaced frequencies that have different time delays become correlated. This means that they would both experience comparable amplitude fading. There exists a certain frequency interval for which the two frequencies *can* become correlated. This frequency gap is dependent upon the delay spread Δ and is called the "coherence" or "correlation" bandwidth (B_c). The normalized magnitude of the delay-spread envelope (using the Laplace transform), gives the correlation function C(f) of the signal. [41] "The precise definition of coherence bandwidth often differs from one reference to another (...) and tends to depend on the extent of the correlation, determined subjectively, over which the two signals are correlated. A typical definition is

$$B_c = \frac{1}{8\Delta}$$

" [11] For the case of a perfectly reflecting enclosure, as $\Delta \to \infty$, the coherence bandwidth goes to zero.

Delay spread is a measure of the time-dispersion experienced by a signal as it scatters off of multiple obstacles. A remarkable aspect about the time-reversal process is that it is able to compress a highly dispersed time signal into a short pulse in time. In our experiment, we expect that temporal compression will concentrate most of the acoustic energy in the enclosure into a short pulse of similar duration to the original one.

The results obtained with the code are displayed in Figure 3.7. It can be observed in (b) that the recorded signal has a very long delay spread and consists of a few direct arrivals composing the ballistic section of the wave field, as well as a more complex diffuse tail. This was shown in figure 3.6

Temporal compression was displayed in Figure 3.7, (d), and it causes the recompressed pulse to recover its original width in time as it is shown in Figure 3.15. The natural effects of dispersion by multiple scattering in the channel are greatly reduced by time-reversal. This causes the pulse width of the refocused pulse to be of the same size as the original.

For communications, it is important that the refocused pulse preserves its original shape. This is because when a message is sent, it is composed of not only one, but several of these pulses, one after the other. These are called "symbols." If one is to encode a binary message onto a sequence of pulses, we want to make sure that the refocused sequence will preserve the binary information of the original one within a certain accuracy. The degree to which various symbols interfere with their neighbors is called "Inter-Symbol Interference" (ISI).

---

[11] [41], p. 52
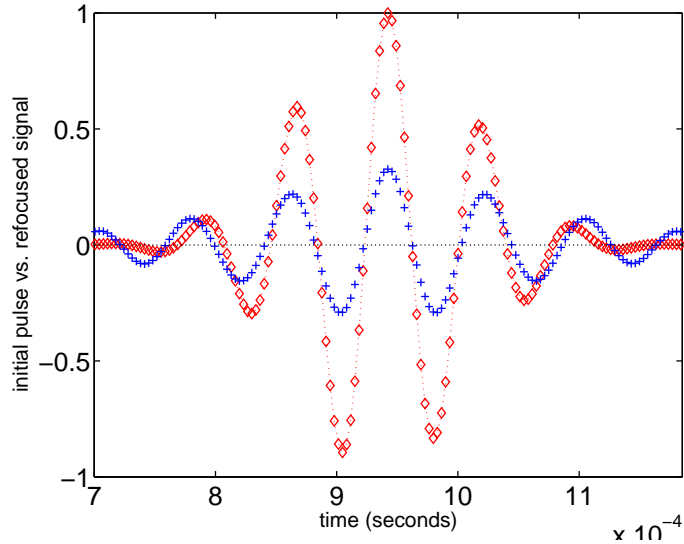
Figure 3.15: Temporal compression and preservation of pulse shape after time-reversal. Original pulse (red) versus refocused one (blue)

Our final goal is to establish en efficient communication link in an enclosure with low ISI, as well as low bit-error rate. If we expect a refocused sequence of pulses to remain faithful to the original sequence, it is a necessary that the shape and nulls of a single pulse be preserved. That we observe no significant distortion of the refocused pulse as evidenced by the comparison with the initial pulse observed in Figure 3.15, is a key element that opens the door for the possibility of encoding several-bit symbols unto more complex sequences of pulses. This is because when coding different bits unto a signal, if the shape of the initial pulse is not maintained with a relatively high degree of accuracy in the recompressed pulse, it will not be possible to recover the transmitted bit sequence with fidelity. Furthermore, when sending trains of pulses, the further away from the center of each symbol, the higher the probability of ISI will be. Thus, maintaining the pulse shape, guarantees that far from the pulse's center, there will be no significant side lobes to interfere with neighboring pulses.

3.6 Comparing Ballistic Arrival Times with Direct Arrivals in Time-Series

In Section 3.3, we presented the division of the recorded wave field into ballistic and diffuse segments as is illustrated in Figure 3.6.

The ballistic part of the coda consists of the direct arrivals of the initial signal to the

detector. The first arrival is called the "line-of-sight" (LOS) component. This pulse arrives at the detector undistorted because it has not interacted with any boundaries in the enclosure. Subsequently, there are the arrivals of the pulse after it bounces off of one, two, three or four walls in the enclosure before it arrives at the detector. These are main arrivals coming from a few reflections with boundaries or other objects in the enclosure. After the ballistic part comes a long tail of diffuse arrivals that arises from rich scattering in the environment. As discussed earlier in Section 3.3, the delay spread is caused by these late multi-path wave arrivals that occur some time after the ballistic arrivals in the coda.

When we perform the numerical time-reversal experiment in an enclosure with perfectly-reflecting boundaries such as Dirichlet, the total energy in the enclosure is conserved. As explained earlier in Section 3.5.2, and illustrated in Figure 3.14 (a), the acoustic field would remain ringing for an infinite time after an initial pulse is emitted. Only when there is absorption present, as displayed in the channel transfer function in Figure 3.14 (b), the delay spread becomes finite.

If we look closely at the ballistic portion of the channel transfer function in Figure 3.14 (a), we realize the direct arrivals are easy to spot. In Figure 3.16 we cut a small time-window and zoom in to analyze the individual main arrivals. We refer to all arrivals that arrive at the detector location before the first 20 ms have elapsed. They resemble individual distinguishable reproductions of the pulse that arrive at specific times t_1, t_2, t_3,etc... at the detector.

The times of arrival t_1, t_2, t_3, etc... of these earlier reproductions of the pulse correspond to classical arrival times that can be calculated knowing the specific path lengths and the the speed of sound in the enclosure c. For each individual copy of the pulse, the time of direct arrival is calculated as

$$ t = \frac{\sqrt{(x_1 - x_0)^2 + (y_1 - y_0)^2}}{c} \tag{3.30} $$

where d is the path length covered from source to detector location. (x_0, y_0) is the source location and (x_1, y_1) is the detector location.

Table 3.1 displays the calculated first 16 arrival times of the reflected initial pulse at the detector. The corresponding elements of the wave field received at the detector are illustrated in figure (3.16).

Because there are multiple paths that can connect the traveling path of a signal between two points in the enclosure, the individual copies of the pulse arrive at the detector at
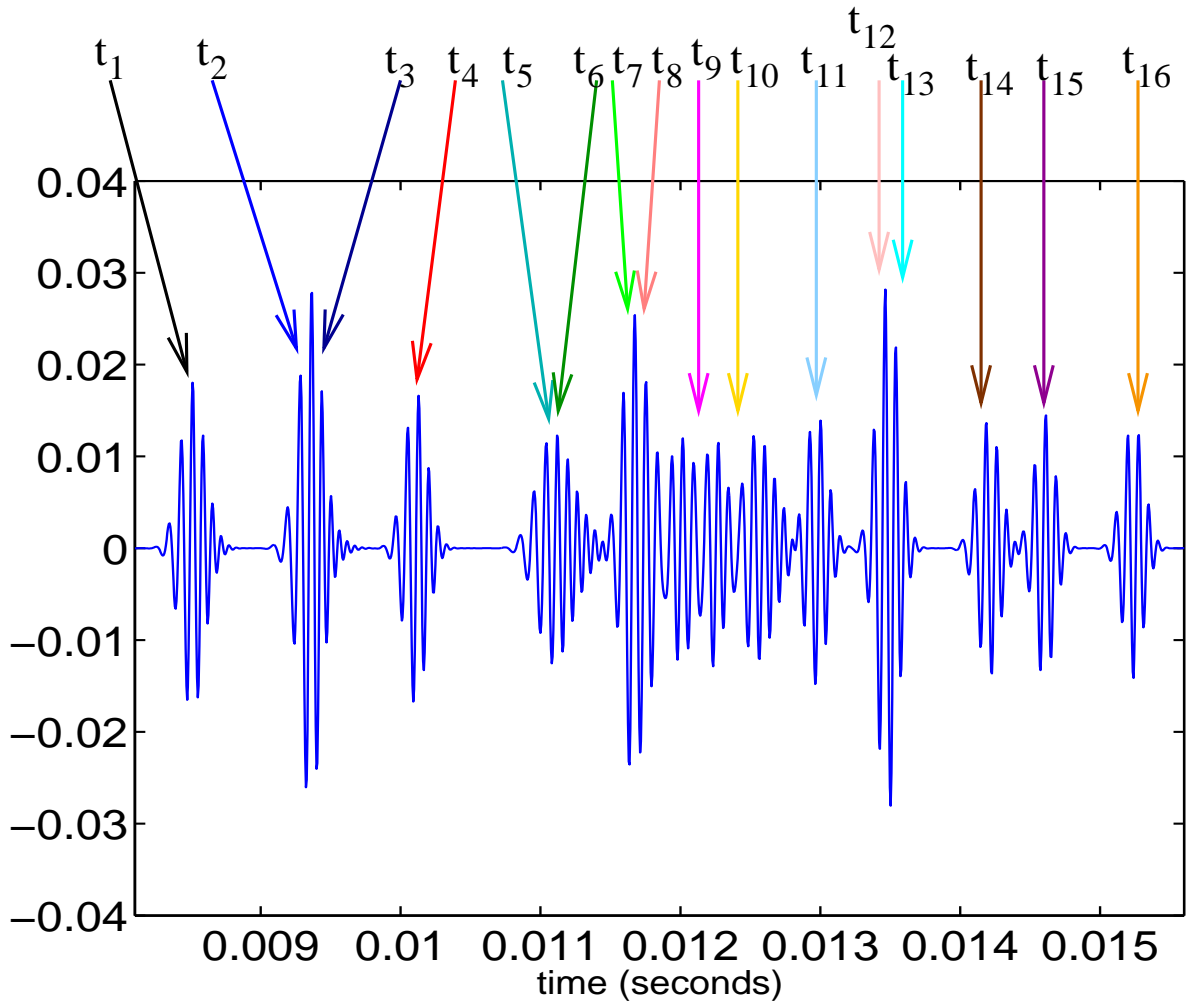
Figure 3.16: Ballistic section of wave field displaying first 16 arrival times. The first black arrow points to $t-1$ which is the immediate LOS component that arrives at the detector undistorted. After this come similar copies of the original pulse from different paths taken in the enclosure. Sometimes, two different paths have a similar arrival time and coincide at the detector and constructively interfere with each other such as for t_2 and t_3. Other times, copies of the pulse that arrive at times like t_9, t_10 and t_10 interfere destructively at the detector

label	number of bounces	time (s)
t_1	0	0.00838
t_2	1	0.00917
t_3	1	0.00930
t_4	2	0.01001
t_5	1	0.01081
t_6	2	0.01152
t_7	1	0.01159
t_8	2	0.01165
t_9	2	0.01216
t_{10}	3	0.01231
t_{11}	2	0.01288
t_{12}	3	0.01338
t_{13}	2	0.01341
t_{14}	3	0.01408
t_{15}	3	0.01452
t_{16}	4	0.01514

Table 3.1:

multiple times. Some very different paths turn out to have nearly identical arrival times at the detector. When this happens, multiple copies of the pulse that arrive very close in time interfere with each other. This is the reason why we observe individual copies of the initial pulse that are distorted in either magnitude or phase due to interference between main arrivals.

In Figure 3.16, t_1 constitutes the LOS arrival. It is the first copy of the pulse that arrives at the detector undistorted from a direct path from source to detector. To illustrate the case for pulses arriving with almost identical times at the detector, we analyze the ones arriving at times t_{12} and t_{13}. From Table 3.1, we read $t_{12} = 13.38$ ms and $t_{13} = 13.41$ ms, and, looking at the ballistic portion of the transfer function in Figure 3.16, we observe how these two pulses interfere constructively to form a distinguishable pulse with almost one and a half times the magnitude as the LOS pulse. In this case, phases and magnitudes add coherently to form a larger pulse. In other instances such as arrival times $t_9 = 12.16$ ms and $t_{10} = 12.31$ ms, the difference in arrival times is enough to create destructive interference and reduce the overall magnitude of the signal to approximately 60% the size of the LOS component.

To figure out the distinct paths that each individual pulse reproduction takes from source to detector, we construct a virtual plane that represents image copies of the enclosure. We use the method of images to find the paths by iteratively placing "ghost" detectors behind

each surface. Using the method of images we argue that since the acoustic pressure must be zero at all boundaries (prescribed by the Dirichlet boundary conditions), there is exactly one primary image detector located in each copy of the enclosure. This is shown in Figure 3.17. We ignore secondary and higher order images due to their low magnitude contribution in the multi-paths.
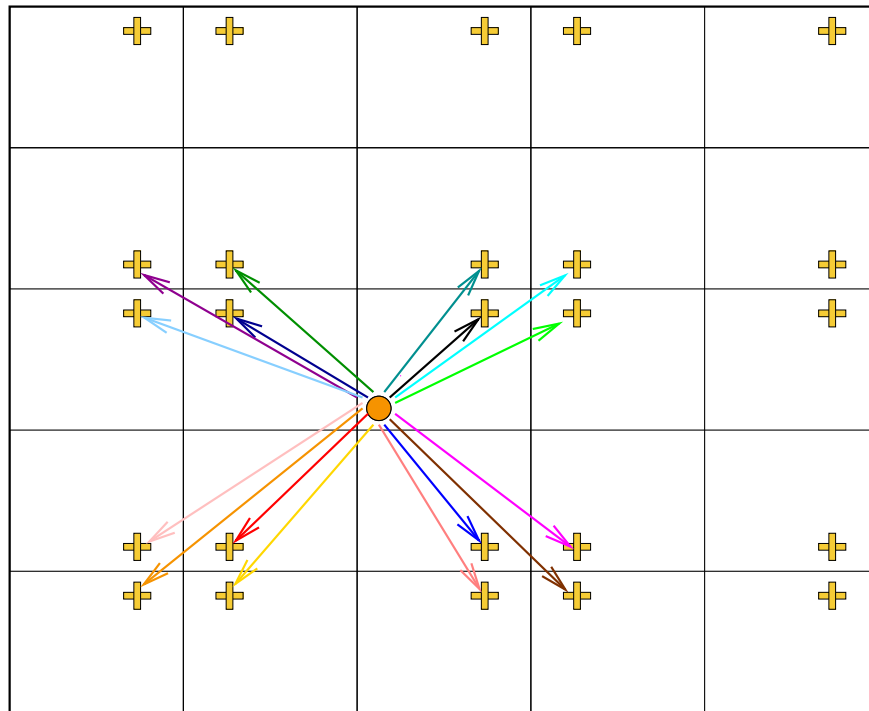
Figure 3.17: Visualization technique with the method of images to discover paths taken by initial pulse after reflection

Figure 3.17 is a simple visualization devise that aids in the reconstruction of the different paths in the enclosure. We use the information from this figure, such as number of bounces and angles of reflection, to build the well-defined paths illustrated in Figure 3.18.

Multiple paths may have a similar arrival time as shown for t_6 and t_7 in the figure. Thus, when they arrive at the detector, there is interference between these signals and the pulse gets distorted. The later decaying section of the channel transfer function arrives at the detector by means of a large number of scattered paths.

After the direct arrivals, the detector records a long tail of diffuse arrivals that bounce and interact with walls and multiple waves before they reach the detector. This tail constitutes the diffuse part of the coda.
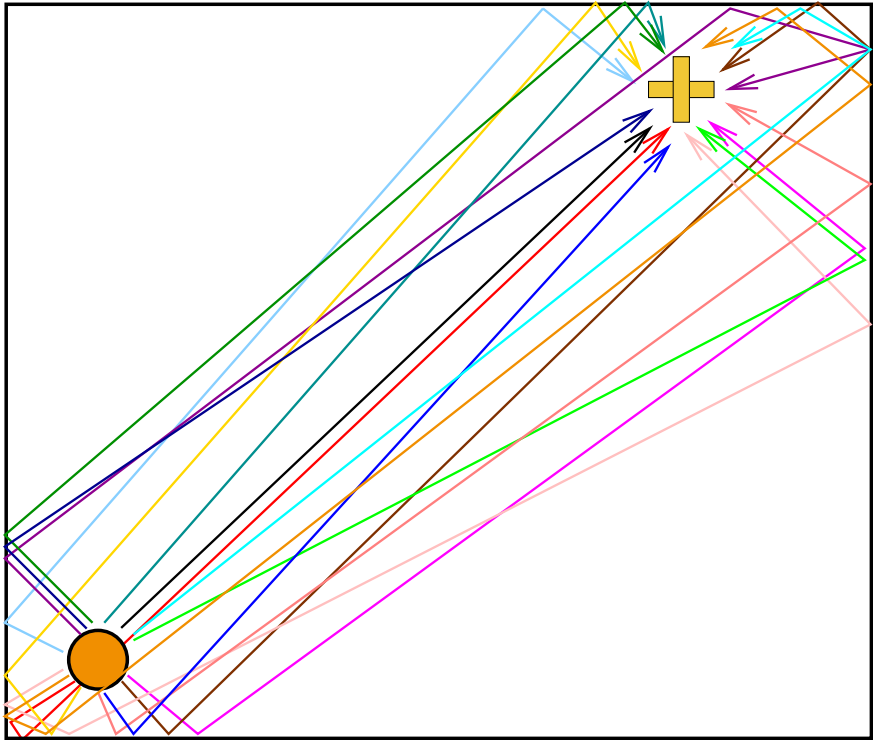
Figure 3.18: Classical arrival times of initial pulse at detector location. Line of sight (LOS) component plus 15 reflected copies of the pulse

3.7 The Initial Pulse and the case for Broad Band-width

The NPS experiment reported in [30] and described in the above section 3.2 uses an initial pulse with a central frequency of 9.5 kHz and bandwidth of $B_{3D} = 750$ Hz. The actual pulse employed by Larraza *et al* is shown in Figure 3.2. To investigate the effect of bandwidth on the time reversal process, we plot an initial pulse function $f(t)$ similar to the one used in the NPS reverberant room experiment in Figure 3.19. This pulse is given by equation (3.31).

$$f(t) = \cos\left(2\pi\nu\left(t - t_0\right)\right) \frac{\sin(2\pi\omega(t - t_0))}{2\pi\omega(t - t_0)} \tag{3.31}$$

where the parameters for the central frequency and bandwidth respectively are $\nu = 9.5$ kHz and $\omega = 750$ Hz.

(a) (b)
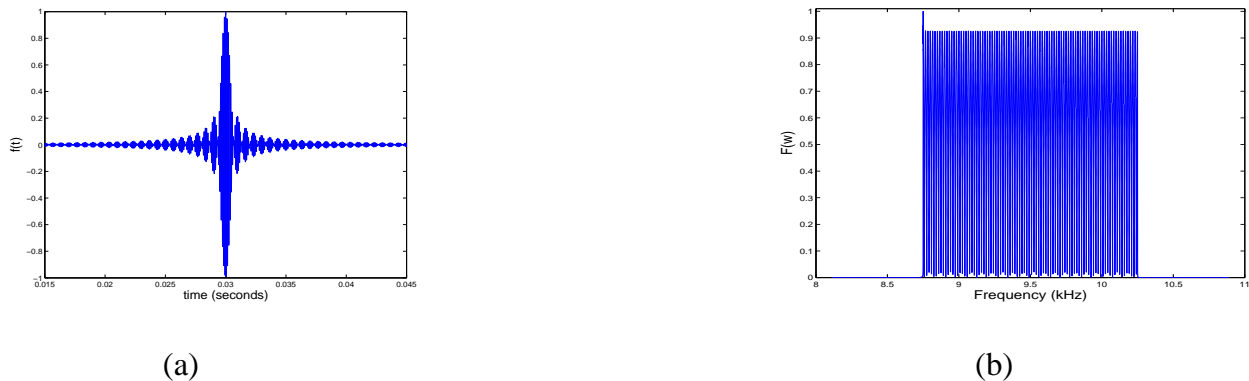
Figure 3.19: (a) Narrow-band pulse with central frequency $\nu = 9.5$ kHz and bandwidth $\omega = 750$ Hz. (b) Fourier transform of the pulse function in frequency domain. The bandwidth is limited by the frequencies $\nu_{min} = 8.75$ kHz and $\nu_{max} = 10.25$ kHz

For our two-dimensional computational experiment, we carried out the time-reversal process using an initial pulse $f(t)$ given by equation (3.31) and with equal frequency parameters for ν and ω. It turns out that we obtained no good quality results in terms of spatial focusing nor temporal compression after time-reversal.

It is a known fact that the time-reversal process takes advantage of broad bandwidths to generate its remarkable spatial and temporal focusing properties. Thus, we carried out the same experiment, this time using the same initial pulse $f(t)$, but with increased bandwidth to 50% the central frequency. The new initial pulse with bandwidth $B_{2D} = 4.25$ kHz is plotted in Figure 3.20. Notice its duration in time is much shorter than the duration of the

pulse with bandwidth B_{3D}. Consequently, the frequency spectra plotted in Figure 3.20, (b) is much broader than the one in Figure 3.19, (b).

(a)   (b)
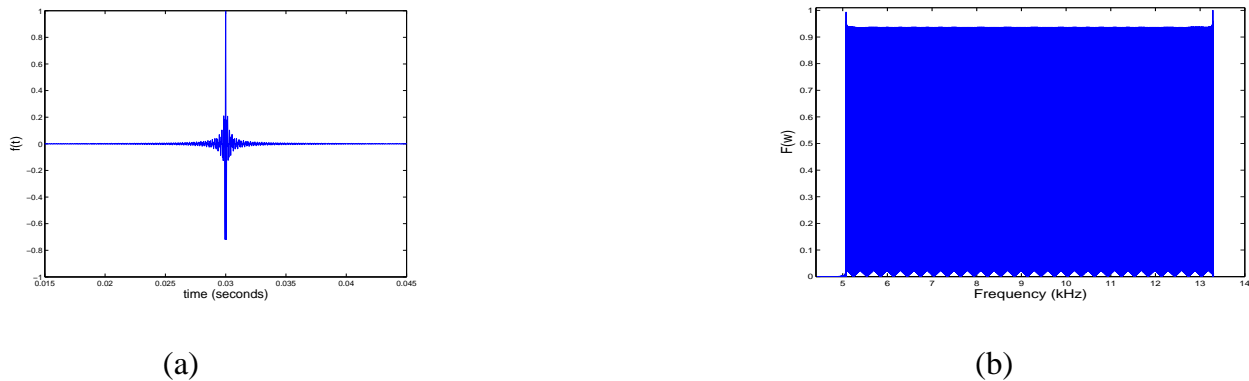
Figure 3.20: Broad-band pulse with central frequency $\nu = 9.5$ kHz and bandwidth $\omega = 4.25$ kHz. (a) narrow pulse function in time, (b) Fourier transform of the pulse function in frequency domain. The bandwidth is limited by the frequencies $\nu_{min} = 5.25$ kHz and $\nu_{max} = 13.75$ kHz

When using the broadband pulse with bandwidth B_{2D} our time-reversal numerical experiment yielded good quality spatial focusing of size half the central wavelength and excellent temporal compression of the time-reversed signal recovering a recompressed pulse with the same duration as the initial pulse $t_w = 0.1$ ms. We argue that the reduced dimensionality of the computational experiment calls for a broader bandwidth than a three dimensional physical experiment carried out in a laboratory at NPS.

The requirement to increase the bandwidth of the initial pulse in order to obtain spatial and temporal refocusing after the numerical time-reversal process in a bi-dimensional enclosure is based on the fact that there are many more scattering paths in three dimensions. The higher the number of reverberations in the enclosure, the larger the angular spread of multipaths. As angular-spread increases, the acoustic field gets scattered in multiple new directions that are absent in two-dimensions. In three dimensions, a pulse with bandwidth of $B_{3D} = 750$ Hz is enough to make the scattered waves refocus at the source at the correct time $t_{focusing} = T - t_0$.

In a sense, adding more frequency band to the initial pulse in two dimensions is equivalent to expanding the effective dimensionality of the enclosure by increasing multipathing. When all physical parameters such as initial pulse function, central frequency, dimensions of enclosure and speed of sound remain the same as in the NPS' physical experiment, increasing the pulse's bandwidth corresponds to an equivalent increase of the recording time T. As

many more reverberations are allowed to occur in the enclosure, there are more elements to add coherently at the source location at the refocusing time.

A simple analysis shows that by changing the bandwidth frequency, ω, the wavelength, λ, gets consequentially affected, and so do the time parameters in the problem. There are three important lengths in the problem: the size of the room given by x_{len} and y_{len}, the wavelength λ and the time $(T - t_0)c$ it takes for the signal to refocus at the source times the speed of sound in air.

If the bandwidth frequency varies, the available wavelengths vary with it. For example, if

$$\frac{\lambda_{2D}}{\lambda_{3D}} < 1$$

as is the case for our numerical simulation, we call η a control parameter, such that

$$\frac{\lambda_{2D}}{\lambda_{3D}} = \eta$$

Thus, if we wait for a time $T_{2D} = \eta T_{3D}$, it is predictable that we shall observe refocusing of the pulse similar to the one observed in the three-dimensional enclosure after a shorter time T_{3D}.

Given that $\lambda = c/\nu$, for the narrow band pulse of bandwidth B_{3D}, we calculate

$$\lambda_{3D_{min}} = c/\nu_{max} = 3.9\text{cm}$$

and

$$\lambda_{3D_{max}} = c/\nu_{min} = 3.3\text{cm}$$

On the other hand, for the broadband pulse of bandwidth B_{2D}, we calculate

$$\lambda_{2D_{min}} = c/\nu_{max} = 2.5\text{cm}$$

and

$$\lambda_{2D_{max}} = c/\nu_{min} = 6.6\text{cm}$$

We estimate the value of η using $\lambda_{2D_{max}}$ and $\lambda_{3D_{min}}$ to take into account the worst case scenario.

$$\eta = \frac{\lambda_{2D_{max}}}{\lambda_{3D_{min}}} = 1.56$$
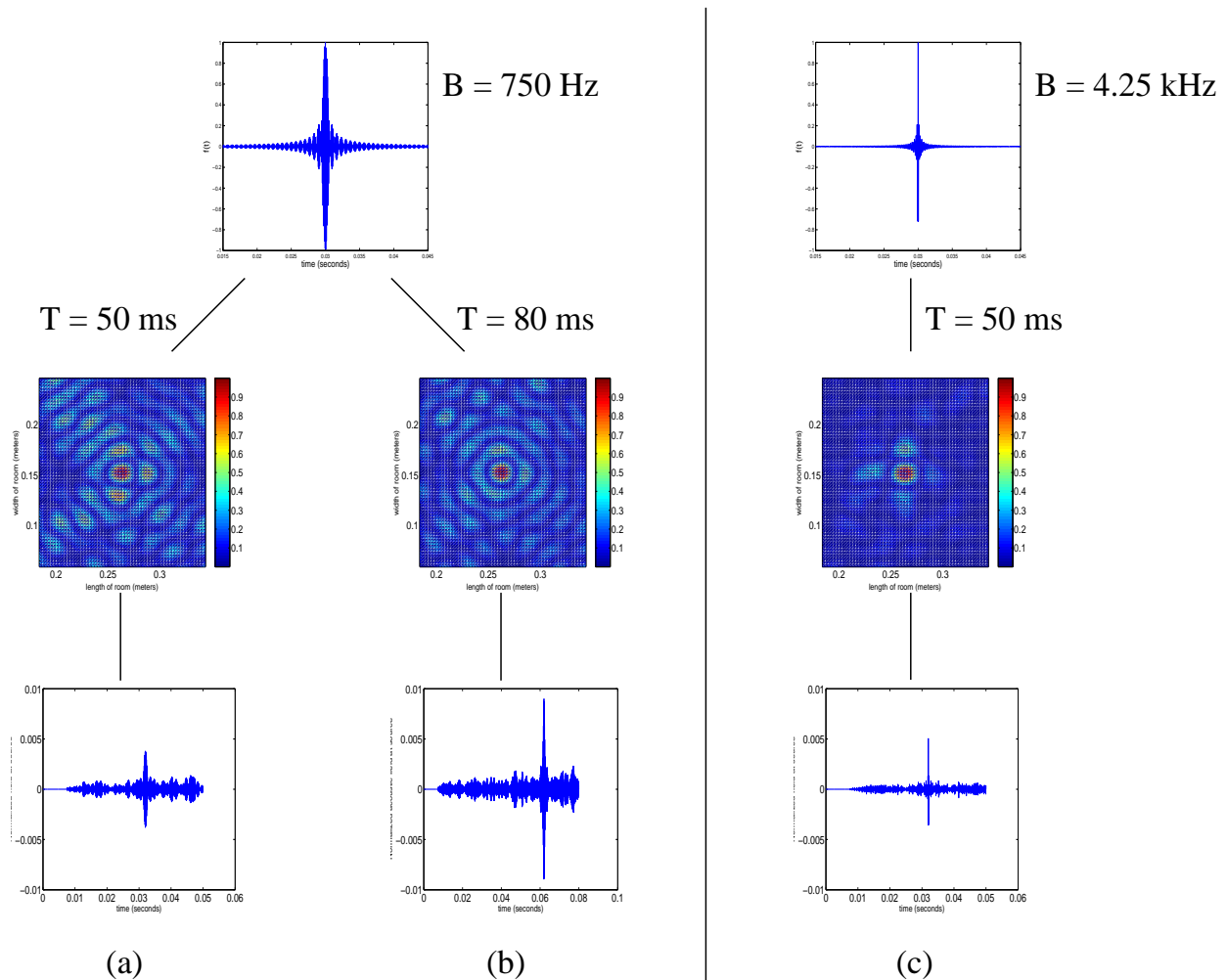
Figure 3.21: Numerical time-reversal experiment in an enclosure with Dirichlet boundary conditions. Columns (a) and (b)show results of the process when a narrow-band pulse of central frequency $\nu = 9.5$ kHz and bandwidth $B = 750$ Hz is used. The difference is that the experiment of column (a) records the acoustic field in the enclosure for a time $T = 50$ ms, whereas the on in column (b) expands the recording time to $T = 80$ ms. Column (c) shows equivalent results when a broadband pulse of same central frequency $\nu = 9.5$ kHz but broader bandwidth $B = 4.25$ kHz is employed. The first row displays the initial pulses used. The second row shows a snapshot of the acoustic field in the enclosure at the refocusing time right around the focusing spot. Third row displays temporal compression of the acoustic field received at the original source location during the backward phase of the time-reversal process

Consequently, we perform the numerical time-reversal experiment in two dimensions using the narrow-band pulse with frequency bandwidth parameter $\omega = 750$ Hz employed in the reverberant chamber in three dimensions. This time, however, we increase the recording

time T from 50 ms to 80 ms.

Figure 3.21 compares the results of a numerical time-reversal experiment in an enclosure with Dirichlet boundary conditions. Columns (a) and (b) display the results of the process when a narrow band pulse of central frequency $\nu = 9.5$ kHz and bandwidth $B = 750$ Hz is used. The difference is that the experiment of column (a) records the acoustic field in the enclosure for a time $T = 50$ ms, whereas the on in column (b) expands the recording time to $T_{2D} = \eta T_{3D} = 80$ ms as suggested earlier. For a recording time of 50 ms, the quality of spatial focusing is not very good as the grass surrounding the main peak reaches a magnitude of about 50%. Similarly, the quality is poor even when the recording time increases to 80 ms, where the spatial side lobes have a magnitude of up to 40%. Also, the characteristics of temporal compression in column (a) is of low quality as the acoustic energy is broadly spread over time, i.e. the side lobes of the main recompressed peak extend to both sides making the received signal broader in time. In (b) temporal compression is qualitatively better. Since more time has passed during the recording phase, more of the energy recompresses at the refocusing time $t_{focusing} = T - t_0$, and therefore at a higher magnitude than in (a). In contrast, column (c) shows equivalent results when a broadband pulse of same central frequency $\nu = 9.5$ kHz and bandwidth $B = 4.25$ kHz is employed. The quality of spatial focusing increases dramatically with respect to the one in columns (a) and (b). Spatial plot of the acoustic field in the enclosure at the refocusing time illustrates a tight focusing spot with a much higher peak-to-grass ratio than in columns (a) and (b). Moreover, the temporal compression yields a compact short pulse in time.

3.8 Time-reversal experiment with Ballistic vs. Diffuse part of Coda

We take the ballistic part of the transfer function and zero-out all components in the diffuse region, we call this the "ballistic transfer function." Similarly, we maintain the diffuse region of the transfer function while zeroing out all elements of the early ballistic region. We call this the "diffuse transfer function." This is shown in figure (3.22). We carry out the numerical time-reversal experiment in an enclosure with Dirichlet boundary conditions. This time, however, during the backward phase of the process we compare the results obtained under two different scenarios: first, when we only send the time-reversed ballistic transfer function as sketched in Figure 3.22, (b), and secondly, when we only send the time-reversed diffuse

Figure 3.22: Time-reversal experiment in an enclosure with Dirichlet boundary conditions. (a) Channel transfer function received at the detector during a time $T = 50$ ms after an initial pulse is emitted from the source. (b) We take the ballistic part of the transfer function and zero-out all components in the diffuse region, we call this the "ballistic transfer function". (c) Similarly, we keep the diffuse region of the transfer function while zeroing out all elements of the early ballistic region. We call this the "diffuse transfer function"

transfer function as sketched in Figure 3.22, (c).
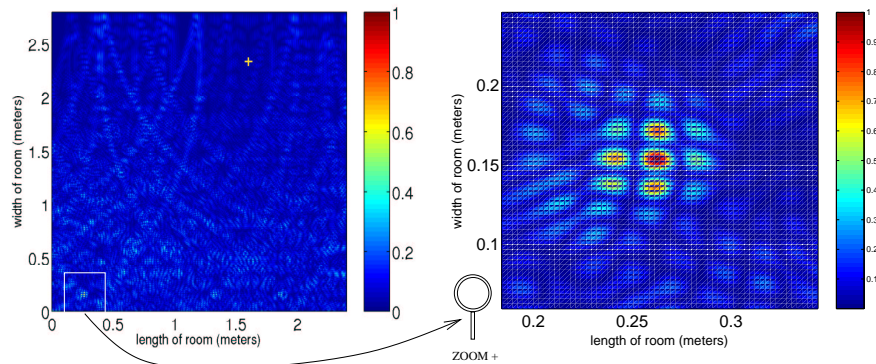
Figure 3.23: Time-reversal experiment in an enclosure with Dirichlet boundary conditions. The backward phase of the process employs the time-reversed ballistic section transfer function as depicted in figure (3.22, (b)). Snapshot of normalized acoustic field in enclosure at refocusing time $t_{focusing} = T - t_0$. Using exclusively the ballistic part of the wave field does not yield good spatial focusing results. The overall pressure grass-level in the enclosure forms a circular pattern and is of the order of up to 40%. The zoom in picture shows existing sidelobes surrounding refocusing spot
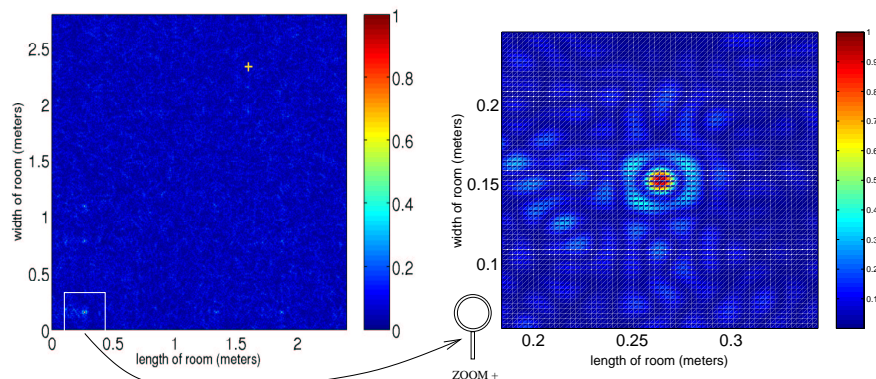
Figure 3.24: Time-reversal experiment in an enclosure with Dirichlet boundary conditions. The backward phase of the process employs the time-reversed diffuse segment of the transfer function as depicted in figure (3.22, (c)). Snapshot of normalized acoustic field in enclosure at refocusing time $t_{focusing} = T - t_0$. In contrast, using exclusively the diffuse part of the wave field yields excellent spatial focusing results. The overall pressure grass-level in the enclosure is reduced to 20% and is homogeneously distributed. The zoom in picture shows a perfectly tight refocusing spot with no existing side lobes
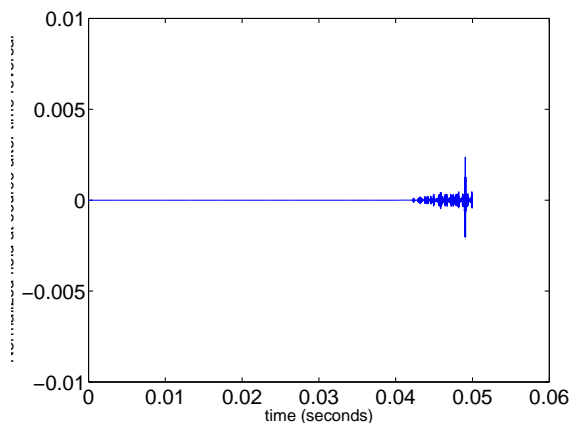
(a) Normalized acoustic field received at the original source location when only the time-reversed ballistic part of the transfer function is employed in the process. Temporal compression is observed at the refocusing time $t_{focusing} = 50$ ms. Magnitude of the recompressed pulse is approximately 0.25% of the initial pulse (most of the acoustic energy is spread out in the enclosure as opposed to concentrating at the source location)
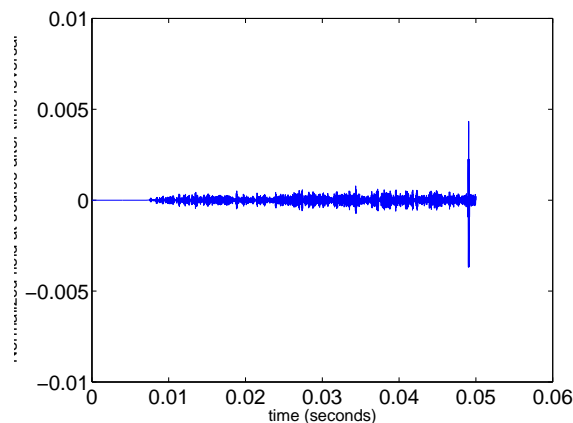
(b) [Normalized acoustic field received at the original source location when only the time-reversed diffuse segment of the transfer function is employed in the process. Temporal compression is observed at the refocusing time $t_{focusing} = 50$ ms. Magnitude of the recompressed pulse is approximately 0.5% of the initial pulse (double the magnitude of wave field received when only the ballistic part of the transfer function is employed). More of the acoustic energy is concentrated just at the focus location than anywhere else in the enclosure

Figure 3.25: Time-reversal experiment in an enclosure with Dirichlet boundary conditions. Spatial focusing dramatically improves when only the diffuse segment of the transfer function is employed in the process versus the ballistic one. Magnitude of temporally compressed pulse is double in this case as well

3.9 Measurement of Additional Physical Quantities

3.9.1 Conservation of Energy

As a check for the code, we performed some additional measurements.

One of the conserved quantities when solving the wave equation in a bounded domain is called the "energy integral" in analogy with the physical energy consisting of a kinetic and a
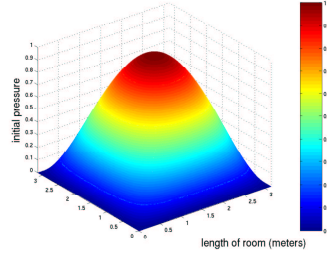
Figure 3.26: Initial pressure disturbance $p(x, y, 0) = x(\pi - x)y(\pi - y)$ for solving initial boundary-value problem in enclosure with Dirichlet boundary conditions and size (π, π)

potential part. We derive the energy integral by multiplying both sides of the homogeneous wave equation by $p_t(x, y, t)$ where p_t is the time derivative of the acoustic pressure, and integrating for all times and all points in space. We consider the two-dimensional bounded domain:

$$0 \leq x \leq x_{len}$$
$$0 \leq y \leq y_{len}$$

and choose to compute the time integral up to a time T.

We start with the homogeneous wave equation

$$p_{tt}(x, y, t) = c^2 \left(p_{xx}(x, y, t) + p_{yy}(x, y, t) \right) \tag{3.33}$$

and multiply both sides by $p_t(x, y, t)$ and integrate over time and for all points in the domain. In the following steps of the derivation we will drop the (x, y, t) and keep this dependence implicit.

$$\int_0^T \int_0^{x_{len}} \int_0^{y_{len}} p_t\, p_{tt}\, dy\, dx\, dt = c^2 \int_0^T \int_0^{x_{len}} \int_0^{y_{len}} p_t\, (p_{xx} + p_{yy})\, dy\, dx\, dt \tag{3.34}$$

After a simple manipulation of the integrals using integration by parts, we obtain :

$$E(t) = \frac{1}{2} \int_0^{x_{len}} \int_0^{y_{len}} \left(\frac{|p_t|^2}{c^2} + |p_x|^2 + |p_y|^2 \right) dy\, dx$$
$$+ \int_0^T \left(\int_0^{y_{len}} (p_t\, p_x)|_0^{x_{len}}\, dy + \int_0^{x_{len}} (p_t\, p_y)\,|_0^{y_{len}}\, dx \right) dt \tag{3.35}$$

where $(p_t\, p_y)\, |_0^{y_{len}}$ means that p_t and p_y are evaluated at the bounaries $y = 0$ and $y = \pi$.

Equation (3.35) yields a value for the total energy integral as a function of time E(t). It is composed of a kinetic energy part

$$E_{kin} = \frac{|p_t|^2}{c^2}$$

that resembles the physical kinetic energy expressed by the square of the momentum. And the potential energy has two parts, a term for the potential energy inside the domain

$$E_{pot}(\text{inside}) = |p_x|^2 + |p_y|^2$$

and a second term for the potential energy *at* the boundaries

$$E_{pot}(\text{boundaries}) = \int_0^T \left(\int_0^{y_{len}} p_t p_x |_0^{x_{len}} dy + \int_0^{x_{len}} p_t p_y |_0^{y_{len}} dx \right) dt$$

We shall now use equation (3.35) to show that the value of the energy integral output by our numerical scheme is consistent with an analytically-calculated value for a specific case. To simplify the calculation, we choose Neumann boundary conditions which conveniently require that both p_x and p_y be zero at their corresponding boundary limits of the domain. This makes the last term $E_{pot}(\text{boundaries})$ disappear.

Using our numerical code to solve the second order acoustic wave equation in a two-dimensional enclosure with Neumann boundary conditions, we evaluate the energy integral. The size of the enclosure is $(x_{len}, y_{len}) = (\pi, \pi)$m and for simplicity the acoustic speed is set to $c = 1m/s$. The mathematical formulation is stated in the following equations

$$p_{tt}(x,y,t) = (\, p_{xx}(x,y,t) \, + \, p_{yy}(x,y,t) \,), \qquad t > 0$$
$$p_x(0,y,t) = 0 \,, \; p_x(\pi,y,t) = 0 \,, \; p_y(x,0,t) = 0 \,, \; p_y(x,\pi,t) = 0$$
$$p(x,y,0) = x(\pi - x)y(\pi - y), \qquad p_t(x,y,0) = 0$$

The wave propagation of the initial pressure disturbance is computed for a time of $T = 20$ s, during which we measure the total energy in the enclosure as a function of time. In this case, the energy integral simplifies to

$$E_{tot}(t) = \frac{1}{2} \int_0^{x_{len}} \int_0^{y_{len}} \left(\frac{(p_t(x,y,t))^2}{c^2} + (p_x(x,y,t))^2 + (p_y(x,y,t))^2 \right) dy dx \qquad (3.37)$$

Now, because one of our initial conditions indicates that $p_t(x,y,0) = 0$, and because the energy integral should be the same for all times, it is always equal to the initial energy at

$t = 0$:

$$E_{tot}(0) = \frac{1}{2} \int_0^\pi \int_0^\pi \left(p_x(x,y,0)\right)^2 + \left(p_y(x,y,0)\right)^2 \, dy dx \tag{3.38}$$

We calculate the analytic solution for the energy by first solving the wave equation. With the aid of the eigenfunctions of the Laplacian in two dimensions, lets consider the following set of solutions

$$p(x,y,t) = \sum_{n,m=1}^\infty a_{n,m} f(w_{n,m}t) \cos(nx) \cos(my) \tag{3.39}$$

where $f(w_{n,m}t) = cos(w_{n,m}t)$ to guarantee that the initial condition $p_t(x,y,0) = 0$ is satisfied.

To find the coefficients $a_{n,m}$, we fit the initial condition for the pressure $p(x,y,0)$ to equation (3.39):

$$x(\pi - x)y(\pi - y) = \sum_{n,m=1}^\infty a_{n,m} \cos(nx) \cos(my) \tag{3.40}$$

Multiplying both sides of this equation by $\cos(lx) \cos(ky)$ and integrating over the entire domain, we calculate for the left side

$$\int_0^\pi x(\pi - x) \cos(lx) \, dx \int_0^\pi y(\pi - y) \cos(ky) \, dy =$$

$$= \frac{\pi^2}{l^2 k^2} \left(1 + (-1)^l\right) \left(1 + (-1)^k\right) \tag{3.41}$$

Integrating the right hand side we get

$$\int_0^\pi \int_0^\pi \sum_{n,m=1}^\infty a_{n,m} \cos(nx) \cos(my) \cos(lx) \cos(ky) dx dy = \frac{\pi^2}{4} a_{l,k} \tag{3.42}$$

where we used the property of orthonormality for the eigenfunctions. Equating both sides and returning to the previous notation with integers n and m, the coefficients $a_{n,m}$ are obtained

$$a_{n,m} = \frac{4}{n^2 m^2} \left(1 + (-1)^n\right) \left(1 + (-1)^m\right) \tag{3.43}$$

Therefore, we have at hand the complete solution to the wave equation (3.39) with the coefficients $a_{n,m}$ given by equation (3.43). Employing this solution, we calculate the initial

energy as prescribed in equation (3.38)

$$E_{tot}(0) = \frac{1}{2} \int_0^\pi \int_0^\pi \left\{ \left(\sum_{n,m=1}^\infty a_{n,m} \left[-n \sin(nx) \cos(my) \right] \right)^2 + \right.$$

$$\left. \left(\sum_{n,m=1}^\infty a_{n,m} \left[-m \sin(my) \cos(nx) \right] \right)^2 \right\} \, dx \, dy \quad (3.44)$$

which is equal to

$$E_{tot}(0) = \frac{\pi^2}{8} \left(\sum_{n,m=1}^\infty a_{n,m}^2 n^2 + \sum_{n,m=1}^\infty a_{n,m}^2 m^2 \right) \quad (3.45)$$

and converges to

$$E_{tot}(0) = 105.43$$

105.4281223834668 We plot the computed energy $E_{tot}(t)$ output by the code as a function of time in Figure 3.27, (a). On physical grounds, because the walls are perfectly-reflecting, we expect this quantity to be conserved over all times and to be equal to the initial one $E_{tot}(0)$. Moreover, we calculate the relative error between the analytically calculated energy $E_{tot}(0)$ and the one computed $E_{tot}(t)$ and plot it in 3.27, (b).

$$\text{relative error} = \frac{\left(\text{Energy}_{\text{computed}} - \text{Energy}_{\text{calculated}} \right)}{\text{Energy}_{\text{calculated}}} \quad (3.46)$$

As expected, energy is constant over all times and equal to the energy in the enclosure at time zero.

3.9.2 Equipartition of Intensity

Besides energy conservation, it is thought that after a sound is initiated in an enclosure, it will start diffusing in it until a diffuse state is reached when the intensity is equally distributed in all space. This is only if the sound has enough energy to last for a time long enough to reach this so called "diffuse behavior" of sound. This "phase" in the acoustic field propagation is reached when the field in the enclosure is no longer auto-correlated.

Typically, acoustic fields in square rooms are highly-correlated for long times compared to the initial pulse width. In the following experiment, we investigate the time after which there is no significant autocorrelation of the acoustic field. Then, we analyze the intensity in the enclosure during times that occur after the decorrelation time t_d.

(a)   dt $=$ 2.4 x 10^{-3}s   (b)
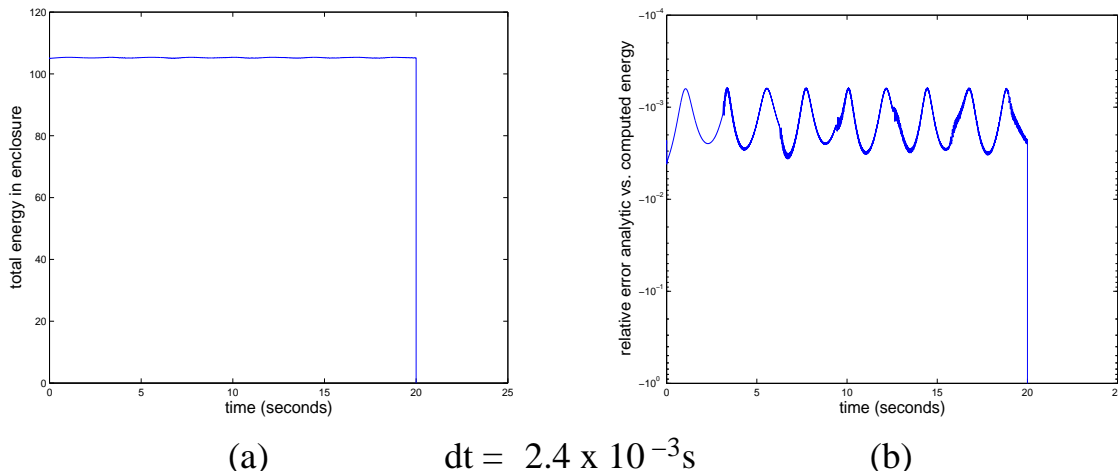
Figure 3.27: Initial boundary value problem with initial pressure disturbance in an enclosure with reflecting boundaries. (a) Computed energy $E_{tot}(t)$ output by the code as a function of time (b) relative error between the analytically calculated energy $E_{tot}(0)$ and the one computed in (a)

Our intention is to prove that when all walls are reflective, such as with the Dirichlet boundary conditions, or when there is little absorption (as we will prove now), the time-average of the mean-square sound is the same everywhere throughout the enclosure.

We use our code to solve the wave equation with an initial disturbance given by a narrow Gaussian function in space localized at (1.2, 1.4) m within the enclosure. After making sure that the energy is conserved for this square displacement, we proceed to measure the normalized intensity in the enclosure averaged over all times from $t = 0$ to $t = 50$ ms.

Figure 3.28 displays the percentage of average intensity in space as compared to the initial intensity in the enclosure when only an initial displacement supplies energy to the enclosure. This time, the initial displacement is present only at a small area of approximately $0.083m^2$. We observe the distribution of the time-average intensity $< (p(x, y, t))^2 >_t$ normalized by the initial intensity $(p(x, y, 0))^2$. As expected, intensity remains highest at the center which is location of the initial displacement.

The intensity in the plot looks somewhat evenly-distributed in the enclosure except at the source location. At this time, the acoustic energy has not had enough time to disperse diffusely across the entire enclosure. It has a preferential location which is where the disturbance initially happen (at the center). Also, all along the $\hat{x}$ and $\hat{y}$ axis we observe streaks of a higher intensity. This is due to "grid effects." Because the code solves the wave equation in the $\hat{x}$ and $\hat{y}$ preferred directions and the source is at the center, there are considerably
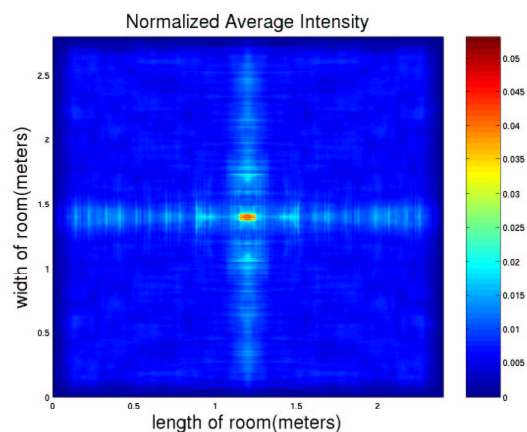
Figure 3.28: Percentage of average intensity in space normalized to the initial intensity in the enclosure when only an initial spatial displacement supplies energy to the enclosure. The initial displacement is present only at time $t = 0$ and it is spread over a square patch area of space of approximately $0.083m^2$. We observe the distribution of intensity in the enclosure. Intensity is highest at the location of the initial displacement. The thick light blue lines crossing the enclosure along the $\hat{x}$ and $\hat{y}$ axis, of the order of 20% are grid effects that occur because the FDTD code has these two directions for the propagation of waves. The direction of most radiation of the initial displacement travels away from its initial location and directly to the walls. Aside from the grid effects and the location of the initial displacement, we observe equipartition of energy in the enclosure.Conditions in the boundaries of the enclosure are reflective Dirichlet

more reflections along this two axes. As it propagates in the enclosure, the initial pressure is reflected off of the four perpendicular walls more than off any other direction. This causes the cross-lines to appear in the figure. However, apart from the grid effects and the intensity at the source location, the time-average of the intensity appears to a certain degree homogeneous across space in the enclosure.

In contrast to Figure 3.28, we shall show the results of measuring the intensity in the enclosure and averaging it over all times *larger* than the time when the sound has achieved diffuse behavior. We shall only included measurements of the intensity in the enclosure after a time of decorrelation t_d of the acoustic field has been reached.

We use our code to solve the wave equation in an enclosure of size $(2.4 , 2.8)$ m. The initial displacement is a narrow Gaussian function in space localized at $(1.2, 1.4)$ m within the enclosure. There is moderate absorption at the walls, with an absorption coefficient of $\kappa = 0.3$. The wave field is recorded by a detector located at $(1.6 , 2.33)$ m.

First, to find the time at which the acoustic field squared is no longer autocorrelated, we plot Figure 3.29.

We select a criteria for estimating the decoherence time when the autocorrelation of the field is less than 10^{-3} of its peak value. Analyzing the semilog-plot in Figure 3.29, the time at which this occurs is $t = 54$ ms.

The time $t = 54$ ms is slightly larger than the original recording time of $t = 50$ ms used earlier. Taking into account the intensity for all times after $t = 54$ ms, we increase the recording time to $t = 250$ ms. If our estimate is right, measuring the intensity for times only greater than $t = 54$ ms, means we observe the behavior of the acoustic field once the multiple reverberations in the room have reached a diffusive state.

Figure 3.29, (a) shows a signal recorded by a detector located at $(1.6 , 2.33)$ m for the full recording time $t = 250$ ms. It shows moderate absorption $\kappa = 0.3$ (its envelope decays with time). Multiple scattering dominates in the enclosure. It is as if it has forgotten the presence of an initial displacement.

We compute the intensity (acoustic field squared) in the enclosure every 100 time steps, beginning after the decorrelation time of $t = 54$ ms.

It is illustrative to show the progression of energy dispersion across the enclosure with time. For this, we measure the intensity in the enclosure at three arbitrary times a)$t = 54$ ms, b)$t = 116$ ms, and c)$t = 225$ ms. We expect the acoustic field distribution to be spread inhomogeneously all across space in the enclosure. This is because we do not expect that at any one time the intensity is the same everywhere in the enclosure. The Figures are shown

(a) (b) (c)
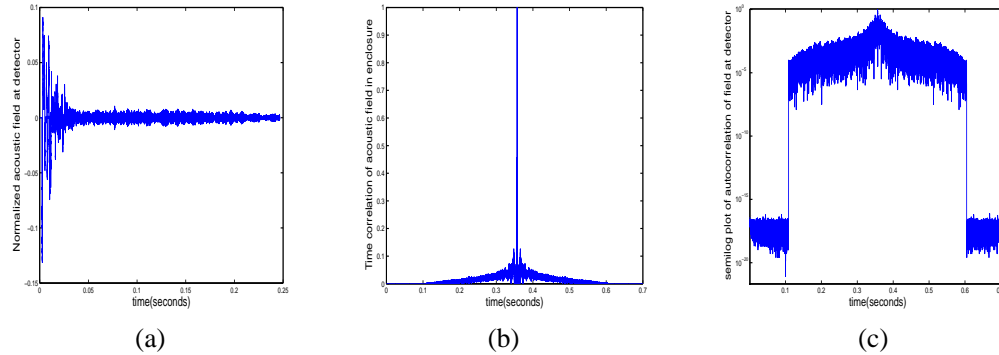
Figure 3.29: (a) Acoustic wave field recorded by a detector located at (1.6 , 2.33) m for a recording time $t = 250$ ms. It shows moderate absorption $\kappa = 0.3$ (its envelope decays significantly with time). (b) time-autocorrelation of the acoustic field squared received at the detector. The purpose of this is to estimate the decoherence time when the autocorrelation of the field is less than 10^{-3} of its peak value. After the decoherence time, it will be more probable to find the acoustic field in a diffuse state. The enclosure is (2.4 , 2.8) m. The initial displacement is a Dirac Delta function in space localized at (1.2, 1.4) m within the enclosure. There is absorption at the walls, with an absorption coefficient of $\kappa = 0.3$. The signal is detected by a detector located at (1.6 , 2.33) m. (b) Semi-log plot of the time-autocorrelation of the acoustic field squared received at the detector in enclosure with absorption.

in 3.31

Now, we *average* the intensity of the acoustic field (we take a snapshot every 100 time steps) after the field is decorrelated. We plot the average intensity in Figure **??**.

Figure 3.31, (a) shows that the multiple reverberations in the enclosure have reached a diffuse state. That is, a state where the strong scattering in the enclosure causes the intensity to occupy all space with equal probability.

Also, in a diffuse sound field, the probability of intensity traveling in any one direction at any point in space is thought to be the same. However, this is very hard to prove computationally. So for now, we just rest on the fact that the average intensity for a diffuse acoustic field is everywhere the same.

We now repeat the same experiment as in part (b), in an enclosure with a very low absorption coefficient $\kappa = 0.07$.

The same conditions as in part (*b*) apply, namely that the size of the two-dimensional enclosure is (2.4 , 2.8) m. The initial displacement is of the form $p(x, y, 0) = \gamma \delta(x - x_0) \delta(y - y_0)$, where γ is some constant and δ is the Dirac Delta function. $(x_0, y_0) = (1.2, 1.4)$ m is the center of the enclosure. The initial velocity is $p_t(x, y, 0) = 0$.

(a)   (b)
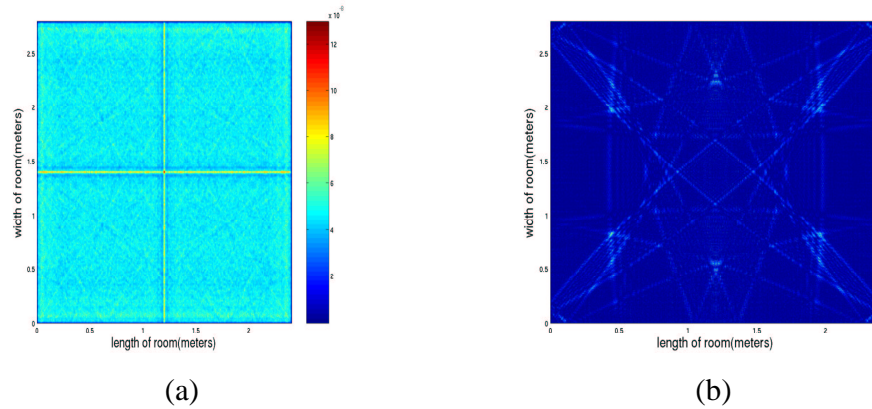
Figure 3.30: (a) According to our estimate, the acoustic field in the enclosure has reached a "diffuse sound field" at $t = 54$ ms, when multiple scattering dominates and the presence of an initial displacement is forgotten. (b) intensity of the acoustic field in the enclosure averaged over a total time of 19 ms. Normalization with respect to the intensity at the initial time $I(0) = (p(x, y, 0))^2$. The average intensity everywhere is homogeneous across the enclosure except for the two cross lines which are grid-effects (b) For comparison, contour map of intensity of acoustic field in the enclosure at an arbitrary time $t = 34$ ms

(a)   (b)   (c)
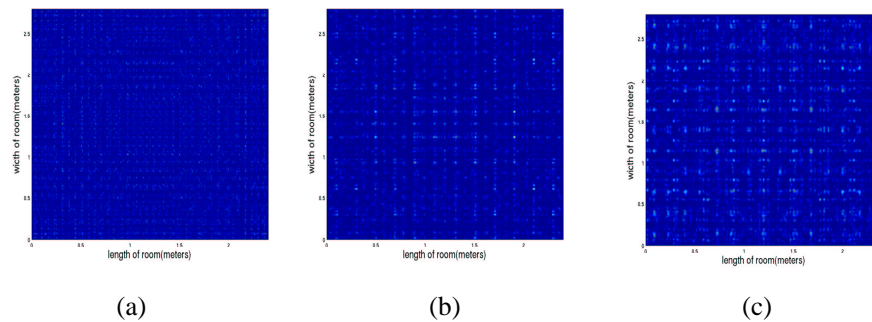
Figure 3.31: (b) Contour map of intensity of acoustic field in the enclosure at times: a)$t = 54$ ms, b)$t = 116$ ms, and c)$t = 225$ ms. During this times, the acoustic field has achieved "diffuse" behavior and is scattered over the entire enclosure. The intensity is not homogeneously distributed everywhere in the enclosure

Figure **??**, (a) shows a signal detected by a detector located at (1.6 , 2.33) m for the full recording time $t = 250$ ms. It shows moderately strong absorption (its envelope decays with time). Multiple scattering dominates in the enclosure. It is as if it has forgotten the presence of an initial displacement.

The following plot in Figure **??** shows the acoustic field at the detector normalized with respect to the magnitude of the initial displacement in an enclosure with absorption coefficient $\kappa = 0.07$. It shows very small absorption (its envelope decays less with time), when compared to the case when the absorption coefficient is $\kappa = 0.3$ in Figure **??**, (a).

(a) (b) (c)
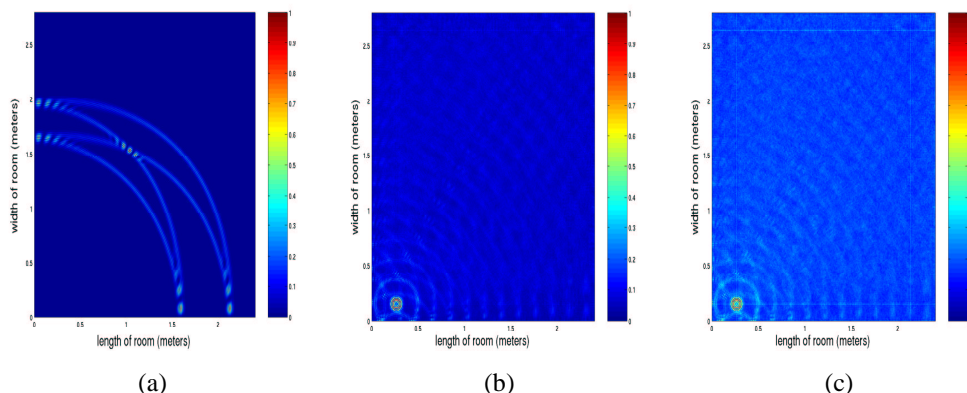
Figure 3.32: (a)Intensity distribution of acoustic field in enclosure with Dirichlet boundary conditions and a transmitting signal at (0.13, 0.31) m Snapshot taken at an arbitrary time of $t = 6.5$ ms. The distribution of intensity is far from homogeneous throughout the enclosure. (b) Intensity distribution of acoustic field in enclosure averaged over all times from $t_0 = 0$ to $t_{final} = 50$ ms. Normalization with respect to the magnitude of intensity $I(0) = (p(x, y, 0))^2$. Plot shows the average intensity is homogeneously distributed in enclsoure. (c) Intensity distribution of acoustic field in enclosure averaged over all times from $t_0 = 50$ ms to $t_{final} = 150$ ms. We waited a longer time to measure the intensity in the enclosure. To computed this avergae we take into accound intensity measurements that occur only after 50 ms and the final time of 150 ms. Plot shows the average intensity is homogeneously distributed in enclsoure

We now plot the time-averaged intensity for times strictly in the diffuse phase of sound.

Figure 3.33, (b) shows equipartition of intensity. It is everywhere the same and distributed homogeneously in the enclosure. This is except for the grid effects in the $\hat{x}$ and $\hat{y}$ axis.

As we compare this plot with the case of moderate absorption in figure **??**, we observe a more even, almost "grainy" distribution of the intensity in the enclosure. This is because we are very close to reflective boundaries where there is no energy loss. This concludes that the theorem of equipartition of energy displays better results in enclosures with reflecting or

(a)   (b)
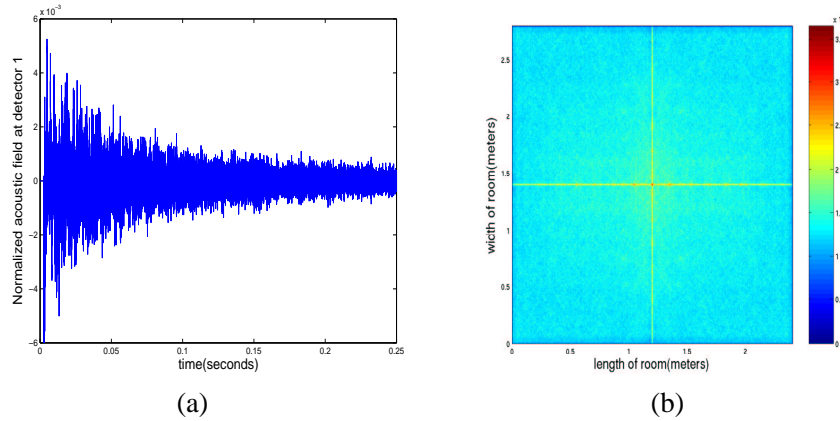
Figure 3.33: (a) Acoustic signal recorded by a detector located at (1.6 , 2.33) m for a recording time $t = 250$ ms. The field is normalized to the magnitude of the initial pressure. The absorption coefficient is small $\kappa = 0.07$. It is possible to see that there is less decay in the signal detected than when $\kappa = 0.3$ in Figure 3.29, (a). (b) contour map of intensity of the acoustic field in the enclosure averaged over a total time of 190 ms after the decoherence time estimated $t = 54$ ms. Normalization with respect to the magnitude of intensity $I(0) = (p(x, y, 0))^2$. Measurements are assumed to be made during the diffuse phase of acoustic behavior. The two cross lines are grid effects due to the finite-difference code computing the wave equation along the $\hat{x}$ and $\hat{y}$ axis. The average intensity everywhere is the same

very low-absorption walls.

As additional proof of the equipartition of intensity in the enclosure, we show the following two plots of the average intensity across the length and width of the room. Keeping a fixed width and length respectively, the figures show a common average intensity, and a peak at the source location. This is different corroboration of equipartition of intensity in the enclosure.

The same experiment yields similar results for the intensity in the enclosure for a fixed width of the room. The average is also $1.35e - 07$ au.
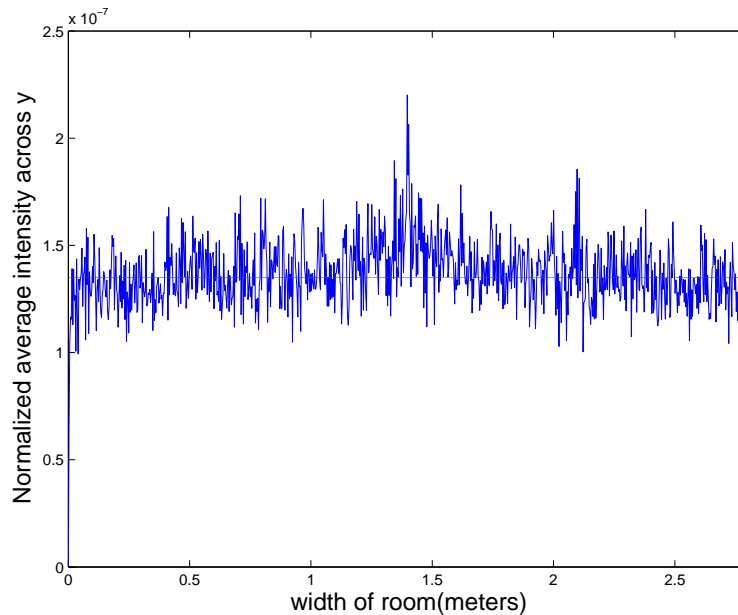
Figure 3.34: Intensity in the enclosure for a fixed length of the room. The average is $1.35e - 07$au. Equipartition of intensity along width in diffuse acoustic field

3.10   Comparison of Time Reversal Results of Numerical Simulation with those of NPS

3.11   Instrumentation Employed in Numerical Experiment

We used a 2.5 GHz Pentium IV machine with cash of 0.5 MB and 2 GB of RAM. We also employed Red Hat Linux version 7.3. The front side bus (fsb) is around 533 MHz. This is equivalent approximately to a two to three year old top of the line computer. Today, a variety of updates include Pentium IV machines with 3.4 GHz. To calculate the decrease in computation time to go from our computer with a processor speed of 2.5 GHz say, to one with 3.4 GHz, we take the ratio

$$2.5/3.4 = 0.74$$

to compute the increase in speed the ratio is

$$1 - 0.74 = 26\%$$

increase in speed. The entire time-reversal process calculation takes 4 hours. Thus, with a newer machine of 3.4 GHz processor, it would take 1 hour less (three hours).

An alternate machine would be a xion which has more cash (2 MB) and front side bus of 800 MHz. A yet different option, would be to use a Silicon Graphics Irix Box machine that uses a MIPS chip. This machine could have done slightly better, however the cost of it exceeds the benefits in improving the time of computation of the code.

Chapter 4

Comparison of Time-Reversal Refocusing Results in Enclosures with Different Boundaries

All enclosures have boundaries, but not all boundaries are the same. Some boundaries reflect all of the energy incident upon them, others absorb most or all of this energy. There are different kinds of boundaries that partially reflect and transmit some of the energy incident upon them, and other boundaries that partially reflect and absorb some of the energy incident upon them. Some boundaries require that the sound pressure on them be zero, whereas others declare that the force on them be zero.

We shall investigate the effect of different boundaries on time-reversal experiments. It is easy to predict what should happen with all-absorbing boundaries, which essentially reproduce free space. Unless the source is completely surrounded by an array of detectors as in the time-reversal cavity (TRC), or a large time-reversal mirror (TRM) is placed in front of it, time-reversal would not yield any focusing results. In the latter case, when adding random scatterers to the medium between source and TRM, the refocusing of the pulse has better quality.

It is also possible to predict what should happen with strongly reflective boundaries. In a time-reversal cavity (TRC), the transducer array samples a closed surface surrounding the acoustic source. Just like the multiple scattering process widens the effective TRM aperture, the reflections from the boundaries of waves propagating in waveguides or cavities have the same widening of the aperture effect. Essentially, it is like replacing some of the TRC transducers by reflecting boundaries that help redirect one part of the incident wave

toward the TRM aperture. [1] Thus, with strongly-reflecting boundaries, refocusing of the pulse should even better than with TRMs and scattering environments that increase their effective aperture.

In this chapter, we shall first explore the results of a time-reversal experiment in a simple two-dimensional enclosure with highly-reflecting boundaries. We shall use the pressure zero at the boundaries condition (Dirichlet boundary conditions) to simulate this enclosure. We will then have a brief discussion on some factors that could affect quality of refocusing in this enclosure. Particularly, we shall show results of experiments with the addition of more detectors into the original enclosure, as well as adding randomly-placed scatterers in the enclosure. Finally, we shall also explore the effects of combining multiple detectors with randomly-placed scatterers in an enclosure. We shall test these different experimental conditions in the case of highly absorbing boundaries as well as moderately absorbing ones.

4.1   Empty Enclosure with Highly Reflecting Walls

We shall model an enclosure with highly reflecting boundaries using the Dirichlet boundary condition, namely, having the pressure vanish at the boundaries. This kind of boundary effects a phase change in the reflected wave. The total energy in the enclosure is conserved for all times.

Mathematical formulation

$$\frac{\partial^2 p}{\partial t^2} + c^2 \nabla^2 p = \delta(\mathbf{r} - \mathbf{r_0}) f(t) \qquad \text{Wave Equation} \qquad (4.1)$$

where $\mathbf{r_0}$ is the source location and the pulse in time is

$$f(t) = \cos\left(2\pi\nu\left(t - t_0\right)\right) \exp\left[-\frac{(t - t_0)^2}{t_w^2}\right]$$

The initial conditions are

$$p(t = 0) = 0 \qquad\qquad (4.2)$$
$$p_t(t = 0) = 0$$

and the boundary condition is

Dirichlet $p = 0$ at boundaries

The computational setup of the experiment, as explained in Chapter 3, is a finite-difference time-domain code in two dimensions that transmits of a signal from a source location to a different detector location in space. The signal is initiated at time t_0. After the signal propagates through the medium, the detector records its time trace for a time $T = 50ms$ much longer than the initial pulse-width. In the backward process, a similar code reverses in time the trace with long delay spread recorded at the detector. It propagates the time-reversed trace and, as a result, refocusing of the initial pulse at the original source location occurs at time T - t_0.

Source and detector are placed in corresponding locations to Larraza's enclosure if a projection along the $\hat{z}$ (height) axis was taken (looking at the floor of the enclosure). Figure (4.1) shows the computational setup for the experiment.
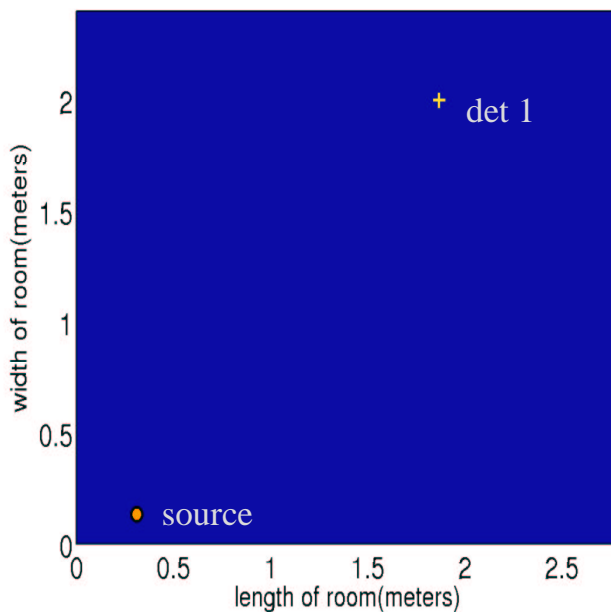
Figure 4.1: Setup of computational experiment. 2D enclosure of size (2.4, 2.8)m, a single detector (yellow cross) at (2.2, 2.6)m and a source (orange circle) at (0.31, 0.13)m

We take a snapshot picture of the acoustic field in the enclosure at time T - t_0. We expect that exactly at this time, the time-reversed signal transmitted by the detector will focus in

space around the source location. Given the quality of spatial focusing reported by Mathias Fink in his experiments in an ultrasonic waveguide [1], we expect the spatial resolution of the signal to be within one half wavelength of the propagating waves.

Separately, in time, we expect to observe a temporal compression that would yield the same original pulse signal in time, lasting for the same time of $0.1ms$. We also expect the signal in time to preserve its shape, conserving the places where it is positive, negative or null. Just as a note, the preservation of this temporal function will prove to be quite important when sending train pulses in Chapter 6. As we will see, this is a good basis for allowing the encoding of binary messages onto time-reversed signals that when refocused after time-reversal will produce a very small bit-error-rate.
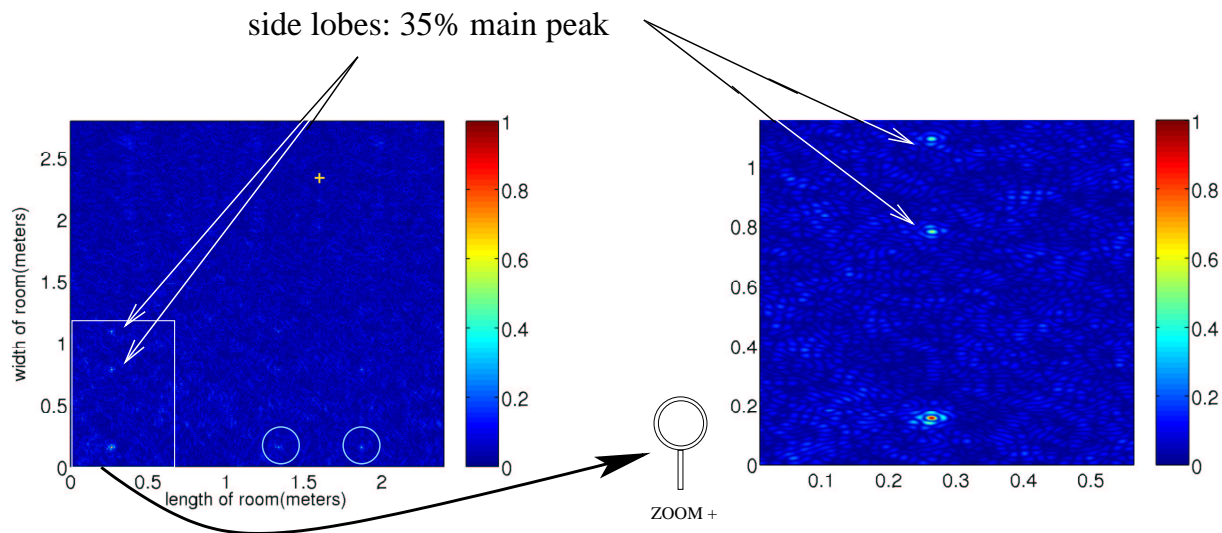
Figure 4.2: Normalized acoustic field after time-reversal at time T - t_0. Enclosure with highly reflecting boundaries and a single detector

4.2   Factors Affecting Quality of Space-Time Refocusing in Enclosures

There are many factors, besides an unchanging environment and a high signal-to-noise ratio that affect time-reversal's performance.One such aspects is the number of transducer detectors used. Another aspect is whether the medium between source and detector is a homogeneous one, or one filled with random scatterers.

We learned in the introduction that it is possible to obtain a better spatial resolution of the pulse, after time-reversal, using random scatterers as a "pseudo-lens" with an angular aperture much wider than the size of a TRM alone. In Fink's experiment with the forest of rods as a random scattering medium, the spatial resolution turned out to be one-sixth of the theoretical limit for the mirror's aperture. [1]

Just like the multiple scattering process widens the effective TRM aperture, the reflections from the boundaries of waves propagating in waveguides or cavities have the same widening of the aperture effect. Essentially, it is like replacing some of the TRC transducers by reflecting boundaries that help redirect one part of the incident wave toward the TRM aperture. [1]

In [4] we read of experiments with ultrasonic waves carried out in a waveguide by Roux. The spatial resolution in the waveguide, delivered a spot of size much smaller than that obtained with a comparable TRM in free space. In essence, in a waveguide or cavity, the boundaries naturally expand the effective aperture of the TRM.

Number of detectors

Our initial hypothesis was that sampling the field at more spatial points in the enclosure with multiple detectors could yield a better spatial resolution of the pulse.

Acoustic time-reversal experiments in waveguides or enclosures with loss in them usually need large arrays of transducer detectors. The decrease in the number of detectors generally affects the aperture of the "refocusing lens", thus diminishing the focusing quality. In free space, with a large array of detectors, information from scattering is received by each element in the array and sent back time-reversed to the source, producing significantly better results than the ones obtained with only a single detector. The multiplicity of paths that many detectors produce yields high quality refocusing results.

Nevertheless, in waveguides or cavities with highly reflecting boundaries, the experiments with only one detector demonstrate excellent temporal and spatial focusing quality. Mathias Fink shows in [[10]] the results of carrying out time reversal of a point-like source with elastic waves using a single transducer detector element. Fink argues the use of reflections is a way of effectively increasing the transducer aperture. [[16]] By using the many reflections with boundaries, the time reversal process creates multipathing and dispersion of sound across an enclosure. So, as we will learn in this chapter, enclosures with reflective walls produce enough multiplicity to yield high quality refocusing with only one transducer detector. However, the more detectors in the enclosure, the more energy is sent back into the enclosure as the time-reversed signals are re-transmitted. This increase in energy increases the peak-to-side-lobes

ratio in the refocused pulse.

In highly reflective enclosures with only one transducer, the spatial focusing reaches a resolution of half the wavelength of sound. Thus, as we will show in this chapter, not much can be gained by adding more detectors in the enclosure, except for a higher peak-to-side-lobe ratio. However, in enclosures where there is loss we shall explore the consequences of time reversal with a single detector, versus with multiple detectors.

To think of the consequences of time reversal in an enclosure with a a single detector and constant absorption at the boundaries we imagine the following *Gedankenexperiment*: Starting with an ideal detector array that has N detectors separated a half-wavelength from each other and surrounds the entire source as in a TRC. Suppose this array has a magnitude of peak-to-side-lobe ratio that can be interpreted as refocusing energy, of size "E." We remove first a single detector from the array and leave N-1 detectors, thus obtaining an energy of refocusing of E - ΔE, where ΔE is the energy amplitude corresponding to a single detector.

We continue to eliminate one by one of the detectors, the energy continuing to decrease by $E - n\Delta E$ where n is the number of detectors eliminated from the experiment. We can continue this process until $n = N$ which means there are no more detectors in the room in which case time-reversal will not work. The more detectors we remove, the more energy is lost to the boundaries as they partially absorb some of the incident energy. There starts a competition to find a balance between the number of detectors and the quantity of absorption that one can have to enable acceptable refocusing results. Thus, the amplitude of the refocusing diminishes linearly with the number of detectors eliminated from the enclosure. The more detectors in the cavity, the more energy captured (in a linear relation). However we shall look to find the relation of a different index of absorption to refocusing quality. By knowing this two factors, it is possible to suggest an optimal scheme where for such index of absorption, one would need at least N number of detectors to have acceptable refocusing of the pulse.

Randomly-placed Scatterers

We learned in the Introduction that, in a time-reversal experiment, the multiple reflections with the boundaries or obstacles in an enclosure allow the redirection of one part of the initial wave toward the TRM, that would normally miss the transducer array. Thus boundaries or inhomogeneities produce multipathing and the TRM appears to have a much larger aperture than its physical size. [1]

In this chapter, we shall explore the consequences in spatial focusing in enclosure with

the addition of randomly-placed scatterers in it. As we will see, there is considerable gain in using scatterers in an enclosure as they remove side lobes due to image sources that would otherwise remain as secondary side lobes of about 35% in the enclosure.

To prevent undesired leak of energy into places other than around the original source, scatterers have proven to be effective in redirecting most of the collected energy back to the source for optimal spatial focusing..

4.2.1 Enclosure with Highly Reflecting Walls, a Single Detector and Randomly-placed Scatterers

We now present the results of carrying out the time-reversal experiment in an enclosure with highly reflecting boundaries and the addition of randomly-placed scatterers.
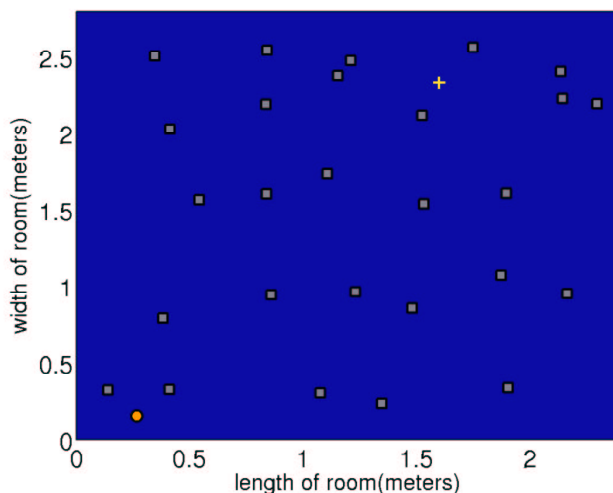
Figure 4.3: Computational setup: room with highly reflecting walls, randomly-placed scatterers (gray squares) and a single detector (yellow cross) at (1.6, 2.333)m

The following results are snapshot of the acoustic field in the enclosure at time T - t_0. As argued above, we expect the scatterers to improve the spatial focusing by making side lobes surrounding the source disappear. As we shall see, this occurs for both Dirichlet and Neumann cases.
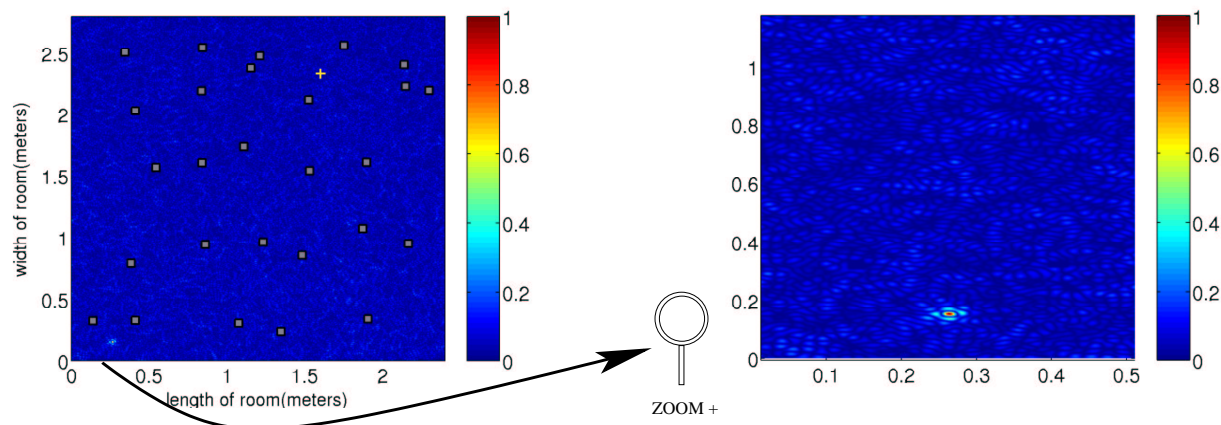
Figure 4.4: Normalized acoustic field after time-reversal at time T - t_0. Enclosure with highly reflecting boundaries, randomly-placed scatterers and a single detector

4.2.2   Enclosure with Highly Reflecting Walls and Multiple Detectors

We now perform the time-reversal experiment in an enclosure with highly reflecting walls and ten detectors. We carry out the time-reversal experiment and take a snapshot of the acoustic field in the enclosure at time T - t_0. The results of this are presented in figure (4.6).
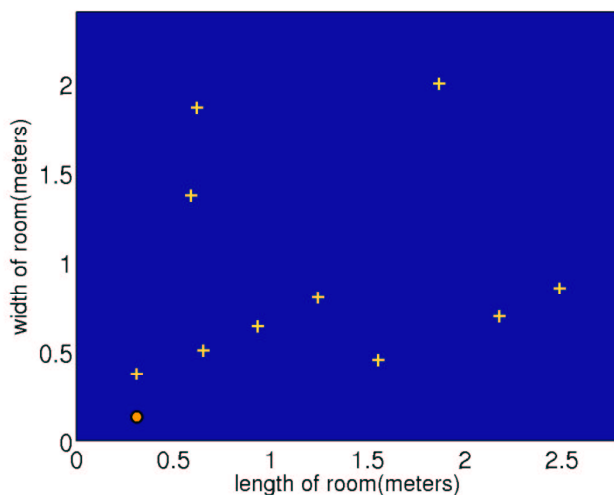
Figure 4.5: Computational setup: room with ten randomly-placed detectors (yellow crosses) at (0.267, 0.436)m, (1.067, 0.933)m, (1.867, 0.81)m, (1.3333, 0.5289)m, (2.133, 0.996)m, (0.56, 0.591)m, (0.507, 1.602)m,(0.80, 0.747)m, (0.533, 2.178)m and (1.6, 2.333)m

The amplitude of the refocused spot is proportional to the number of detectors. As
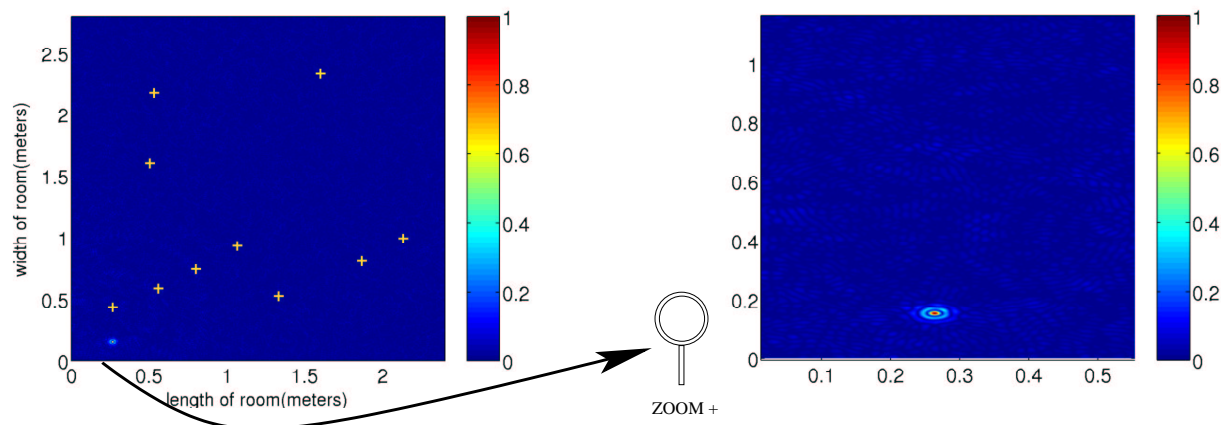
Figure 4.6: Normalized acoustic field after time-reversal at time T - t_0. Enclosure with highly reflecting boundaries and ten detectors

shown in figure (4.6), in the presence of multiple detectors in the enclosure, the more energy collected in the time-reversal process the better the peak-to-side-lobe ratio is. This improves the spatial focusing, in the sense that since the amplitude of the refocused pulse is ten times larger than with a single detector, it vanishes the secondary side lobes of the main pulse. Also, it is observed that overall in the entire enclosure, multiple detectors yield a higher peak-to-grass ratio. That is why the background in this picture (4.6) shows a darker blue (very small magnitude) than the background in figure (4.4)'s brighter blue (a bit higher magnitude) where the random scatterers are present.

4.2.3 An Array of Detectors

Twenty detectors are set up

4.2.4 Enclosure with Highly Reflecting Walls, Multiple Detectors and Randomly-Placed Scatterers

We now combine the addition of randomly-placed scatterers to an enclosure with highly reflecting walls and ten detectors. We perform the time-reversal experiment and take a snapshot of the acoustic field in the enclosure at time T - t_0. Since the ten detectors already increase the peak-to-side-lobe ratio so as to make the side-lobes disappear, we expect the side-lobes to be absent from the following results. The results are presented in figure (4.9).
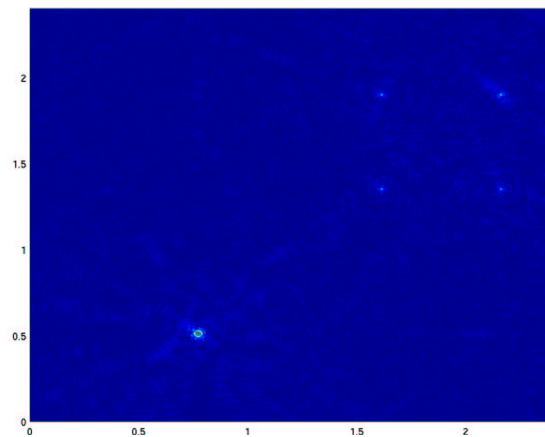
Figure 4.7: Normalized acoustic field after time-reversal at time T - t_0. Enclosure with highly reflecting boundaries and a twenty-detector array
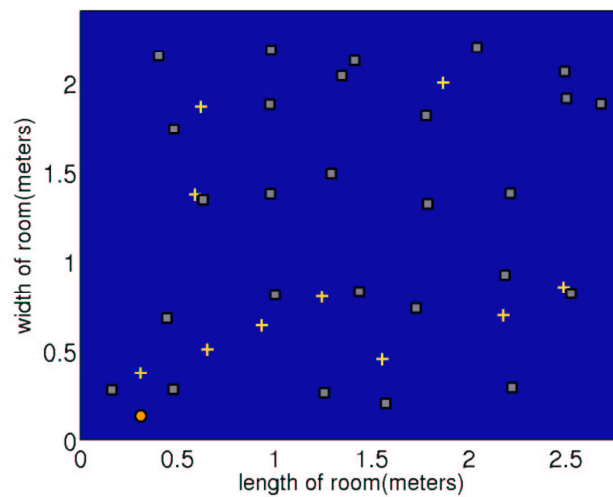
Figure 4.8: Computational setup: room with randomly-placed ten detectors (yellow crosses) and scatterers (gray squares)
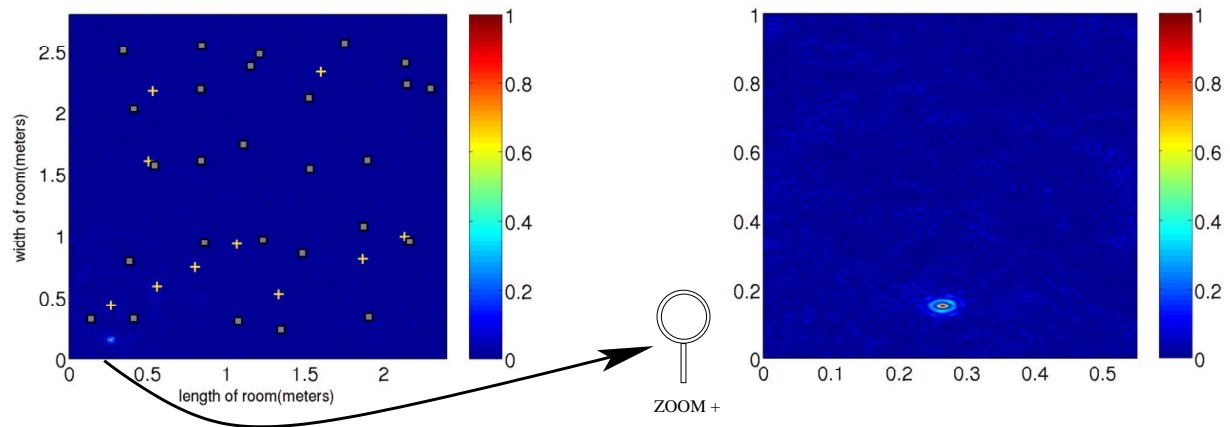
Figure 4.9: Normalized acoustic field after time-reversal at time T - t_0. Enclosure with highly reflecting boundaries, randomly-placed scatterers and ten detectors

Following are the main conclusions we draw about the impact of adding detectors and scatterers to a time-reversal enclosure.

- Multiple detectors and scatterers make side lobes disappear

- Multiple detectors do better at reducing the peak-to-side-lobe ratio than multiple scatterers alone

4.3 Empty Enclosure with Neumann Boundaries

We shall model an enclosure with highly reflecting boundaries using the Neumann boundary condition, namely, having the force vanish at the boundaries. This kind of boundary effects no phase change in the reflected wave. The total energy in the enclosure is conserved for all times.

Mathematical formulation

$$\frac{\partial^2 p}{\partial t^2} + c^2 \nabla^2 p = \delta(\mathbf{r} - \mathbf{r_0}) f(t) \qquad \text{Wave Equation} \qquad (4.3)$$

where $\mathbf{r_0}$ is the source location and the pulse in time is

$$f(t) = \cos\left(2\pi\nu\left(t - t_0\right)\right) \exp\left[-\frac{(t - t_0)^2}{t_w^2}\right]$$

The initial conditions are

$$p(t = 0) = 0 \tag{4.4}$$
$$p_t(t = 0) = 0$$

and the boundary condition is

$$\text{Neumann} \quad \frac{\partial p}{\partial n} = 0 \quad \text{at boundaries}$$

We now present the results of carrying out the time-reversal experiment in an enclosure with Neumann boundary conditions The following figure (4.10) is a snapshot of the acoustic field in the enclosure at time T - t_0.
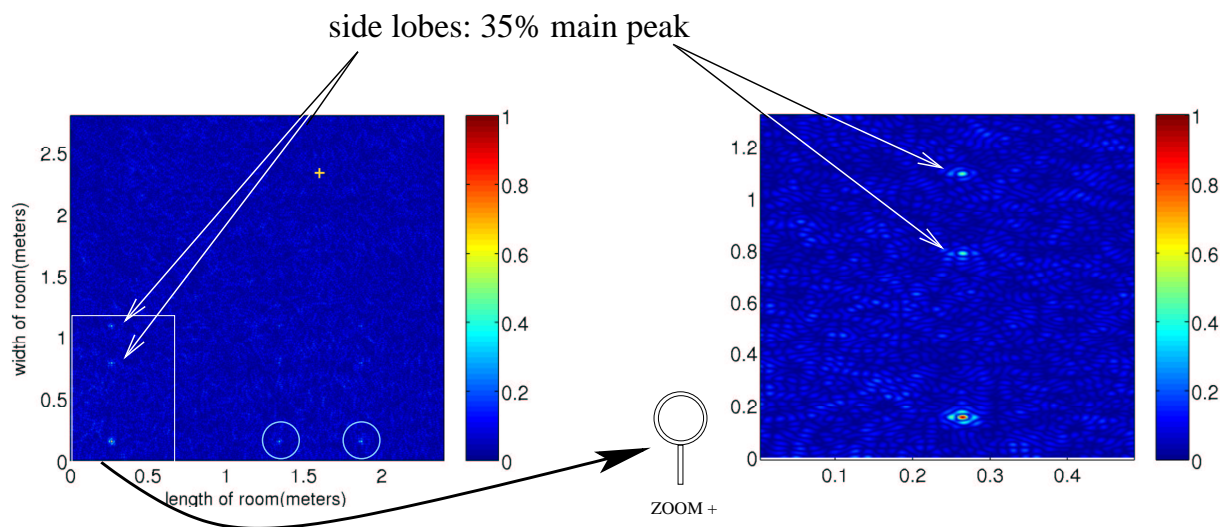
Figure 4.10: Normalized Acoustic Field after Time-Reversal. Room with ImedanceNeumann Boundary Conditions and a Single Detector (yellow cross) at (1.6, 2.333)m

Just as in the Dirichlet boundary conditions case, the Neumann boundaries conserve the energy in the enclosure. The difference between the two boundary conditions is that, in the Dirichlet case, there is a phase shift in the reflected waves off the walls. IN the Neumann boundaries case, however, there is no such phase shift.

It is important to mention that phase shift or not, the results of time-reversal are the same. Having no phase shift in the reflected waves does not modify the results of time-reversal. As long as the energy is conserved in the enclosure (with either Dirichlet or Neumann boundary

conditions) the impact of adding scatterers and detectors to the enclosure are the same.

Thus, we shall just note that, in an enclosure with Neumann boundaries and randomly-placed scatterers we obtain the same results as displayed in the similar case with Dirichlet boundary conditions in figure (4.4).

Also, for the case of an enclosure with Neumann boundaries and multiple detectors, we obtain the same results as displayed in the similar case with Dirichlet boundary conditions in figure (4.6).

Finally, for the case of an enclosure with Neumann boundaries, multiple detectors and randomly-placed scatterers, we obtain the same results as displayed in the similar case with Dirichlet boundary conditions in figure (4.9).

4.4 Absorbing Boundaries

Time-reversal yields sharp compression in space and time for Dirichlet and Neumann rooms. Multiple detectors and scatterers make side lobes disappear. Multiple detectors do better at reducing the grass than multiple scatterers alone. We shall now explore what happens in a room with absorption. Physically, absorption does not conserve energy in the enclosure, thus, the available information gets smaller in magnitude as it goes from bounce to bounce with the walls. As we will show, absorption brakes the time-reversal symmetry of the equations because the boundary conditions include a first derivative with respect to time. This first derivative changes sign under time-reversal.

Mathematical formulation

$$\frac{\partial^2 p}{\partial t^2} + c^2 \nabla^2 p = \delta(\mathbf{r} - \mathbf{r_0}) f(t) \qquad \text{Wave Equation} \qquad (4.5)$$

where $\mathbf{r_0}$ is the source location and the pulse in time is

$$f(t) = \cos\left(2\pi\nu\left(t - t_0\right)\right) \exp\left[-\frac{(t - t_0)^2}{t_w^2}\right]$$

The initial conditions are

$$p(t = 0) = 0 \qquad\qquad (4.6)$$
$$p_t(t = 0) = 0$$

And the boundary condition is

$$\text{Absorption} \quad \frac{\partial p}{\partial t} = \kappa c \frac{\partial p}{\partial n} \quad \text{at boundaries}$$

In all the following experiments, we used the maximum value of the coefficient of absorption, $\kappa = 1$. This simulates a strongly absorbing ,medium. In the end, we will show and compare with results of carrying out the time-reversal experiment in an enclosure with moderate and low absorption coefficients.

4.4.1 Empty Enclosure with Highly Absorbing Boundaries

The following figure shows a snap picture of the acoustic field in the enclosure exactly at the refocusing time $t = T - t_0$. It is at this time, after the time reversal process, that we expect to see a spatially focused spot at the source location. We recall that it was this that was observed in both Dirichlet and Neumann boundary cases. Ad the following figure (4.11) shows, in an enclosure with high impedance at the walls we observe a very poor quality refocusing of the pulse.

The results displayed in figure (4.11) show a less than perfect refocusing at the source location. Since there is only a single detector in an absorbing enclosure, it is natural to expect the refocusing to be limited in space by exhibiting side-lobes or ghost points as in the Dirichlet and Neumann enclosures. However, what we observe in this absorbing enclosure, is a smeared refocusing area that lies on the arc of a circle. The center of this circle appears to be the detector location and its radius the distance between source and detector.

We shall recall that in the case with Dirichlet and Neumann boundary conditions, when there is only a single detector present in the enclosure, we obtain a very tight refocusing spot at the source location. In addition to this, we observe a number of side lobes surrounding it. We have seen how this side lobes are extinguished when we place random scatterers in the enclosure in figure (4.3).

We have also observed side lobes disappear when there are multiple detectors in the
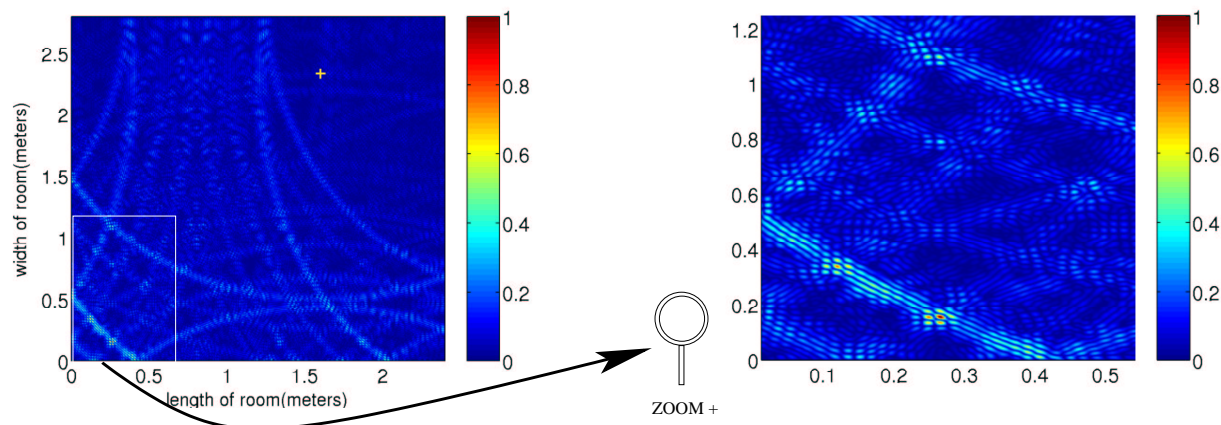
Figure 4.11: Normalized acoustic field after time-reversal at time T - t_0. Enclosure with high impedance at the boundaries and a single detector (yellow cross) at (1.6, 2.333)m $\kappa = 1$

enclosure in figure (4.6). Multiple detectors not only make the side lobes disappear, but also improve peak-to-grass ratio of the refocused pulse with respect to the entire enclosure.

These results have lead us to believe that in the case of an enclosure with highly absorbing boundary conditions, the spatial focusing after the time-reversal process will improve after the addition of either multiple scatterers or multiple detectors. Following this argument, it is possible to envision the possibility that, as more energy is collected by multiple detectors, the smeared out focusing may turn into a self-contained spatial spot.

4.4.2 Enclosure with Highly Absorbing Boundaries and Randomly-placed Scatterers

First, we observe how the effect of the randomly-placed scatterers is to break the symmetry around the arc, making it look less like an arc of a full circle. However, the scatterers do not make the refocusing spot more tightly focused.

4.4.3 Enclosure with Highly Absorbing Boundaries and Multiple Detectors

Secondly, we observe how the effect of having multiple detectors in the enclosure affect the spatial resolution of the pulse in the enclosure.

What we observe in this experiment, is that the area of refocusing of the energy close to the original source has the shape of a circular ring. With these results, we conclude that
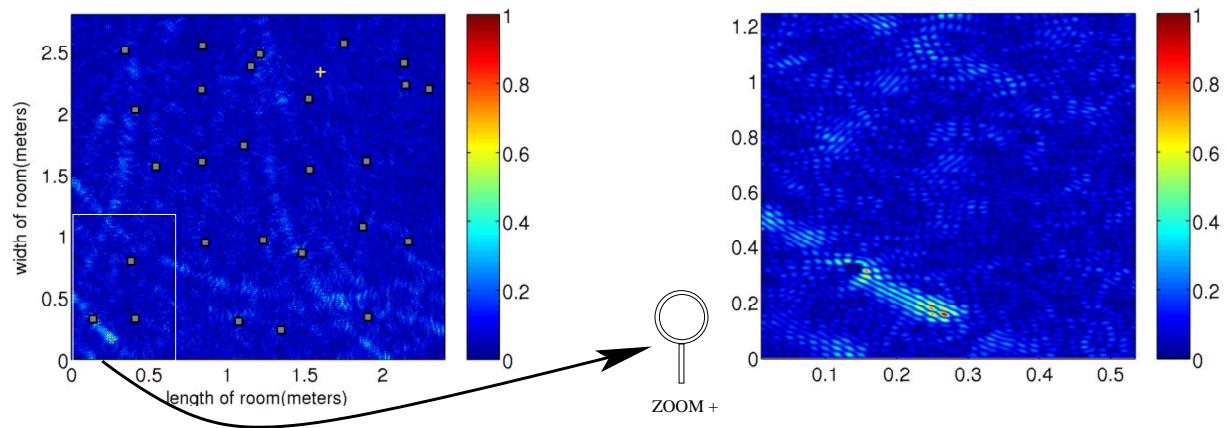
Figure 4.12: Normalized acoustic field after time-reversal at time T - t_0. Enclosure with high impedance at the boundaries, multiple scatterers (gray squares) and a Single Detector (yellow cross) at (1.6, 2.333)m, $\kappa = 1$
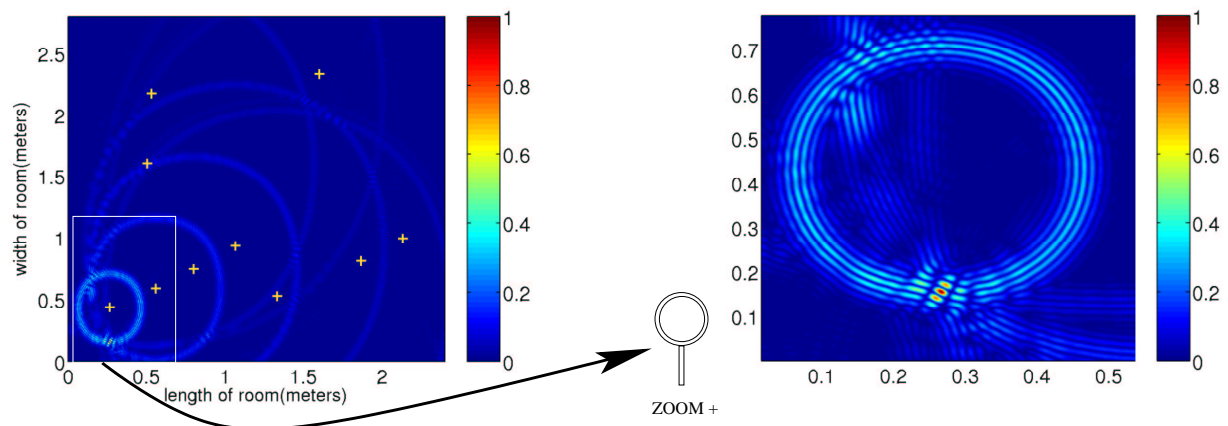
Figure 4.13: Normalized acoustic field after time-reversal at time T - t_0. Enclosure with high impedance at the boundaries, and multiple detectors (yellow crosses), $\kappa = 1$

adding more detectors to the enclosure does not improve the size or shape of the refocusing energy under absorptive boundary conditions. It only changes the distribution of energy that with a single detector is smeared out on an arc, and with multiple detectors forms a closed ring.

Contrary to what occurs in the case of Dirichlet or Neumann boundary conditions, where the addition of multiple detectors in the enclosure make the secondary side lobes disappear, in the case of high absorption at the walls, multiple detectors create a very defined circular pattern of which the source is just a small point on its diameter.

In the subsequent section 4.5, we shall investigate the origin of this circular pattern and the conditions under which it arises.

4.4.4 Enclosure with Highly Absorbing Boundaries, Multiple Detectors and Randomly-Placed Scatterers
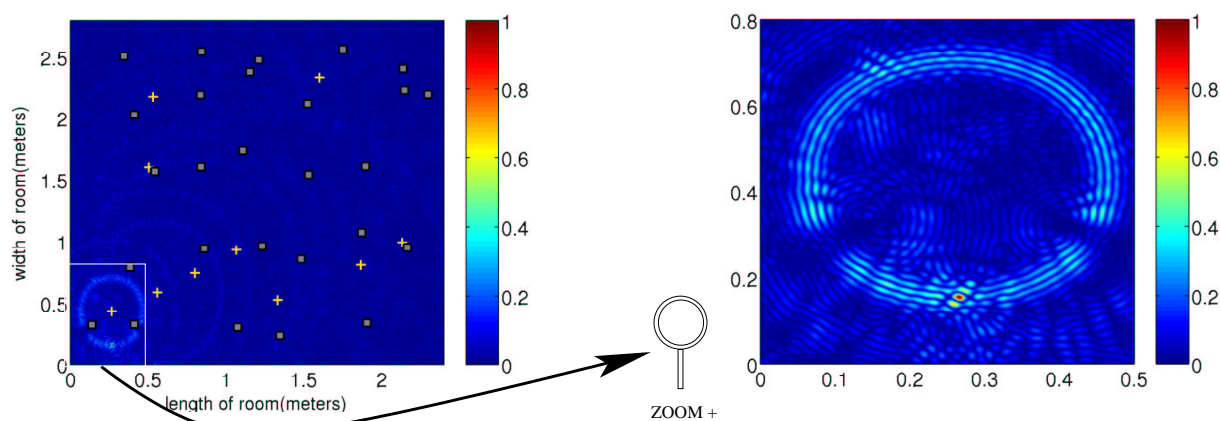
Figure 4.14: Normalized acoustic field after time-reversal at time T - t_0. Enclosure with high impedance at the boundaries, multiple scatterers (gray squares) and ten detectors, $\kappa = 1$

As we observe from figure (4.14), carrying out the experiment with ten detectors and 26 randomly-placed scatterers does not improve the shape of the refocused pulse. We conclude that neither scatterers nor detectors are successful at improving the refocusing of the original pulse at the source location.

What we observe in the zoomed area of the refocusing of the field close to the source is that the spatial focusing does not improve the size or shape of the refocusing energy under highly-absorptive boundary conditions.

Adding more detectors to the enclosure, combined with the existence of scatterers does not improve the size or shape of the refocusing energy under absorptive boundary conditions.

The effects of the multiple scatterers is to break the symmetry of the refocused ring. By displaying two broken cuts around the circular ring, we see how these are due simply to the presence of the scatterers at those precise two locations close to the source.

4.5 Analysis of Observed Circular Wave Patterns

As we analyze the appearance of the circular wave patterns, a few questions arise such as: how do the secondary circular wave patterns emerge?, why are they circular and not of different shape?. Are they produced by the higher frequency components of the partially absorbed waves? Are they dependent on location of source or detectors, and if so, in what way?

It becomes imperative to explore if the secondary circular wave patterns in the enclosure with absorption are inherent in the way the boundary conditions work at the walls. We shall also explore if their origin comes from undesired constructive interference between reflected waves that come back partially absorbed by the boundaries.

4.5.1 Low-Pass Filter

One of the first hypothesis that came to mind when analyzing the particular effects of secondary wave patterns in enclosures is that absorption may be cutting out the high-frequency components of the modes generated in the enclosure.

As this signal is time-reversed at the detector location and re-transmitted into the enclosure, it is possible that the absorption mechanism has artificially cut-out the higher frequency components of the signal, leaving only the lower frequency components of it to time-reverse.

For this, we suggest an experiment in an energy-conserving Dirichlet-boundary enclosure, where we are to perform the time-reversal experiment. After the forward phase is completed, when we obtain the time-trace at the detector, we shall cut out the high frequency components of it. Following that by time-reversing this signal and re-transmitting it into the same medium. As the higher frequencies are cut out, we shall observe if similar secondary circular wave patterns appear in the enclosure. If they appear, this would mean that the proposed mechanism could in some way be responsible for the effect.

The trick is to do a simple signal processing to pass the waveform received at the detector

through a low-pass filter. This cuts out the high-frequency components from it. I then time-reverse the filtered waveform and send it back into the enclosure. A low-pass filter is constructed that cuts out high frequencies from the captured signal at the detector. This is time-reversed and re-transmitted into the same medium. The results are shown in figure (4.16).

To build a low-pass filter, I first Fourier transform the received waveform at the detector and multiply it times a Gaussian function that eliminates the high end tails of the frequency spectra. Then I perform an inverse Fourier transform on the low-pass filtered waveform and time-reverse this. Finally, I send this back into the enclosure and record the effects. The hypothesis is that, if one observes the circularly-shaped ghost images appear again, then absorption is the probable cause for the high-frequency components of the field to be cut out; and in turn, this is the cause for the circularly-shaped secondary wave patterns to appear.

The idea behind this test is that the more absorption an enclosed system has, the more it resembles an outdoor medium, i.e. the more the refocused peak will be a sinc function and develop side lobes. On the other hand, the better insulated a room is, the sharper the refocused peak will be after time reversal. Since all the high-frequency components are the ones getting most of the bounces around the room, they will contribute in great part to the formation of the peak. Now, if there is absorption, these high frequency components are cut out in the process and only the lower modes remain. Therefore, the main peak will be reconstructed with less precision than in the non-absorbing case, it will be like a sinc function displaying side lobes.

After carefully performing this experiment, this hypothesis could not be corroborated. The circularly-shaped wave patterns do not appear as the experiment is performed and results after time-reversal are recorded. Thus, we can conclude, that absorption is not the mechanism, responsible for creating this patterns in the waveform in the enclosure.

We discovered that the circular wave patterns are not a result of the high-frequency components of the signal received. We conclude they are due to a different cause that we shall investigate further.

4.5.2 Changing Source Location

The second thing we decided to investigate was whether the secondary circular wave patterns constitute an effect of the location of the source and detectors in the enclosure.
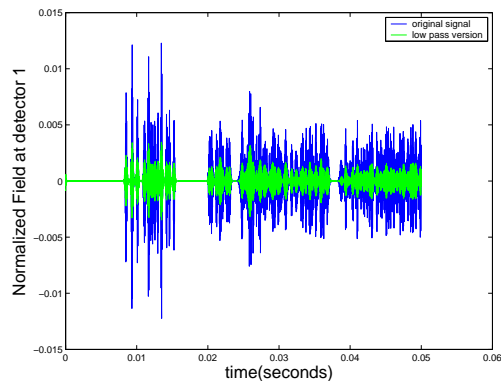
Figure 4.15: Original detector signal received in a Dirichlet boundary room (blue signal) compared with the same signal, after being filtered through a low-pass filter (green signal). We time-reverse this low-pass filtered detector and send it back in the second phase of the time-reversal process
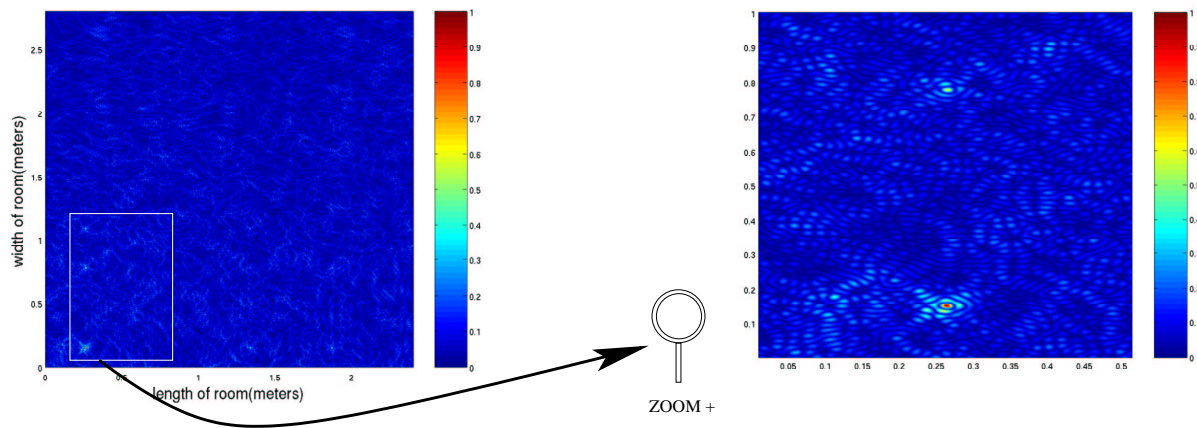
Figure 4.16: Normalized acoustic field after time-reversal at time T - t_0. Enclosure with Dirichlet boundary conditions. After sending back a low-pass filtered version of the obtained detector

We explore whether the particular shape of the secondary wave-patterns is dependent on the location of the source. Consequently, we show the results of an experiment carried out with exactly the same experimental conditions for absorption at the boundaries and multiple detectors, but where the source is moved to the center of the enclosure.

The following figure (4.17) shows a contour plot of the normalized acoustic field after the time-reversal process, at the refocusing time $T - t_0$. If our hypothesis that the source's location is inducing this secondary effects, was right, we would expect the spatial refocusing of the pulse at the original source location, the center. And, no more circular wave patterns.
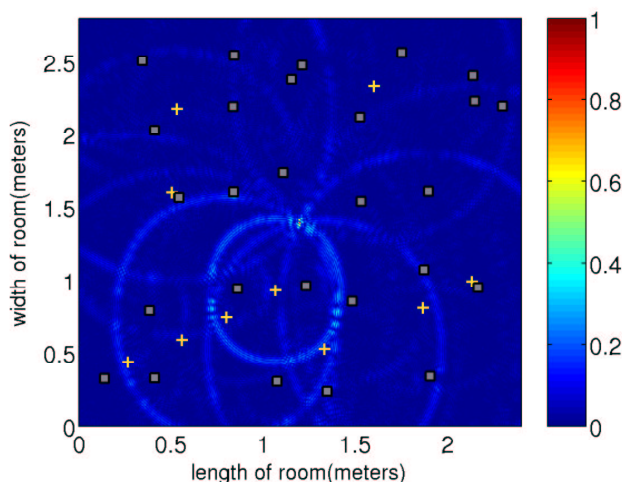
Figure 4.17: Normalized acoustic field after time-reversal at time T - t_0. Enclosure with high impedance at the boundaries, multiple scatterers (gray squares) and ten detectors, $\kappa = 1$

At this point we can observe that the secondary circular wave patterns, although changed, still appear. They do not become less apparent or dimmer. There is a circle of larger magnitude close to the source.

This experiment leads us to eliminate the hypothesis that the particular shape of the secondary circular wave patterns is an effect of the source being too close to the wall.

When our model parameter, $\kappa = 1$, the boundary condition we use, simulates a simplified version of the more complex phenomena of wave absorption at the boundaries of an enclosure. In our boundary condition, absorption happens mostly for the waves incident in a perpendicular direction to the boundaries. Constructive interference of the perpendicularly-reflected waves at the boundaries does not seem to be responsible for the secondary circular wave patterns.

The fact that there is constructive interference at several points of cross-section between

different secondary circular patterns introduces undesired noise in the enclosure. This leaves the peak-to-noise ratio at a value significantly higher than in the case with no absorption at the boundaries.

At this point, it is important to note that the density of detectors in the left lower quadrant is higher than the one in any other area of the enclosure. This suggests why there is a circular pattern of larger magnitude situated toward the left lower quadrant in both figures (4.17) and (4.13). Furthermore, this suggests the possibility that these patterns are dependent on the location of detectors in the enclosure.

4.5.3 Changing Detector Location

A different hypothesis is that the detectors and their location in the enclosure are the main cause in the creation of the circularly-shaped wave patterns. The concept behind this idea is that after the source transmits the initial pulse, the detectors capture a waveform coming from a particular direction (from the source). There is an inherent asymmetry in the problem, in that, after the captured waveform is time-reversed, the detectors transmit the signals in all directions in space into the enclosure. It is perhaps this data that initially contains directional information, and then is re-transmitted in an omni-directional way, that is responsible for the constructive interference patterns in the enclosure.

Additional support for this hypothesis of the detectors being responsible for the wave patterns, is the differences observed in the single-detector case, versus the ten-detectors case. In the single-detector case, the images are much more disordered and look more like circles of greater radius that haven't quite come to close on themselves. Whereas, in the ten-detector case, the circles do close around the detectors and also interfere with themselves constructively to form the observed wave patterns.

We replace the old configuration of detectors with a new one shown in figure (4.18). The new detector configuration breaks the symmetry that concentrated more detectors in the lower left hand quadrant of the enclosure and establishes a more even detector-density setting for the time-reversal experiment. The source remains at its original location in the lower left hand corner. And the 26 scatterers remain in their original location.

We observe that the secondary circular wave patterns are still present in this experiment with new detector locations. However, it is important to note that the location, magnitude and shape of circular wave patterns differs from the ones obtained form a similar experiment with different detector locations (figure(4.14)). The conclusion drawn from this experiment
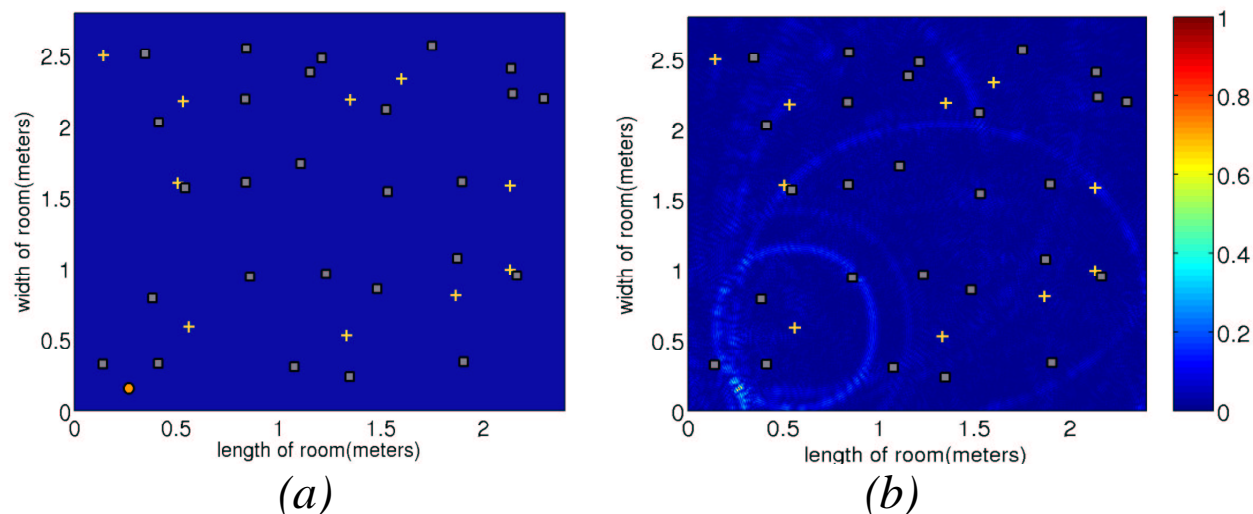
Figure 4.18: (a) Computational setup: enclosure with high absorption at the walls, source (orange circle), ten detectors (yellow crosses) in new locations and randomly-placed scatterers (gray squares) $\kappa = 1$ (b) Results of carrying out time-reversal in enclosure (a). Normalized acoustic field in enclosure with highly-absorbing boundaries after time-reversal. Snapshot at time $T - t_0$

is that these wave patterns patterns are directly connected to the detector location. It is our task to investigate this relation.

The circle of maximum magnitude remains close to the source, in the lower left quadrant. This is also the prominent, most pronounced of all circular patterns. This indicates that the detectors closest to the source are the ones determining the appearance of the main circle of highest magnitude.

In figure (4.12), the density of detectors was higher in the lower left quadrant of the enclosure, the same quadrant where the source is located. In contrast, figure (4.18) displays a considerable decrease in the magnitude of energy concentrated on the circular wave patterns. It is as if the patterns become dimmer or less noticeable when the experiment takes place with this more evenly-distributed configuration of detectors.

This leads us to conclude that the magnitude of the circular ghost wave patterns' is dependent on the distance of the detectors to the source. This makes sense if we think that in the case of free-space for example, the Green's function that describes a wave traveling from source to detector in two dimensions is proportional to one over the distance between source and detector.

$$\frac{1}{\rho_0}$$

where

$$\rho_0 = \sqrt{(x_1 - x_0)^2 + (y_1 - y_0)^2}$$

and (x_0, y_0) is the source location and (x_1, y_1) is the detector location.

We continue with an experiment where we use the original detector configuration of figure (4.12). We divide the enclosure into four quadrants. First, we turn off the detectors located in quadrant one and perform the time-reversal experiment and observe the results. We do the same thing for quadrants two, three and four.

4.5.4   The Four Quadrants Experiment

We divide the enclosure into four quadrants. We show the four partitions in figure (4.19) for an enclosure with ten detectors and randomly-placed scatterers.

After carrying out the time-reversal experiment for the four cases where one of the quadrants is turned off during the full time-reversal process, we take a snapshot of the acoustic field in the enclosure at the refocusing time $T - t_0$. The following figure shows these four snap pictures. It is at this time, after the time reversal process, that we expect to see a spatially focused spot at the source location. The experiment is performed in the entire enclosure as the detectors in each quadrant are turned off. We expect the most dramatic results to occur when quadrant one is turned off. This is because it is the one where detectors lie closest to the source. Thus, it is the one that -when on- will display the highest magnitude circular wave pattern. As it is turned off, we expect to see the high magnitude circular pattern disappear.

As discussed earlier, quadrant 1 has the highest density of detectors in the enclosure, and it is the closest quadrant to the source. The figures (4.20) show that when quadrant 1 detectors are off, the main circular ghost wave near the source does not appear. It is mainly the detectors in this quadrant closest to the source that produce the higher magnitude circular wave pattern.

When quadrant 4 is off, the detectors in quadrant 1 become the closest to the source. This makes detectors in quadrant 1 bear the most responsibility for the formation of the circular pattern near the source. It is observed that the main circular wave pattern appears with an intensity of 65% the refocused peak. This high intensity is again indicative that mainly the detectors in quadrant 1 produce the higher magnitude circular wave pattern.
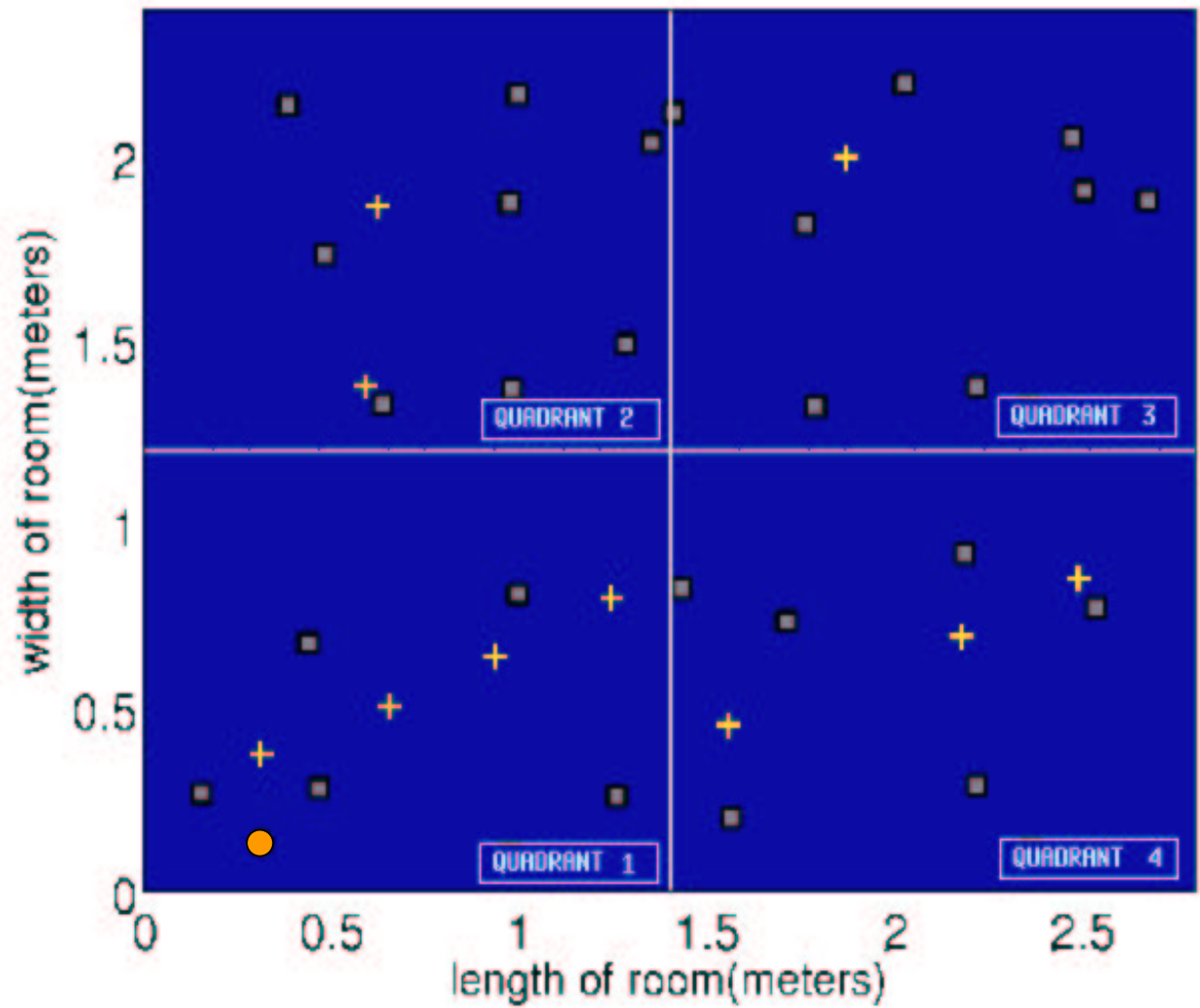
Figure 4.19: (a) Enclosure divided into four quadrants, source (orange circle), ten detectors (yellow crosses) and randomly-placed scatterers (gray squares) in enclosure
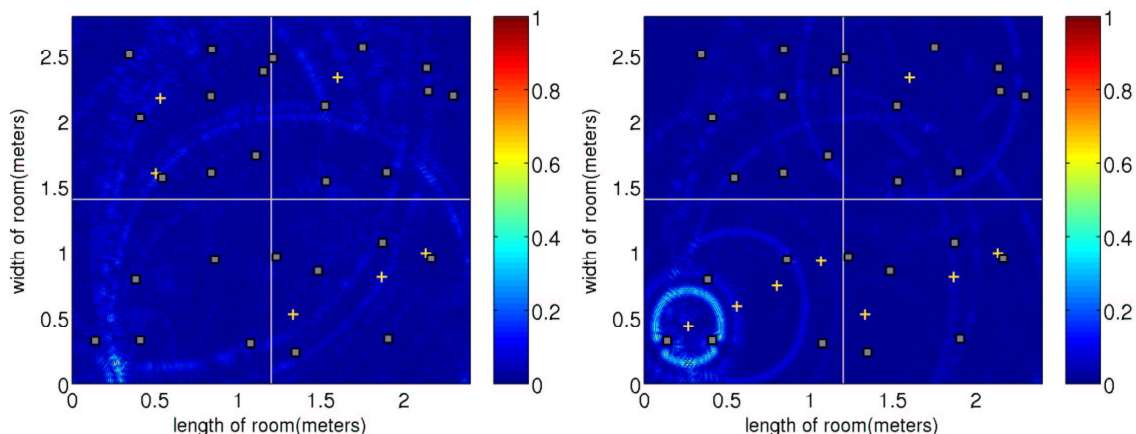
(a) Normalized acoustic field in enclosure with highly-absorbing walls. Snapshot taken at time $T - t_0$ after the time-reversal process with detectors located in quadrant one (lower left hand corner) off

(b) Normalized acoustic field in enclosure with highly-absorbing walls. Snapshot taken at time $T - t_0$ after the time-reversal process with detectors located in quadrant two (upper left hand corner) off
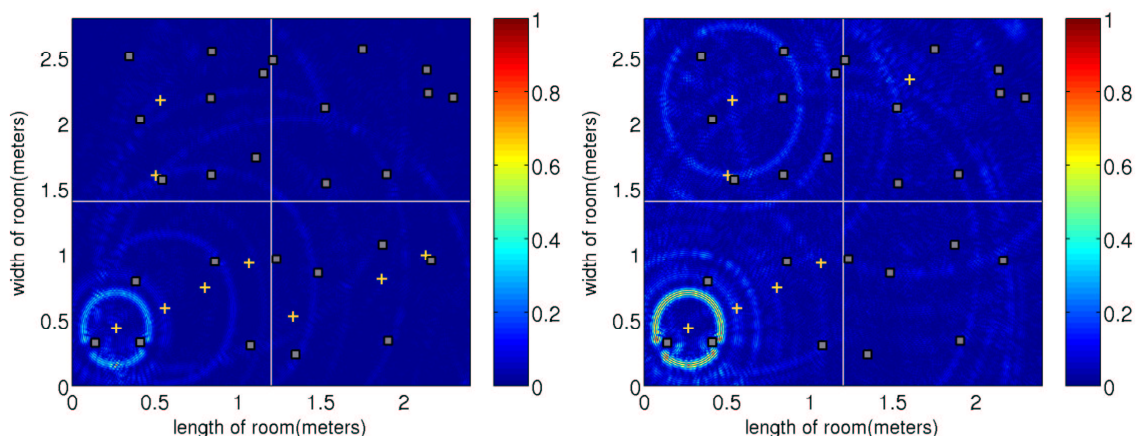
(c) Normalized acoustic field in enclosure with highly-absorbing walls. Snapshot taken at time $T - t_0$ after the time-reversal process with detectors located in quadrant three (upper right hand corner) off

(d) Normalized acoustic field in enclosure with highly-absorbing walls. Snapshot taken at time $T - t_0$ after the time-reversal process with detectors located in quadrant four (lower right hand corner) off

Figure 4.20: Enclosure with highly-absorbing walls and randomly-placed scatterers with ten detectors. Detectors located in each of the quadrants 1, 2, 3 and 4 are turned off during each one of the four time-reversal experiments, $\kappa = 1$

When detectors in quadrant 3 and in quadrant 4 are turned off, we see a similar scenario. The main circular wave pattern does form (as an effect of detectors in quadrant 1). However, it appears with smaller magnitude than its worst case of 65% the refocused peak.

If we look closer, we see that when detectors in quadrant 2 are turned off, the main circular wave pattern appears to be of slightly higher magnitude than when detectors in quadrant 3 are turned off. This is because there are more detectors in quadrant 2 than in quadrant 3, where there is a single one.

The four quadrants experiment, displayed in figures (4.20) determine the main cause for the appearance of the main circular wave pattern as connected to the group of detectors in quadrant 1.

4.5.5 Detector Time-Traces Comparison of Dirichlet versus Impedance Boundary Conditions

It is important to look at the time-traces received at one of the detectors for the cases of an enclosure with highly reflecting boundary conditions as compared to the case of an enclosure with highly absorbing boundary conditions.
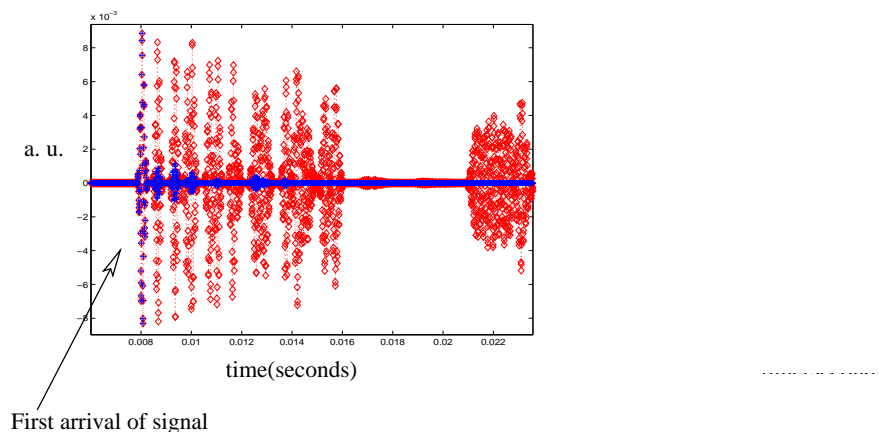
Figure 4.21: Normalized acoustic field at detector in room with reflective (red) and absorptive (blue) boundaries. $\kappa = 1$ for the room with absorption

It is easy to see in figure (4.21) that in the case of absorption at the boundaries (blue trace) the main component of the signal received at the detector is the first arrival of the pulse. What the detector receives after that is qualitatively insignificant.

Just as a check, we compare the time of arrival of the first ballistic component of the pulse received at the detector in the following circumstances: Neumann vs. Dirichlet, and

Neumann vs. Impedance boundary conditions. It is evident that the "time of first arrival" must be the same for all cases, since the arrival of this first signal component is a direct arrival from source to detector. It takes place before the pulse gets reflected by any of the walls. It constitutes a pure "line-of-sight" (LOS) traveling of pulse.
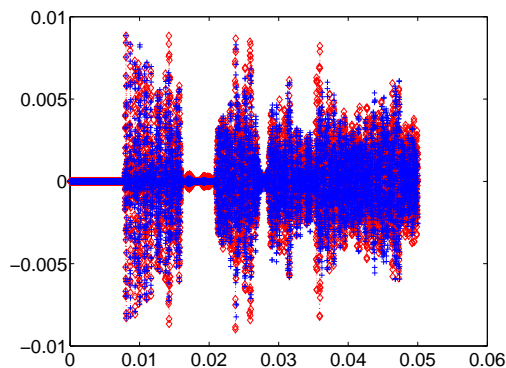
Figure 4.22: Comparison Plot of Normalized Field captured with detector in Enclosure with Reflective walls (red) vs. with Neumann boundary conditions (blue). Direct arrivals coincide
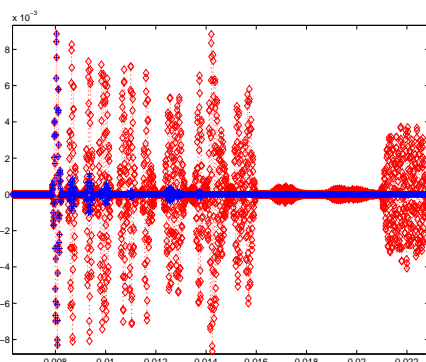
Figure 4.23: Comparison Plot of Normalized Field captured with detector in Enclosure with Neumann walls (red) vs. Absorbing boundary conditions (blue). Direct arrivals coincide

The observation from figures (4.21), (4.22) and (4.23) shows that the time of main arrival coincides in all three cases. Classically, it can be computed by

$$t = \frac{\rho_0}{c} = 0.0074 \quad s \qquad\qquad \text{time of direct arrival}$$

where again,

$$\rho_0 = \sqrt{(x_1 - x_0)^2 + (y_1 - y_0)^2}$$

the distance between (x_0, y_0) (the source location) and (x_1, y_1) (the detector location).

The difference between the signals obtained under these three different boundary conditions are evident after the direct arrival in the three figures (4.21), (4.22) and (4.23). The varied arrival times and magnitudes of the different bounces with the walls after the direct arrival, show a diverse structure that differs from others in each case.

As expected, Dirichlet and Neumann boundary conditions describe very similar physical scenarios, the only difference being that in Dirichlet there is a 180° phase shift when reflection occurs at the boundaries, whereas in the Neumann problem this phase shift is absent. The case of absorption at the walls, however, for $\kappa = 1$ is shown to kill most of the wave arrivals after this direct arrival pulse.

Like we said earlier, in a room with absorbing boundary conditions, the direct arrival is essentially where most information about the enclosure is stored. Anything else after the direct arrival is of magnitude too small to be of significance. See (4.21)

To confirm this experimentally, we experiment with sending back two different versions of the time-reversed signal. One, keeping only the direct arrival and sending zero after that. A second one, taking out the first arrival, and sending only the part of the wave that is received after this first arrival. To have an additional confirmation that the main circular wave pattern is caused mostly by the direct arrival, we look at the results in the following figure (4.24).

From figure (4.24) we see that the main circular wave pattern of highest magnitude appears when detector sends back only the direct arrival. In contrast, when the detector sends out the part received after the direct arrival, there is no refocusing of energy at any particular place.

Consequently, the circular wave pattern is an effect unrelated to the boundaries of the enclosure. It is caused by the direct arrival of the pulse from detector to source in the backward phase of the time-reversal process. If this is true, the effect should be similar in an unbounded domain.

To give proof of this, we solve analytically the time-reversal problem in two dimensions in free space. We then take a snapshot of the acoustic field at the refocusing time $T - t_0$, and expect to observe a similar circular wave pattern appear close to the source.

To explain the phenomena, we think of a time-reversal experiment in free space with a single detector. This idea is presented in the schematic of figure (4.25). The blue man is considered the source and the red man is the detector in the time-reversal process. When the blue man sends out a pulse, it travels for some time until it reaches the red man at the
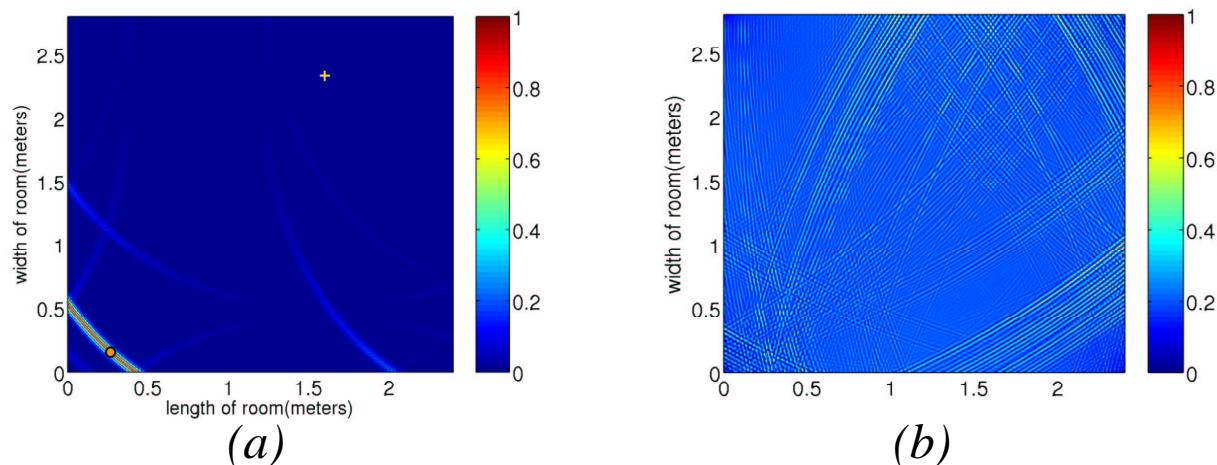
Figure 4.24: Enclosure with highly-absorbing walls, source (orange circle) and a single detector (yellow cross) at $(1.6, 2.33)m$. Results show a contour map of the normalized acoustic field at time $T - t_0$. In part a), the detector sends back only the time-reversed direct arrival. Part b) shows the same enclosure, this time sending the time-reversed recorded signal received after the direct arrival

time the outgoing blue spherical sound wave touches it. On the backward phase, the red man emits a time-reversed pulse that travels back to the blue man and reaches it when the spherical red outgoing wave achieves contact with the blue man. Using this analogy, the circular wave patterns we observe in the experimental results are just like what the blue man sees after the time-reversal process. Close the original source (blue man), at time $T - t_0$ he observes the time-reversed spherical wave (in red) that has the detector (red man) at its center and touches the source location.
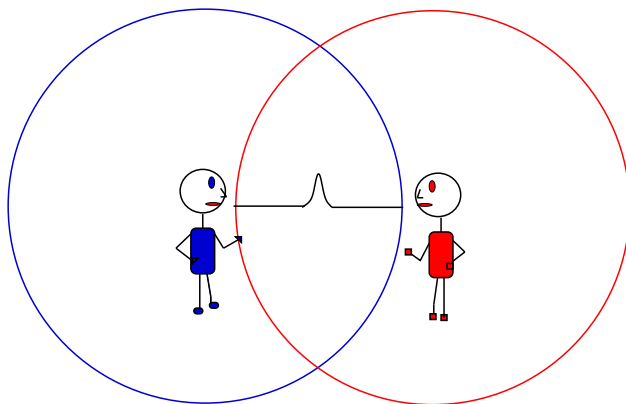
Figure 4.25: Schematic of Time-Reversal in Free Space with a Single Detector

4.5.6 Mathematical Analysis of Time-Reversal in Free-Space

What creates a circle (in the case of ten detectors figure (4.13)) or the arc of a circle (in the case of a single detector in figure (4.11)) in the lower left hand corner close to the source, is the lack of good refocusing that also occurs in free space when too much absorption is present ($\kappa = 1$).

In general, the Green's function in two dimensions for an unbounded domain describes a wave traveling from point (ζ, η) at time τ to a different measuring point (x, y) at time t. This Green's function is a solution to the wave equation with a Dirac delta source pulse, equation (4.7). IN two dimensions, the Green's function is given by equation (4.8).

$$\frac{\partial^2 G}{\partial t^2} - c^2 \nabla^2 G = \delta(x - \zeta)\delta(y - \eta)\delta(t - t_0) \tag{4.7}$$

$$G(x - \zeta, y - \eta, t - t_0) = \left(\frac{1}{2\pi c}\right) \frac{\left(H(c(t - t_0) - \sqrt{(x - \zeta)^2 + (y - \eta)^2}\right)}{\sqrt{c^2(t - t_0)^2 - ((x - \zeta)^2 + (y - \eta)^2)}} \tag{4.8}$$

where $H(x)$ is a Heaviside function used to represent discontinuous functions:

$$H\ (x) = \begin{cases} 1 & if \quad x \geq 0 \\ 0 & if \quad x < 0 \end{cases}$$

In our case we set the source at location (x_0, y_0), and a single detector at (x_1, y_1). We send an acoustical pulse from a Dirac delta source to the detector. We use Green's function in two-dimensions, equation (4.8)to describe this wave propagation. We set the pulse to start at $t_0 = 0$. After sending out a pulse from the source into the medium, we capture the following signal at the detector during a total time T

$$det(\tau) = \left(\frac{1}{2\pi c}\right) \frac{H\left(c\,(\tau) - \sqrt{(x_1 - x_0)^2 + (y_1 - y_0)^2}\right)}{\sqrt{c^2\,(\tau)^2 - ((x_1 - x_0)^2 + (y_1 - y_0)^2)}} \tag{4.9}$$

where we designate τ to be the recording time of the signal at the detector.

On the way backward in the time-reversal process, we must solve the following equation:

$$\frac{\partial^2 p}{\partial t^2} - c^2 \nabla^2 p = \delta(x - x_1)\delta(y - y_1)\overline{det(\tau)} \tag{4.10}$$

where $\overline{det(\tau)}$ represents the time-reversed signal collected at the detector for a total time T. And the pressure, p is given by

$$p = \iint_{\mathbb{R}^2} \int_0^t G(x - x_1, y - y_1, t' - \tau)\delta(x - x_1)\delta(y - y_1)\overline{det(\tau)}d\tau \qquad (4.11)$$

where t' is an integration a dummy variable.

After time-reversal, $\tau \to (T - \tau)$. Under time-reversal, equation (4.9) becomes

$$\overline{det(\tau)} = det(T - \tau) = \left(\frac{1}{2\pi c}\right)\frac{H\left(c(T - \tau) - \rho_0\right)}{\sqrt{c^2\left(T - \tau\right)^2 - \rho_0^2}} \qquad (4.12)$$

where $\rho_0 = \sqrt{(x_1 - x_0)^2 + (y_1 - y_0)^2}$ is the distance between the source and the detector, and $\rho_1 = \sqrt{(x - x_1)^2 + (y - y_1)^2}$ is the distance between the detector and the measuring point (x, y). Considering that we have initialized our pulse at $t_0 = 0$. This is the data collected at the detector.

Thus, at the end of the time-reversal process, we obtain the following result for the pressure in free space:

$$p = \left(\frac{1}{2\pi c}\right)^2 \iint_{\mathbb{R}^2} \int_0^t \frac{H\left(c\left(t - \tau\right) - \rho_1\right)H\left(c\left(T - \tau\right) - \rho_0\right)d\tau}{\sqrt{\left(c^2\left(t - \tau\right)^2 - \rho_1^2\right)}\sqrt{\left(c^2\left(T - \tau\right)^2 - \rho_0^2\right)}} \qquad (4.13)$$

4.5.7 Analytic and Numeric Comparison of Refocused Acoustic Fields after Time-Reversal

We compute the integral in equation (4.13) numerically and we pick time $t = T$ (the refocusing time) to evaluate it. The next section displays the results of evaluating this integral in at time T. If the pictures display the same circular wave patterns, we will be certain that the mechanism of absorption is a good one,whereby the room is made to resemble free space when the maximum absorption coefficient $\kappa = 1$ is used.

4.5.8 Conclusions on Absorbing Boundaries

Comparing the schematic in figure (4.25) to the analytical results obtain with the following nine detector locations in figure (4.28)

The circular shape of the wave patterns arises from the spherical wave traveling back to the detector after time-reversal and not having sufficient energy, nor a focusing lens such as a random medium to refocus at a single spot in space. Depending on the distance of each
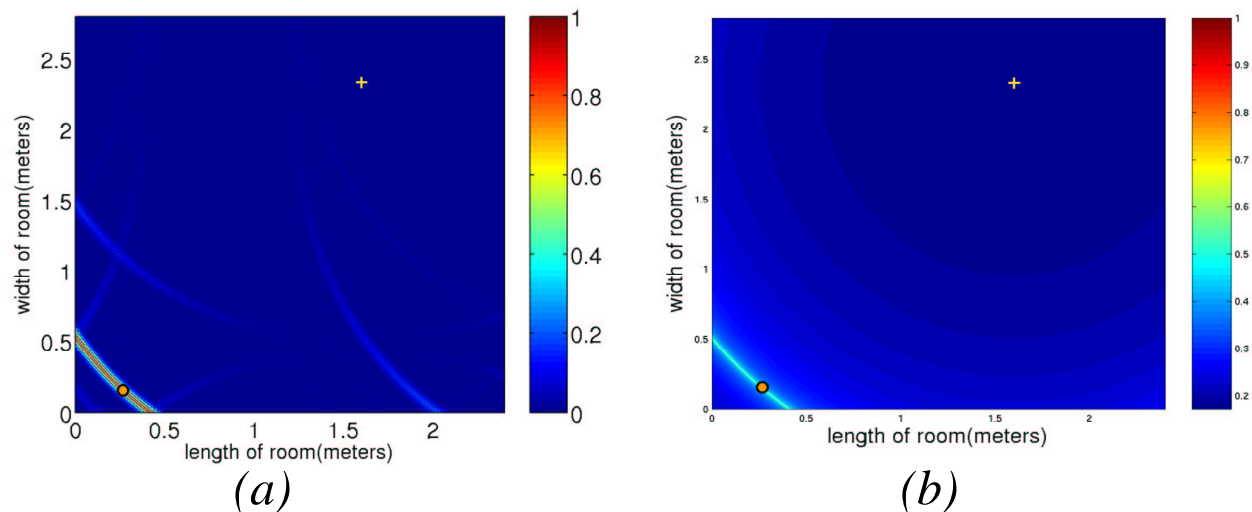
Figure 4.26: Room with highly-absorbing boundary conditions, $\kappa = 1$. A source (orange circle) and a single detector (yellow cross) are displayed. Comparison of acoustic field after time-reversal at time T. (a) computational simulation in absorptive room (b) analytic calculation in free space
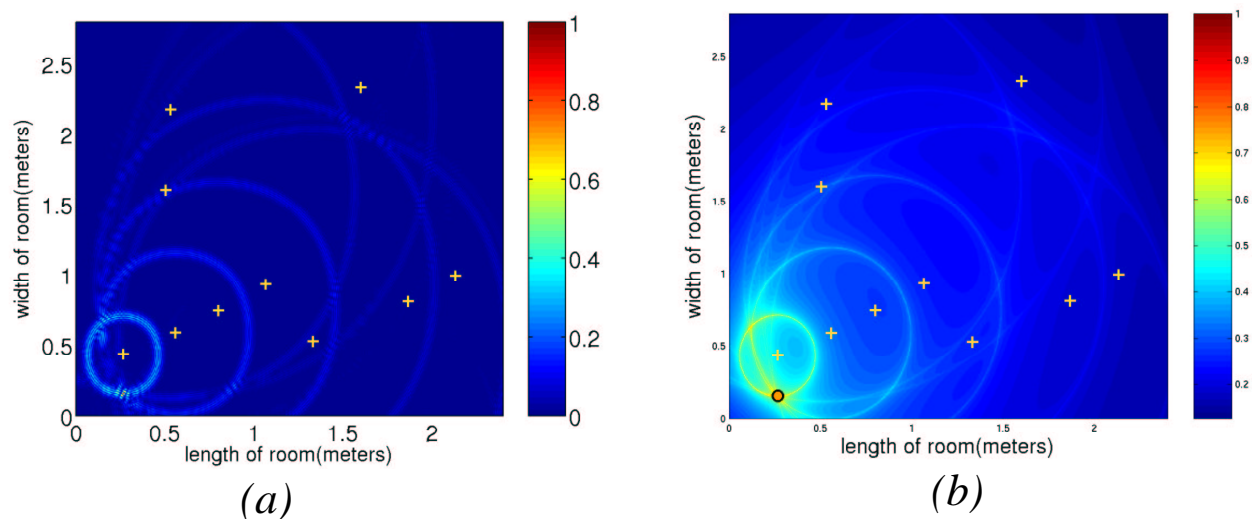
Figure 4.27: Room with highly-absorbing boundary conditions, $\kappa = 1$. A source (orange circle) and a multiple detectors (yellow crosses) are displayed. Comparison of acoustic field after time-reversal at time T. (a) computational simulation in absorptive room (b) analytic calculation in free space
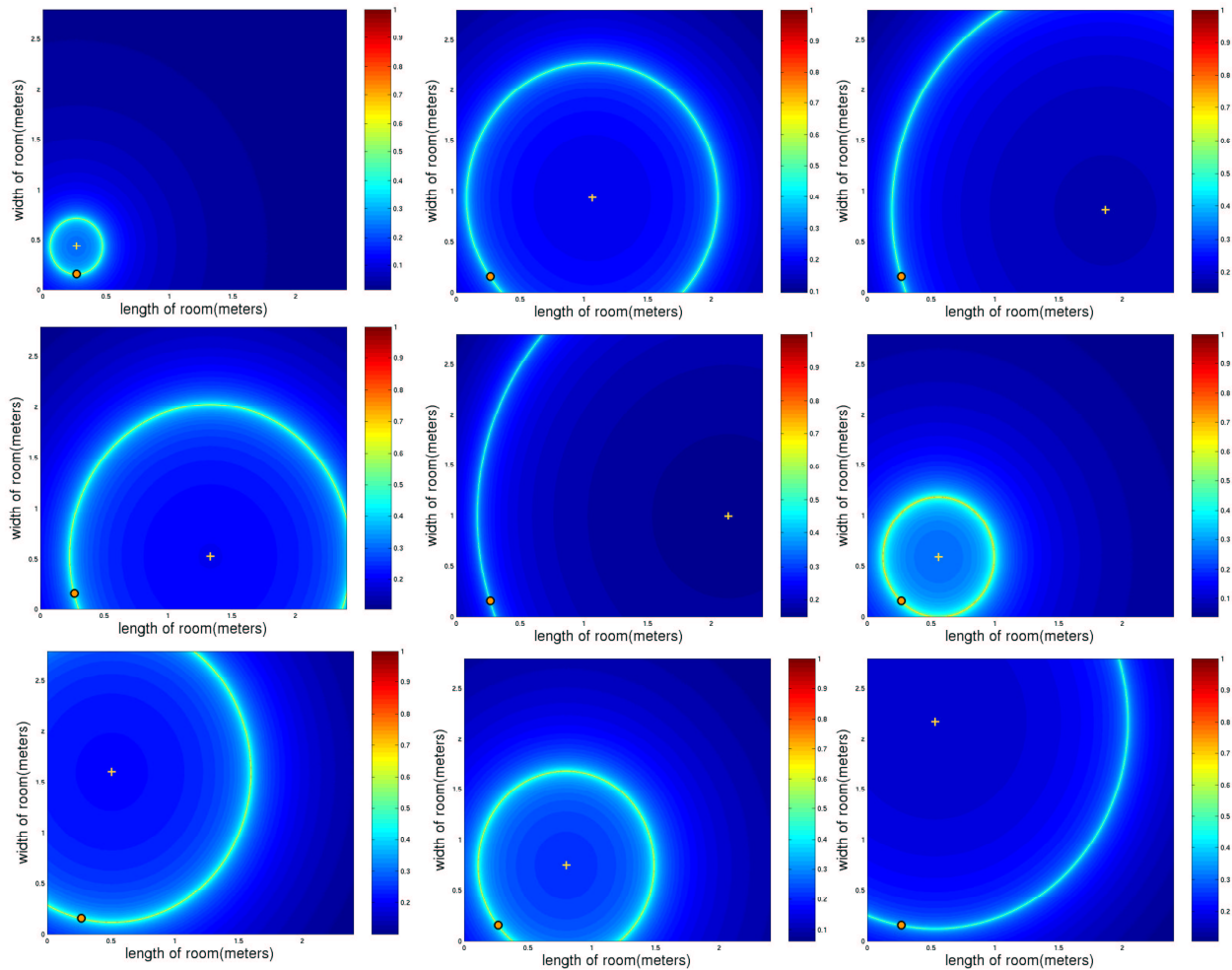
Figure 4.28: Results of analytical calculation in free space. Normalized acoustic field at the time of refocusing after time reversal. Results in free-space assume an initial Dirac delta pulse in time and space. Maximum occurs at the recording time T = 0.05 s. Each figure starting from top left and reading to the right represents the refocused energy when only (detector 1, detector 2, detector 3, ... , detector9) is present

detector to the original source, the magnitude of the circular refocusing goes as one over the square root of this distance. Thus, the more dominant circles will be the ones formed by detectors closer to the source. It is these close detectors that eventually form the dominant circle that appears in most of the figures explored up to now. If we remove some of the dominant detectors close to the source, by say, switching them off, we see that the main dominant circle disappears.

- Scatterers help improve spatial focusing by making side lobes disappear in both Dirichlet and Neumann cases.

- Multiple detectors are better at reducing the grass surrounding the refocused pulse than scatterers alone

- In rooms with absorption as $\kappa \to 1$, the simulation approaches free-space phenomena where only line-of-sight (LOS) arrival is important

- As $\kappa \to 0$ and absorption in the room diminishes, we obtain better refocusing results

4.5.9 Comparing results for different values of the absorption parameter κ

Most of the experiments discussed in previous sections were carried out with a maximum absorption coefficient $\kappa = 1$. As mentioned earlier, as $\kappa \to 0$ absorption in the room diminishes. Thus, we obtain better refocusing results. The following figures show the results of carrying out the time-reversal experiment in an absorbing room with a source and a single detector. The snapshots are taken at the refocusing time $T - t_0$ and go from moderately absorbing ($\kappa = 0.5$) to very low absorption ($\kappa = 0.5$) conditions. In the latter case, as expected, results resemble the ones obtained in a room with reflecting boundary conditions such as Dirichlet.

We have thus devised a computational model that is able to produce different amounts of absorption at the boundaries of a two-dimensional room. By controlling the parameter κ, we can control how absorptive the boundaries are. Thus, in principle we could model boundaries made up of different materials with different absorption coefficients and determine whether time-reversal would work in such enclosures or not. The main goal is to establish a communications link in an acoustic enclosure, so this model provides insight into the materials with which a room should be built in order to have time reversal work. Or, it may

suggest the addition of a random-scattering media in the path from source to detector so as to act as a converging "pseudo-lens" in enclosures where the absorption is so large that an extra lensing device is needed to redirect the energy toward the original source and produce better refocusing results.
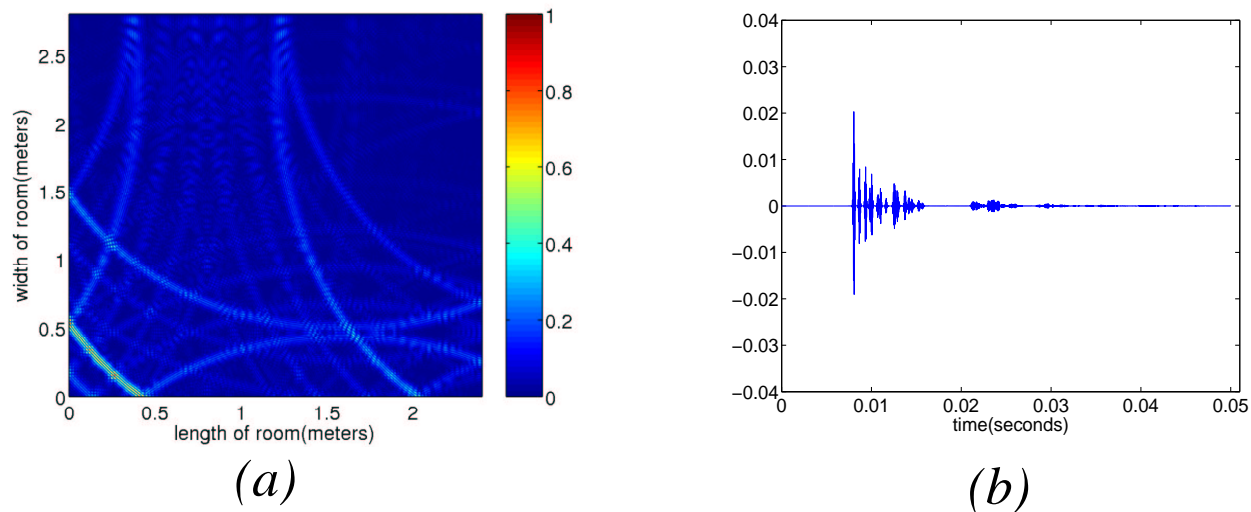
Figure 4.29: Normalized acoustic field after time-reversal in enclosure with absorbing boundaries and a single detector. Snapshot at time $T - t_0$. $\kappa = 0.5$
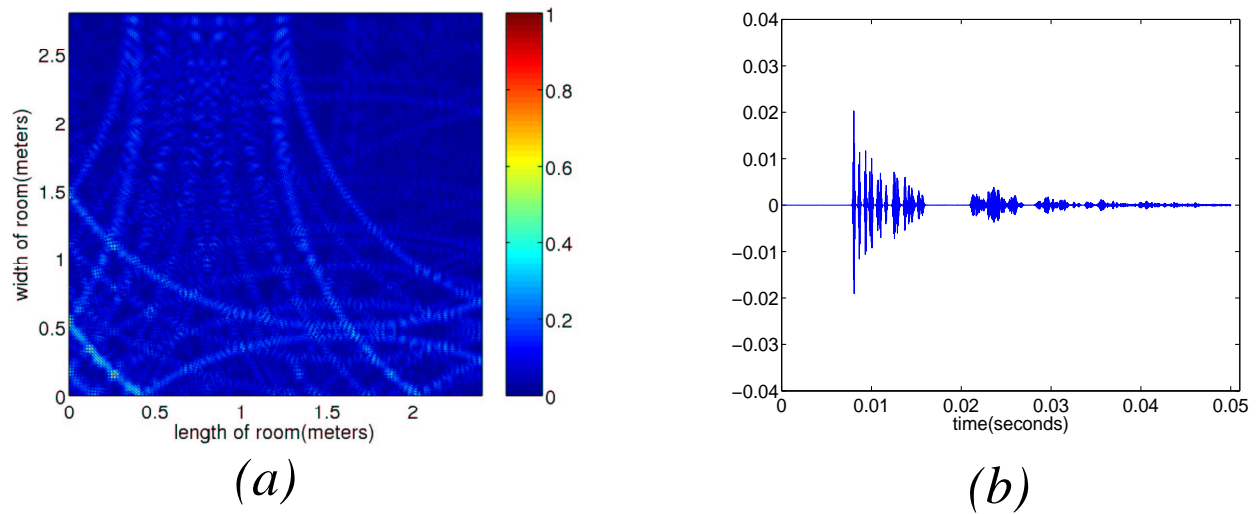
Figure 4.30: Normalized acoustic field after time-reversal in enclosure with absorbing boundaries and a single detector. Snapshot at time $T - t_0$. $\kappa = 0.3$
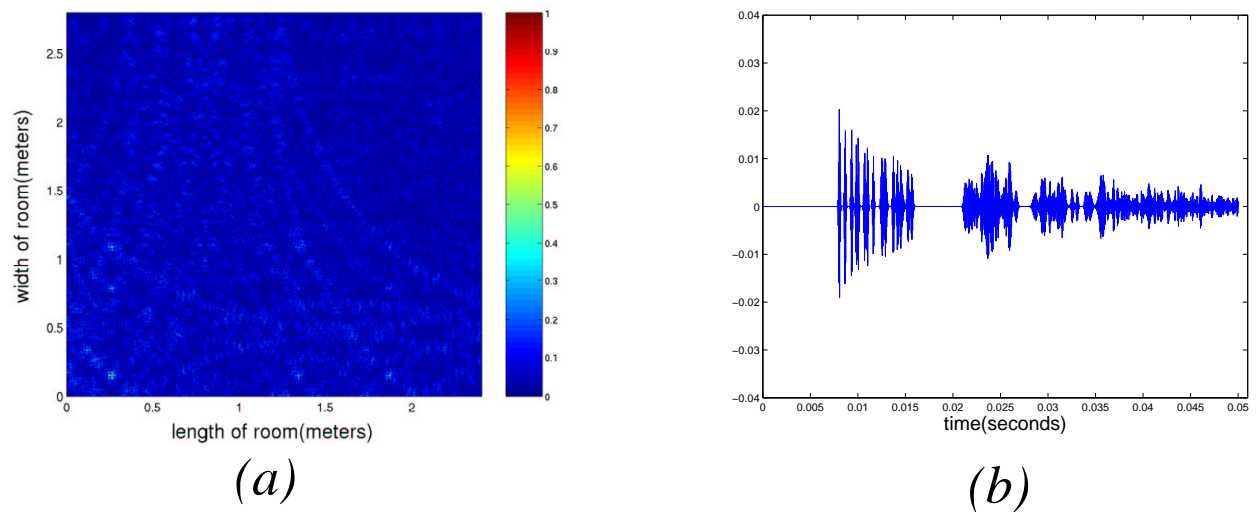
Figure 4.31: Normalized acoustic field after time-reversal in enclosure with absorbing boundaries and a single detector. Snapshot at time $T - t_0$. $\kappa = 0.1$

(a)

(b)
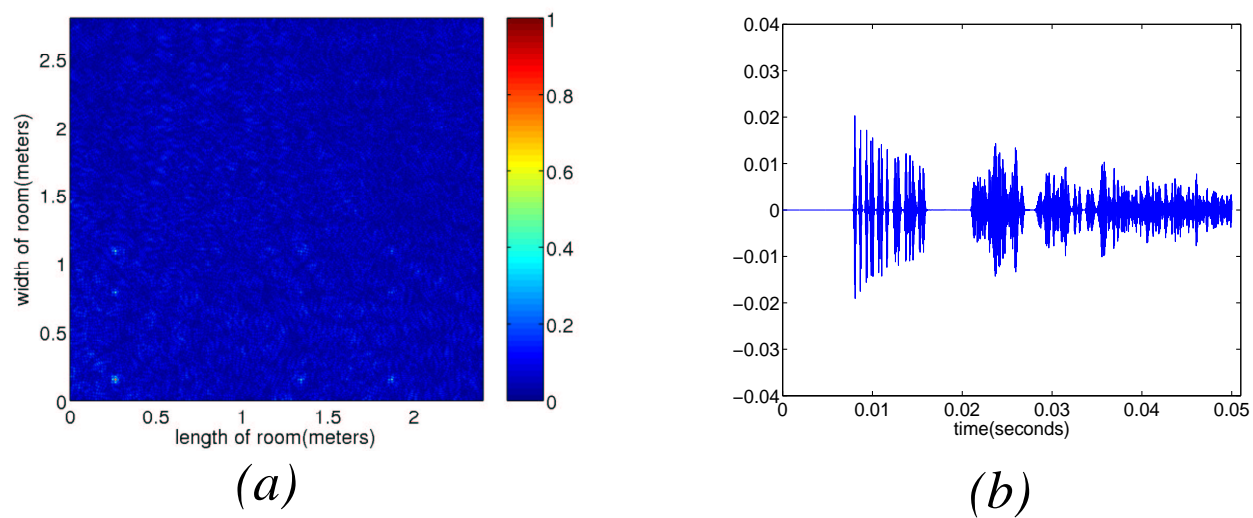
Figure 4.32: Normalized acoustic field after time-reversal in enclosure with absorbing boundaries and a single detector. Snapshot at time $T - t_0$. $\kappa = 0.05$

Chapter 5

Keyhole Experiments

5.1   Traditional Physics Definition of Keyhole versus New Definition for Wireless Communications

In a paper titled "Keyhole Effects in MIMO Wireless Channels - Measurements and Theory" [42], AF Molisch *et al* present the first measurement of an effect named "keyhole" or "pinhole" in Wireless Communications. In multiple-input multiple-output (MIMO) communication systems both the transmitter and receiver array consists on more than one antenna. This enables the system to have multiple channels for communications between transmitter and receiver antennas. [32]

The Bell-labs layered space-time (BLAST) communication technique, proposed by Foschini [[?] "BLAST is a wireless communications technique which uses multi-element antennas at both transmitter and receiver to permit transmission rates far in excess of those possible using conventional approaches." [1] This is because the richly-scattering environment between receivers and transmitters causes each signal to appear uncorrelated with the ones at other receive antennas. The reason why this happens is that signals from every transmitter have a very specific spatial signature at each receiver antenna. Thus, the receiver is able to adequately separate the signals sent by specific transmitter antennas. The scattering environment acts like a very large aperture lens that allows the resolution of individual transmitters. If the signals arriving at the receiver antennas are correlated, then the high-spectral efficiency is reduced. [44]

The capacity of a MIMO system in an ideal multipath channel "is approximately N times

---

[1] [43]

the capacity of a single antenna system, where N is the smaller of the number of transmit or receive antenna elements."[2] It turns out, however, that "correlated signals at the antenna elements lead to a decrease in the capacity." [42]

The ideal definition of "keyhole," presented in [33] and [44]. "It is related to scenarios where rich scattering around the transmitter and receiver leads to low correlation of the signals, while other propagation effects, like diffraction or waveguiding, lead to a rank reduction of the transfer function matrix."[3]

Thus, a keyhole effect occurs when the correlation between signals in antenna elements is low, but there is a reduction of diversity in the channels by some other physical effect that causes the capacity of the system as a whole to diminish significantly. There has been research for finding the keyhole effect due to tunnels, corridors or diffraction in indoor environments. But, because of noise and alternative propagation paths, AF Molisch *et al* conclude that "the keyhole effect due to real-world waveguides like tunnels or corridors will usually be very difficult to measure."[4]

In [44], Valenzuela *et al.* discuss a physical keyhole as a screen with small hole placed between two arrays of transmitter and receiver antennas surrounded by clutter. Because of the rich scattering caused by the clutter near the antennas the signals appear to be uncorrelated. However, since the keyhole is the only way that the radio waves can travel from the transmitter to the receiver antennas, the channel matrix has a single degree of freedom. A second example of a physical keyhole is a waveguide that opens to a room with scatterers like an office with furniture in it. The waveguide limits the number of modes that can travel through it from transmitter to receiver antenna. When the walls of the waveguide are lossy, the lowest order mode dominates at large distances from the source. Thus, "scattering in the waveguide regions surrounding both receiver and transmitter would not improve the richness of the channel."[5] While the signals may be uncorrelated, the capacity of the channel is reduced by the waveguide which limits the modes of wave propagation.

In outdoor wave propagation, a keyhole is due to diffraction of the main signal path by a roof edge near the remote antennas. Theory by Reinaldo Valenzuela *et al* in [44] affirms that the existence of a roof edge acts as an equivalent horizontal line source with varying current strength along its length. The experiment imagines a base antenna atop a building and a remote antenna surrounded by clutter at a large distance from the base antenna. (this

---

[2] [42]
[3] [42]
[4] [42]
[5] [44], p. 363

horizontal distance should be much larger than the vertical distance from base antenna to remote one in the ground). When the remote antennas transmit a signal, the remote field at the base antenna is perceived as diffracted due to the edge of a roof. When the base antennas constitute a vertical array, the channel matrix is a dyad, with only one degree of freedom. The resulting field measured at the base station looses its diversity in the vertical direction. It is said that the richness of the perceived channel is collapsed and a "keyhole" is formed. Thus, the only way to increase the capacity in this case, would be to separate the antennas horizontally, assuming low correlation between them is also ensured.

In [??], Paulraj *et al* confirm that "the realization of high MIMO capacity depends not only on the fading correlation between individual antennas but also on the rank behavior of the channel." [6] A similar sort of "pin-hole" effect is described, where again spatial correlation at the transmitter and receiver is very low, but the channel has low rank, and thus low capacity. "Such a channel is dubbed a 'pin-hole' because scattering (fading) energy travels through a very thin air pipe, preventing the rank to build up."[7] The rank behavior of the channel is considered to be dependent mostly by the range and the scattering radii. This situation occurs, comments Paulraj, "for very large distances between transmitter and receiver." [8] Comparing with a ray tracing-based channel simulation, the authors are able to test the impact of the rank on the capacity of the channel as well as the capacity (as rank) as a function of the scattering radii.

Inspired by Thomas Young's famous "double-slit experiment," [45] we set out to perform time-reversal experiments in an enclosure where we force sound to pass through a keyhole on the way from the source to the detector.

The original experiment by Young was done with light around the early 1800s. The experimental setup is shown in figure 5.1. Basically, a source of light passes initially through a keyhole which causes it to become a coherent source of light. After this keyhole, there is a screen with two slits in it. Light must pass through this screen on its way to a final detection plane where a specific interference fringes pattern is observed.

The existence of this fringe patterns was one of the first confirmations that light undergoes diffraction and that light has wavelike properties.

In the experiment, Young "brought into the sunbeam a slip of card, about one-thirtieth of an inch in breadth, and observed its shadow,.... , the shadow itself was divided by [similar] parallel fringes, [of smaller number], according to the distance at which the shadow was

---

[6]**??**, p. 1083
[7]**??**, p. 1086
[8]**??**, p. 1084

observed, but leaving the middle of the shadow always white" [9]
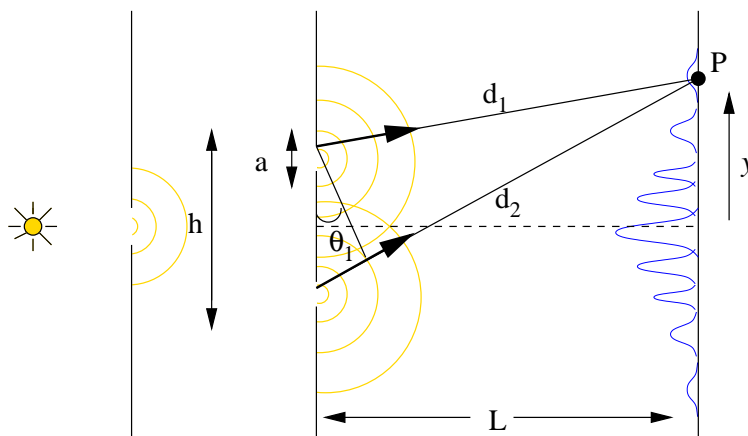
Figure 5.1: Original Double-Slit Experiment by Thomas Young. A source of light passes initially through a keyhole that turns into a coherent source of light. After the keyhole, there is a screen with two slits in it. Light must pass through this screen on its way to a final detection plane where a specific interference pattern is observed

It is the difference in phase between waves arriving at P after traveling distances d_1 and d_2 that produces the interference pattern. The phase difference is $k(d_2 - d_1)$, where $k = 2\pi/\lambda$. Bright fringes occur when this difference is $0, \pm 2\pi, \pm 4\pi, ... \pm 2n\pi$, where n is an integer. [47]. Bright fringes occur at this points, when y and h are both small compared to L.

The path difference between d_1 and d_2 is given by the extra bit of distance d_2 has to travel. It can be related to θ_1 by

$$\sin \theta = \frac{\text{path difference}}{h} = \frac{\lambda}{h}$$

Since for a bright fringe the path difference is equal to an integer of the wavelength. Also,

$$\tan \theta = \frac{y}{L}$$

where y measures the distance from the central bright fringe to the first bright fringe. Now, for small values of the angle θ

$$\lambda = \frac{y\,h}{L}$$

Based on Young's experiment, we set out to carry out an acoustic analog of Young's

---

[9] [46], p. 2

double slit experiment in an enclosure. We set out to do a time reversal experiment where we use a coherent source (we don't need the first keyhole as our source is already guaranteed coherent). We let this coherent source pass through a slit where the size of the slit is very small compared to the distance between the slit and the observational screen.

Our desire was to record the wave field incident on the observing screen over a time much longer than the original pulse, time-reverse it and send it back into the same medium. We expected the process of time-reversal to "remember" the wave pattern over time, and use this information to recover the pulse shape and refocus back at the source location.

Although no distinct interference pattern can be observed (due to the complexity of the multiple reflections interfering with each other at the observational screen), the time reversal experiment yielded successful refocusing results in both time and space.

5.2 Theory of Waves Traveling Through Keyholes

Having a wall with a keyhole in it reduces the number of paths that a signal can take on its way from source to detector. Specially, the line-of-sight (LOS) path is now restricted to fewer possibilities where the geometry allows direct passage of sound from source through keyhole to detector.

At the plane of the keyhole, diffraction of the acoustic field by the keyhole will split the incident wavefront into several sub-wavefronts that are transmitted through it. There are more emerging paths on one side of the keyhole as there are incident paths on the other side of it.

5.3 Results with Keyhole Aperture Greater than λ and Wall of Detectors

The experiment is carried out in an enclosure with Dirichlet boundary conditions, of size (2 , 1.5) m. A single source located at (0.11, 0.67) m. The keyhole measures either 13 cm (5λ) or 2 cm (0.75λ) for two different experiments. It is located at (44, 75) cm, close to the middle of the left wall. The detector is the entire length of the right hand side wall (1.5 m), and is located 2.2 cm away from it.

The experiment is carried out in an enclosure with Dirichlet boundary conditions, of size (2 , 1.5) m. A single source located at (0.11, 0.67) m. The keyhole measures either 13 cm

Figure 5.2: Experimental setup of the keyhole time-reversal experiment. The enclosure size is (2, 1.5) m. "a" is the aperture of the keyhole. In our experiments $a = 0.75\lambda$ and $a = 5\lambda$. Note that source and detector have the same y-position, while the keyhole seats slightly above that. Some experiments are carried out with the entire right hand wall as detector, and others with a single detector located at (1.97, 0.67) m as shown in the figure

(5λ) or 2 cm (0.75λ) for two different experiments. It is located at (44, 75) cm, close to the middle of the left wall. The detector is the entire length of the right hand side wall (1.5 m), and is located 2.2 cm away from it.

We experimented when the size of the keyhole is of the order or less than λ, and in both cases we obtain very good refocusing. In addition to this, there appears to be a bright side lobe above the refocusing point. Results with keyhole measuring 13 cm (5λ) are shown in figure (5.3).

Amplification of the recompressed pulse is expected due to the large number of detectors (900) in the array at the right hand side wall. We have previously seen how multiple detectors increase the SNR in the enclosure and decrease side lobes.
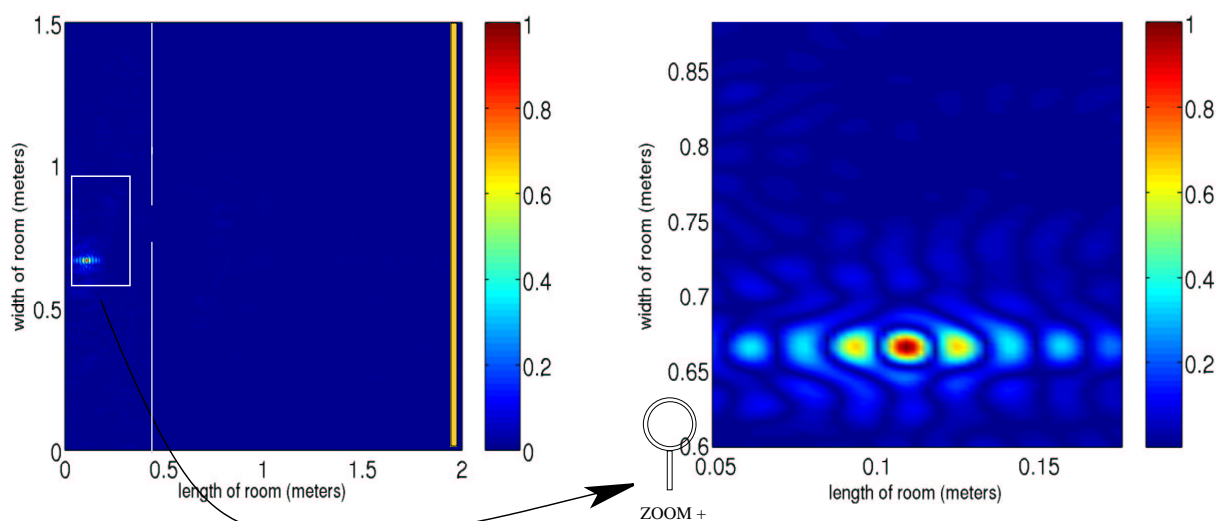
Figure 5.3: Keyhole size: 13 cm (5λ). There is refocusing back at the source location and no side lobes. The reason for such good refocusing is the large number of detectors in the array (900) at the right hand side wall. This also increases the SNR in the enclosure. The keyhole is large enough to let enough sound go through without diffraction effects.

Also, after the time-reversal process, there is time compression of the time-reversed pulse back at the source. This recompressed signal preserves the null crossings of the original pulse in time. The results are shown in figure (5.8) and are essential for the application of time-reversal to communications in enclosures with entrances, windows, doors, etc... on the order of the signal's central wavelength. Results with keyhole measuring 2 cm (0.75λ) are shown in figure (5.7)

(a)

(b)

Figure 5.4: Temporal compression of signal after time-reversal. Normalized with respect to magnitude of initial pulse. Time-reversal experiment carried out in a perfectly-reflecting enclosure with Dirichlet boundary conditions. The enclosure size is (2, 1.5) m. A single source located at (0.11, 0.67) m. They keyhole measures 13 cm (5λ) and is located at (44, 75) cm. The detector is the entire length of the right hand side wall (1.5 m), and is located 2.2 cm away from it. (a) Recompressed signal received at original source at the refocusing time $t = T - t_0$ (b) Initial pulse (red) vs. recompressed signal (blue). We observe a six-fold amplification of the recompressed pulse

5.4 Results with Keyhole Aperture Greater than λ and *a Single* Detector

The experiment is carried out in an enclosure with Dirichlet boundary conditions, of size (2 , 1.5) m. A single source located at (0.11, 0.67) m. The keyhole measures either 13 cm (5λ) or 2 cm (0.75λ) for two different experiments. It is located at (44, 75) cm, close to the middle of the left wall. The detector is located at (1.9, 0.67) m, close to the right hand side wall (2.2 cm away from it). Note that the source and detector have the same y-position of 0.67 m, whereas the keyhole is located slightly above this line at 0.75 m. This accounts for the asymmetry of the results.
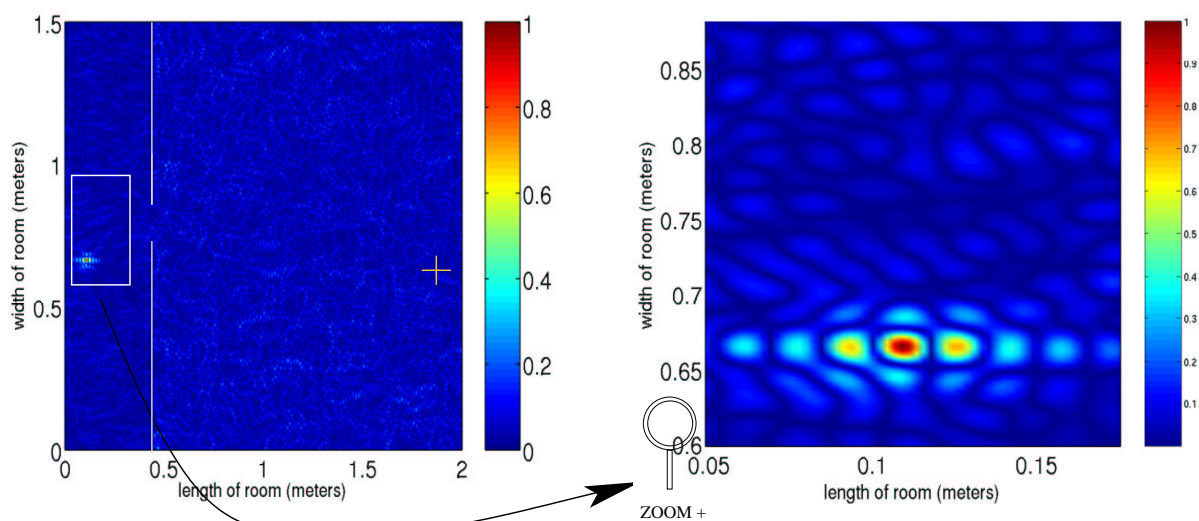
Figure 5.5: Keyhole size: 5λ. There is refocusing back at the source location and no side lobe exists. The keyhole is situated slightly above the middle half horizontal line connecting source and detector

Also, for on the order of λ size keyhole and a single detector, there is temporal compression of the time-reversed signal after time-reversal. The recompressed signal preserves the null crossings of the original pulse in time. The results are shown in figure (5.8) and are essential for the application of time-reversal to *single channel* communications in enclosures with small keyholes, smaller than the signal's central wavelength.

Figure 5.6: Temporal compression of signal after time-reversal. Normalized with respect to magnitude of initial pulse. Time-reversal experiment carried out in a perfectly-reflecting enclosure with Dirichlet boundary conditions. The enclosure size is (2, 1.5) m. A single source located at (0.11, 0.67) m. They keyhole measures 13 cm (5λ) and is located at (44, 75) cm. The detector is at position (1.97, 0.67) m. Note that source and detector have the same y-position, whereas the keyhole is slightly above that. (a) Recompressed signal received at original source at the refocusing time $t = T - t_0$ (b) Initial pulse (red) vs. recompressed signal (blue) (amplified by 100)

5.5 The Role of Diffraction in Time Reversal: Results with Keyhole Aperture Smaller than λ and Wall of Detectors

5.5.1 Asymmetric Relative Vertical Position of Source and Keyhole
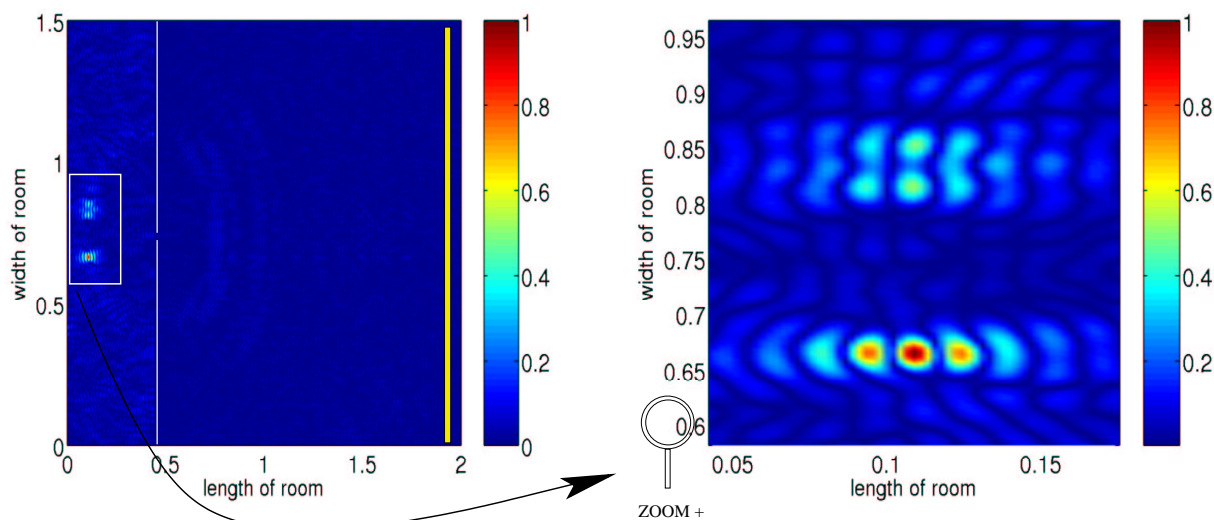
Figure 5.7: Keyhole size: 0.75λ. There is refocusing back at the source location and a side lobe above it. The keyhole is smaller than the central wavelength, thus the side lobe arises from diffraction effects with the edges of the keyhole. Note that the keyhole is situated slightly above the middle half line, above the source and detector height. The side lobe is of magnitude 35% the magnitude of the main peak

One of the effects arising from diffraction of the keyhole is that the keyhole acts as an additional source. Time-reversal still produces space-time refocusing, however, there are new effects such as image sources that arise from having a keyhole smaller than the central wavelength in the system. In figure (5.7) we observe spatial refocusing of the signal at the original source location. Moreover, we also observe a "ghost point" or image source right above the source location. This secondary peak has a magnitude of 40% the one of the main peak. This effect is due to the presence of a keyhole of size smaller than the central wavelength. Both source and secondary image source appear to be equidistant from the keyhole.

An additional complexity in the spatial distribution of source and keyhole is the asymmetry. Not only is it harder for the acoustic field to travel through a keyhole smaller than the central wavelength, but it also must travel slightly downward from the keyhole's y-position in order to reach the source .

In figure (5.7), note that there appears to be a spherical wavefront propagating to the left of the wall with the keyhole as if the keyhole were itself another source. Also, there are two pairs of spherical wavefronts propagating to the right of the wall with the keyhole. Again, they look as if though their source is the keyhole itself.

Also, for a less than λ size keyhole, there is temporal compression of the time-reversed signal after time-reversal. And, this recompressed signal preserves the null crossings of the original pulse in time. The results are shown in figure (5.8) and are essential for the application of time-reversal to communications in enclosures with small keyholes, smaller than the signal's central wavelength.

5.5.2   Symmetric Relative Vertical Position of Source and Keyhole

The following numerical experiment is carried out in a similar enclosure of size (2, 1.5) m, except this time the source and keyhole are located symmetrically on the same vertical position in the enclosure. A single source located at (0.11, 0.76) m sends an initial pulse that propagates in the enclosure with a keyhole. They keyhole measures 2 cm (0.75λ) and is located at (44, 76) cm. During a time of 50 ms, the entire right hand side wall serves as a detector by receiving the signal arriving at it from the multiple scattering. Specifically, 2 cm to the left of the wall, there is a 900-detector array that spans the entire width of the room (1.5 m). After recording it, it time-reverses the signal and sends it back into the same medium. The signal propagates back through the same keyhole and finally refocuses in space and time back at the original source location.

Figure(5.9) displays a focus point at the source location (0.11, 0.67) m, and a "jet stream" of secondary image sources to the right of the keyhole. Each one of the secondary image sources lies on the same y-position along a line midway in the enclosure. Coincident with the source and keyhole, this line contains images of secondary sources all the way from the keyhole to the end of the detector wall. Counting from the left, the second image source has the highest magnitude of all. Its peak is even higher than the refocused signal at the source location.

We can observe that when the size of the keyhole is less than the central wavelength,

(a)

(b)

Figure 5.8: Temporal compression of signal after time-reversal. Normalized with respect to magnitude of initial pulse. Time-reversal experiment carried out in a perfectly-reflecting enclosure with Dirichlet boundary conditions. The enclosure size is (2, 1.5) m. A single source located 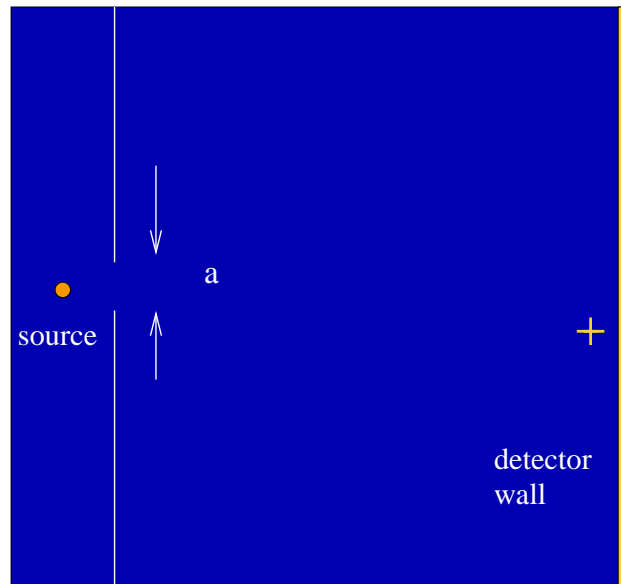at (0.11, 0.67) m. They keyhole measures 2 cm (0.75λ) and is located at (44, 75) cm. The detector is the entire length of the right hand side wall (1.5 m), and is located 2.2 cm away from it. (a) Recompressed signal received at original source at the refocusing time $t = T - t_0$. Normalized to its maximum magnitude. (b) Initial pulse (red) vs. recompressed signal (blue)
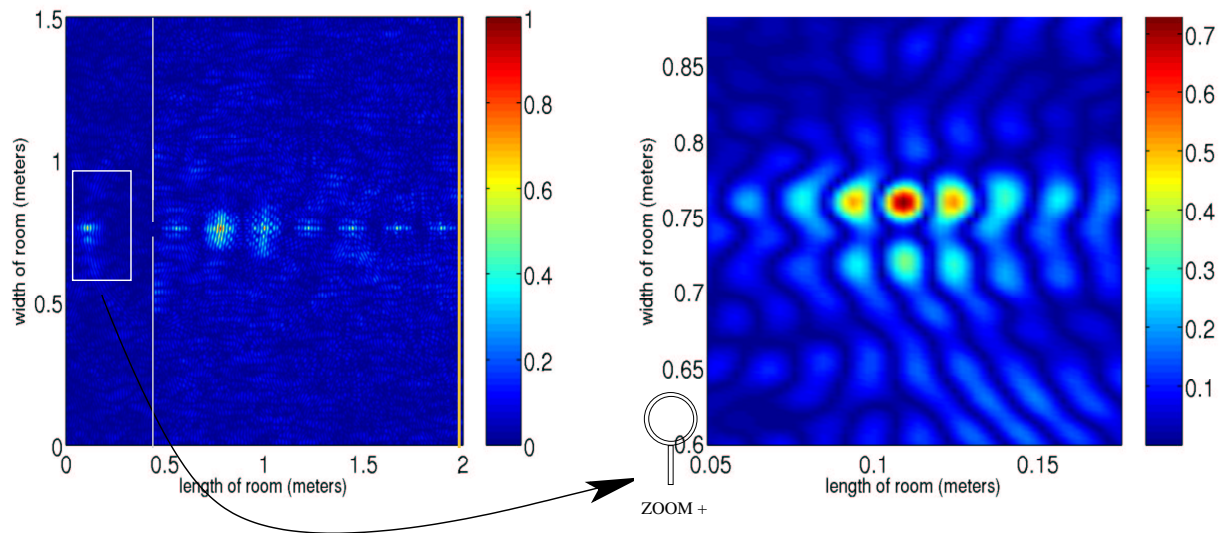
Figure 5.9: Keyhole size: 0.75λ. There is refocusing back at the source location and a "jet" of ghost points. The keyhole is smaller than the central wavelength, thus the ghost points arise from diffraction effects with the edges of the keyhole. The main ghost point in the jet is of magnitude 80% the magnitude of the main peak

there is not enough time for all the acoustic energy in the enclosure to go through the keyhole back into the source location. A large amount of acoustic energy stays trapped in the right hand side of the enclosure, unable to reach the source by the refocusing time $t = T - t_0$.

Having the entire wall of detectors does significantly amplify the recovered signal. Even though we observe a tight refocusing of the signal at the source, its magnitude is greatly reduced from the observed six-fold amplification of figure (5.4). That amplification was observed in a similar numerical experiment but a keyhole size of 5λ. In the latter case where the keyhole is only 0.75λ, the magnitude of the refocused pulse is only half the size the original.

We will later see in figure (5.13), that in a numerical experiment with a keyhole smaller than the central wavelength and a single detector, the recovered signal must be amplified 500 times before its magnitude is comparable to the one of the initial pulse.

For a less than λ size keyhole, there is temporal compression of the time-reversed signal after time-reversal. And, this recompressed signal preserves the null crossings of the original pulse in time. The results are shown in figure (5.10) and are essential for the application of time-reversal to communications in enclosures with small keyholes, smaller than the signal's central wavelength.
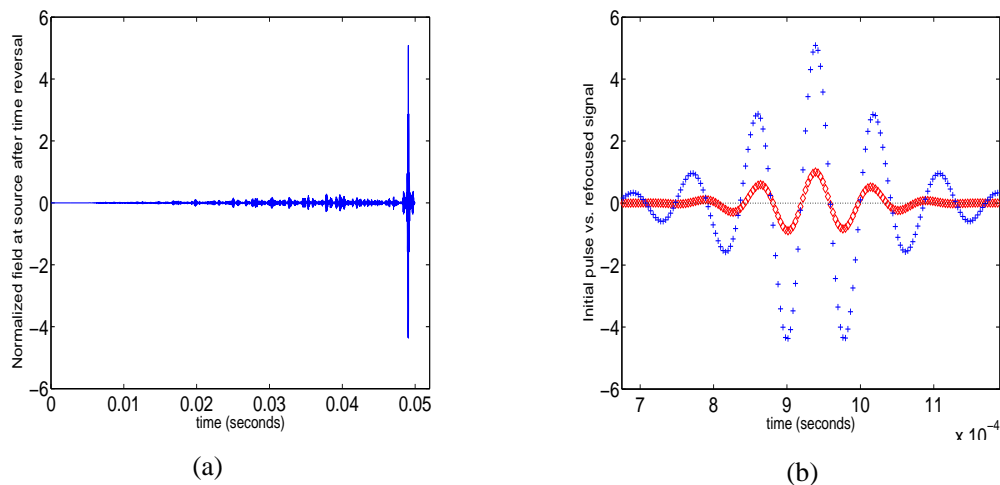
(a)   (b)

Figure 5.10: Temporal compression of signal after time-reversal. Normalized with respect to magnitude of initial pulse. Time-reversal experiment carried out in a perfectly-reflecting enclosure with Dirichlet boundary conditions. The enclosure size is (2, 1.5) m. A single source located at (0.11, 0.76) m. They keyhole measures 2 cm (0.75λ) and is located at (44, 76) cm. The detector is the entire length of the right hand side wall (1.5 m), and is located 2.2 cm away from it. (a) Recompresse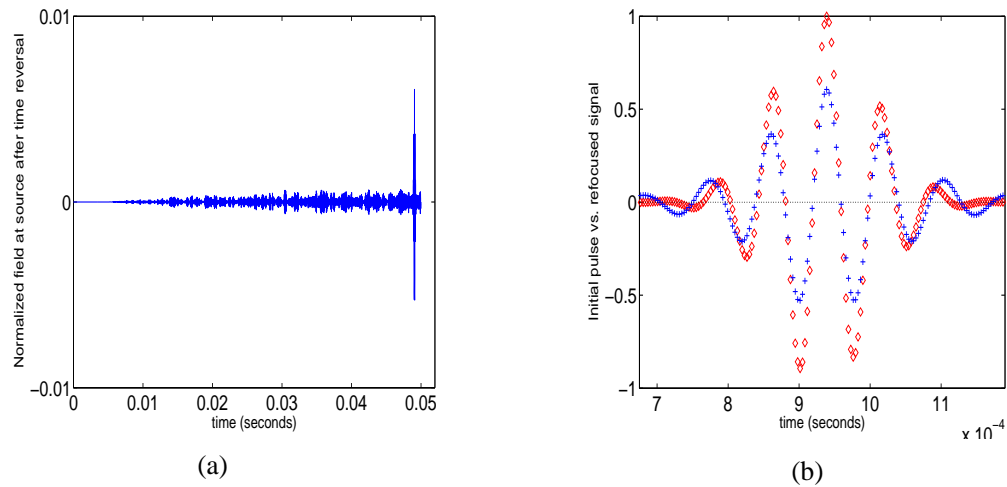d signal received at original source at the refocusing time $t = T - t_0$ (b) Initial pulse (red) vs. recompressed signal (blue)

In figure (5.10), note the magnitude of the recompressed pulse is slightly higher than half the original signal (60%) when source is off-axis with keyhole as in figure (5.8). This is because the access back to the source is easier when the keyhole is located at the same vertical level as the source in the enclosure.

5.5.3 Symmetric Vertical Relative Position of Source and Keyhole and Increased Horizontal Distance

Finally, we carry out the following time-reversal experiment in a similar enclosure of size is (2, 1.5) m. However, this time the wall that contains the keyhole is located twice as far from the source as in previous numerical experiment shown in figure 5.9.A single source located at (0.11, 0.76) m sends out an initial pulse that propagates in the enclosure. We investigate the role of the distance from source to keyhole in the observed secondary image sources to the right hand side of the keyhole.

They keyhole measures 2 cm (0.75λ) and is located at (89, 76) cm. The detector is the entire length of the right hand side wall (1.5 m), and is located 2.2 cm to the left of it.

For a less than λ size keyhole and a single detector, all three lying in the same horizontal
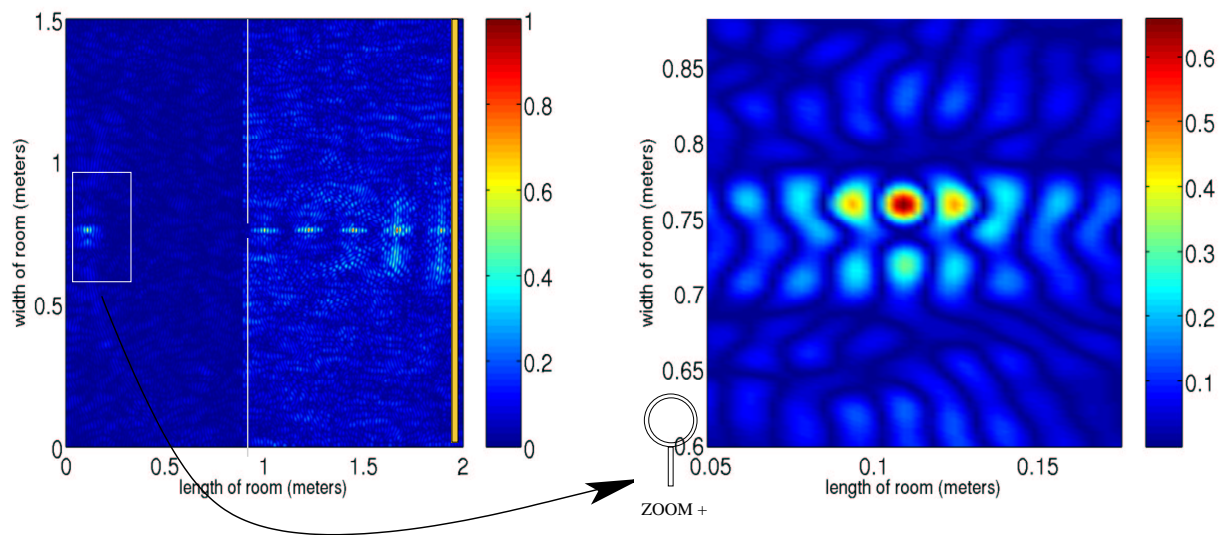
Figure 5.11: Time-reversal experiment carried out in a perfectly-reflecting enclosure with Dirichlet boundary conditions. Snapshot of acoustic field at the refocusing time $t = T - t_0$. The enclosure size is $(2, 1.5)$ m. A single source located at $(0.11, 0.76)$ m. They keyhole measures 2 cm (0.75λ) and is located at $(89, 76)$ cm. The detector is the entire length of the right hand side wall $(1.5$ m$)$, and is located 2.2 cm to the left of it. There is refocusing back at the source location plus a "jet stream" of image sources to the right side of the wall with the keyhole. Also, there is a spherical wave front passing through the source as if the keyhole was a source

line across the enclosure we obtain similar temporal compression results as the ones in figure (5.10). This is because the magnitude of the recompressed signal depends mostly on the number of detectors (in both cases 900) present in the time-reversal experiment. The only difference between the two numerical experiments is that in this case, the wall with the keyhole is moved further to the right. We observe temporal compression of the time-reversed signal after time-reversal. The recompressed signal preserves the null crossings of the original pulse in time. The results are shown in figure (5.12) and are essential for the application of time-reversal to communications in enclosures with small keyholes, when they are smaller than the signal's central wavelength.

(a) (b)

Figure 5.12: Temporal compression of signal after time-reversal. Normalized with respect to magnitude of initial pulse. Time-reversal experiment carried out in a perfectly-reflecting enclosure with Dirichlet boundary conditions. The enclosure size is (2, 1.5) m. A single source located at (0.11, 0.76) m. They keyhole measures 2 cm (0.75λ) and is located at (89, 76) cm. The detector is the entire length of the right hand side wall (1.5 m), and is located 2.2 cm to the left of it. (a) Recompressed signal received at original source at refocusing time $t = T - t_0$ (b) Initial pulse (red) vs. recompressed signal (blue)

5.6   Results with Keyhole Aperture Smaller than λ and a *Single* Detector

5.6.1   Asymmetric Vertical Relative Position of Source and Keyhole

A single detector is less able to collect sufficient energy for space-time refocusing in a time-reversal process. Thus, although we observe a tight spatial focusing of the signal at the original source location in figure (5.13), we also observe how the SNR in the right hand side of the enclosure is of magnitude 40%. This means that a large anmoount of the acoustic energy stays trapped in the forward phase of the time-reversal process when it reaches the right hand side of the keyhole. On the backward phase of the process, there is no sufficient time for some of this energy to travel back through the small keyhole and refocus back at the source. This causes that the amplitude of the recompressed pulse (as shown in figure 5.14) must be amplified 500 times before it reaches a size comparable to the initial pulse.
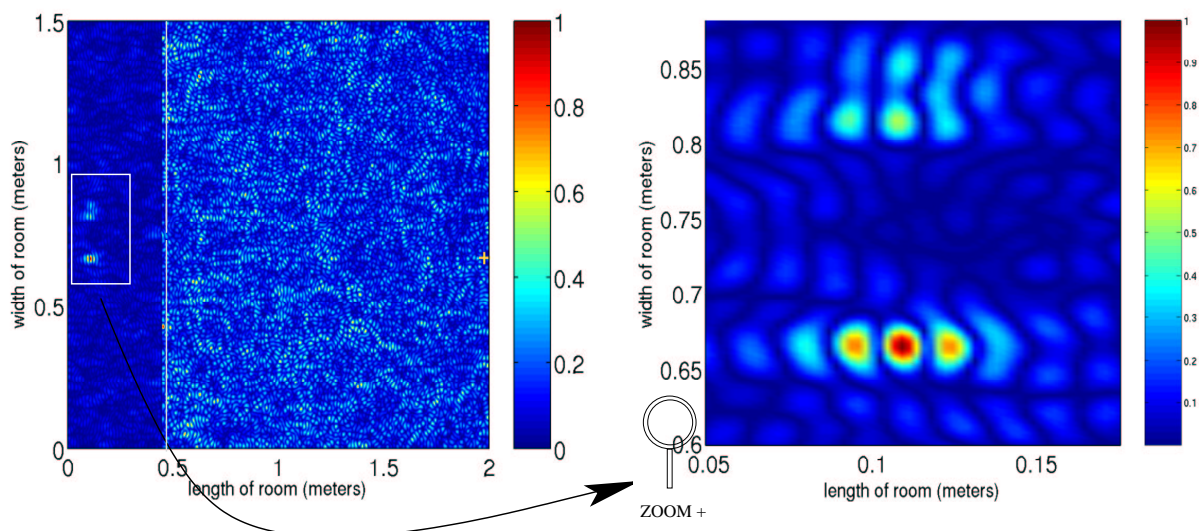
Figure 5.13: Keyhole size: 0.75λ. There is refocusing back at the source location and a side lobe above it due to the fact that the keyhole is situated slightly above the middle half line connecting source and detector. Right at the height of the keyhole, above the source, there is a side lobe of 35% the magnitude of the main peak

For a less than λ size keyhole and a single detector, there is temporal compression of the time-reversed signal after time-reversal. The recompressed signal preserves the null

crossings of the original pulse in time. The results, shown in figure (5.14), are essential for the application of time-reversal to *single channel* communications in enclosures with small keyholes, smaller than the signal's central wavelength.
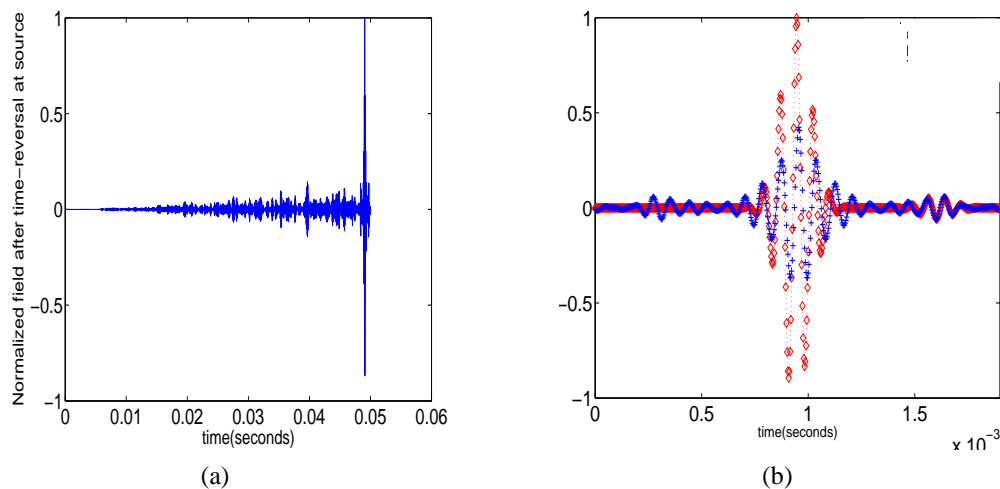

(a)   (b)
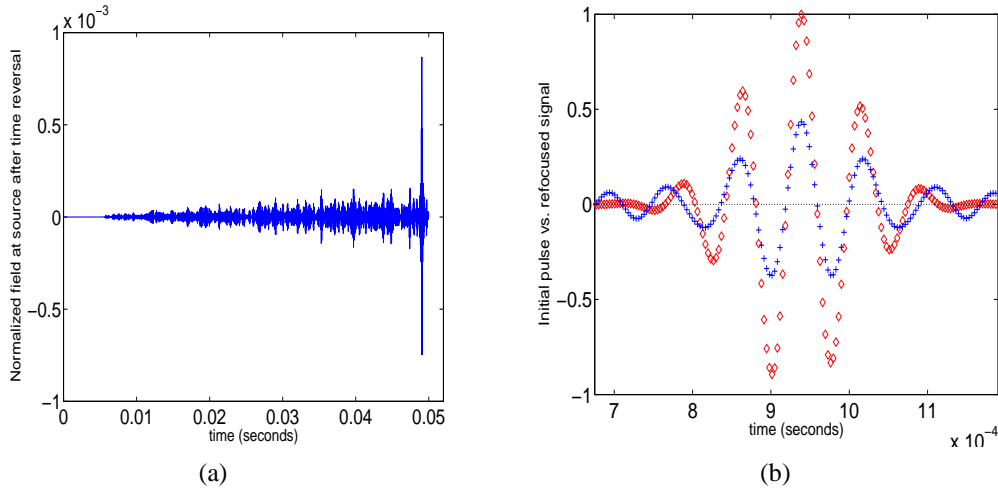
Figure 5.14: Temporal compression of signal after time-reversal. Normalized with respect to magnitude of initial pulse. Time-reversal experiment carried out in a perfectly-reflecting enclosure with Dirichlet boundary conditions. The enclosure size is (2, 1.5) m. A single source located at (0.11, 0.67) m. They keyhole measures 2 cm (0.75λ) and is located at (44, 75) cm. The detector is at position (1.97, 0.67) m. Note that source and detector have the same y-position, whereas the keyhole is slightly above that. (a) Recompressed signal received at original source at the refocusing time $t = T - t_0$ (b) Initial pulse (red) vs. recompressed signal (blue) (amplified by 500)

## 5.6.2   Symmetric Vertical Relative Position of Source and Keyhole

Playing with the symmetry of the system, we explore the causes for the secondary image sources appearing in figures 5.13, 5.9 and 5.7.

In contrast to figure 5.13 where the source (and detector) was in a different vertical position than the keyhole, figure 5.15 displays the results of a similar numerical experiment when source, detector and keyhole lie all in the same vertical position in the enclosure. In comparison, the latter figure shows that the acoustic field at the time of recompression $t = T - t_0$ is more likely to pass through the keyhole on its way to the source as in the latter case. The SNR of the symmetric case (5.15) is higher than the one in the asymmetric case (5.13).

The keyhole size is less than λ; and the source and a single detector, all three lie in the
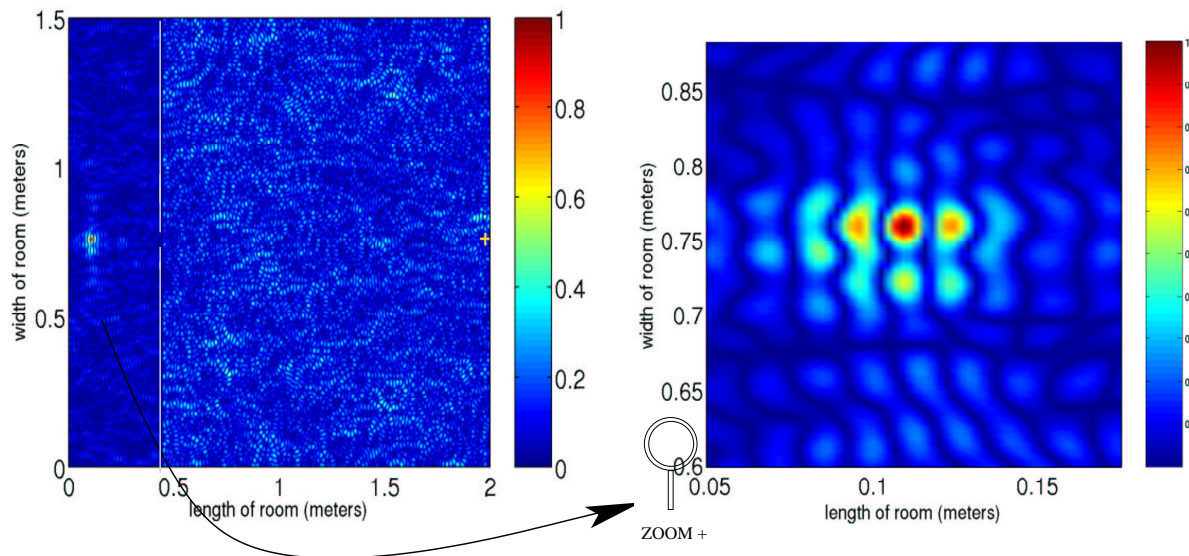
Figure 5.15: Keyhole size: 0.75λ. There is refocusing back at the source location and no side lobe exists. The source, keyhole and detector all have the same y-position. The boundary conditions are perfectly reflecting Dirichlet. Snapshot of acoustic field after time-reversal, refocusing time $t = T - t_0$

same horizontal line across the enclosure. There is temporal compression of the time-reversed signal after time-reversal. Just as in the asymmetric case of figure 5.14, the recompressed signal must be amplified 500 times to be comparable in magnitude to the initial pulse. Nevertheless, the recompressed signal preserves the null crossings of the original pulse in time. The results are shown in figure (5.16) and are essential for the application of time-reversal to *single channel* communications in enclosures with small keyholes, smaller than the signal's central wavelength.

5.6.3   Increased Vertical Relative Position of Source and Keyhole

We continue with the exploration of the cause for the observed secondary image sources produced in numerical experiments of the time-reversal process in enclosures with keyholes in them. We now explore the location dependence of the main secondary image source above the real source observed in figure 5.13. We carry out the following numerical experiment with a keyhole of size 0.75λ. Figure 5.17 shows there is refocusing back at the source location and the side lobe has changed position from the one in figure 5.13. This is because the source in this experiment has been moved to a new location in the lower left hand corner at (11, 33) cm. The keyhole remains at (44, 76) cm and the detector at (1.97, 0.67) m. The boundary
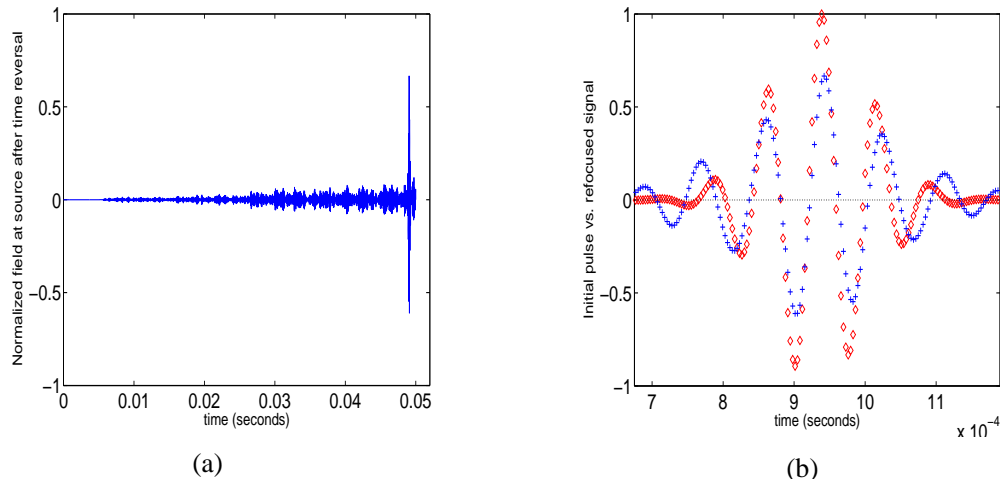
(a)

(b)
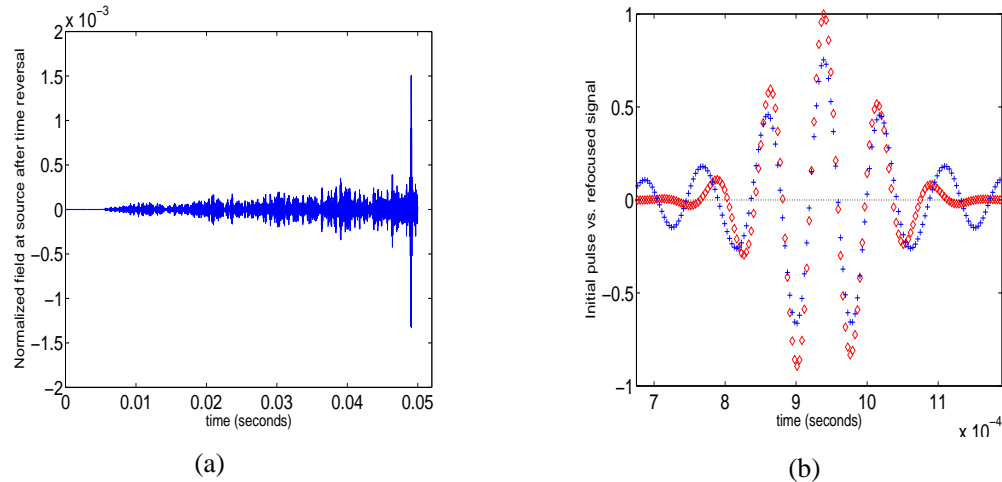
Figure 5.16: Temporal compression of signal after time-reversal. Normalized with respect to magnitude of initial pulse. Time-reversal experiment carried out in a perfectly-reflecting enclosure with Dirichlet boundary conditions. The enclosure size is (2, 1.5) m. A single source located at (0.11, 0.76) m. They keyhole measures 2 cm (0.75λ) and is located at (44, 76) cm. The detector is at position (1.97, 0.76) m. Note that source, keyhole and detector have the same y-position. (a) Recompressed signal received at original source at refocusing time $t = T - t_0$ (b) Initial pulse (red) vs. recompressed signal (blue) (amplified by 500)

conditions are perfectly reflecting Dirichlet. We take a snapshot of the acoustic field after time-reversal, at the refocusing time $t = T - t_0$. We observe a dimmer secondary image source above the real source. Note that the keyhole is equidistant to both real source and secondary image source.
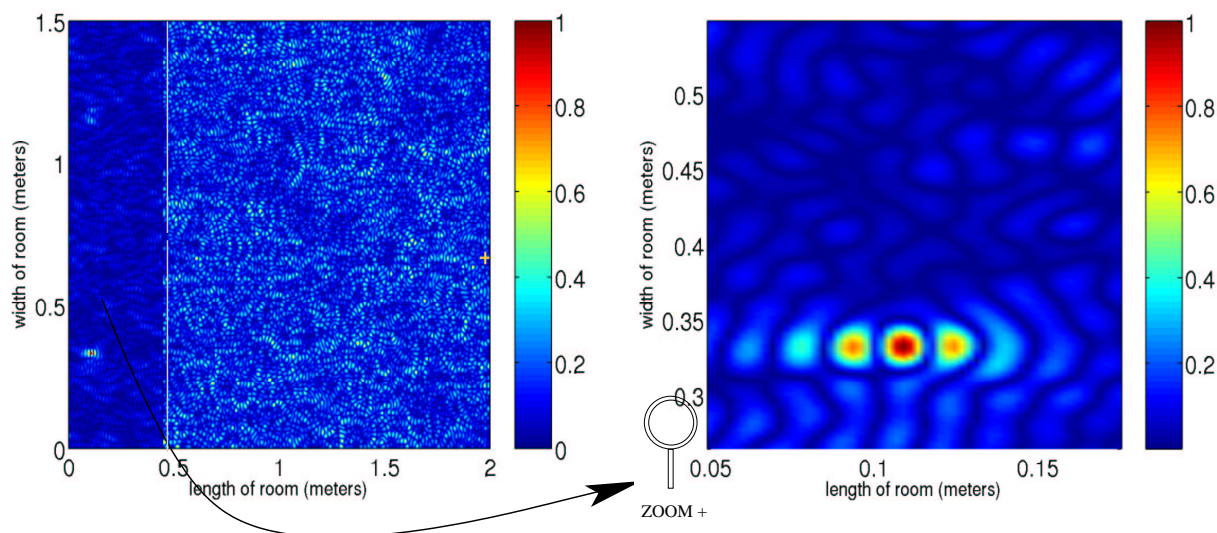
Figure 5.17: Keyhole size: 0.75λ. There is refocusing back at the source location and one side lobe above the real source. This is because the source is moved to a new location in the lower left hand corner at $(11, 33)$ cm. The keyhole is at $(44, 76)$ cm and detector $(1.97, 0.67)$ m. The boundary conditions are perfectly reflecting Dirichlet. Snapshot of acoustic field after time-reversal, refocusing time $t = T - t_0$
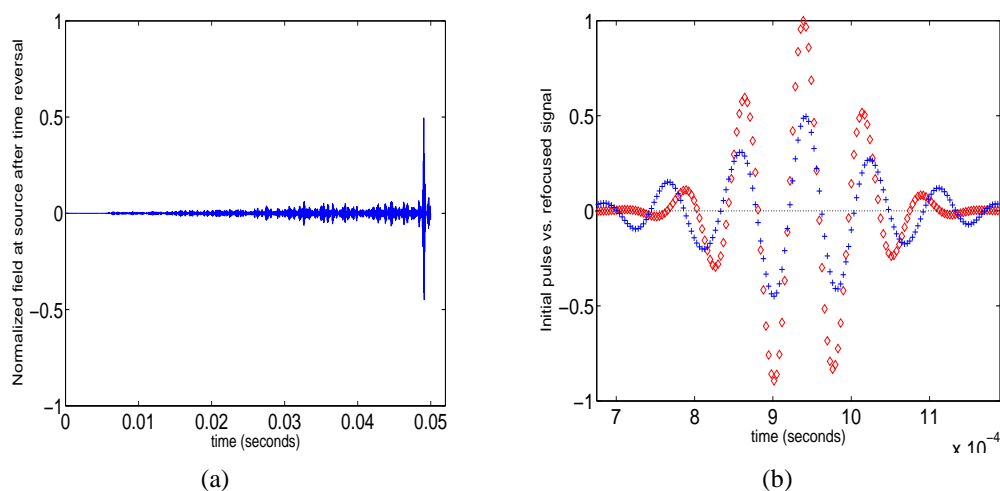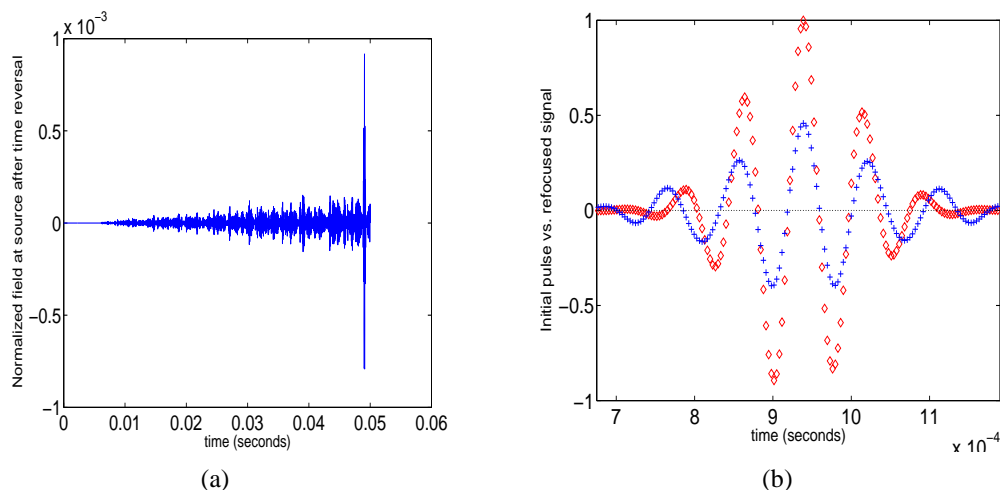

Figure 5.18: Temporal compression of signal after time-reversal. Normalized with respect to magnitude of initial pulse. Time-reversal experiment carried out in a perfectly-reflecting enclosure with Dirichlet boundary conditions. The enclosure size is $(2, 1.5)$ m. A single source located at $(0.11, 0.33)$ m. They keyhole measures 2 cm (0.75λ) and is located at $(44, 76)$ cm. The detector is at position $(1.97, 0.76)$ m. Note that source, keyhole and detector have the same y-position. (a) Recompressed signal received at original source at refocusing time $t = T - t_0$ (b) Initial pulse (red) vs. recompressed signal (blue) (amplified by 500)

5.7   Acoustic Time-Reversal Through Corridors

We have seen time-reversal work when sound passes through keyholes of size on the order and smaller than λ. We now place a "knife-blade" corridor coming out from the keyhole aperture. If we had absorption at the walls and the boundaries of the waveguide are perfectly-reflecting, we would expect the waveguide to extend the detected signal's duration before it decays to zero. However, in the present case we start with no absorption at the boundaries. We carry out the following experiments with Dirichlet boundary conditions.

The waveguide is located in the center of the enclosure as shown in figure (5.19). It is 13 cm wide (5λ) and 1.24 m long (47λ). The source is located at (0.11, 0.67) m close to the left hand wall, and the detector array is as long as the entire right hand side wall, and it seats 2.2 cm away from it. Other experiments are carried out with a single detector located at (1.97, 0.67) m as shown. We investigate the effect of corridors inside enclosures on the spatial quality of the time-reversal focus. Specifically, we observe if corridors make the side lobes obtained with a keyhole disappear.
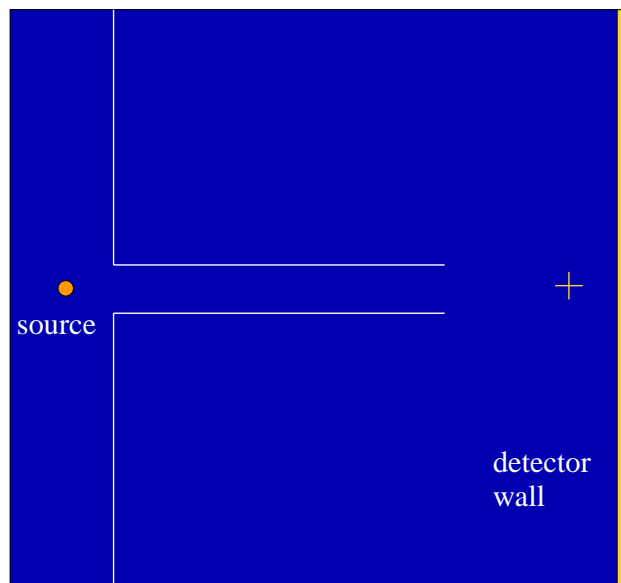
Figure 5.19: Experimental setup of the keyhole-corridor time-reversal experiment. The waveguide is 13 cm wide (5λ) and 1.24 m long (47λ). The source is located at (0.11, 0.67) m close to the left hand wall, and the detector array is as long as the entire right hand side wall, and it seats 2.2 cm away from it. Other experiments with a single detector located at (1.97, 0.67) m as shown in the figure

Figure 5.20 displays a tight refocused spot at the source location. There are no side lobes
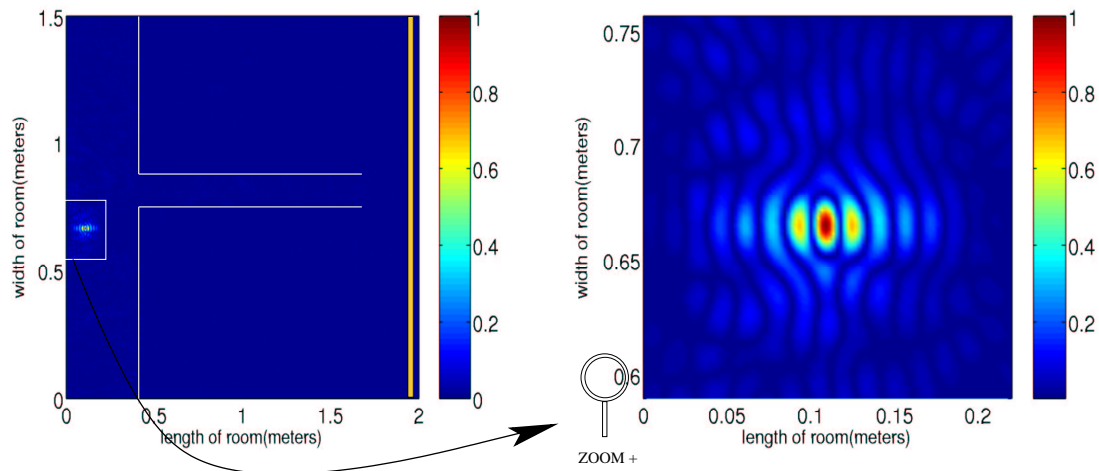
Figure 5.20: Normalized acoustic field in enclosure after time-reversal. Snapshot at time $t = T - t_0$. The quality of spatial focusing is remarkably good. Not only is the spot compacted to an area of $\lambda/2$, but the overall signal to noise ration (SNR) in the enclosure is almost zero. This is due to the many detectors (900) recording at the right hand side wall

as most of the energy is concentrated at the source location. To have a more accentuated picture of the main peak refocusing versus the SNR in the enclosure, in figure (5.21), we plot a three-dimensional map of the normalized acoustic field in the enclosure at the refocusing time $t = T - t_0$.
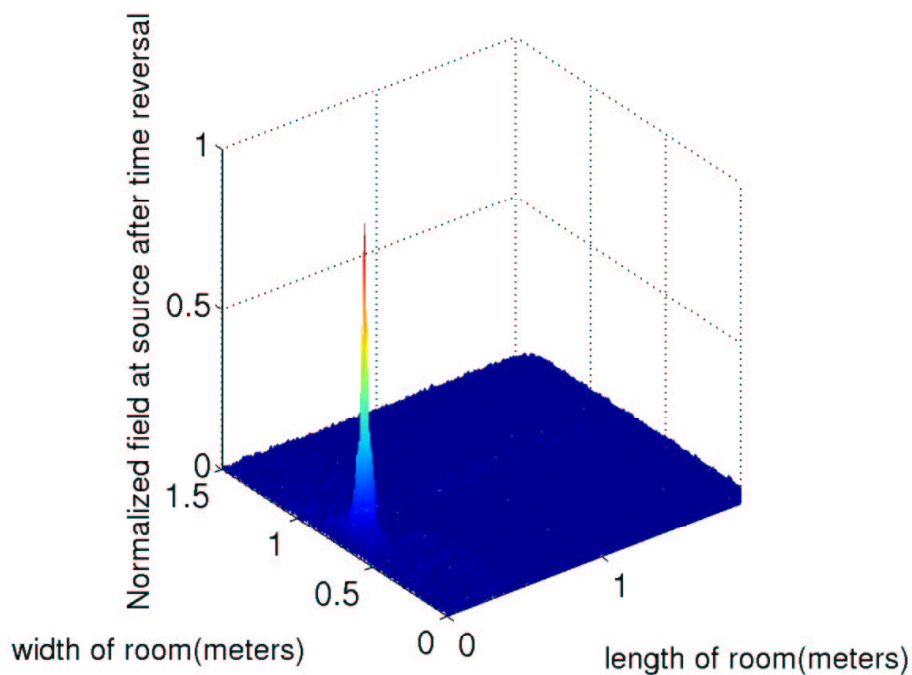
Figure 5.21: Map of normalized acoustic field in enclosure after time-reversal. Illustration of negligible noise in enclosure after time-reversal experiment. Very high SNR with no side lobes surrounding the main peak. Snapshot at time $t = T - t_0$
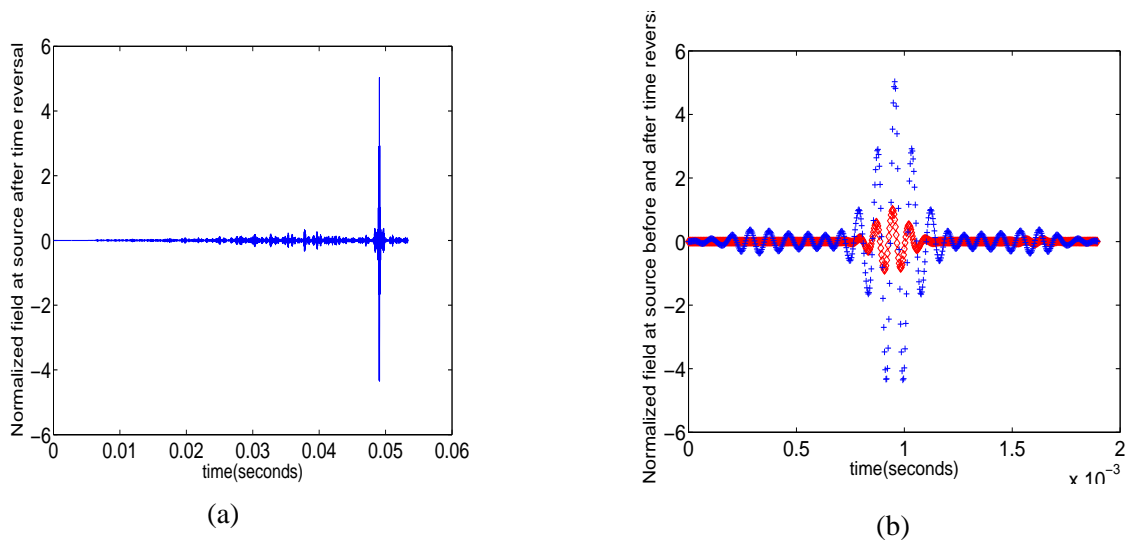
Figure 5.22: (a) Normalized field (with respect to the initial source) received at the original source location. Note that it is 6 times larger in magnitude than the initial source. Although there is conservation of energy, due to the large number of detectors, the SNR in the cavity is greatly reduced and the recompressed signal amplified. (b) normalized acoustic field (with respect to the initial source) at source (blue) versus the initial pulse (red)
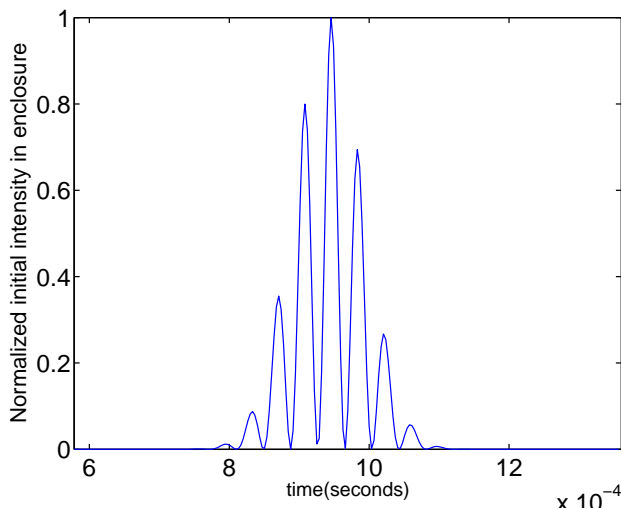
Figure 5.23: Initial intensity measured as the square of the source field at the initial time $t = t0 = 9.49e - 4$. Most of the intensity at the source is concentrated here at this point in time

5.8   Time-Reversal in Corridors with *a Single* Detector

We continue our investigation of acoustic time-reversal in enclosures with corridors in them. We research and make conclusions on both the spatial quality of the time-reversal focus, and the temporal compression of the signal. We simulate a corridor inside an enclosure with a "knife blade" waveguide located in the center as shown in figure (5.19). The boundaries of the waveguide are perfectly-reflecting (Dirichlet boundary conditions).

This size of the waveguide is 13 cm wide (5λ) and 1.24 m long (47λ). The source is located at (0.11, 0.67) m close to the left hand wall, and a single detector seats at (1.97, 0.67) m as shown in figure (5.19). We investigate the effect of corridors inside enclosures when a single detector collects the reflected signal over a period of time much larger than the duration of the initial pulse. Specifically, we look to see the size and magnitude of side lobes, if they exist.
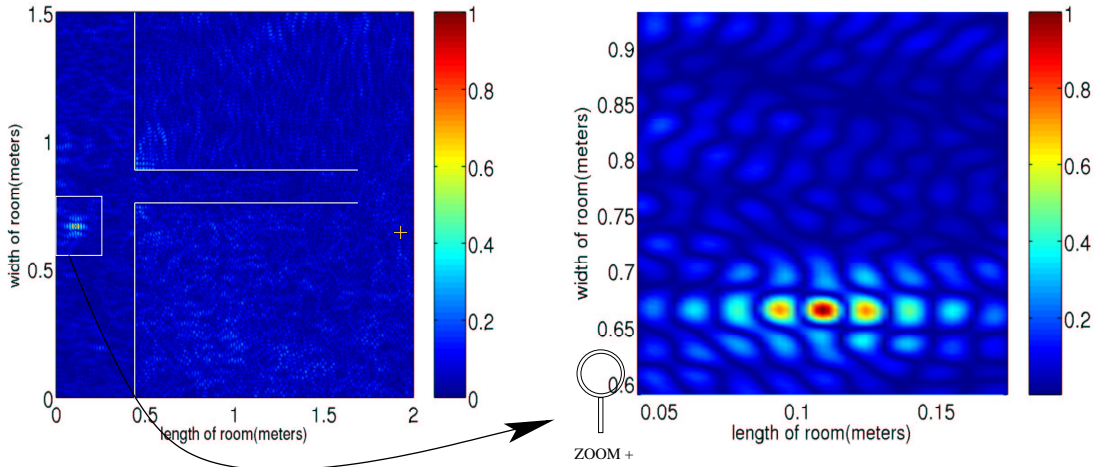
Figure 5.24: Normalized acoustic field in enclosure after time-reversal. Snapshot at time $t = T - t_0$. The quality of spatial focusing is good. The signal focuses to a tight spot in an area of $\lambda/2$ at the source. The average signal to noise ration (SNR) in the enclosure is 25% the magnitude of the main peak. There are no side lobes.

5.8.1   Conservation of Energy

To understand the cause for the amplification in the refocused pulse, (how it is related to Fink's "bazooka" effect); we will define the Energy as:

From the inhomogeneous wave equation

$$\frac{\partial^2 u}{\partial t^2} + c^2 \nabla^2 u = f(x, y, t) \tag{5.1}$$

we define the energy squared as

$$E^2 = \left(\int_{R^2} |\frac{\partial u}{\partial t}|^2 + |\nabla u|^2 \right) dx dy \tag{5.2}$$

which should be smaller or equal to

$$\frac{1}{2} \frac{dE^2}{dt} \leq \int_{R^2} f(x, y, t) \, \frac{\partial u}{\partial t} \, dx \, dy \tag{5.3}$$

By the Cauchy-Schwarz inequality, equation (5.3) is smaller or equal to

$$\int_{R^2} ||f(x, y, t|| \, ||\frac{\partial u}{\partial t}|| \, dx \, dy \tag{5.4}$$

Because the two members of the integral in equation (5.3) are positive; equation(5.4)
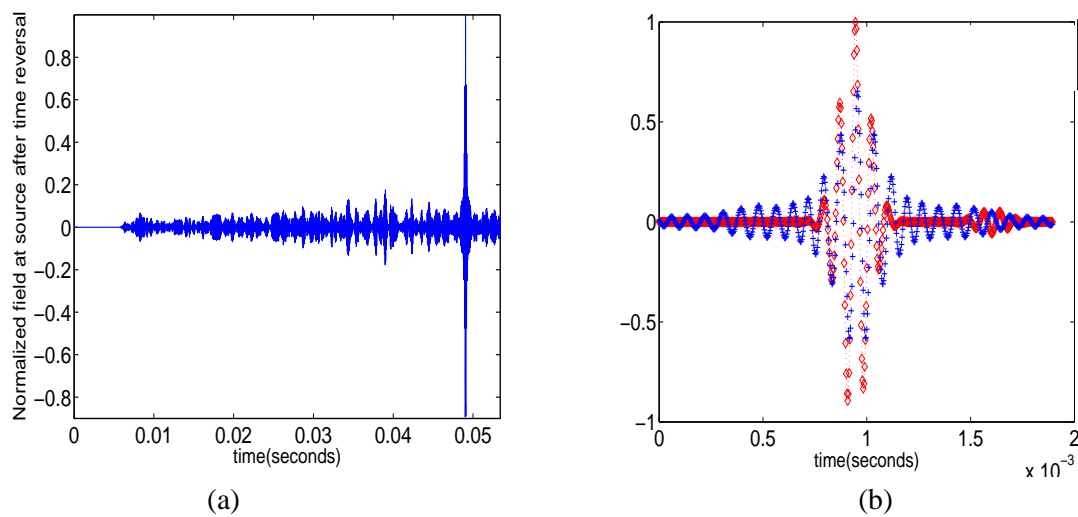
Figure 5.25: Temporal compression of signal after time-reversal. Acoustic field in time measured at source location. Field is normalized with respect to magnitude of initial pulse. Time-reversal experiment carried out in a perfectly-reflecting enclosure with Dirichlet boundary conditions. The enclosure size is (2, 1.5) m. The source is located at (0.11, 0.67) m. The waveguide aids in channeling energy back to the original source. A single detector collects the signal. (a) Recompressed signal received at original source at the refocusing time $t = T - t_0$ (b) Initial pulse (red) vs. recompressed signal (blue) (amplified by 100)

must be smaller or equal to the energy E.

$$\int_{R^2} ||f(x,y,t)|| \, ||\frac{\partial u}{\partial t}|| \, dx \, dy \leq \int_{R^2} ||f(x,y,t)|| \, E \tag{5.5}$$

Thus, the energy as a function of time is given by

$$E(t) \leq E_0 + \int_0^T ||f(x,y,t|| dt \tag{5.6}$$

In our case $f(x,y,t) = \delta(x - x_0)\delta(y - y_0)g(t)$ and $E(t=0) = 0$.

So, we require that the total energy I put into my system is equal to $E_bwd = \beta E_f wd$ where β is usually $0 \leq \beta \leq 1$ due to conservation of energy.

This translates into

$$E(t) \leq E_0 + \int_0^T ||f(x,y,t|| dt = \beta \int_0^T \sum_{n=1}^{M} d_n^{TR} dt \tag{5.7}$$

where $E_0 = 0$, M is the total number of detectors, and d_n^{TR} are the time-reversed detected signals that we send back into the room in the backward phase.

So, the size of the amplification of the pulse (once we require conservation of energy) is in reality $A_{final} = \beta A_{initial}$, where A represents the amplitude.

$$E_{fwd} = \int_0^T ||f(x,y,t)|| \, dt = 2.73x10^{-06} \text{ s} \tag{5.8}$$

$$E_{bwd} = \int_0^T \sum_{n=1}^{M} d_n^{TR} dt \tag{5.9}$$

and computing β we obtain

$$\beta = \frac{E_b wd}{E_f wd} = 0.7688$$

Thus, even though the energy is conserved, the pulse is amplified due to the large number of detectors at the right hand side wall.

If we measure the energy defined as

$$E = \int_{R^2} |\frac{du}{dt}|^2 + |\nabla u|^2 \, dx \, dy$$

and measure it in the forward and backward phases, we obtain the following:
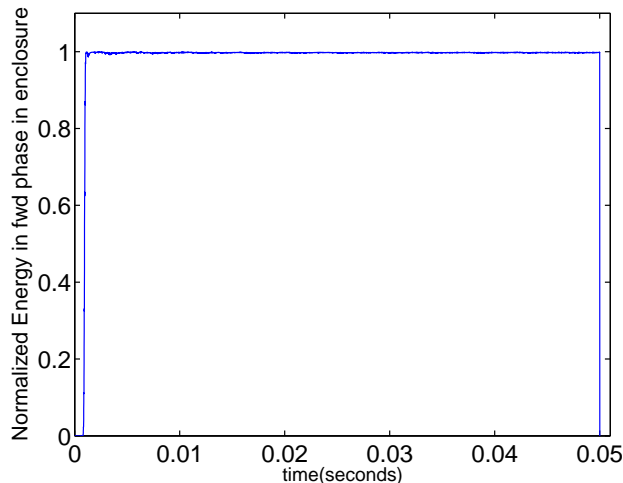
Figure 5.26: Energy as measured by equation equation (5.10) in the forward phase of the time-reversal experiment

5.8.2   1-Bit Time-Reversal: Signal Amplification

In [[48]], Mathias Fink *et al.* modify the received wave field at the detector in a simple way: the amplitude of the wave field is set to ± 1 depending on the original sign of the received wave field. They refer to this as a "1-bit time-reversal experiment." This 1-bit wave field retains the instantaneous phase information from the original wave field, but does not contain any amplitude information. It is then time-reversed and sent back into the medium. "Through a higher-order multiple scattering medium, authors have shown that classical time-reversal and 1-bit time-reversal provide the same temporal and spatial focusing results." [10] This serves as additional proof that the process of time-reversal is robust.

In [2], Derode *et al* report the results of carrying out the time reversal experiments using an initial pulse which scatters through 2000 steel rods immersed in water. Furthermore, in [25] a short ultrasonic pulse is transmitted and propagates through a similar forest of steel rods. A time-reversal mirror of 128-channels makes use of multiple scattering to compress the scattered waves into a pulse and focus it back onto the source. "Paradoxically, we show that the results are even better when the scattered signals are digitized over one bit. Both temporal and spatial resolutions remain unchanged, while the compressed pulse is amplified by 12 dB, and the signal-to-noise ratio is lowered by 1.2 dB" [11]

---

[10] [48], p. 2850
[11] [25], p. 6343

To prove that both classical and 1-bit time-reversal experiments produce the same temporal results, we carry out the time-reversal experiment in a perfectly reflecting enclosure with Dirichlet boundary conditions. We employ the same initial pulse for the following experiments. This pulse is sent from the same source location. It is illustrated in figure 5.27.
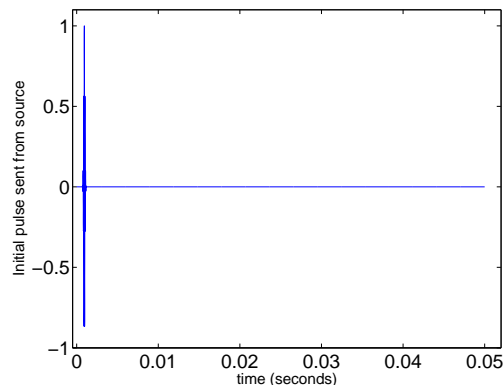
Figure 5.27: Initial pulse sent form source

We perform the time-reversal experiment in a perfectly-reflecting enclosure with Dirichlet boundary conditions. The enclosure size is (2.4, 2.8) m. A single source located at (0.267, 0.156) m while the detector is at position (1.6, 2.3) m. After the process, we receive the following recompressed pulse shown in figure 5.28.

(a)   (b)
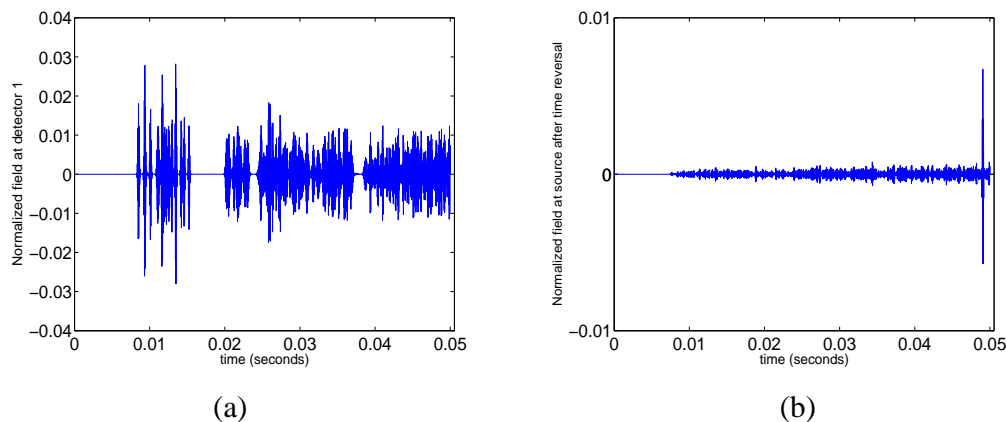
Figure 5.28: Temporal compression of signal after time-reversal. Normalized with respect to magnitude of initial pulse. Time-reversal experiment carried out in a perfectly-reflecting enclosure with Dirichlet boundary conditions. The enclosure size is (2.4, 2.8) m. A single source located at (0.267, 0.156) m while the detector is at position (1.6, 2.3) m. (a) Wave field received at detector during $T = 50$ ms. (b) Recompressed signal received at original source at the refocusing time $t = T - t_0$

If we now carry out the 1-bit time-reversal experiment in the same perfectly reflecting enclosure with Dirichlet boundary conditions we receive the following recompressed pulse shown in figure 5.29. And, just as predicted, no amplification of the recompressed signal is observed in figure.

(a)   (b)
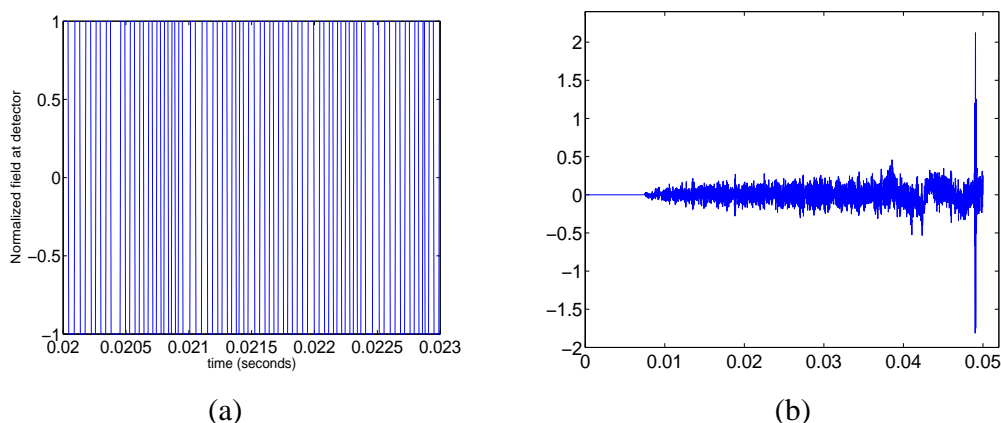
Figure 5.29: Temporal compression of signal after time-reversal. Normalized with respect to magnitude of initial pulse. Time-reversal experiment carried out in a perfectly-reflecting enclosure with Dirichlet boundary conditions. The enclosure size is (2.4, 2.8) m. A single source located at (0.267, 0.156) m while the detector is at position (1.6, 2.3) m. (a) Modified 1-bit wave field received at detector during $T = 50$ ms. (b) Recompressed signal received at original source at the refocusing time $t = T - t_0$

In contrast to this, further experiments by Fink *et al* investigate the process of time-reversal with the combination of a 1-bit ultrasonic wave field and a solid waveguide. Under this circumstances, Fink finds that the instantaneous power delivered at the focus of the solid waveguide is much higher than the power delivered from a classical time-reversal experiment. [48] Thus, he concludes that the "combination of 1-bit time-reversal and a solid waveguide would then lead to shock-wave lithotripsy with low-power electronics." [12]   In acoustic communications, this would be a different way of amplifying the signal received at a specific location.

Note: the same initial pulse is sent from the source in both the classical and the 1-bit time-reversal experiments. The source is illustrated in figure 5.27. The classical normalized acoustic field received at detector during $T = 50$ ms is illustrated in figure 5.30.

The classical normalized acoustic field received at the source at the refocusing time $t = T - t_0$. This is illustrated in figure 5.32.

---

[12] [48], p. 2850
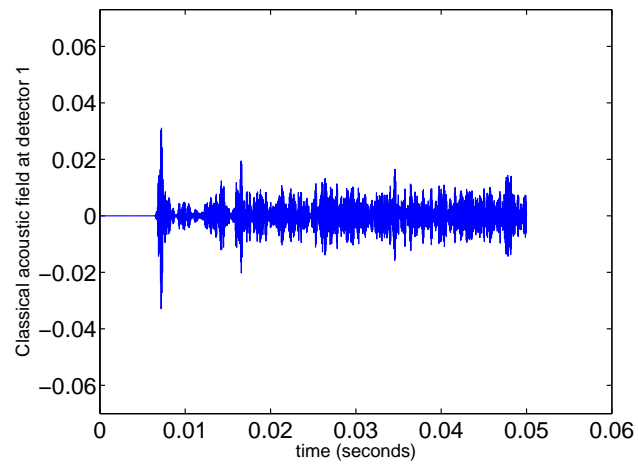
Figure 5.30: Classical normalized acoustic field received at detector during $T = 50$ ms
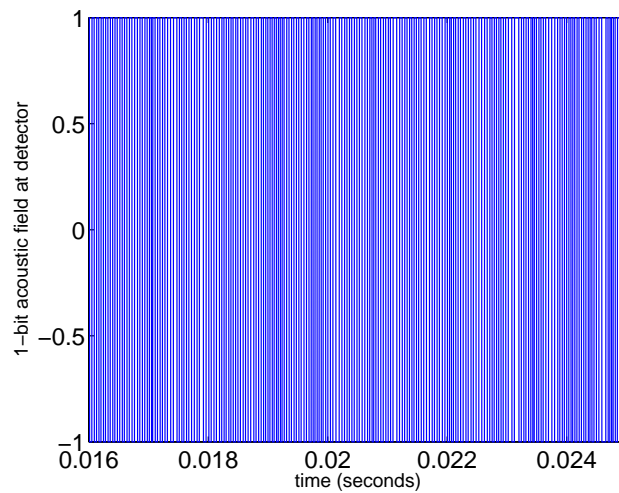
Figure 5.31: 1-bit normalized acoustic field received at detector during $T = 50$ ms
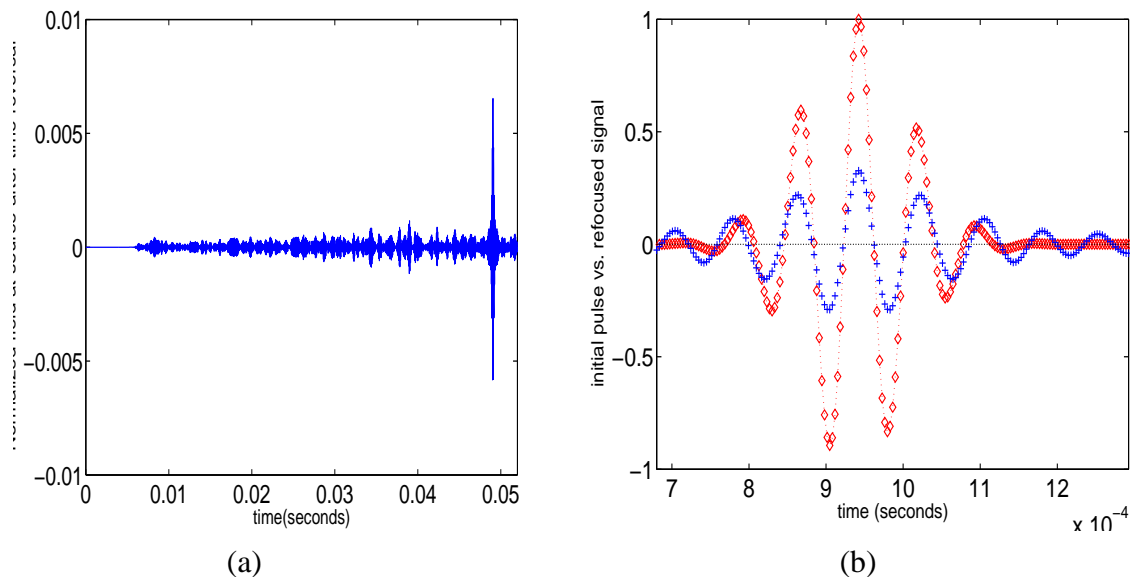
Figure 5.32: Classical normalized acoustic field received at source after time-reversal at refocusing time $t = T - t_0$. Maximum value $= 0.0065$ (a.u.) (a) Magnitude of recompressed signal is less than 10% the magnitude of the initial pulse. (b) red (initial pulse), blue(50 times recompressed pulse after time-reversal) Preservation of nulls

The 1-bit normalized acoustic field received at the source at the refocusing time $t = T - t_0$. This is illustrated in figure 5.33.

We take a snapshot of the normalized acoustic field in the enclosure at the refocusing time $t = T - t_0$. Just as in the keyhole experiments, figures(5.3 and 5.7); the entrance to the corridor is located slightly above the source location. The source is at the same height as the detector across the enclosure.

(a)   (b)
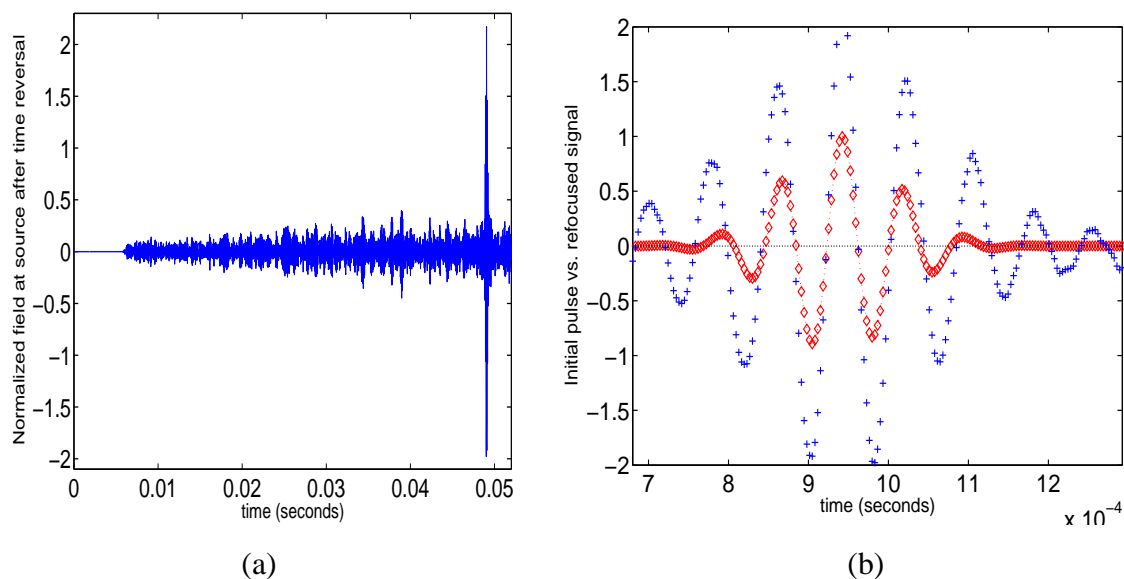
Figure 5.33: 1-bit normalized acoustic field received at source after time-reversal at refocusing time $t = T - t_0$. Received signal is amplified by approximately 300. Maximum value $= 2.1711$ (a.u.) (a) Magnitude of recompressed signal is approximately double the magnitude of the initial pulse. (b) red (initial pulse), blue(recompressed pulse after time-reversal) Preservation of nulls
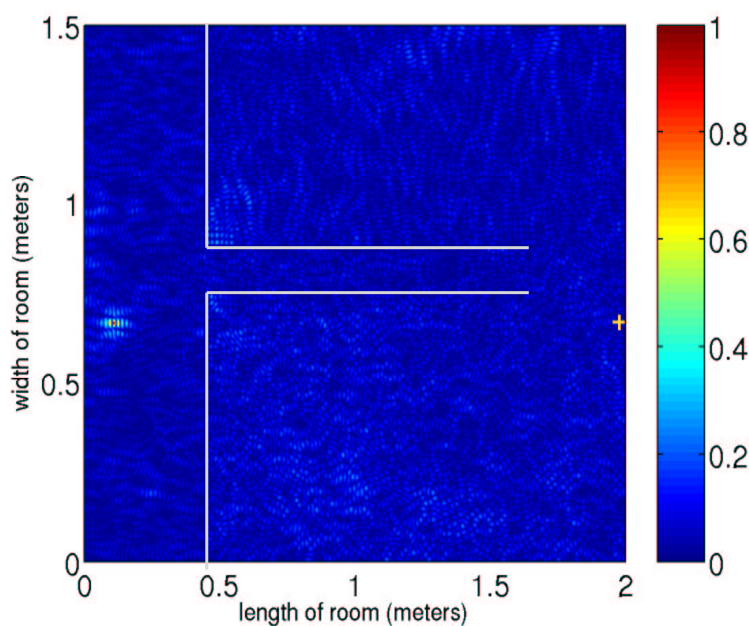
Figure 5.34: Normalized acoustic field after time reversal. Snapshot at refocusing time $t = T - t_0$. Classical time-reversal experiment
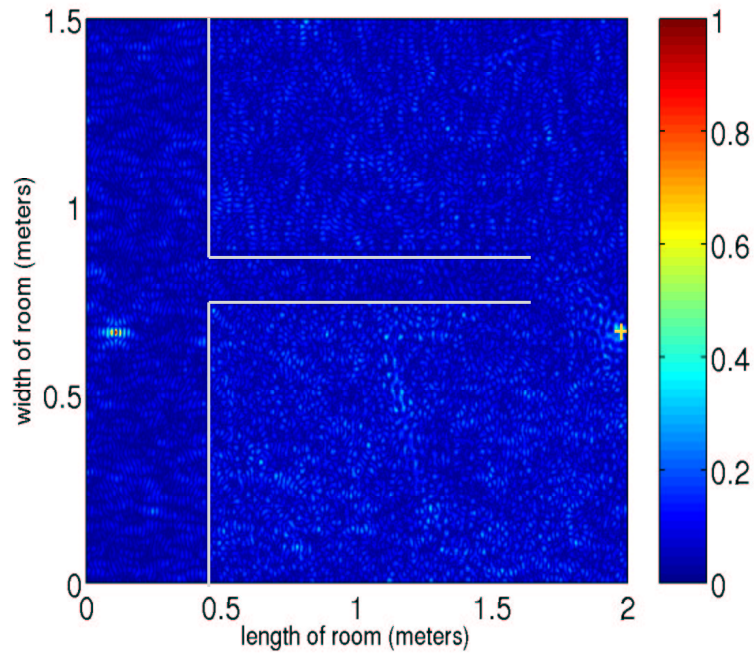
Figure 5.35: Normalized acoustic field after time reversal. Snapshot at refocusing time $t = T - t_0$. 1-bit time-reversal experiment. Lack of information on magnitude of detected wave field causes some small bright (40% of main peak intensity) spots to appear, particularly in the lower half of the room

If we now go back to the numerical experiments with absorption, we recall that for an absorption coefficient $\kappa = 0.3$ we obtain the results shown in figure (4.30). Absorption is strong enough that time-reversal yields a very poor-quality spatial refocusing.

In [[48]] Fink *et al* make use of a solid waveguide to generate temporally recompressed signals with a stronger amplitude than in a similar experiment but in the absence of a waveguide. He claims "the instantaneous power delivered in water at the focus of the solid waveguide is much higher than the power directly transmitted into water from a classically focused transducer." [13]

The final goal is the use of time-reversal in lithotripsy, when the recompression of a waveguide creates high-amplitude shock waves in a tissue or in a fluid with the use of only a few transducers. Similarly, for communications, we could use existent or build new corridors in buildings with absorption at the walls so that the waveguides help us increase the amplitude of the recompressed signal when absorption threatens to decrease it. This counteracting measure by a waveguide is created by a solid perfectly-reflecting waveguide.

In Fink's experiment, time reversal is performed between a point source in water and seven 8-mm-diam piezoelectric transducers attached to a section of a 3.2-cm-diam, 50-cm-long duraluminium cylinder. The central frequency is 1 MHz with a 75% bandwidth, which corresponds to a 5-mm central wavelength for compressional waves in duraluminium. The bottom end of the metallic cylinder is immersed in water at a distance d from the source (d between 0 and 10 cm). Each transducer is connected to an electronic circuitry. [[48]]

In the experiment, the signal sent from the source spreads in time because of reverberations on the interfaces of the solid waveguide. The signal lasts more than 2000 μs, i.e., around 1000 times the length of the initial pulse. In a duraluminium sample, 2 ms corresponds approximately for a longitudinal wave to a 10-m distance (20 times the length of the waveguide). Thus, many round trips inside the cylinder are present in the dispersed signal. The results show a remarkable time-compression on the initial source. This confirms that the instantaneous amplitude information which has been ignored with 1-bit time-reversal is not necessary to successfully perform a time reversal experiment in a solid waveguide. The instantaneous power obtained with 1-bit time-reversal is higher than the power transmitted into the water without a waveguide.[[48]]

To recreate similar results, we carry out a simple time-reversal experiment in an enclosure of size (2, 1.5) m and absorbing boundary conditions. The absorption coefficient is moderately strong $\kappa = 0.3$. The source is located at (0.11, 0.33) m. The waveguide aids in

---

[13] [48], p. 2849

channeling energy back to the original source. A single detector at (1.97, 0.67) m collects the signal in time.

Figure 5.36: Normalized acoustic field in enclosure after time-reversal. Snapshot at time $t = T - t_0$. The quality of spatial focusing is good. The signal focuses to a tight spot in an area of $\lambda/2$ at the source. The detector is still on, because absorption is moderate $\kappa = 0.3$, the highest peak is concentrated at the detector (which is sending the quantized signal of absolute magnitude 1.

The principle governing the solid waveguide TRM, claims Fink, "acts as an acoustic resonator able to transmit very intense pulses with only a few transducers." [14] Dispersion of a short pulse into a long low-amplitude signal , together with amplification, causes the recompressed signal to have a higher intensity.

It should be noted that more energy is added to the waveguide (and to the source) when 1-bit time-reversal is done. This is because when absorption is present, the natural decrease of the signal in time is counteracted by the 1-bit quantization of magnitude +1. In fact, as Fink observes "the maximum amplitude of the output of a linear system is obtained using as input the sign of the time-reversed impulse response of the system." [15] A 1-bit signal is advantageous over an amplitude-modulated one in the sense that its easier to generate and process electronically.

When the absorption coefficient is much lower $\kappa = 0.05$, we obtain the results shown in figures (5.40 and 5.41) for a classical time-reversal experiment. Now, if we quantize the detected signal into a 1-bit signal as before, we observe the improved results in figures (5.42

---

[14] [48], p. 2853
[15] [48], p. 2852

(a)   (b)
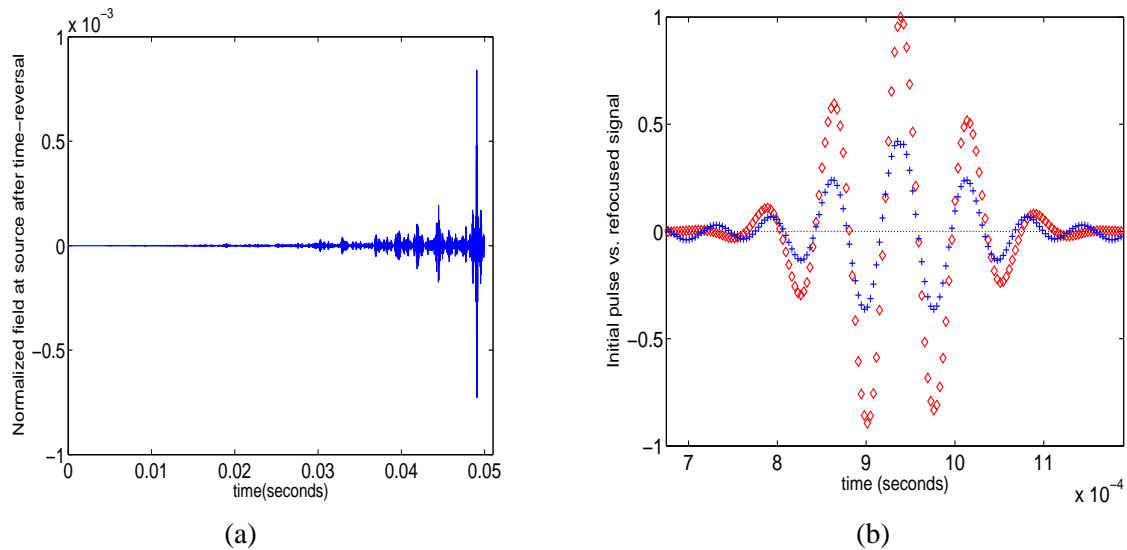
Figure 5.37: Temporal compression of signal after time-reversal. Acoustic field in time measured at source location. Field is normalized with respect to magnitude of initial pulse. Time-reversal experiment carried out in a perfectly-reflecting enclosure with Dirichlet boundary conditions. The enclosure size is $(2, 1.5)$ m. The source is located at $(0.11, 0.33)$ m. The waveguide aids in channeling energy back to the original source. A single detector at $(1.97, 0.67)$ m collects the signal in time. $\kappa = 0.3$ (a) Recompressed signal received at original source at the refocusing time $t = T - t_0$ (b) Initial pulse (red) vs. recompressed signal (blue) (amplified 500 times)
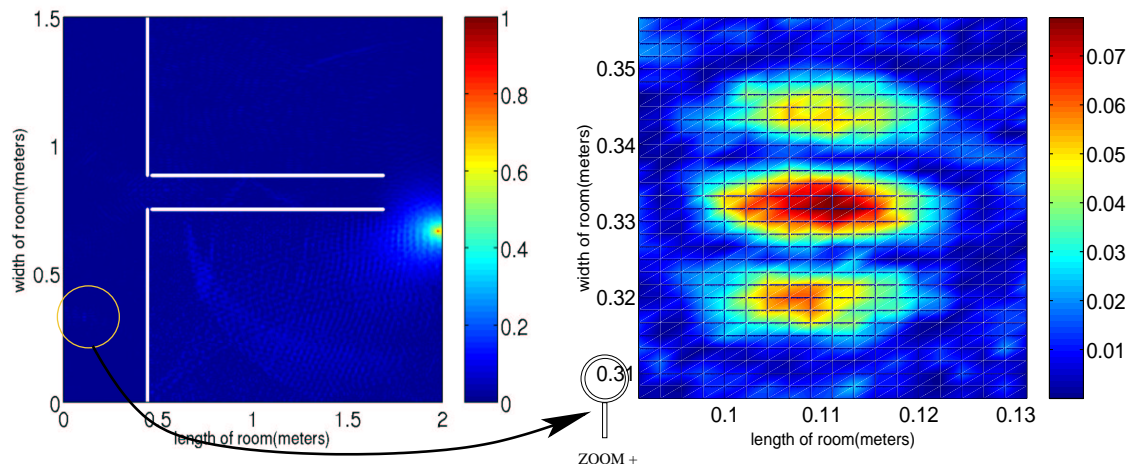
Figure 5.38: Normalized acoustic field in enclosure after time-reversal. Snapshot at time $t = T - t_0$. The quality of spatial focusing is good. The signal focuses to a tight spot in an area of $\lambda/2$ at the source. The detector is still on, because absorption is moderate $\kappa = 0.3$, the highest peak is concentrated at the detector (which is sending the quantized signal of absolute magnitude 1.

(a)

(b)
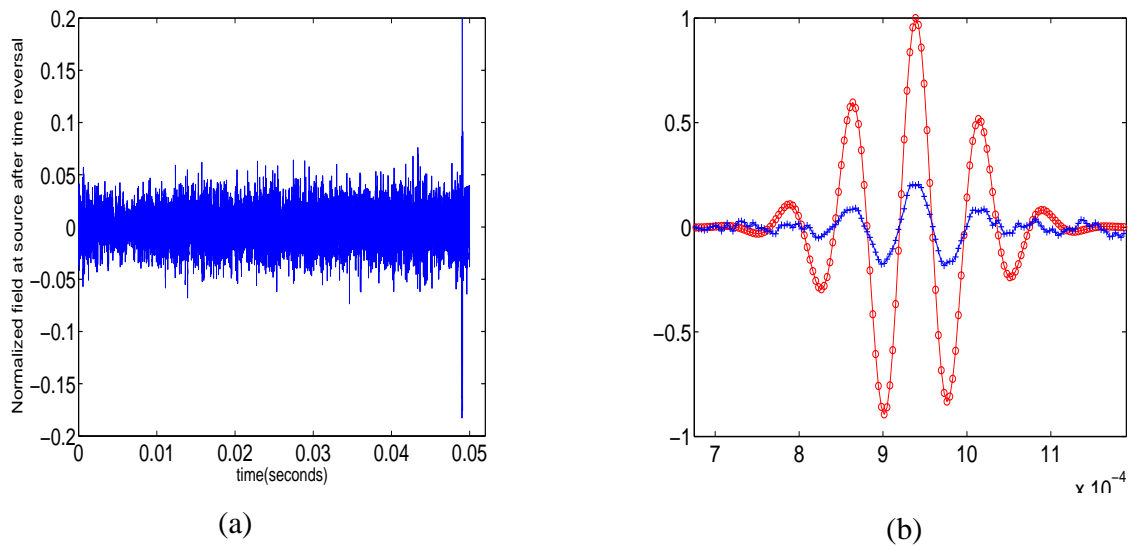
Figure 5.39: Temporal compression of signal after time-reversal. Acoustic field in time measured at source location. Field is normalized with respect to magnitude of initial pulse. Time-reversal experiment carried out in a perfectly-reflecting enclosure with Dirichlet boundary conditions. The enclosure size is $(2, 1.5)$ m. The source is located at $(0.11, 0.33)$ m. The waveguide aids in channeling energy back to the original source. A single detector at $(1.97, 0.67)$ m collects the signal in time. $\kappa = 0.3$. (a) Recompressed signal received at original source at the refocusing time $t = T - t_0$ (b) Initial pulse (red) vs. recompressed signal (blue)

and 5.43).
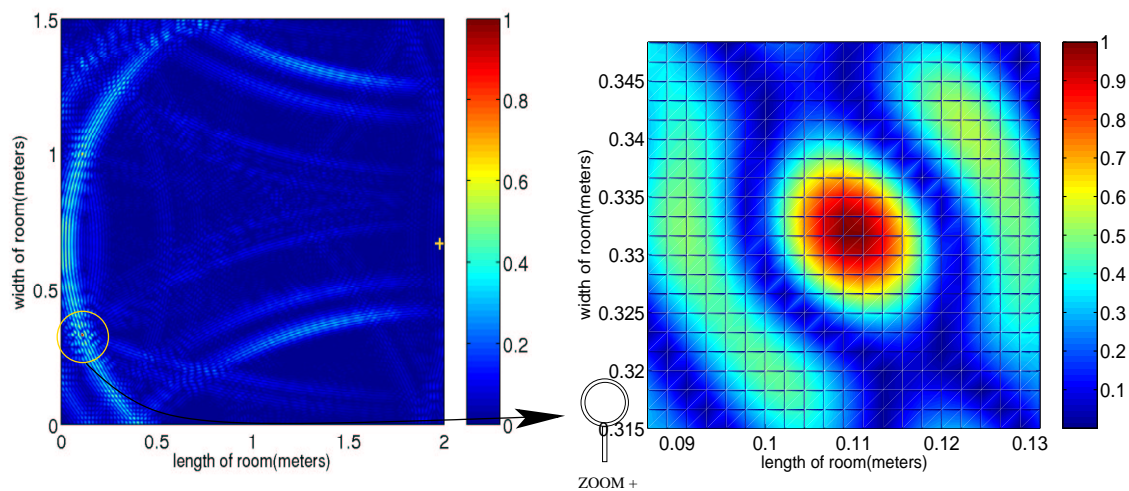
Figure 5.40: Normalized acoustic field in enclosure after time-reversal. Snapshot at time $t = T - t_0$. The quality of spatial focusing is good. The signal focuses to a tight spot in an area of $\lambda/2$ at the source. The detector is still on, because absorption is moderate $\kappa = 0.05$, the highest peak is concentrated at the detector (which is sending the quantized signal of absolute magnitude 1.

Note that the absolute value of the magnitude at the detector is 1 because at the refocusing time, the beacon is still turned on and sending the 1-bit signal into the enclosure. The absolute value at the source is 0.57 which explains why it the spatial tight spot is not observable in this plot. It is because the absolute magnitude of the beacon is 43% greater than the absolute value at the source. However, if we only concentrate our investigation on what we obtain at the source (disregarding what the beacon is sending which is not relevant to refocusing of the signal), we observe (in the zoom figure) a tight spatial focus within half of the central wavelength.

(a)

(b)
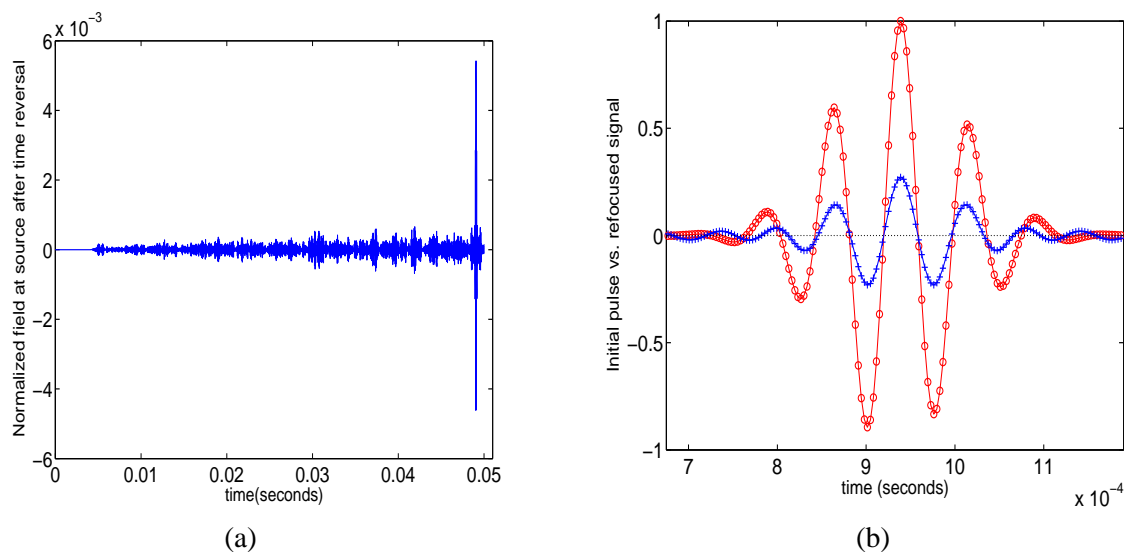
Figure 5.41: Temporal compression of signal after time-reversal. Acoustic field in time measured at source location. Field is normalized with respect to magnitude of initial pulse. Time-reversal experiment carried out in a perfectly-reflecting enclosure with Dirichlet boundary conditions. The enclosure size is $(2, 1.5)$ m. The source is located at $(0.11, 0.33)$ m. The waveguide aids in channeling energy back to the original source. A single detector at $(1.97, 0.67)$ m collects the signal in time. $\kappa = 0.05$ (a) Recompressed signal received at original source at the refocusing time $t = T - t_0$ (b) Initial pulse (red) vs. recompressed signal (blue) (amplified 500 times)
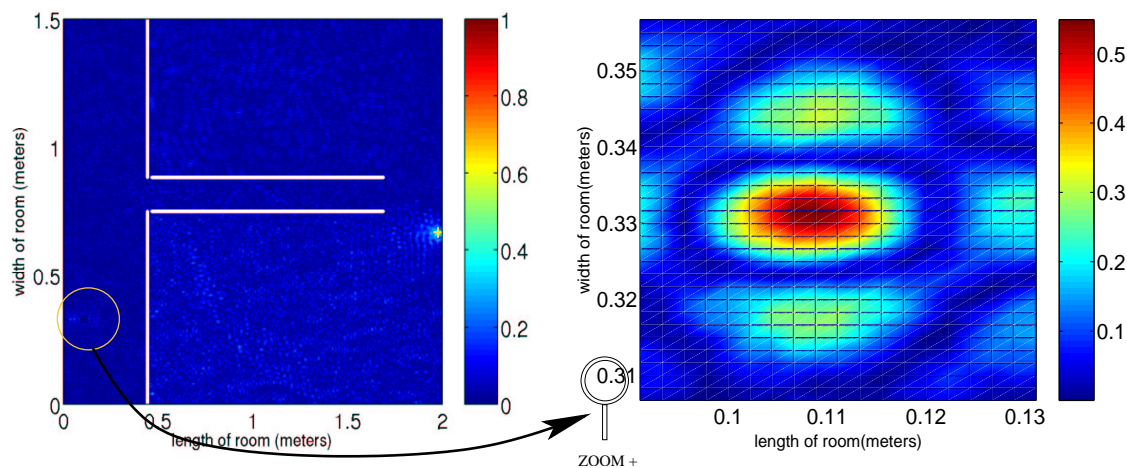
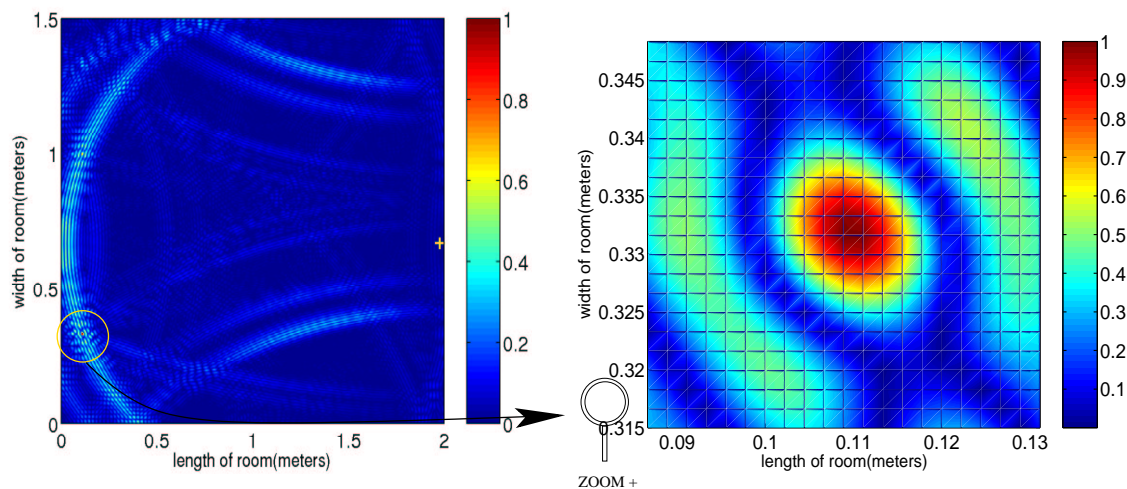Figure 5.42: Normalized acoustic field in enclosure after time-reversal. Snapshot at time $t = T - t_0$. The quality of spatial focusing is good. The signal focuses to a tight spot in an area of $\lambda/2$ at the source. The detector is still on, because absorption is moderate $\kappa = 0.05$, the highest peak is concentrated at the detector (which is sending the quantized signal of absolute magnitude 1.
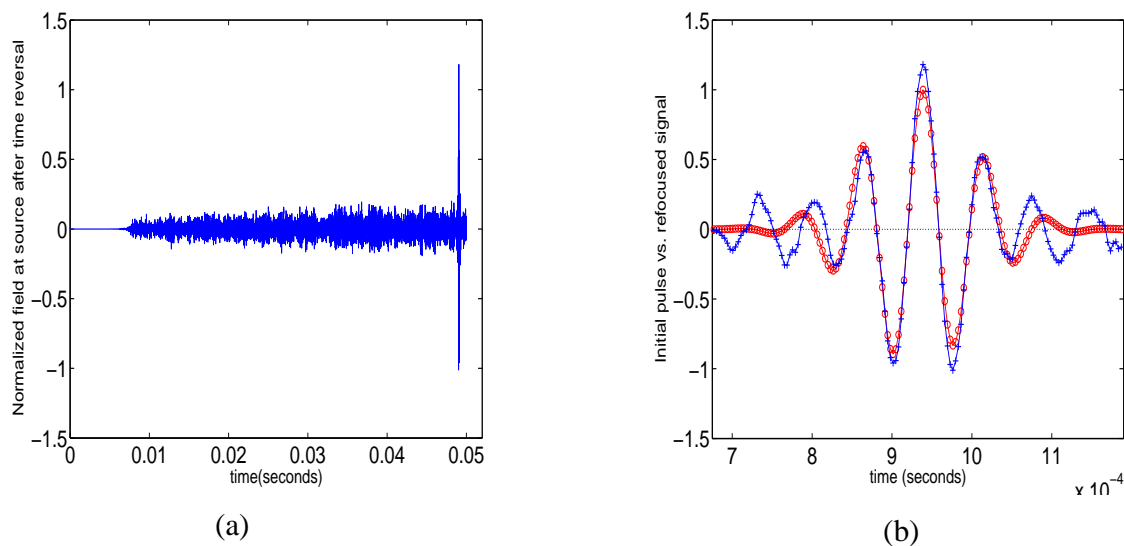
Figure 5.43: Temporal compression of signal after time-reversal. Acoustic field in time measured at source location. Field is normalized with respect to magnitude of initial pulse. Time-reversal experiment carried out in a perfectly-reflecting enclosure with Dirichlet boundary conditions. The enclosure size is $(2, 1.5)$ m. The source is located at $(0.11, 0.33)$ m. The waveguide aids in channeling energy back to the original source. A single detector at $(1.97, 0.67)$ m collects the signal in time. $\kappa = 0.05$. (a) Recompressed signal received at original source at the refocusing time $t = T - t_0$ (b) Initial pulse (red) vs. recompressed signal (blue)

5.9   Time-Reversal in Complex Indoor Structures
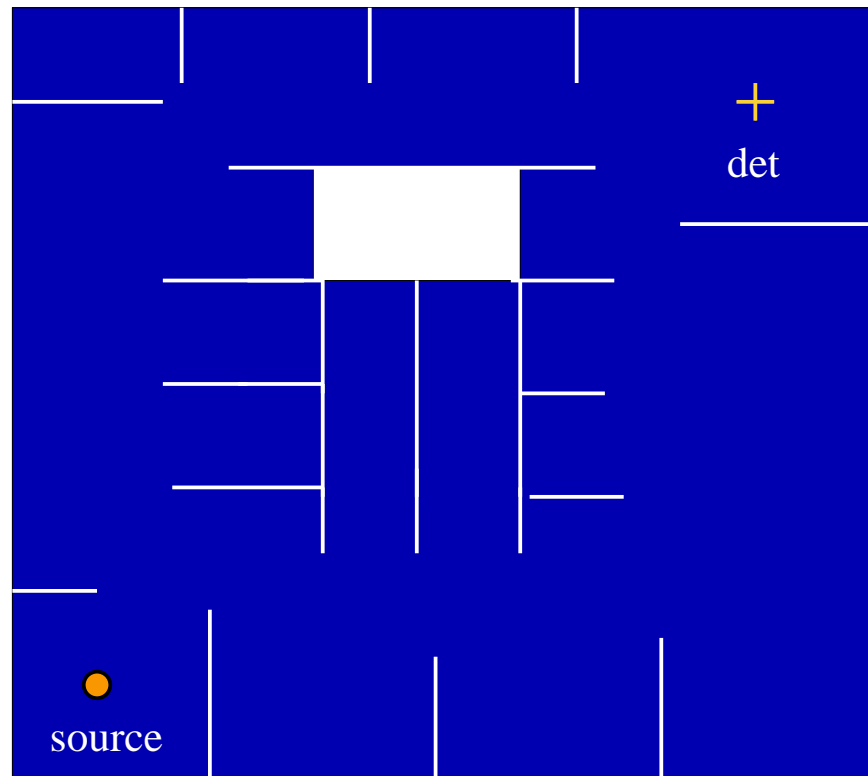
Figure 5.44: Image of experimental setup of a typical office distribution with clusters, open areas and corridors

5.9.1   Results of Time-Reversal from Clutter-To-Clear Area

Now, if there is absorption, the we obtain the following results for $\kappa = 0.3$.

5.9.2   Results of Time-Reversal from Clear-To-Clutter Area

If there is absorption at the walls, in this case $\kappa = 0.3$ we get the following results
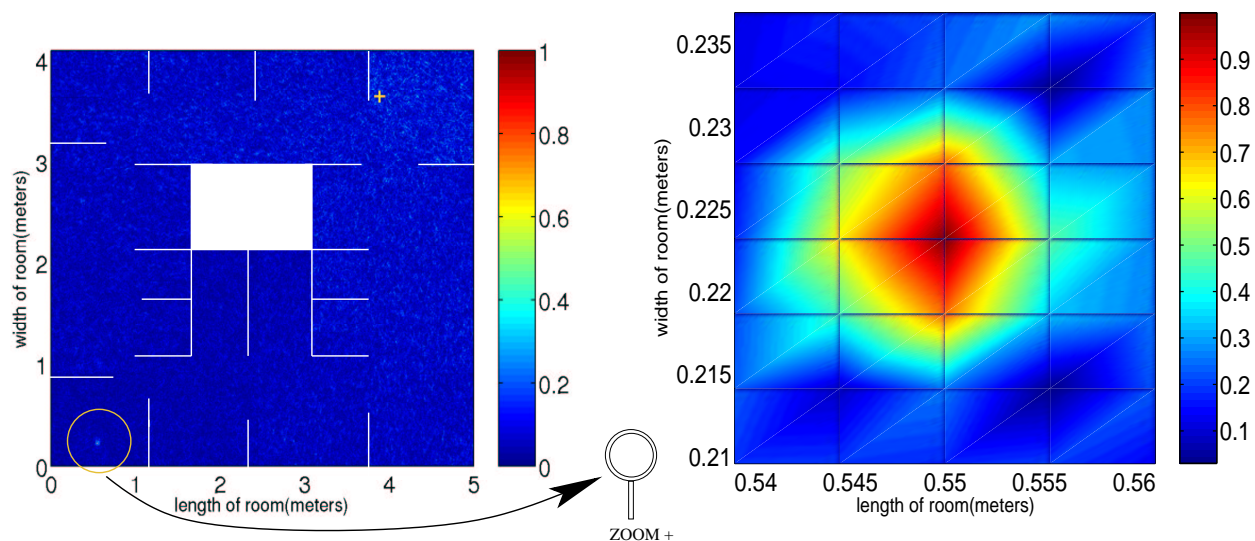
Figure 5.45: Zoom of normalized acoustic field in the simulated office enclosure after time-reversal. Snapshot at refocusing time $t = T - t_0$

(a)

(b)
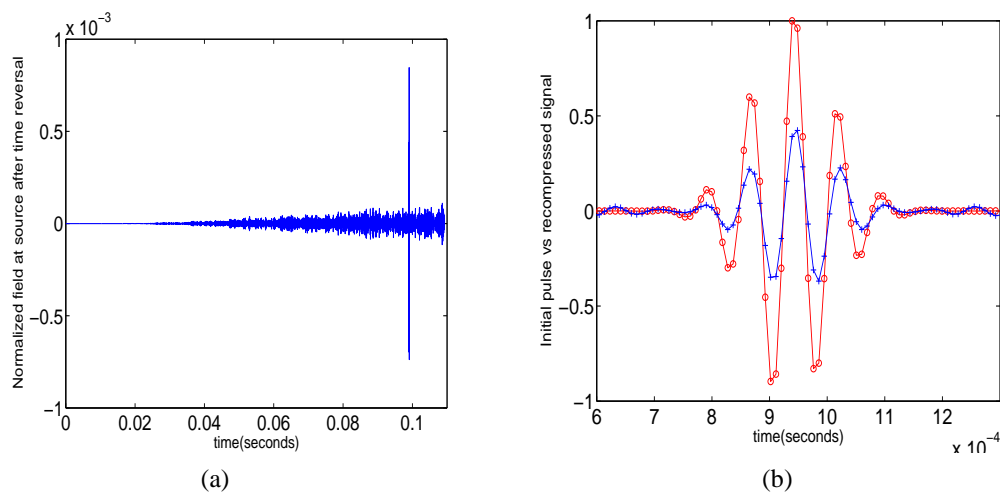
Figure 5.46: Temporal compression of signal after time-reversal. Normalized with respect to magnitude of initial pulse. Time-reversal experiment carried out in a complex indoor structure with perfectly-reflecting boundary conditions. The enclosure size is $(5.0, 4.1)$ m, and there is a source at $(55, 22)$ cm m and single detector located at $(3.89, 3.64)$ m. (a) Recompressed signal received at original source at refocusing time $t = T - t_0$ (b) Initial pulse (red) vs. recompressed signal (blue) (amplified by 500)
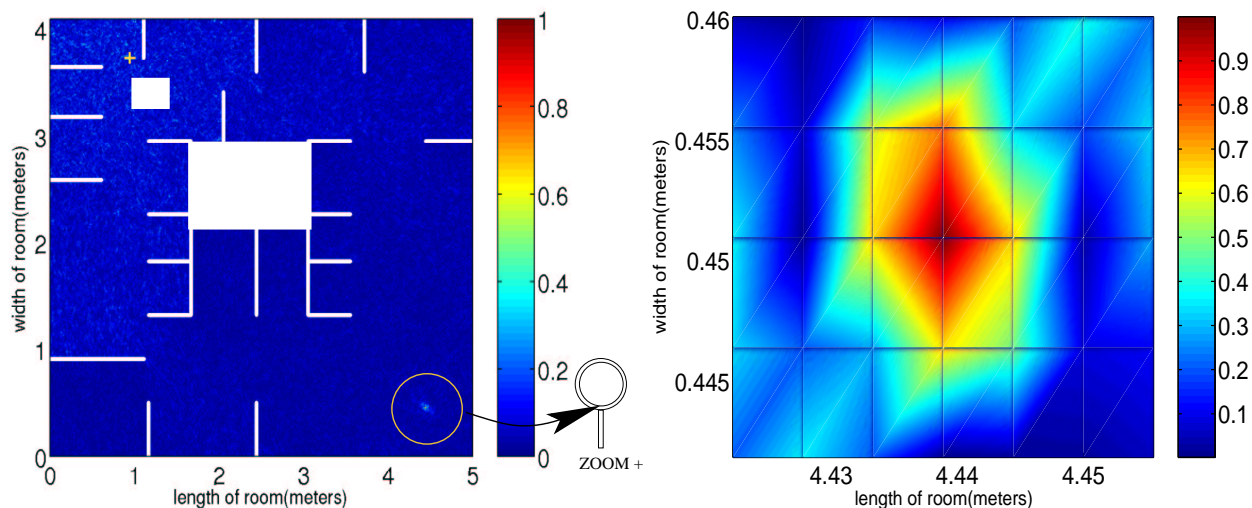
Figure 5.47: Complex office building structure. The enclosure size is $(5.0, 4.1)$ m, and there is a single detector located at $(0.94, 3.7)$ m. Snapshot of acoustic field in enclosure at refocusing time of $t = T - t_0 = 99.1$ ms. There is refocusing back at the source location $(4.44, 0.45)$ m. The refocusing spot has a size of half of the central wavelength (1.3 cm). The boundary conditions are perfectly reflecting Dirichlet. All walls and obstacles are 100% Dirichlet (they reflect all acoustic energy back)
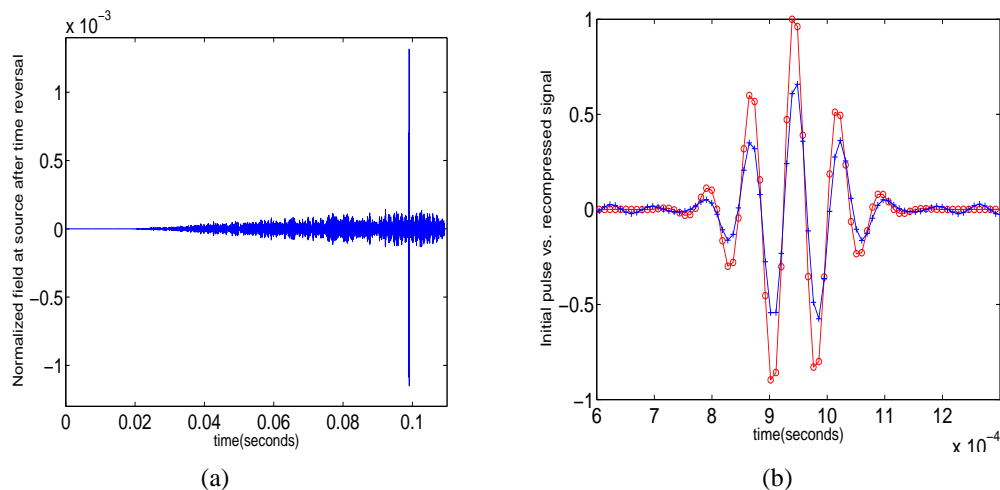
Figure 5.48: Temporal compression of signal after time-reversal. Normalized with respect to magnitude of initial pulse. Time-reversal experiment carried out in a perfectly-reflecting enclosure with Dirichlet boundary conditions. The enclosure size is $(5.0, 4.1)$ m, and there is a source at $(4.44, 0.45)$ m and single detector located at $(0.94, 3.7)$ m. (a) Recompressed signal received at original source at refocusing time $t = T - t_0$ (b) Initial pulse (red) vs. recompressed signal (blue) (amplified by 500)
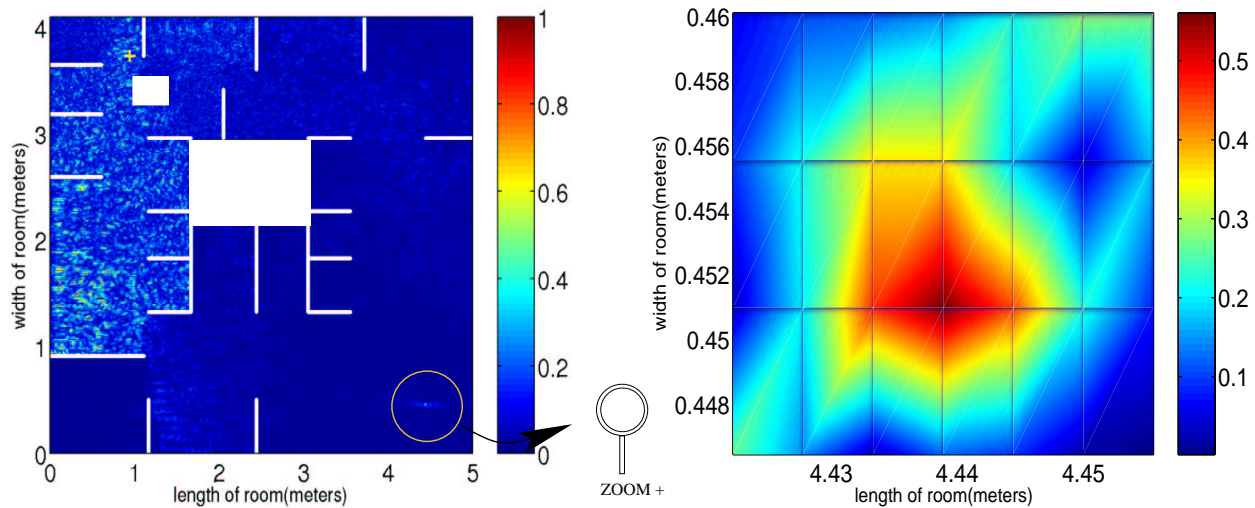
Figure 5.49: Complex office building structure. The enclosure size is (5.0, 4.1) m, and there is a single detector located at (0.94, 3.7) m. Snapshot of acoustic field in enclosure at refocusing time of $t = T - t_0 = 99.1$ ms. There is refocusing back at the source location (4.44, 0.45) m. $\kappa = 0.3$. The refocusing spot has a size of half of the central wavelength (1.3 cm). The boundary conditions are perfectly reflecting Dirichlet. All walls and obstacles are 100% Dirichlet (they reflect all acoustic energy back)
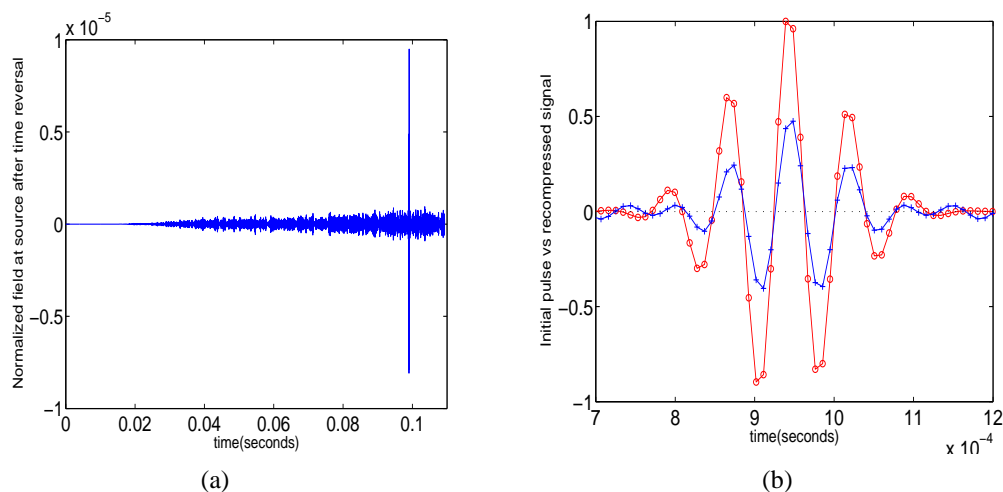
Figure 5.50: Temporal compression of signal after time-reversal. Normalized with respect to magnitude of initial pulse. Time-reversal experiment carried out in a perfectly-reflecting enclosure with Dirichlet boundary conditions. The enclosure size is (5.0, 4.1) m, and there is a source at (4.44, 0.45) m and single detector located at (0.94, 3.7) m. $\kappa = 0.3$. Maximum magnitude of recompressed signal is 9.4939e-06 normalized with the initial pulse. (a) Recompressed signal received at original source at refocusing time $t = T - t_0$ (b) Initial pulse (red) vs. recompressed signal (blue) (amplified by 50000)
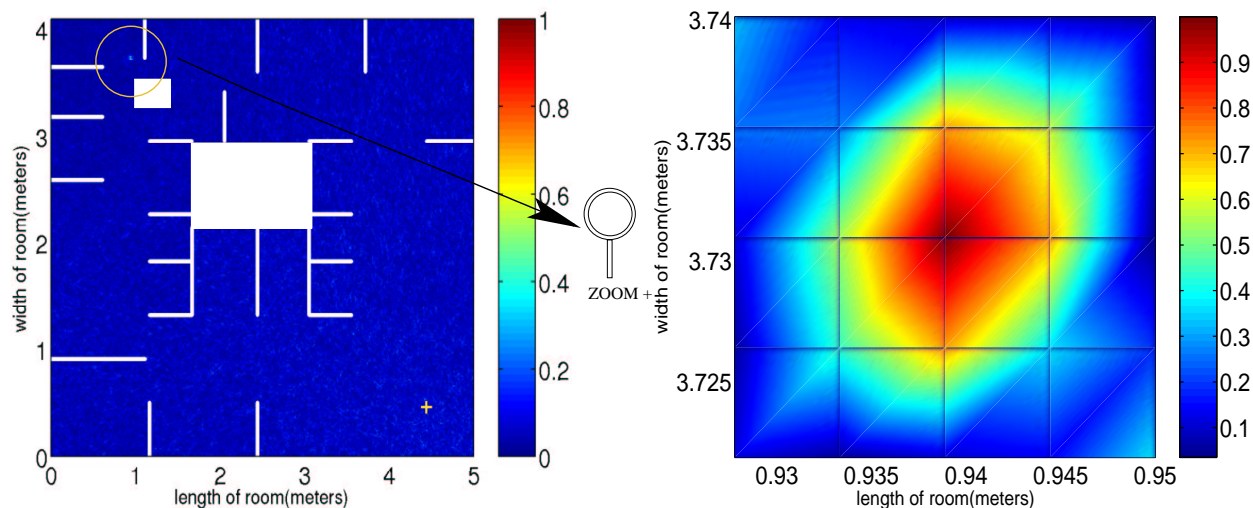
Figure 5.51: Complex office building structure. The enclosure size is (5.0, 4.1) m, and there is a single detector located at (4.44, 0.45) m. Snapshot of acoustic field in enclosure at refocusing time of $t = T - t_0 = 99.1$ ms. There is refocusing back at the source location (0.94, 3.7) m. The refocusing spot has a size of half of the central wavelength (1.3 cm). The boundary conditions are perfectly reflecting Dirichlet. All walls and obstacles are 100% Dirichlet (they reflect all acoustic energy back)
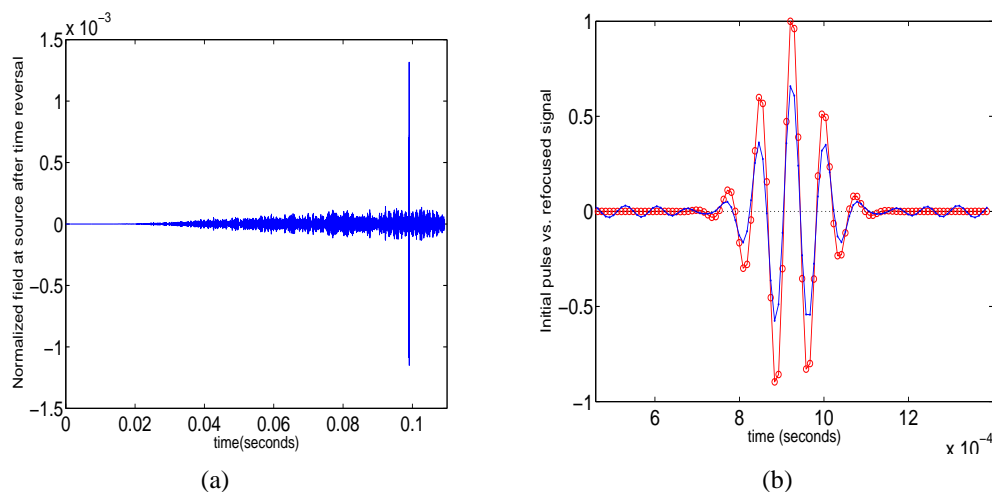
Figure 5.52: Temporal compression of signal after time-reversal. Normalized with respect to magnitude of initial pulse. Time-reversal experiment carried out in a perfectly-reflecting enclosure with Dirichlet boundary conditions. The enclosure size is (5.0, 4.1) m, and there is a source at (0.94, 3.7) m and single detector located at (4.44, 0.45) m. (a) Recompressed signal received at original source at refocusing time $t = T - t_0$ (b) Initial pulse (red) vs. recompressed signal (blue) (amplified by 500)
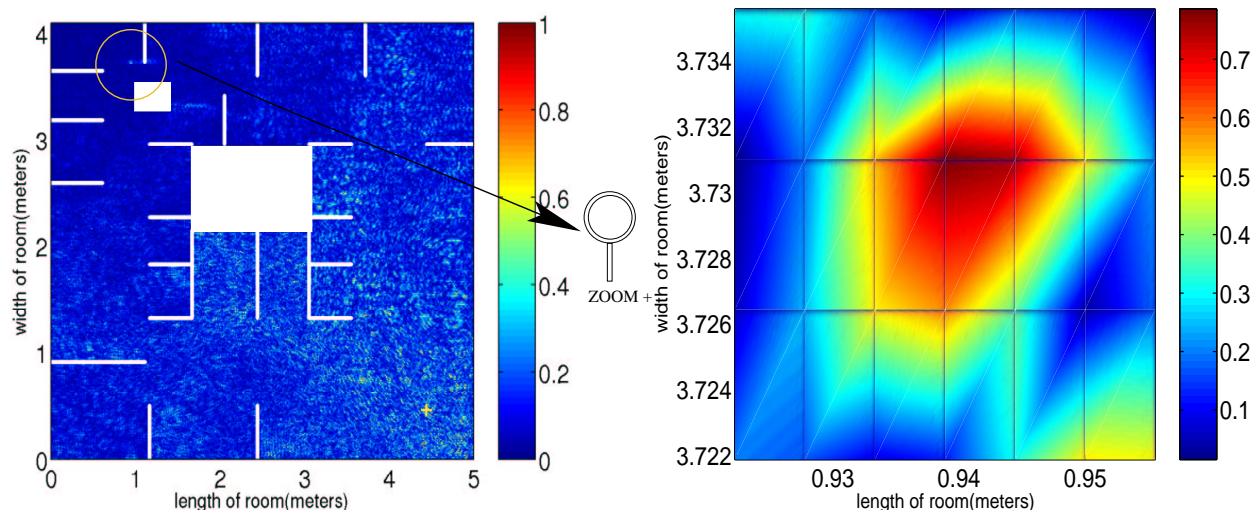
Figure 5.53: Complex office building structure. The enclosure size is (5.0, 4.1) m, and there is a single detector located at (4.44, 0.45) m. Snapshot of acoustic field in enclosure at refocusing time of $t = T - t_0 = 99.1$ ms. $\kappa = 0.3$ There is refocusing back at the source location (0.94, 3.7) m. The refocusing spot has a size of half of the central wavelength (1.3 cm). The boundary conditions are perfectly reflecting Dirichlet. All walls and obstacles are 100% Dirichlet (they reflect all acoustic energy back)
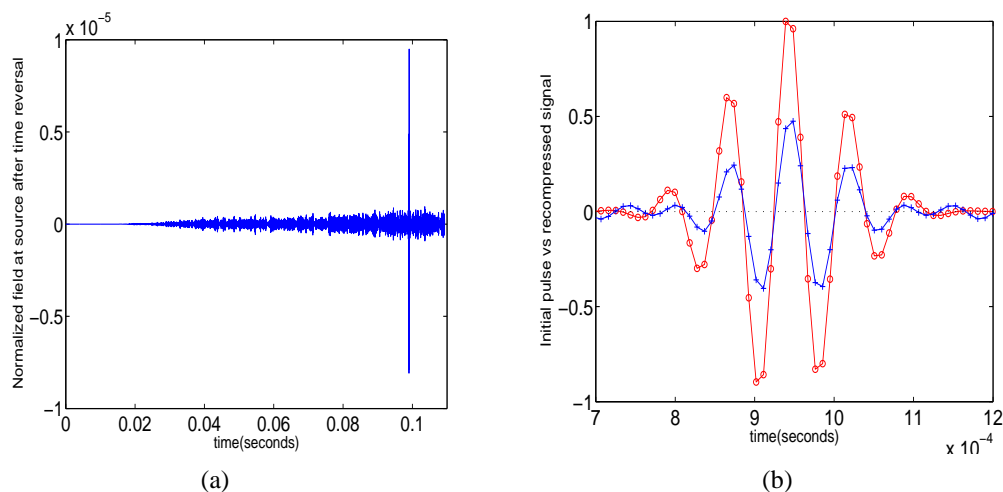
Figure 5.54: Temporal compression of signal after time-reversal. Normalized with respect to magnitude of initial pulse. Time-reversal experiment carried out in a perfectly-reflecting enclosure with Dirichlet boundary conditions. The enclosure size is (5.0, 4.1) m, and there is a source at (0.94, 3.7) m and single detector located at (4.44, 0.45) m. Maximum magnitude of recompressed signal is 9.4939e-06 normalized with the initial pulse. (a) Recompressed signal received at original source at refocusing time $t = T - t_0$. $\kappa = 0.3$. (b) Initial pulse (red) vs. recompressed signal (blue) (amplified by 50000)

Chapter 6

Communications: Train Pulses

6.0.3 Raised Cosine Pulse-Shaping Function

There are many ways in which an analog signal can be used for transmitting information. For example, the amplitude modulation from a sound wave can be converted into binary digits (zeros and ones) to transmit information in binary form.

Nyquist's theorem states that if samples of an analog signal are taken at twice the highest possible frequency, the waveform reproduced from the binary data will closely resemble the original signal. The transmitter and receiver are synchronized and agree the times at which the waveform should be "taped" (measured) to reconstruct the original waveform. The more a channel is tapped the more the received information will resemble the transmitted one.

For a baseband pulse amplitude modulation (BPAM) the coefficients ± 1 are multiplied by the time-reversed signal obtained in the channel. This corresponds to a bit, and the $\pm$ depend on whether the transmitted bit is 1 or 0.

In single-input, single-output (SISO) communication systems with time-reversal an initial pulse is sent from the source and recorded for a long time T at a receiver. The receiver has thus, learned the channel. The receiver then time-reverses the recorded time-trace and encodes a bit stream onto it. It builds this bitstream by phase shifting the time-reversed trace in time and multiplying each copy of the sequence by one of the coefficients $\pm$. It shifts a copy of the time-reversed trace by a specific Δt. This parameter will control the separation in time between each symbol sent in the sequence. The receiver the sends back the time-reversed encoded bit-stream. For a number M of total symbols encoded, each bit will refocus at the source location at the following times: T, T + $1\Delta t$, T + $2\Delta t$,......., T + $(M-1)\Delta t$, T + $M\Delta t$. The source tis then able to decode the stream by tapping the amplitude of

the received time-trace at the corresponding inter-symbol times. If the pulse experiences no distortion in the process, the amplitude measured should correspond exactly to the sequence of $\pm$s encoded onto the bitstream. However, because the signals get somewhat distorted in the process, the amplitude of one symbol interferes with the amplitude of its neghboring symbol and inter-symbol interference occurs. It is this interference that decreases the quality of the communications link. Thus, it is necessary to find a specific Δt for which the inter-symbol interference is small, and yet there is use of a good portion of the channel. The balance between maximization of channel used to encode and minimization of inter-symbol interference is a delicate one, and must be achieved to generate effective communication channels.

In a general SISO communications link in an enclosure, the signal experiences multipath fading from transmitter to receiver. Also, by interacting with boundaries such as walls, furniture and other obstacles, propagating waves interfere. If the difference in path length from a wave traveling from two obstacles to the receiver is comparable to the inter-symbol period, there will be inter-symbol interference. As the signal disperses in the channel, contrributrions from multiple paths arrive at the receiver simultaneoulsy and interfere with ecah other. By adding a prior step to the SISO process using time-reversal, there are many gains in terms of the link's performance.

Natural time-dispersion of the signal is counteracted by the temporal compresison characteristic of time-reversal methods. This tends to reduce inter-symbol interference at the receiver. Thus, the requirement for sophoisticated signal processing decoders at the receiver can be eliminated. Also, by knowing the channel, the transmitter is able to transmit a signal that will focus only in a localized area around the intended receiver, thus mitigating undesired interference between other users or different frequency bands in the area. Furthermore, this reduces undesired interference between multiple users in a single-input multiple-output (SIMO) communications link such as a wireless base antenna with multiple clients' mobiles.

The two main advantages to using time-reversal in a SISO communication link are the quality of spatial focusing and temporal compression due to the time-reversal process. Through the former, we ensure that only the intended receiver gets a clear signal. Through the latter, it is possible to reduce inter-symbol interference at the receiver.

To test the quality of spatial focusingh and temporal compression in a time-reversal SISO communications channel, we start by experimenting with a simple pulse-shaping function (6.1). The goal of this first experiment is simply to test whether a time-reversal process preserves the null crossings of the initiall pulse function. We devise a method for measuring
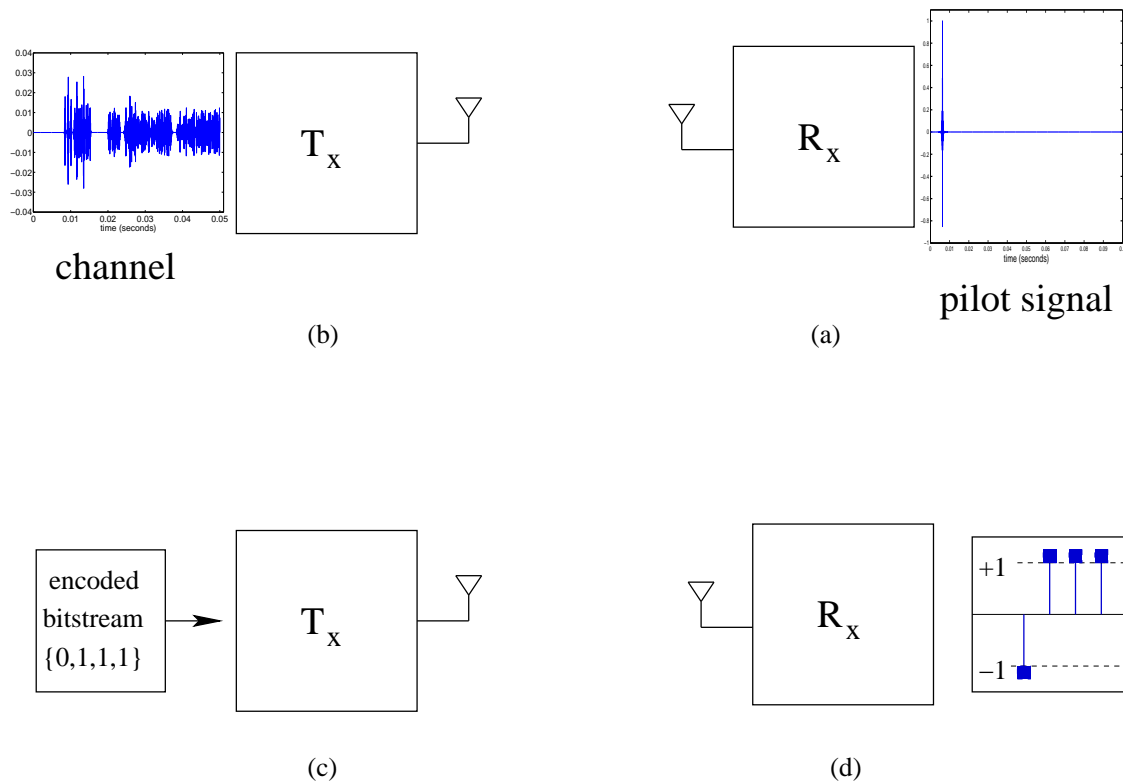
Figure 6.1: TR-SISO communications link. (a) First, the Receiver R_x sends out a pilot signal that travels through a rich scattering medium on its way to the transmitter T_x (b) The transmitter records the resulting waveform for a period of time T. Thus, it learns the channel for this initial pulse (c) The transmitter uses the time-reversed waveform to encode a bitstream that transmits back into the medium (d) Because of spatial focusing, the waveform will refocus only at the receiver location. Due to temporal compression, the sequence of bits can be recovered nearly free of inter-symbol inteference by tapping the channel at the corresponding symbol separation. (Transmitter and receiver agree about inter-symbol separation prior to the communications link)

and comparing inter-symbol interference (ISI) for pulse functions of different bandwidths.

Subsequently, in subsection 6.0.4, we build up the initial pulse by adding a carrier wave in it and test for preservation of null-crossings once again. We test for ISI and compare several distinct pulses.

Finally, in section 6.0.6, we transmit an initial pilot signal from the intended receiver to the transmitter. With this knowledge of the channel, we encode a specific bitstream onto the time-reversed waveform at the transmitter and send it traveling through the medium. Each symbol in the bitstream is delayed in time from the next by a specific Δt that is known by both transmitter and receiver. The result is that the bitstream refocuses back at the receiver location and the bit information that carries the coded message is recovered by tapping the received waveform at intervals of Δt.

Time-Reversal Exoeriment with a Pulse-Shaping Function

The following numerical time-reversal experiment is carried out in a two-dimensional enclosure of size (2.4 2.8) m. The boundary conditions at the walls are Dirichlet. A simple pulse-shaping function (6.2) is sent from a source located at (26, 15) cm at time t_0. The signal propagates through the enclosure for a total time of $T = 100ms$. During this time, a detector located at (1.6, 2.3) m records the received signal.

In the second phase of the numerical experiment, the wavefield at the detector is time-reversed and sent back into the same channel. Once more, we record the acoustic field in the enclosure for an additional $T = 100ms$. We observe that there is temporal compression and spatial focusing of the acoustic field in the enclosure. Exactly at the theoretically predicted refocusing time of $t = T - t_0$, we take a snapshot of the acoustic field distributed in the enclosure. We present the results in figure (6.3). The temporal compression of the time-reversed signal is illustrated in figure (6.4).

$$f(x, y, t) = \left(\frac{\sin(\pi(t - t_0)/\tau)}{\pi(t - t_0)/\tau} \frac{\cos(\pi\beta(t - t_0)/\tau)}{\left(1 - \frac{4\beta^2(t-t_0)^2}{\tau^2}\right)} \right) \delta(x - x_s)\delta(y - y_s) \qquad (6.1)$$

where (x_s, y_s) is the source location. The initial time is $t_0 = 6.3$ ms. The roll-off factor is $\beta = 0.2$ and $\tau = 1/(2B)$ and B is the signal's bandwidth.

The pulse-shaping function we use is a raised cosine pulse given by equation (6.1). It is displayed in figure (6.2). The times at which this pulse crosses the zero axis are determined by the parameter τ. The null-crossings occur at intervals of multiples of τ such as

$\pm 1\tau, \pm 2\tau, \pm 3\tau, ...$
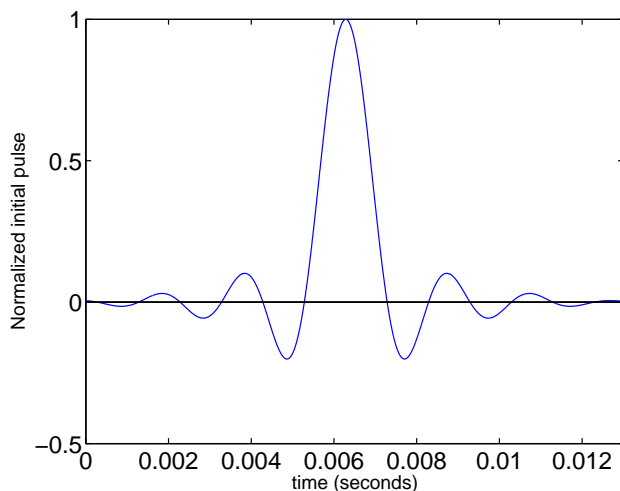
Figure 6.2: Initial pulse f(x,y,t) written in equation (6.1) sent from the source at time t_0

Our goal is to investigate the quality of the temporal refocusing of the pulse, i.e. the preservation of the null-crossings after time-reversal. We tap the signal obtained after time-reversal at the specified locations of the null-crossings. Ideally, if we measure the acoustic field at this times it should yield zero. However, due to pulse distortion during the communications we expect the magnitude of the caoustic field at this times to be different than zero. We realize that this magnitude is caused by unwanted interference at this particular times. We consider the simple pulse-shaping function (6.2) as a bitstream itself, in which the amplitude of the pulse say at half-multiples of τ carries the bitstream information. By measuring the amplitude at the same times in the acoustic field received after the time-reversal process, we test the temporal compresison quality of the refocused wavefield by the amount of undesired interference found at the tapping times.

The results obtained for the acoustic field in the enclosure at the refocusing time $T - t_0$ and the corresponding spatial focusing of the signal are displayed in figure (6.3).

We observe in figure (6.3) that the refocused signal is located () cm away from the source location. It is displaced from the desired focusing location of (26, 15) cm. This displacement from the original source location is due to the fact that the bandwidth of the pulse 6.1 is only $1kHz$, since the duration of the pulse is 1 ms. Since the wavelength of the wave propagating is large compared to the dimensions of the enclosure, the error in distance from the refocused spot to the correct location of the source is of the order of the central wavelength, which is

The results obtained showing the temporal compression of the recompressed signal are

Figure 6.3: Snapshot of normalized acoustic field in enclosure of size (2.4 2.8) m. The boundary conditions are Dirichlet. The source is located at (26, 15) cm and a single detector is at (1.6, 2.3) m. The source is a pulse with a period (defined as the distance from peak to first zero) of $Tau =$. The data shown occurs at the refocusing time $t = T - t0$. Clearly, the area of refocusing is wider than in the case of a narrower pulse, and it is also displaced from the source position by () m.

displayed in figure (6.4). After about 5 or 6 of the first null-crossings, the recompressed signal shows significant distortion, which signifies that for tap times larger than 6, the inter-symbol interference will be too high to transmit a message with confidence.

Qualitatively, we see from figure (6.4) that the shape of the pulse is somewhat preserved under the time-reversal process. However, it is important to analyze the results in a quantitative fashion.

Measurement of Inter-Symbol Interference

The method we devised to measure ISI is the following

$$\mathbf{ISI} = \left(\frac{\sum_{n \neq 0} p_n}{p_0} \right) \tag{6.2}$$

where each p_n corresponds to the power of the recompressed acoustic field at the source location measured at a particular point in time. The specific n time points at which we investigate the value of the recompressed signal ("tap points") correspond to the points where the initial source function $f(x,y,t)$ crosses zero. We see in figure 6.3 that the tap

Figure 6.4: Time-reversal experiment in an enclosure of size (2.4 2.8) m. The boundary conditions are Dirichlet. The source is located at (26, 15) cm and a single detector is at (1.6, 2.3) m. The source is a pulse with a period (defined as the distance from peak to first zero) of $\tau =$. The zeros of the initial source function f(x,y,t) in 6.1 (shown here in red) are located at $\pm 1\tau, \pm 2\tau, \pm 3\tau, ...$ Plot shows initial pulse (red) versus recompressed signal obtained at the source location (blue) (amplified by $1.5x10^7$)

points are located at $\pm 1\tau, \pm 2\tau, \pm 3\tau, ...$ Ideally, we would like the channel to not introduce any interference where the signal is supposed to be zero. This is because when sending multiple pulses, this interference can lead to inter-symbol interference, thereby lowering the effectiveness of the communications channel. When we measure the acoustic field of the recompressed signal at the corresponding tap locations, we generally observe a power measurement different than zero. This is because the initial pulse has gotten distorted in time, during the time-reversal process. We pick the first twenty zeros (ten to each side) of the function as our taps for the channel. We add the magnitudes p_n of the power measurement at each one of the tap points and normalize it with the power at the peak of the recompressed signal p_0. The more the pulse has gotten distorted by the process, the higher the ISI will be. We expect that as the bandwidth of the initial pulse gets increased, the ISI should decrease. That is because time-reversal rests on the principle of broad bandwidth, so the more bandwidth, the better the time-reversal results are.

When considering sending multiple pulses, the preservations of nulls of the recompressed signal is highly important as this will determine how much interference is added to the signal by the process of time-reversal. This undesired interference is what causes different symbols to interfere with each other and can distort the messages sent.

6.0.4 Pulse-Shaping Function with an Oscillatory Carrier

The following time-reversal experiment is carried out in a two-dimensional enclosure of size (2.4 2.8) m. The boundary conditions are Dirichlet. The source is located at (26, 15) cm and a single detector records the transmitted signal for a time of 100 ms. The detector is placed at (1.6, 2.3) m. The initial pulse is sent from the source at time t_0 and has a central frequency oscillatory cosine of frequency $\nu = 13kHz$. f(x,y,t) is written in equation (6.3). The "envelope" of the signal is the same one used in equation (6.1). In the Fourier frequency domain, adding the oscillatory part to the initial pulse will only shift the frequency of the pulse to higher. As this shift occurs, the pulse is better able to survey high-frequency (smaller length scales) aspects of the enclosure. Therefore, we expect the results to obtain better spatial focusing and temporal compression than the ones obtained previously in section 6.0.3

$$f(x,y,t) = \left(\frac{\sin(\pi(t-t_0)/\tau)}{\pi(t-t_0)/\tau} \frac{\cos(\pi\beta(t-t_0)/\tau)}{(1 - \frac{4\beta^2(t-t_0)^2}{\tau^2})} \right) \cos(2\pi\nu(\mathbf{t} - \mathbf{t_0}))\delta(x - x_s)\delta(y - y_s) \quad (6.3)$$

where the pulse central frequency is given by the $\cos(2\pi\nu(t - t_0))$, and $\nu = 13$ kHz and $t_0 = 6.3$ ms. The roll-off factor is $\beta = 0.2$ and $\tau = 1/(2B)$ and B is the signal's bandwidth. Also, x_s and y_s are the $\hat{x}$ and $\hat{y}$ locations of the source correspondingly.

The initial pulse is displayed in figure (6.0.5). Note that by multiplying the cosine term by the envelope of the sinc function does not change where the zeros of the recompressed signal occur. They remain to be determined by τ, and they are located at $\pm 1\tau, \pm 2\tau, \pm 3\tau, ...$ Thus, we continue to tap the channel at times which are multiples of $\pm\tau$ to investigate the rate of ISI given by the current initial pulse.
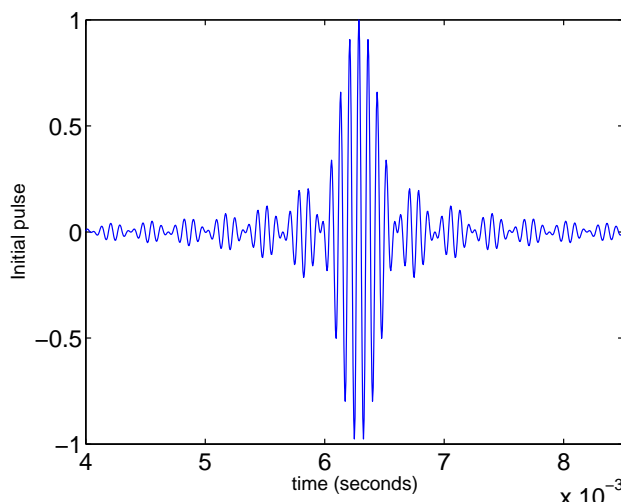
Figure 6.5: Initial pulse f(x,y,t) written in equation (6.3) sent from the source

A source located at $(26, 15)$ cm in the enclosure sends out the initial pulse 6.3 at time t_0. It propagates through the enclosure for a time of $T = 100ms$. During this time, a detector located at $(1.6, 2.3)$ m records the received signal as the pulse surveys the medium multiple times. In the second phase of the experiment, the signal at the detector is time-reversed and sent back into the same channel. We wait for another $T = 100ms$ and note that exactly at a the time of $t = T - t_0$ there is temporal compression and spatial focusing of the signal in the enclosure. We take a snapshot of the acoustic field in the enclosure at this refocusing time and present the results in figure (6.6). The temporal compression of the time-reversed signal is illustrated in figure (6.7). Most of the energy in the enclosure has been gathered and compressed in time to a short pulse at time $T - t_0$.

After the time-reversal process, we compare the initial pulse with the obtained recompressed signal. Our goal is to measure the ISI obtained using this experimental conditions. Particularly, we are interested in measuring ISI as a function of bandwidth of the initial pulse.
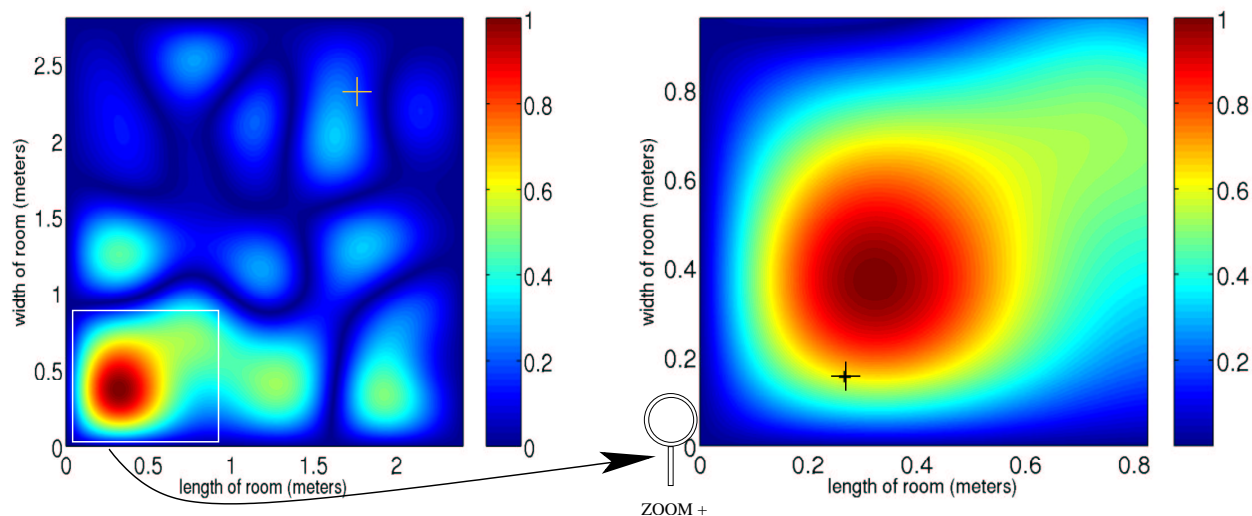
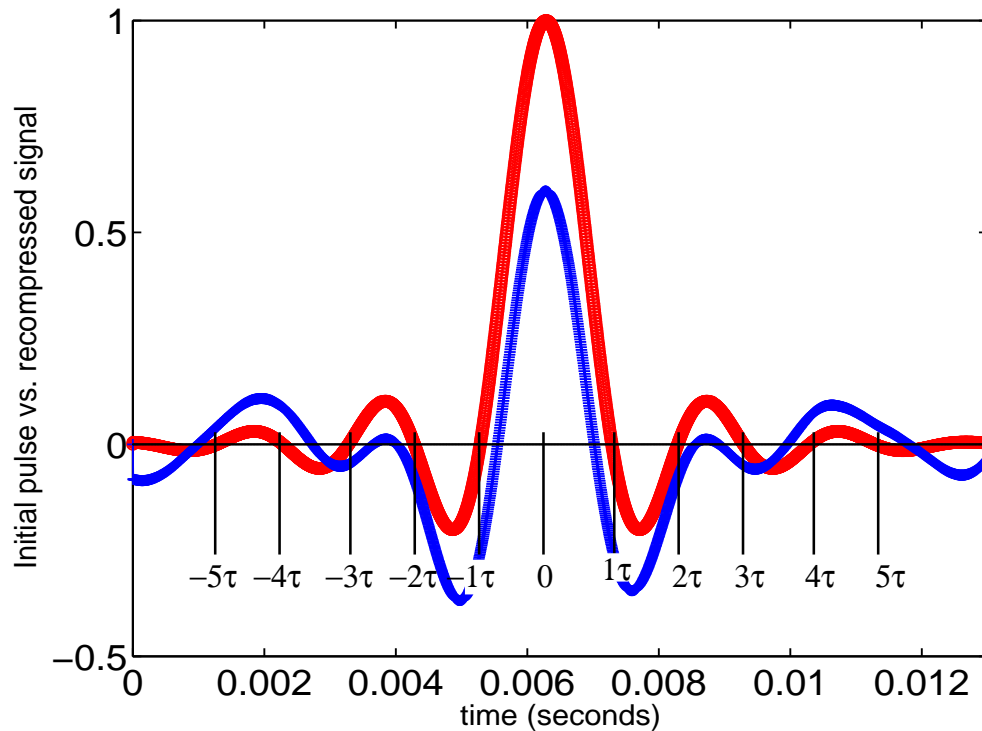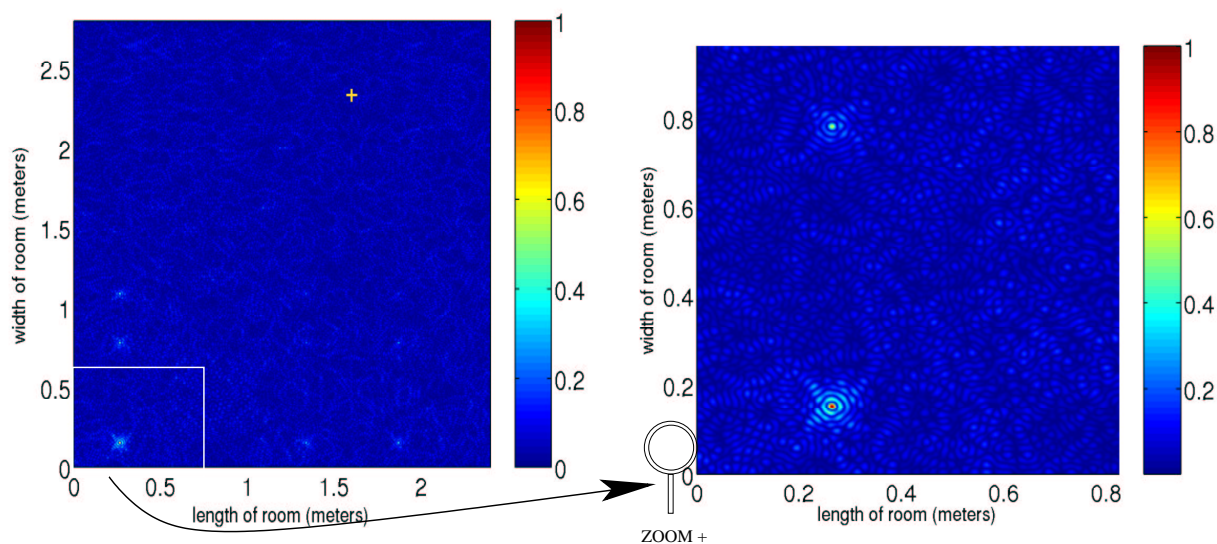Figure 6.6: Snapshot of normalized acoustic field in enclosure of size (2.4 2.8) m. The boundary conditions are Dirichlet. The source is located at (26, 15) cm and a single detector is at (1.6, 2.3) m. The source is a pulse with a period (defined as the distance from peak to first zero) of $Tau =$. The data shown occurs at the refocusing time $t = T - t0$. Clearly, the area of refocusing is more tightly contained than when the experiment is carried out with an initial pulse that does not contain the oscillatory cosine. It is illustrative to compare with a similar measurement using this pulse in figure(6.3). The focusing of the pulse takes place as expected at the source location
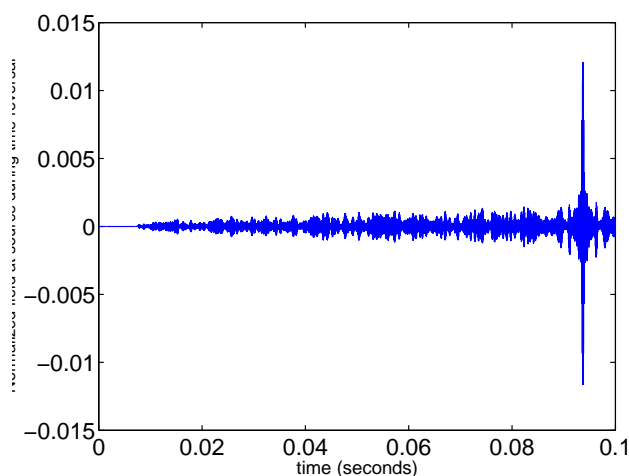
Figure 6.7: Normalized acoustic field measured at source location during the backward phase of the time-reversal process. It is clear that the signal returns recompressed at the refocusing time $t = T - t_0$

As we have said before, the broader the bandwidth of the initial pulse, the more higher frequencies are able to survey the channel, and the better the results get both spatially and temporally. Because we are doing the experiment in an enclosure with perfectly reflecting walls, the quality of spatial refocusing has an optimal size of half the central wavelength of the pulse. This size will not change as the bandwidth increases since it cannot get any better than that. However, as we will see, increasing the bandwidth causes the time compression to preserve the shape of the pulse increasingly better. This in turn lowers the ISI. We expect that at some critical bandwidth the ISI cannot have a lower value. We call this the maximum bandwidth as it is the maximum bandwidth that benefits the time-reversal experiment in terms of lowering the ISI in the recompressed signal. For values of the bandwidth larger than the critical bandwidth, we expect the ISI to remain constant. Evidently the reverse is true, the smaller the bandwidth of the pulse, the higher the value of the ISI will be.

Results obtained for the temporal compression of the recompressed signal are displayed in figure (6.8). We plot the initial pulse (in red) versus the recompressed signal after time reversal (in blue). We do this for a relevant window of time and tap the channel in order to measure the ISI.

The inter-symbol interference in this case is ISI = (only 6 compared to 40% when the cosine oscilatory part of the initial pulse was removed).

6.0.5   Graph of Inter-Symbol Interference Versus Bandwidth

For a single bandwidth pulse, we expect the ISI to increase as we include more null-crossings in the ISI measurement. For example, if we only include the first five zero-crossings to the right of the maximum of the pulse funtion, then chances are ISI will be low since the pulse has not deteriorated much around its center. In contrast to this, if we include the first 300 zero-crossings, we expect the ISI to be much higher. The farther away from the pulse center we measure the value of interference, the higher the distortion.

A more illustrating plot is the one of ISI versus bandwidth. We carry out the time-reversal process for pulses of the form in equation 6.3 wiith different bandwidths. We record the acoustic field refocused at the source location as a function of time. Using these time-compressed wavefields for different bandwidth pulses, we measure the ISI for each pulse. We decide the number of taps and consider this measurement for all different pulses. Prescribed in formula 6.2, the tap times are always given by $\pm 1\tau, \pm 2\tau, \pm 3\tau, ...$ where $B = 1/2\tau$ is the bandwidth of the pulse. We use similar pulses with bandwidth of 0.17 kHz, 0.25 kHz, 0.33
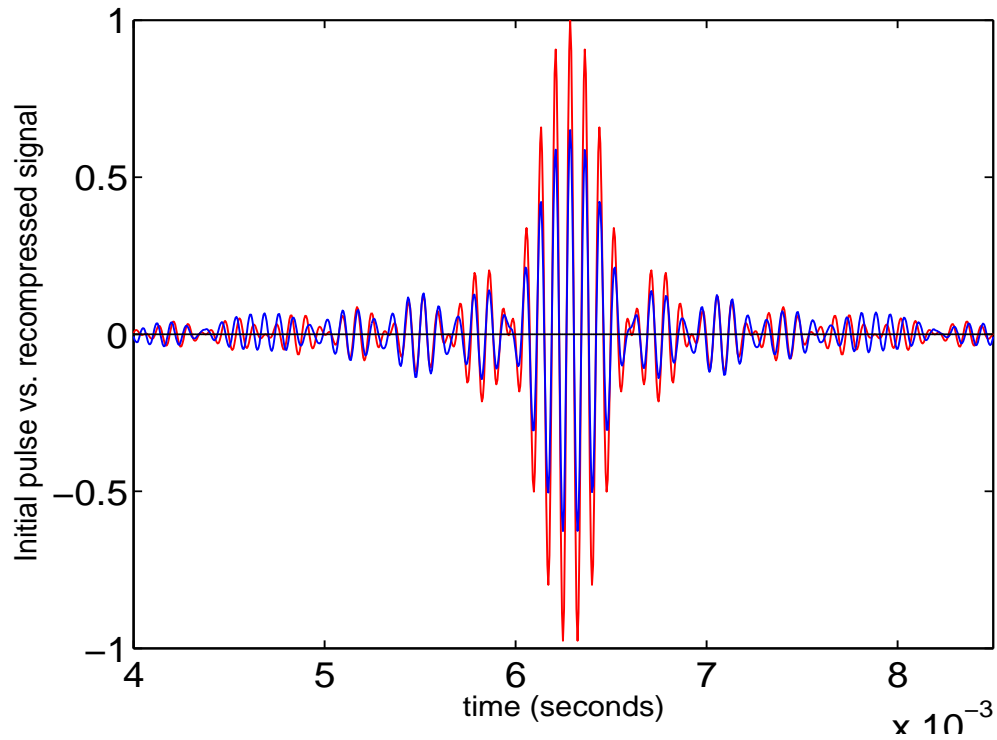
Figure 6.8: Time-reversal experiment in an enclosure of size (2.4 2.8) m. The boundary conditions are Dirichlet. The source is located at (26, 15) cm and a single detector is at (1.6, 2.3) m. The source is a pulse with a period (defined as the distance from peak to first zero) of $Tau =$. The zeros of the source function f(x,y,t) in 6.3 are located at $\pm 1\tau, \pm 2\tau, \pm 3\tau, ...$ Initial pulse sent from source location (red) plotted versus the recompressed signal obtained at the source location (blue) (amplified by $1.5x10^7$)
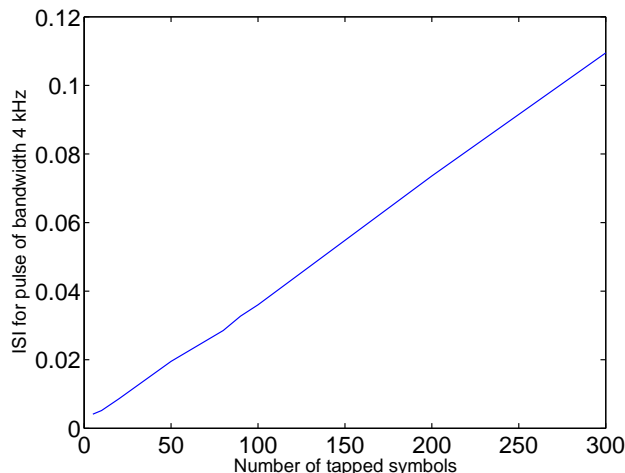
Figure 6.9: For an initial pulse of the form in equation 6.3 with a bandwidth of 4 kHz. Using the recompressed signal after time-reversal, we tap it at the predicted null-crossings of the pulse. Prescribed in formula 6.2, the tap times are always given by $\pm 1\tau, \pm 2\tau, \pm 3\tau, ...$ where $B = 1/2\tau$ is the bandwidth of the pulse. We measure the ISI for different numbers of taps and plot it against number of taps included in analysis As the number of taps increases, the value of the ISI increases linearly

kHz, 0.4 kHz, 0.5 kHz, 1 kHz, 2 kHz and 4 kHz. Figure **??** shows the ISI obtained by tapping the power of the channel for the first five zero-crossings to the right of the pulse center.

Time-reversal rests on the principle of broad band. As the number of frequencies that survey the medium during time reversal increases, the time-compression results get significantly better. This is because for a broader pulse in the frequency domain (shorter in the time domain), there exist many more time scales at which effects of interference are taking place in the process. The more time-scales, the better the information obtained about the channel after time-reversal. The more information, the more we are able to reconstruct the channel efficiently and without errors. Thus, the broader the bandwidth the smaller the ISI. A different way to think about this is that is considering the length scales of the problem. Since sound propagates at the same speed of $c = 343 m/s$ in the enclosure, and $\lambda = c/\nu$, the higher the frequencies included in the bandwidth of the pulse, the smaller the wavelengths of the propagating waves. When the wavelength used to probea richly scattering environment is small compared to the distances of the enclosure, it is possible to distinguish even the smaller detailed structure like obstacles of size of order λ in the enclosure. Thherefore, small obstacles like furniture, corners, doors, etc that would remain unprobed by a narrow bandwidth pulse, will come to light when using a broad bandwidth pulse. And, the more small

details about the acoustic field are picked up the detector during a time-reversal process, the better is it able to reconstruct the original pulse at the source location.

The higher the frequency of the initial pulse, the faster the rate at which waves will probe the scattering medium and arrive at the receiver. The faster they arrive at the receiver, the less chance of ISI exists? (going out on a limb?) Because the amount of information that a wave can carry is related to its bandwidth, lower frequencies implies fewer bits can be transmitted per second.
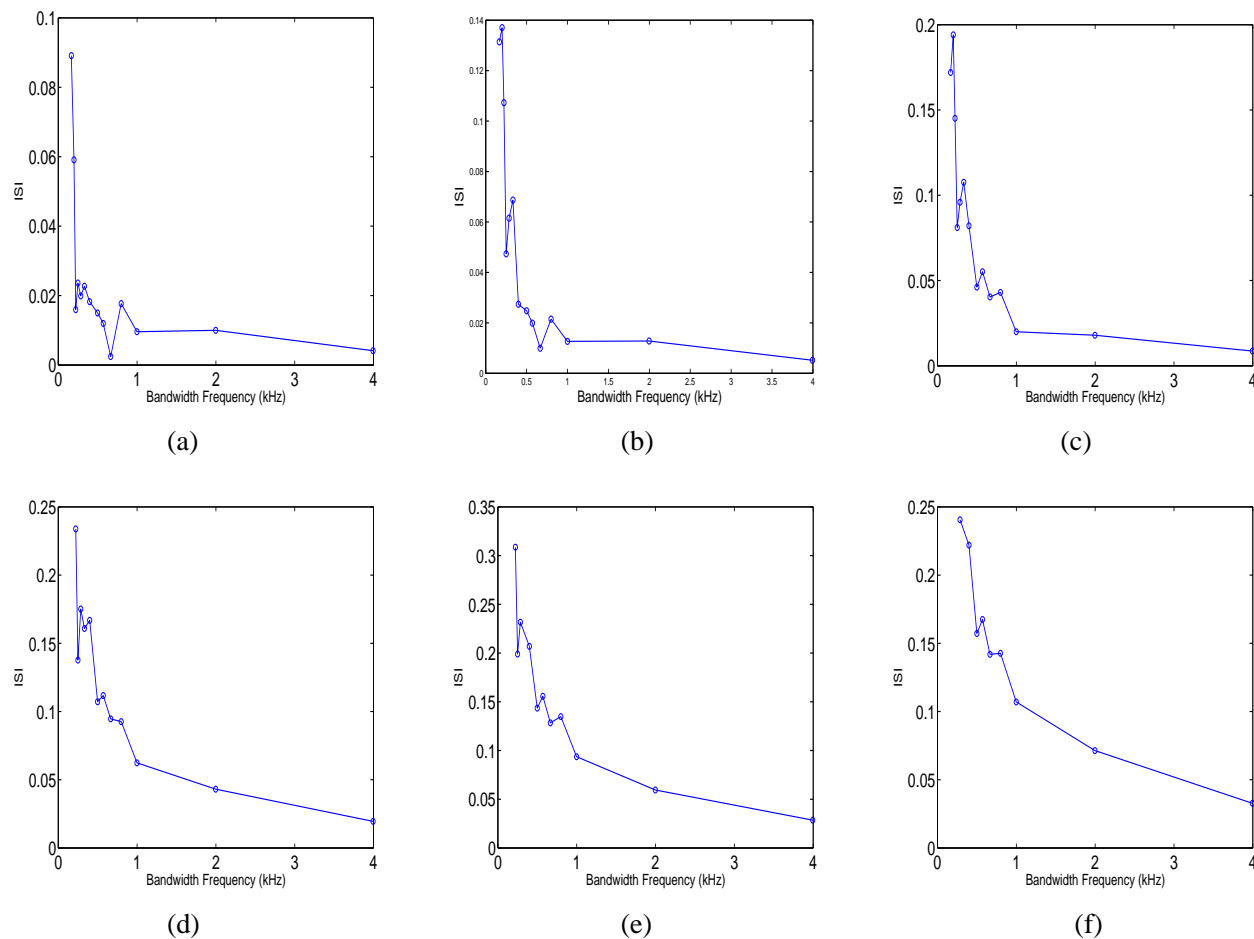
Figure 6.10: PLot of ISI versus bandwidth. Using the time-compressed wavefields obtained after time-reversal for different bandwidth pulses, we measure the ISI for the first twenty zero-crossings to the right of the pulse's center. The broader the pulse bandwidth the lower the ISI in the channel

Time-reversla is expected to yield good temporal compression results when the pulse used has a broadband. However, when narrow-band pulses are used, we expect the temporal compression and spatial resolution results of time-reversal to diminish in quality.

When investigating ISI for the broadband pulse of 13 kHz modulated by a pulse of frequency 8 kHz,

When a carrier wave is amplitude-modulated such as written in equation (6.3) and displayed in figure (), sideband frequencies are created both above and below the carrier wave's central frequency. This causes the wave to use a greater part of the frequency spectrum than if it was a single carrier wave with no modulation.

In our case, a 13 kHz carrier wave that is modulated by a broadband pulse-shaping function of 8 kHz will develop sideband frequencies at $\nu_{min} = 5$ kHz and $\nu_{max} = 21$ kHz. Therefore, this signal requires a band space of 16 kHz. In contrast to this, when the same 13 kHz carrier wave is modulated by a narrowband pulse-shaping function of frequency 500 Hz, then sideband frequencies are created at $\nu_{max} = 13.5$ kHz and $\nu_{min} = 12.5$ kHz. And this signal requires a band space of only 1 kHz. As the modulating signal becomes lower in frequency (and its period τ increases), the bandwidth required decreases. In fact, at any instant in time, the bandwidth of an amplitude-modulated carrier wave is double the modulating frequency at that time. This is further illustrated from the above two examples in which the band increases by 16 kHz and 1 Hz respectively. Thus, the bandwidth increases to double the modulating frequency (8 kHz and 500 Hz respectively).

The bandwidth, B, of a signal determines the signal's period in time $\tau = 1/2B$. The duration in time is twice the distance from the peak to the first zero. For the signals in the previous example, the period of the 13 kHz carrier wave that is modulated by a broadband pulse-shaping function of 8 kHz is $\tau_1 = 1/2(16kHz) = 31\mu s$. Whereas the period of the 13 kHz carrier wave that is modulated by a narrowband pulse-shaping function of 500 Hz is $\tau_2 = 1/2(1kHz) = 0.5ms$.

By the same token, when the modulating frequency becomes higher, the array of wavelengths of the traveling waves increases. Thus, for the 13 kHz carrier wave that is modulated by a broadband pulse-shaping function of 8 kHz, the wavelengths now have a broader range between $\lambda_{min} = c/\nu_{max} = 1.6$ cm and $\lambda_{max} = c/\nu_{min} = 6.8$ cm. In contrast, for the 13 kHz carrier wave that is modulated by a narrowband pulse-shaping function of 500 Hz, the wavelengths range between a shorter range from $\lambda_{min} = 2.5$ cm and $\lambda_{max} = 2.7$ cm.

Suppose we record the acoustic wavefield in the enclosure for $T = 100$ ms. This corresponds to 3200 times the broadband pulse's width in time. Instead, for a narrowband pulse modulated by a 500 Hz signal, a recording time of $T = 100$ ms corresponds to only 200 times the pulse duration in time.

Using the formula for classical velocity $v = d/t$ where v is the velocity, d is the distance

and t the time, we compute the length in space that a wave traveling at the speed of sound $c = 343m/s$ reaches over a period of 100 ms.

In a total recording time of $T = 100$ ms, a the broadband pulse wave traveling at the speed of sound $c = 343m/s$ will cover an average distance of

$$d_{avg} = \frac{(d_{max} + d_{min})}{2} = \frac{T}{\tau_1} \frac{(\lambda_{max} + \lambda_{min})}{2} = 3200\,(4.2cm) = 134m \tag{6.4}$$

The dimensions of the enclosure (2.4, 2.8) m dictate that there are about 35 λ_{max}s in the $\hat{x}$ dimension and 147 λ_{min}s in the $\hat{x}$ dimension. Comparatively, there are roughly 41 λ_{max}s in the $\hat{y}$ dimension and 170 λ_{min}s in the $\hat{y}$ dimension. This indicates that in a recording time of $T = 100$ ms the broadband pulse will cover an avergae distance of 3200 wavelengths. This corresponds to 56 equivalent $\hat{x}$ dimensions and 48 equivalent $\hat{y}$ dimensions.

Correspondingly, for the narrowband pulse, the average distance covered in a recording time of $T = 100$ ms is much smaller

$$d_{avg} = \frac{(d_{max} + d_{min})}{2} = \frac{T}{\tau_2} \frac{(\lambda_{max} + \lambda_{min})}{2} = 200\,(2.6) = 5.2m \tag{6.5}$$

In this case, there are roughly 92 λ_{max}s in the $\hat{x}$ dimension and 96 λ_{min}s in the $\hat{x}$ dimension. Comparatively, there are roughly 107 λ_{max}s in the $\hat{y}$ dimension and 112 λ_{min}s in the $\hat{y}$ dimension. This indicates that in a recording time of $T = 100$ ms the broadband pulse will cover an avergae distance of 200 wavelengths. This corresponds to 2.2 equivalent $\hat{x}$ dimensions and 1.9 equivalent $\hat{y}$ dimensions.

In order to obtain good results from a time-reversal experiment, we want the pulse to travel about 50 times an equivalent length dimension of the enclosure. This is similar to requiring that the recording time be at least a few hundred times the pulse duration. For the time-reversal experiments using narrowband pulses, it is then best to increase the recording time. We double it to $T = 200$ ms (approximately 400 times the narrow pulse width). During this time, a wave will travel an average distance of 10.4 m, which will now equal to 4.3 (3.7) times the equivalent length of the $\hat{x}$, $(\hat{y})$ dimension respectively of the enclosure.

Finally, the rate at which the broadband waves arrive at the receiver is approximately $rate = D/\tau_1 = 82,000$ waves per second. The distance between transmitter and receiver in the enclosure is $D = 2.56$ m. Similarly, the rate at which the narrowband waves arrive at the receiver is approximately $rate = D/\tau_2 = 5,000$ waves per second. A rate which is much slower than the rate for a broadband pulse.

When we investigate the ISI for the narrow-bandwidth pulses such as the ones with a

bandwidth lying between the values of 1 Hz - 1 k Hz

increased the total recording time from 100 ms to 200 ms. This is because in order to explore the ISI occuring in more than the first 20 zero-crossings to the right side of the pulse's maximum point we need to go out in time

6.0.6   Time-Reversal Sending Multiple Pulses

Chapter 7

Conclusion

7.1 Contribution of This Work

7.1.1 Significance and Future Work

.1 Appendix1

Now comes the tricky part, what is the acceleration of a volume element of the fluid $\frac{d\mathbf{v}}{dt}$? The important thing to consider is that the coordinates of this fluid element change in time as the fluid flows.

Equation (2.22) is expressed in a Lagrangian coordinate system, i.e. the coordinate system moves with each particle as the particle moves in time. Using this coordinate system, it is traditional to describe the velocity of a particle in terms of its position vector. When discussing fluid motion, however, it is more convenient to use the Eulerian coordinate system, where velocity is a function of both space and time. The Lagrangian describes the changes with respect to time of a given particle moving in the fluid. The Eulerian system, on the other hand, is stationary, and the velocity is thus described as of that of a volume element of the fluid and it has two parts: the change in velocity of a point in space, and the change due to any gradient in the velocity field. Using the Eulerian coordinate system, we measure the change in velocity of the fluid in a coordinate system fixed in space, such as the laboratory. We show the velocity at each point. Different points in the fluid are continuously streaming through one point in this fixed coordinate system.

When discussing a field variable such as the velocity in the Lagrangian coordinate system, a change in the velocity in a time δt would simple be:

$$d\mathbf{v} = \frac{D\mathbf{v}}{Dt}\delta t \tag{1}$$

We use the upper letters D/Dt to emphasize this is a Lagrangian description. In a time δt the particle has moved a distance δx, δy, δz in the directions x,y and z respectively.

In contrast, in the Eulerian coordinate system, the velocity will depend on x,y,z and t: $\mathbf{v} = \mathbf{v}(x, y, z, t)$ and thus, a change in velocity of the fluid in a time δt measured at a fixed coordinate system in the laboratory is expressed as:

$$d\mathbf{v}(x, y, z, t) = \frac{\partial \mathbf{v}}{\partial t}\delta t + \frac{\partial \mathbf{v}}{\partial x}\delta x + \frac{\partial \mathbf{v}}{\partial y}\delta y + \frac{\partial \mathbf{v}}{\partial z}\delta z \tag{2}$$

We are describing the same physical phenomena, so both descriptions should correspond to the same thing

$$\frac{D\mathbf{v}}{Dt}\delta t = \frac{\partial \mathbf{v}}{\partial t}\delta t + \frac{\partial \mathbf{v}}{\partial x}\delta x + \frac{\partial \mathbf{v}}{\partial y}\delta y + \frac{\partial \mathbf{v}}{\partial z}\delta z \tag{3}$$

Diving by δt

$$\frac{D\mathbf{v}}{Dt} = \frac{\partial \mathbf{v}}{dt} + \frac{\partial \mathbf{v}}{dx}\frac{\delta x}{\delta t} + \frac{\partial \mathbf{v}}{dy}\frac{\delta y}{\delta t} + \frac{\partial \mathbf{v}}{dz}\frac{\delta z}{\delta t} \tag{4}$$

For very small δt, $\delta x/\delta t$, $\delta y/\delta t$ and $\delta z/\delta t$ approximate the velocities of the particle in the directions of x,y,z, that we call $\mathbf{u}$, $\mathbf{v}$, $\mathbf{w}$ respectively. Thus,

$$\frac{D\mathbf{v}}{Dt} = \frac{\partial \mathbf{v}}{dt} + \frac{\partial \mathbf{v}}{dx}\mathbf{u} + \frac{\partial \mathbf{v}}{dy}\mathbf{v} + \frac{\partial \mathbf{v}}{dz}\mathbf{w} \tag{5}$$

which in vector notation is

$$\frac{D\mathbf{v}}{Dt} = \frac{\partial \mathbf{v}}{dt} + (\mathbf{v} \cdot \nabla)\mathbf{v} \tag{6}$$

The equation of motion then becomes

$$\boxed{\rho[\frac{\partial \mathbf{v}}{\partial t} + (\mathbf{v} \cdot \nabla)\mathbf{v}] = -\nabla p} \tag{7}$$

This is known as Euler's equation.

.2   appendix2

.2.1   Robin or Mixed Boundary Conditions

When codes are written in the frequency domain, a number of papers use boundary conditions of the Robin type:

$$\frac{\partial \hat{p}}{\partial n} = \alpha \hat{p} \tag{8}$$

where α is sometimes called the "wall impedance" and is frequency dependent $\alpha = \alpha(\omega)$. In our case we are interested in simulating the effects of time reversal in the time-domain. Thus, this boundary condition would translate into the time-domain as

$$\frac{\partial p}{\partial n} = \int \alpha(t - t')p(t')dt' \tag{9}$$

However, our model requires a wall impedance that is independent of time.

One approach we used in an attempt to simulate the absorption of acoustic waves by the walls of the enclosure is to use "mixed or Robin boundary conditions in the time-domain. These are given by determining both the pressure and the net force at the boundaries of the enclosure. The following derivation is taken from [[39], p. 90]

$$\left(\frac{\partial p}{\partial n}\right)_0 - a_0 p\,(0) = 0 \qquad\qquad \mathrm{at}x = 0 \tag{10a}$$

$$\left(\frac{\partial p}{\partial n}\right)_{l_x} + a_l p\,(0) = 0 \qquad\qquad \mathrm{at}x = l_x \tag{10b}$$

$$0 < x < l_x \tag{10c}$$

In the following analysis which will continue to be in one-dimension, we investigate the consequences of using these boundary conditions. We will conclude that they do not generate absorption at the boundaries for the case of the wave equation. We use [[39]] as a basis for the following derivation. First, we use separation of variables for the wave equation and write its solution as:

$$p\,(x,t) = X\,(x)\,T\,(t) \tag{11}$$

and we consider some initial conditions $p(x,0) = \phi(x)$ and $p_t(x,0) = \psi(x)$. We need to

solve the space problem

$$\frac{d^2 X(x)}{dx^2} = -\lambda X(x) \tag{12}$$

separate from the time equation

$$\frac{d^2 T(t)}{dt^2} = -c^2 \lambda T(t) \tag{13}$$

Boundary conditions (10a) become:

$$\left(\frac{\partial X}{\partial x}\right) - a_0 X = 0 \qquad \qquad \text{at} x = 0 \tag{14a}$$

$$\left(\frac{\partial X}{\partial x}\right) + a_l X = 0 \qquad \qquad \text{at} x = l_x \tag{14b}$$

We consider first the positive eigenvalues $\lambda = \beta^2 > 0$ and we write the general solution to the ordinary differential equation (12) as

$$X(x) = A_1 \cos(\beta x) + A_2 \sin(\beta x) \tag{15}$$

Requiring condition (14a) at the left end and condition (14b) at the right end, we obtain a transcendental equation for β

$$\left(\beta^2 - a_0 a_l\right) \tan\beta l = (a_0 + a_l)\beta \tag{16}$$

Any positive root of this equation would yield an eigenvalue. We calculate the roots numerically using Newton's bisection method and plot the results for the case of radiation at both ends $a_0 > 0$ and $a_l > 0$ in figure (1)
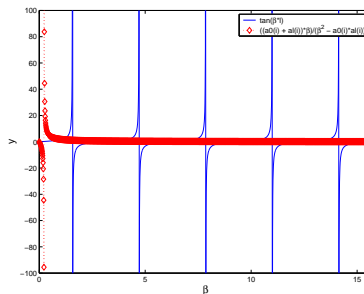

Figure 1: Positive eigenvalues of transcendental equation for β

The eigenvalues λ_n are all positive

$$n^2 \frac{\pi^2}{l^2} < \lambda_n < (n+1)^2 \frac{\pi^2}{l^2} \qquad (n = 0, 1, 2, 3, ...) \qquad (17)$$

and β

$$\lim_{n \to \infty} \beta_n = n \frac{\pi}{l_x} \qquad (18)$$

We found the corresponding β for the case of absorption at $x = 0$ and radiation at $x = l_x$ but more radiation than absorption

$$a_0 < 0, \qquad a_l > 0, \qquad a_0 + a_l > 0 \qquad (19)$$

for which there are three cases:

1. if and only if $a_0 + a_l > -a_0 a_l l_x$ holds, which means there is "much more" radiation than absorption, there is one positive eigenvalue $0 < \lambda_0 < (\pi/2l_x)^2$. The rest are all positive eigenvalues.

2. when $a_0 + a_l = -a_0 a_l l_x$ there exists a zero eigenvalue $\lambda = 0$, all the rest are positive.

3. when $a_0 < 0$ and $a_l > -a_0$ and $a_0 + a_l < -a_0 a_l l_x$ only one negative eigenvalue exists $\lambda = -\gamma^2 < 0$, and the rest are all positive.

The final result for the wave equation with boundary conditions given by (10a) and (10b) is

$$p(x, t) = \sum_{n=1}^{\infty} T_n(t) X_n(x) \qquad (20)$$

where

$$p(x, t) = \left(A_0 \exp^{\gamma_0 ct} + B_) \exp^{-\gamma_0 ct} \right) \left(\cosh(\gamma_0 x) + \frac{a_0}{\gamma_0} \sinh(\gamma_0 x) \right) + \sum_{n=1}^{\infty} \left(A_n \cos\left(\sqrt{\lambda_n} ct\right) + B_n \sin\left(\sqrt{\lambda_n} ct\right) \right) \qquad (21)$$

The last derivation gave us the solution to the two-dimensional wave equation with Robin boundary conditions. We can now explore mathematically whether the energy is conserved in the domain.

The time rate of change of the total energy $E_t ot$ is given by

$$\frac{\partial E_t ot}{\partial t} = \frac{1}{2} \int\limits_0^{l_x} \left(c^- 2 (\frac{\partial p}{\partial t})^2 + (\frac{\partial p}{\partial x})^2 \right) dx + \frac{1}{2} a_l [p(l_x, t)]^2 + \frac{1}{2} a_0 [p(0,t)]^2 = 0 \qquad (22)$$

which proves that energy is conserved. While "some of the internal energy is "borrowed" to the boundary when $a_0 > 0$ and $a_l > 0$. and some of it is "gained" from it if $a_0 < 0$ and $a_l < 0$" [1].

.2.2   Random Coefficients for Robin Boundary Conditions

We then carried out the time-reversal experiment in an enclosure using random coefficients a_0, a_l, b_0, b_l. We tried to create a kind of "wall roughness." In a sense, if the sharing of energy along a boundary is not constant, but varies around a mean, this would reproduce random boundary conditions at the walls. The regions where these coefficients vary are on the order of the size of the wavelength λ. For each boundary, we design a randomly varying Robin coefficient as shown in figure 2.
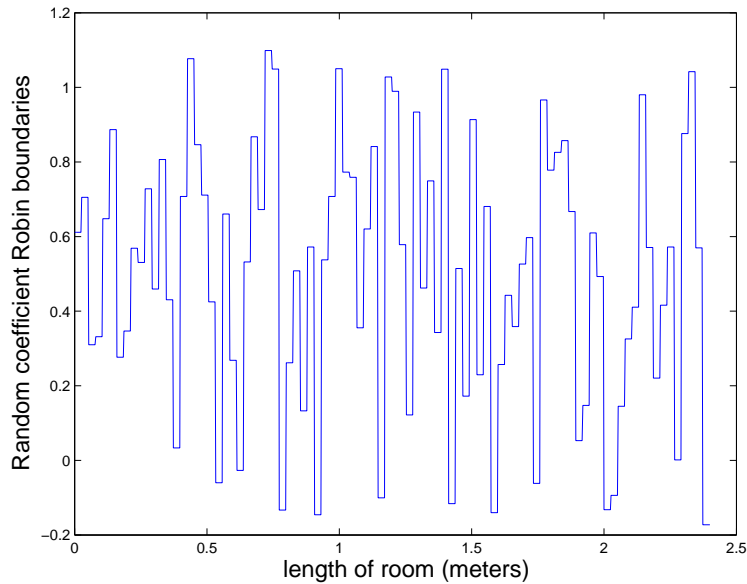
Figure 2: Random coefficient for Robin boundary conditions. Mean value 0.4993, variance 0.1216

The results of doing this condition at the boundaries did not change the outcome of the experiment as compared to the case of constant Robin boundary conditions. We argue that

---

[1] [39], p.99

because overall energy is conserved, the manner in which the "sharing of energy" at the boundaries occurs is independent of spatial focusing and temporal compression results in time-reversal experiments.

Bibliography

[1] Fink M. and Prada C. Acoustic time-reversal mirrors. *Inverse Problems*, 17:R1–R38, 2001.

[2] A. Derode, P. Roux, and M. Fink. Robust acoustic time-reversal with high-order multiple scattering. *Phys. Rev. Lett.*, 75:4206–4209, 1995.

[3] R. K. Snieder and J. A. Scales. Time-reversed imaging as a diagnostic of wave and particle chaos. *Phys. Rev. E*, 58:5668–75, 1998.

[4] Philippe Roux, Benoit Roman, and Mathias Fink. Time-reversal in an ultrasonic waveguide. *Applied Physics Letters*, 70(14):1811–1813, 1997.

[5] Antares Parvulescu. Matched-signal ("mess") processing by the ocean. *JASA*, 98:943, 1995.

[6] Jackson D.R. and Dowling D. R. Phase conjugation in underwater acoustics. *JASA*, 89:171–181, 1991.

[7] Dowling D. R. Acoustic pulse compression using passive phase-conjugate processing. *JASA*, 95:1450–1458, 1994.

[8] W.A. Kuperman, W.S. Hodgkiss, H.C. Song, T. Akal, C. Ferla, and D.R. Jackson. Phase conjugation in the ocean: Experimental demonstration of an acoustic time-reversal mirror. *JASA*, 103(1):25–40, 1998.

[9] W. S. Hodgkiss, H. C. Song, W. A. Kuperman, T. Akal, C. Ferla, and D. R. Jackson. A long-range and variable focus phase-conjugation experiment in shallow water. *JASA*, 105(3):1597–1604, 1999.

[10] C. Draeger and M. Fink. One channel time-reversal of elastic waves in a chaotic 2d-silicon cavity. *Phys. Rev. Lett.*, 79(3):407–410, 1997.

[11] Sylvain Yon, Mickael Tanter, and Mathias Fink. Sound focusing in rooms: The time-reversal approach. *The Journal of the Acoustical Society of America*, 113(3):1533–1543, 2003.

[12] Philippe Roux and Mathias Fink. Time-reversal in waveguide: Study of the temporal and spatial focusing. *JASA*, 107:2418–2429, 2000.

[13] M. Heinemann, A. Larraza, and K. B. Smith. Experimenatl studies of applications of time-reversal acoustics to noncoherent underwater communications. *JASA*, 113:3111–3116, 2003.

[14] K. B. Smith, A. M. Abrantes, and A. Larraza. Examination of time-reversal acoustics in shallow water and applications to noncoherent underwater communications. *JASA*, 113:3095–3110, 2003.

[15] A. Derode, A. Toupin, J. de Rosny, M. Tanter, S. Yon, and Mathias Fink. Taking advantage of multiple scattering to communicate with time-reversal antennas. *Phys. Rev. Letters*, 90:014301, 2003.

[16] C. Draeger and M. Fink. One-channel time reversal in a chaotic two-dimensional silicon cavity. *JASA*, 101:3090, 1997.

[17] Carsten Draeger, Jean-Christian Aime, and Mathias Fink. One-channel time-reversal in chaotic cavities: Experimental results. *JASA*, 105:618–625, 1999.

[18] C. Draeger and M. Fink. One-channel time-reversal in chaotic cavities: Theoretical limits. *JASA*, 105:611–625, 1999.

[19] Mathias Fink. Time reversed acoustics. *Physics Today*, 50(3):34–40, 1997.

[20] Mathias Fink. Chaos and time-reversal acoustics. *Physica Scripta*, 90:268–277, 2001.

[21] Guillaume Bal and Lenya Ryzhik. Time reversal and refocusing in random media. *SIAM J. Appl. Math*, 63(5):1475–1498, 2003.

[22] Guillaume Bal and Lenya Ryzhik. Time reversal for classical waves in random media. *C. R. Acad. Sci. Paris, Serie I*, 333:1041–1046, 2001.

[23] P. Blomgren, G. Papanicolaou, and H. Zhao. Super-resolution in time-reversal acoustics. *Journal of the Acoustical Society of America*, 111:230–248, 2002.

[24] G. Papanicolaou, L. Ryzhik, and K. Solna. Statistical stability in time reversal. *Accepted for publication in SIAM Journal of Applied Mathematics*, 2003.

[25] Arnaud Derode, Arnaud Tourin, and Mathias Fink. Ultrasonic pulse compression with one-bit time reversal through multiple scattering. *Journal of Applied Physics*, 85(9):6343–6352, 1999.

[26] G. F. Edelmann, T. Akal, W.S. Hodgkiss, S. Kim, and W. A. Kuperman. An initial demonstration of underwater acoustic communications using time reversal. *IEEE J. Ocean. Eng.*, 27:602–609, 2002.

[27] W.A. Kuperman, W.S. Hodgkiss, H.C. Song, T. Akal, C. Ferla, and D.R. Jackson. Phase conjugation in the ocean: Experimental demonstration of an acoustic time-reversal mirror. *JASA*, 103(1):25–40, 1998.

[28] Jackson D.R., Rouseff D., Fox W.L.J., Jones C.D., Ritcey J.A., and Dowling D.R. Underwater acoustic communication by passive phase conjugation: Theory and experimental results. *IEEE Journal of Oceanic Engineering*, 26:821–831, 2001.

[29] A. Kim, P. Blomgren, and G. Papanicolaou. Spatial focusing and intersymbol interference in time reversal communications. *submitted for publication*, 2003.

[30] M. G. Heinemann, A. Larraza, and K. B. Smith. Acoustic communications in an enclosure using single-channel time-reversal acoustics. *App. Phys. Letters*, 80:694–696, 2002.

[31] James V. Candy, Alan W. Meyer, Andrew J. Poggio, and Brian L. Guidry. Time-reversal processing for an acoustic communications experiment in a highly reverberant environment. *JASA*, 115(4):1621–1631, 2004.

[32] G. J. Foschini and M. J. Gans. On the limits of wireless communications in fading environments when using multiple antennas. *Wireless Personal Communications*, 6:311–335, 1998.

[33] D. Gesbert, H. Bolcskei, D. Gore, and A. Paulraj. Mimo wireless channels: Capacity and performance prediction. *GLOBECOM 2000 - IEEE Global Telecommunications Conference*, 1:1083–1088, November, 2000.

[34] Heinrich Kuttruff. *Room Acoustics.* Spon Press, Institute fur Technische Akustik, Technische Hochschule Aachen, Germany, 2001.

[35] Leo L. Beranek. *Acoustics.* McGraw-Hill, Massachusetts Institute of Technology, 1954.

[36] David T. Blackstock. *Fundamentals of physical acoustics.* John Wiley and Sons, Inc., University of Texas, Austin, 2000.

[37] S. V. Tsynkov. Numerical solution of problems on unbounded domains: A review. *Appl. Numer. Math.*, 27:465–532, 1998.

[38] Daniel Noreland. Impedance boundary conditions for acoustic waves in a duct with a step discontinuity. Technical Report 2003-032, Department of Information Technology, Uppsala University, may 2003.

[39] Walter A. Strauss. *Partial differential equations: an introduction.* John Wiley and Sons, Inc., Brown University, March 3, 1992.

[40] John C. Strikwerda. *Finite Difference Schemes and Partial Differential Equations.* Wadsworth and Brooks, University of Wisconsin, Madison, 1989.

[41] William C. Y. Lee. *Mobile Communications Engineering.* McGraw-Hill, Second Edition, Walnut Creek, California, 1997.

[42] P. Almers, F. Tufvesson, and AF Molisch. Keyhole effects in mimo wireless channels - measurements and theory. *GLOBECOM 2003 - IEEE Global Telecommunications Conference*, 22(1):1781 – 1785, December, 2003.

[43] Blast: Bell labs layered space-time. high-level overview.

[44] Dmitry Chizhik, Gerard J. Foschini, Michael J. Gans, and Reinaldo A. Valenzuela. Keyholes,correlations,and capacities of multielement transmit and receive antennas. *EEE Transactions on Wireless Communications*, 2:361–368, April, 2002.

[45] Thomas Young. The bakerian lecture: On the theory of light and colours. *Philosophical Transactions of the Royal Society of London*, 92:387–397, 1802.

[46] Thomas Young. The bakerian lecture: Experiments and calculations relative to physical optics. *Philosophical Transactions of the Royal Society of London*, 94:1–16, 1804.

[47] Grant R. Fowles. *Introduction to Modern Optics.* Holt, Rinehart and Winston, Inc., New York, 1989.

[48] Gabriel Montaldo, Phillippe Roux, Arnaud Derode, Carlos Negreira, and Mathias Fink. Generation of very high pressure pulses with 1-bit time reversal in a solid waveguide. *JASA*, 110(6):2849–2857, 2001.